TECHNISCHE UNIVERSITÄT MÜNCHEN

Physik-Department
Lehrstuhl für Funktionelle Materialien

Pressure sensitive adhesives - inner structure and adhesive performance

Dipl.-Phys. Univ. Markus Schindler

Vollständiger Abdruck der von der Fakultät für Physik der Technischen Universität München zur Erlangung des akademischen Grades eines

Doktors der Naturwissenschaften (Dr. rer. nat.)

genehmigten Dissertation.

Vorsitzender:	Univ.-Prof. Dr. Martin Zacharias
Prüfer der Dissertation:	1. apl.-Prof. Dr. Peter Müller-Buschbaum
	2. Univ.-Prof. Dr. Friedrich Simmel

Die Dissertation wurde am 30.10.2014 bei der Technischen Universität München eingereicht und durch die Fakultät für Physik am 28.11.2014 angenommen.

Abstract

In the presented thesis, the inner structure of acrylic pressure sensitive adhesive (PSA) films comprising of two components is investigated. The main focus lies on the chemical composition in the near-surface region and at the adhesive-adherent interface. The composition at these interfaces is tuned by different post-production treatments of the solution cast adhesive layers and by different cleaning procedures of the adherents. Scattering with x-rays and neutrons allows for structural investigations on the nanometer scale. The inner structure is correlated with the adhesive performance, which is addressed via mechanical probe tack tests. Moreover, a dependency of the failure mechanism during bond rupture on the ambient relative humidity is revealed. The macroscopic tack performance of the PSA and different metals is investigated. The metal film growth on (adhesive) polymer film templates is followed with in-situ x-ray scattering aiming at the metal-adhesive interactions. The near-surface structure formation of diblock copolymers is investigated by in-situ neutron scattering during solution casting, revealing the underlying kinetics details with a resolution on the nanoscale.

Zusammenfassung

Die innere Struktur von akrylatbasierten, zwei-komponentigen Haftklebstofffilmen (PSA Filme) wird untersucht. Der Hauptfokus liegt dabei auf der lokalen chemischen Zusammensetzung nahe der Oberfläche und an der Grenzfläche zum Substrat. Diese lokalen Zusammensetzungen werden mittels Nachbehandlungen der PSA-Filme, bzw. durch verschiedene Reinigungsverfahren der Substrate, gezielt beeinflusst und eingestellt. Röntgen- und Neutronenstreuung ermöglichen eine strukturelle Untersuchung auf der Nanometer-Skala. Korrelationen der inneren Struktur mit dem mechanischen Klebeverhalten, erhalten aus Stempel-Tests, werden aufgezeigt. Eine Abhängigkeit des Versagensmechanismus der Klebeverbindung in Stempel-Tests von der relativen Luftfeuchte wird beobachtet. Das makroskopische Klebeverhalten der untersuchten PSA-Filme in Kombination mit verschiedenen Metallen wird untersucht. Desweiteren wird das Wachstum von Metallschichten auf (adhäsiven) Polymerfilmen mit in-situ Röntgen-Streuexperimenten verfolgt, im Hinblick auf die Wechselwirkungen zwischen Metall und Klebstoff. Die oberflächennahe Strukturbildung von Diblock Copolymeren während des Lösungsgießens wird mittels in-situ Neutronenstreuung untersucht und die zugrundeliegende Kinetik aufgedeckt.

Contents

1. Introduction

The application of adhesives has already a long history. While up to the 19th century glues were made of plants and animals, the fabrication of adhesives is nowadays almost entirely based on synthetic chemicals [1]. As long as their history as wide is the range of applications for adhesive bonding. Many kinds of industries, for instance in the automotive or aircraft production, have already replaced their traditional ways of joining workpieces like welding or riveting by adhesive bonding. Examples of the major advantages of this kind of joining are for instance the resulting weight and cost reduction as well as the omitted need of structural weakening of the work pieces. Also human beings are subjects to adhesive bonding, e.g. in case of dental treatments [2]. Everyday-life applications of adhesives are often found to exhibit a moderate bonding strength for bond-and-release tasks like medical patches, duct tape or sticky notes. These examples are representatives of the class of pressure sensitive adhesives (PSAs). A strength of adhesives in general is the ability to join very different kinds of material, e.g. glass, paper, wood or metal [3].
PSAs are used for the immediate and also permanent bonding to almost any surface even under small pressure [4, 5, 6] . This feature of immediate adhesive bonding without the need of solvents is in literature also referred to as "instantaneous adhesion" or "quick stick" [7]. The reason for their variability lies also in the chemical nature of the involved polymers, with acrylates, rubbers and silicones being prominent representatives [8]. The attractive forces leading to adhesive bonds using PSAs are typically van der Waals forces. Therefore, no chemical reaction, melting or solvent evaporation are involved in the bond formation. The adhesive joint sustains a certain level of stress before the bond ruptures. This process of debonding is rather complex due to the dissipation of energy via plastic deformation and mechanical failure of the adhesive. Therefore, an adhesive must be balanced in terms of adhesive and cohesive strength [9].
A complete understanding of the physical processes during debonding has not been achieved so far, because the deformation of viscoelastic adhesives involves highly nonlinear effects. Moreover, due to the ability to be tuned to the desired needs by certain additives, PSAs are usually comprised of more than one component, which leads to an almost arbitrarily high complexity of the system. Some implications can be phase separation or inhomogeneous spatial distributions of the different components in the additive.

Among the different types of PSAs already mentioned above are acrylate based PSAs, which are investigated in this thesis. They typically consist of statistical copolymers, in which the two kinds of monomers fulfill the desired needs concerning adhesive and cohesive properties [4]. Block copolymers are more rarely used, but still are used in specific applications. In this work the PSAs consist of the monomers ethylhexylacrylate (EHA) being the soft and sticky component and methylmethacrylate, representing the glassy and stiff material. Commercial PSAs include many additives which are chosen on an empirical trial-and-error basis which is faster and cheaper than investigations of the involved fundamentals. Consequently, a deeper understanding of the influence of the involved additives exhibits only a slow progress.
For an unambiguous interpretation of the performed structural and mechanical investigations, this work is focused on two-component systems. The adhesive performance of such model systems for PSAs has already been investigated in literature [10, 11, 12]. Also the near-surface composition has been addressed by x-ray reflectivity [13], recently. The present work adds the investigation of i.a. the composition of the PSA in vicinity of the adhesive-adherent interface. The local composition at this buried interface is of utmost importance for possible predictions concerning duration and strength of the adhesive bond. The probe to access this adhesive-adherent interface are neutrons, which are able to penetrate both adhesive and adherent up to large depths. The methods of choice for investigations of this kind are neutron reflectivity (NR) and grazing incidence small angle neutron scattering (GISANS). While NR provides insights into the composition profiles of layered structures, GISANS offers in addition the information about i.a. the size of lateral structures.
After introducing the theoretical background of this thesis (chapter 2) the experimental methods used are detailed in chapter 3. Subsequently, the sample preparation is addressed in chapter 4.

Figure 1.1 summarizes the different aspects dealt with in the present thesis. These projects are briefly explained in the following. Chapter 5 provides insights into the inner structure of the model PSA poly(ethylhexylacrylate-stat-20 methyl methacrylate) and its adhesive performance (figure 1.1a). The main focus in this chapter is on the inner structure of the PSA film at and close to the surface and also at the adhesive-adherent interface. The question to answer is: If and how does the inner structure affect the adhesive performance? Moreover, to what degree can the performance be tuned to the desired needs? For this purpose post-production treatments with different relative humidities are applied. Also, the autoadhesion of poly(methyl methacrylate) is addressed in this chapter, which is of high interest e.g. for crack healing in polymeric materials.
Chapter 6 deals with a common adhesive application in industries, the adhesive joining of

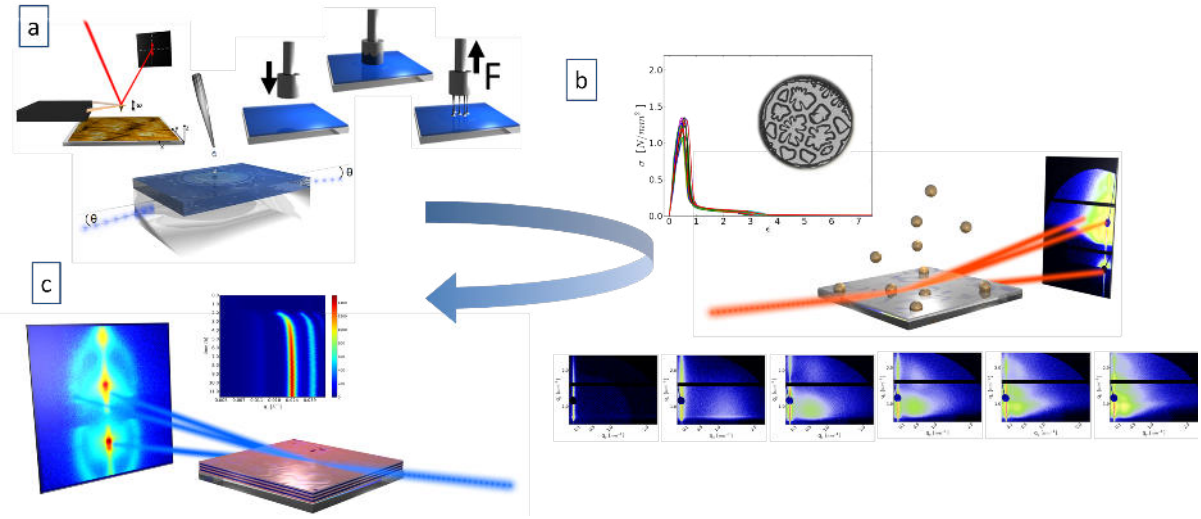

Figure 1.1.: Overview: The inner structure of a model pressure sensitive adhesive is investigated and related to its adhesive performance. Among the different techniques applied for this task are the three techniques depicted in a: Atomic force microscopy, neutron reflectivity and tack test. To investigate the bonds of metal and the model PSA (b), tack tests are performed. The metal growth on adhesive films is investigated with in-situ grazing incidence small angle x-ray scattering. Insights into the structure formation in polymer films upon solution casting are obtained by in-situ investigations of the structural evolution during drying of diblock copolymers (c). The applied techniques are neutron reflectivity and grazing incidence small angle neutron scattering.

metal work pieces (figure 1.1b). This goal can in principle be achieved by two approaches. At first, an adhesive layer can be applied on a metal surface, which is the most common case. Therefore, the tack performance of the model PSA in combination with different metal adherents is investigated. The obvious question is: How does the adhesive performance depend on the chosen metal? In another approach, the metal layer is grown on the already pre-existing adhesive polymer film. Therefore, the metal film growth and the inner structure of the metal layer are also investigated in this chapter to find out how metal films grow on different polymer templates.
Finally, in chapter 7, the structure formation of diblock copolymers during solution casting is investigated (figure 1.1c). For the first time, in-situ GISANS measurements are successfully performed at the liquid-air interface.

2. Theoretical aspects

In this chapter the key-factors for the establishment of adhesive bonds are explained. At first, van der Waals forces are introduced, which are the most relevant forces in adhesive bonding using pressure-sensitive adhesives. Subsequently, the theoretical background of surface tensions (also called surface energy) and wetting of surfaces is explained. Furthermore, the polymer-specific feature of viscoelasticity is described, along with a theoretical treatment of the tack-test. This method is used in this work to investigate the adhesive performance of a model PSA and reveals the different failure mechanisms of the adhesive bonds. These mechanisms are also addressed in this chapter. The inner structure of polymers in general and in particular of PSAs, as well as the structural evolution, are mainly governed by polymer-polymer and polymer-solvent interactions. Therefore, these interactions are also dealt with in this chapter. Scattering techniques, utilizing both x-rays and neutrons, are applied to obtain information about the spatial composition of the individual components in the polymer films on the nano-scale. While reflectivity measurements yield information about layered architectures in perpendicular direction to the sample surface, grazing incidence techniques are capable of detection and quantification also of lateral structures. The theoretical background for these techniques is explained in the end of this chapter.

2.1. Adhesion

In this section the theoretical background of adhesion is addressed. Starting from van der Waals forces, the fundamental forces responsible for the adhesion of PSAs, the main factors which influence the strength of an adhesive bond are explained. At first, the theory of surface tension and surface wetting is detailed. The polymer-specific phenomenon of viscoelasticity is subsequently addressed, before this section concludes with the theory of the tack-test and an overview over different failure mechanisms, which can occur during the debonding of an adhesive joint.

2.1.1. Adhesion, cohesion

In the case of PSAs the ability to establish adhesive bonds is mainly due to Van der Waals forces [4]. Other possibilities for adhesive joints without chemical reactions taking place can be of electrostatic nature or based on diffusion and polymer chain entanglement (see also section 5.6) [14]. Van der Waals forces can be categorized in three different kinds of interactions [1, 15]. The Keesom energy is derived from the attraction of two permanent dipoles $\vec{\mu_1}$ and $\vec{\mu_2}$ with a distance r and results in equation (2.1),

$$E_{Keesom} = -\frac{\vec{\mu_1}^2 \vec{\mu_2}^2}{3(4\pi\epsilon_0)^2 k_B T r^6}, \tag{2.1}$$

ϵ_0 being the dielectric permittivity in vacuum, k_B the Boltzmann constant and T the temperature [15]. For only one permanent dipole and another molecule with polarizability α, the permanent dipole can induce an additional dipole moment in the second molecule. This interaction is called Debye interaction which leads to the energy relation in equation (2.2) [15].

$$E_{Debye} = -\frac{\vec{\mu}^2 \alpha}{(4\pi\epsilon_0) r^6}. \tag{2.2}$$

The third van der Waals force results from two polarizable molecules. A spontaneous dipole moment is created in the first molecule via fluctuations in the electron shell. This induces a dipole in the second molecule and results in an attractive force. The corresponding energy is called London energy:

$$E_{London} = -\frac{3(\alpha_1\alpha_2)^2 I_1 I_2}{2(I_1 + I_2) r^6}, \tag{2.3}$$

with I_i being the ionization potentials of both molecules [15]. Due to the proportionality of all three contributions to r^{-6} they can be written in a single term with one contribution of each interaction:

$$E_{vdW} = -\frac{C_{Keesom} + C_{Debye} + C_{London}}{r^6} = -\frac{C_{vdW}}{r^6}. \tag{2.4}$$

At very small distances the Pauli principle takes effect [16] and outweighs the attractive forces. Therefore, two molecules cannot approach each other to an arbitrary vicinity due to the resulting repulsive potential. The total potential, taking van der Waals forces and the Pauli principle into account, is called Lennard-Jones potential [17] (see equation (2.5)).

$$E_{Lenard-Jones} = \frac{C_{Pauli}}{d^{12}} - \frac{C_{vdW}}{d^6} \tag{2.5}$$

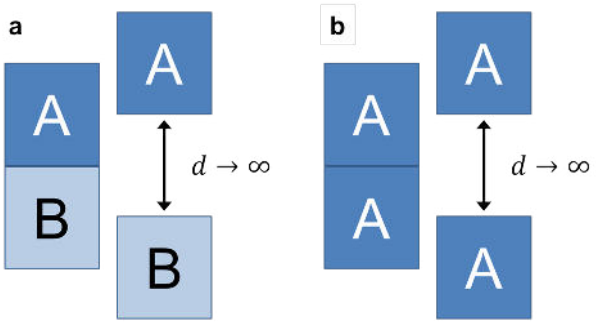

Figure 2.1: a) Work of adhesion: Separation of materials A and B from contact to infinite distance. b) Work of cohesion: Separation of two parts of the same material A from contact to infinite distance.

The thermodynamic work of adhesion $W_{Adhesion}$ is defined as the work necessary to separate two materials in contact to an infinite distance (see figure 2.1) [18]. This quantity is entirely thermodynamic which means it does not account for energy dissipation in form of e.g. deformation and therefore is not to be mixed up with the tack energy obtained from tack measurements (see chapter 2.1.4). To separate two materials of the same kind the work of cohesion $W_{Cohesion}$ is necessary [19].

2.1.2. Surface energy, wetting

The surface energy or surface tension γ_A is defined as the energy E needed to increase the surface area $\mathfrak{A}$ of a material by its unit area (2.6):

$$\gamma_A = \frac{E}{\mathfrak{A}}. \tag{2.6}$$

From the cohesion point of view the surface area of a material A can be increased by splitting it into two parts (see figure 2.1 b) and the surface energy can be written as

$$\gamma_A = \frac{1}{2} W_{AA}. \tag{2.7}$$

In case of adhesion, where two immiscible materials A and B get in contact, the free energy is minimized by a change in interfacial area. The resulting interfacial energy resembles the corresponding free energy change per unit area and is referred to as the Dupré equation [18]

$$\gamma_{AB} = \frac{1}{2} W_{AA} + \frac{1}{2} W_{BB} - W_{AB} = \gamma_A + \gamma_B - W_{AB}. \tag{2.8}$$

In practice, the Dupré equation is used for liquid-solid interfaces and therefore reads

$$\gamma_{SL} = \gamma_S + \gamma_L - W_{SL}. \tag{2.9}$$

This situation can be discribed using the Young and Young-Dupré equations [18]:

$$\text{Young-Dupré equation: } \gamma_B \left(1 + \cos(\Theta)\right) = W_{AB} \tag{2.10}$$

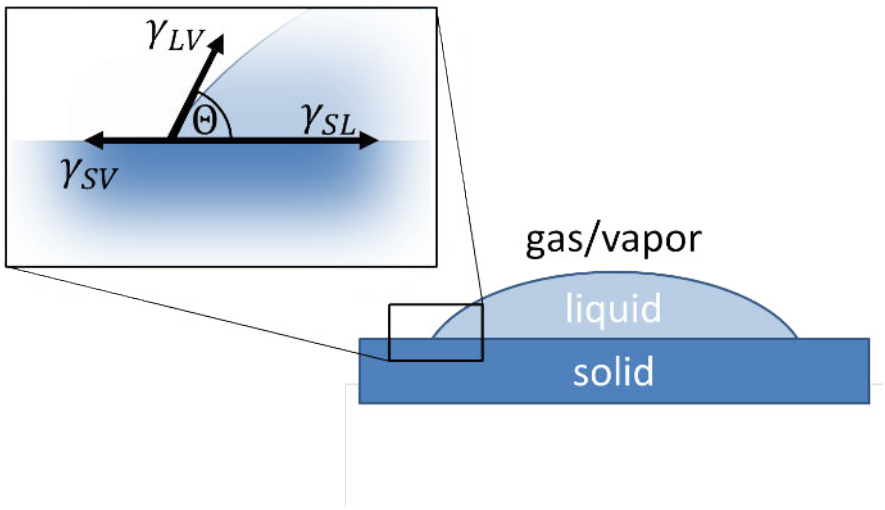

Figure 2.2.: A liquid (L) wetting a solid (S) under ambient conditions (V). Θ denotes the contact angle.

$$\text{Young equation: } \gamma_{AB} + \gamma_B \cos(\Theta) = \gamma_A. \tag{2.11}$$

Equation 2.10 yields the work of adhesion of a liquid droplet on a solid substrate based on the contact angle and the surface energy of the liquid. The Young equation (equation 2.11) provides means to access the interfacial energies from known single surface energies and a measured contact angle. The work of adhesion does not enter in equation 2.11.
An important prerequisite for strong adhesive bonding is proper wetting [20], which means that the contact angle Θ between adhesive and adherent needs to fulfill $\Theta \leq 90°$ (see figure 2.2). More detailed discussions about wetting, its statics and dynamics and major impact factors can be found in [14, 21, 22, 23, 24]. To derive the surface energies of a given solid, Owens and Wendt [25] used the Young equation, knowing the surface tensions of a set of test liquids. These surface tensions were deduced from contact angle measurements on the solid specimen. This approach is based on the postulation that a surface tension can always be described as the sum of a dispersive and a polar part [26]. The London forces are the origin for the dispersive contribution, while the Keesom and Debye forces determine the polar part (see section 2.1.1). For an exemplary liquid L on a solid S this approach reads

$$\gamma_L = \gamma_L^d + \gamma_L^p \text{ and } \gamma_S = \gamma_S^d + \gamma_S^p. \tag{2.12}$$

The relation to the solid-liquid interfacial tension becomes

$$\gamma_{SL} = \gamma_S + \gamma_L - 2\sqrt{\gamma_S^d \gamma_L^d} - 2\sqrt{\gamma_S^p \gamma_L^p}, \tag{2.13}$$

and by the use of the Young equation, equation 2.14 can be derived [25]:

$$1 + \cos\Theta = 2\sqrt{\gamma_S^d}\frac{\sqrt{\gamma_L^d}}{\gamma_L} + 2\sqrt{\gamma_S^p}\frac{\sqrt{\gamma_L^p}}{\gamma_L}. \tag{2.14}$$

For clarity the subscripts for the liquids can be skipped and only the solid under investigation is subscripted in the following. Equation 2.14 can be rewritten as a linear equation:

$$\frac{(1+\cos(\Theta))\,\gamma}{2\sqrt{\gamma^d}} = \sqrt{\gamma_{solid}^d} + \sqrt{\gamma_{solid}^p}\sqrt{\frac{\gamma}{\gamma^d} - 1}. \tag{2.15}$$

This linear equation has a slope $\sqrt{\gamma_{solid}^p}$ and an intersection with the y-axis at $\sqrt{\gamma_{solid}^d}$. All terms are known, except the contact angle Θ, which is the quantity to be measured. This non-destructive method to derive the dispersive and the polar part of the surface tension via contact angle measurements is called Owens-Wendt method. Six different test liquids are used in this work to improve the accuracy of the resulting surface tension. A linear fit to the six measured data points was done to minimize the measurement uncertainty.

2.1.3. Viscoelasticity

The strength of a successfully installed adhesive bond depends also on the ability of the adhesive to dissipate energy while debonding, meaning sustaining a certain level of stress [27]. In PSAs this is usually realized via mechanical deformation. Viscoelasticity is an unique property of polymers and applies especially to PSAs. So-called creep experiments can be carried out to address this feature [28]. In these experiments, a force is instantaneously applied to the specimen and the time dependent deformation of the polymer is measured. This elongation is commonly normalized to the original sample length to obtain the time-dependent longitudinal strain ϵ(t). After a time t, the force is removed and the recovery process of the specimen can be followed. Considering sufficiently small applied forces the reaction of the polymer can be described by linear equations. Figure 2.3 schematically shows possible results for the strain for an uniaxial applied tensile load. It is obvious that viscoelasticity is not just a superposition of viscocity and elasticity, but comprises also a phenomenon called anelasticity. An elastic specimen under an applied constant force follows Hook's law (figure 2.3a), while a material exhibiting viscous flow undergoes permanent deformation accompanied by stress relaxation (figure 2.3b). The behavior of a viscoelastic polymer is shown in figure 2.3c, where the anelastisity can be observed as a retarded elasticity. The time-dependent longitudinal strain ϵ(t) can be specified more precisely $\epsilon(t) = \epsilon_{zz}(t)$. The first index refers to the direction of the normal vector of the surface on which the force acts upon. The second index denotes the direction of the stress component [28]. By normalizing the acting force to the area it is

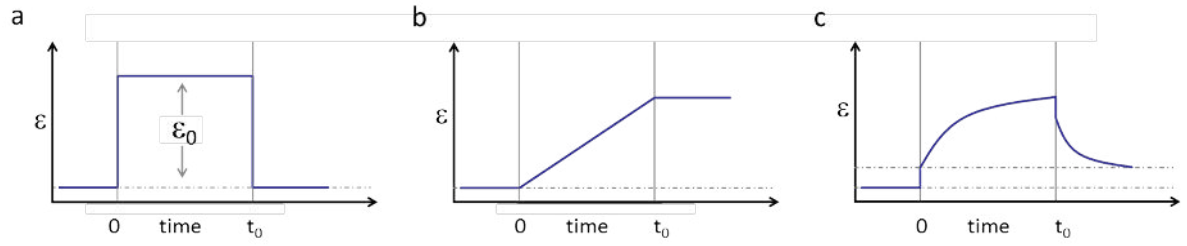

Figure 2.3.: Longitudinal strain evolution versus time for different behaviors: a) elasticity, b) viscosity, c) viscoelasticity.

acting on, a constant tensile stress σ_{zz}^0 is derived. Finally, the tensile creep compliance $\tilde{D}(t) = \epsilon_{zz}(t)/\sigma_{zz}^0$ can be introduced [28].
Another approach to access the viscoelastic properties is the stress relaxation experiment. In this method a constant tensile strain ϵ_{zz}^0 is imposed to the specimen and the time dependent stress $\sigma_{zz}(t)$ is measured. Thereby, the tensile modulus $\tilde{E}(t) = \sigma_{zz}(t)/\epsilon_{zz}^0$ is obtained [28].
In a third kind of experiment a periodically varying stress field $\sigma_{zz}(t) = \sigma_{zz}^0 \exp[-i\omega t]$ is applied. The resulting strain reads [28]

$$\epsilon_{zz}(t) = \epsilon_{zz}^0 \exp[i\Phi] \exp[-i\omega t]. \tag{2.16}$$

The dynamic tensile compliance $\tilde{D}(\omega)$ and along with it the dynamic tensile modulus $\tilde{E}(\omega)$ follow:

$$\tilde{D}(\omega) = \frac{\epsilon_{zz}(t)}{\sigma_{zz}(t)} = \tilde{D}' + i\tilde{D}'' \tag{2.17}$$

$$\tilde{E}(\omega) = \left(\tilde{D}(\omega)\right)^{-1} = \tilde{E}' + i\tilde{E}''. \tag{2.18}$$

In applications the dynamic shear modulus $\tilde{G}(\omega)$ of PSAs is of utmost importance and therefore experiments usually adress this quantity [28]:

$$\tilde{G}(\omega) = \frac{\sigma_{zx}(t)}{\epsilon_{zx}(t)} = \frac{\sigma_{zx}^0 \exp[-i\omega t]}{\epsilon_{zx}^0 \exp[i\Phi] \exp[-i\omega t]} = \frac{\sigma_{zx}^0}{\epsilon_{zx}^0} \exp[-i\Phi] = \tilde{G}'(\omega) + i\tilde{G}''(\omega). \tag{2.19}$$

$\tilde{G}'$ is referred to as storage modulus and $\tilde{G}''$ as loss modulus. $\tilde{G}'$ is the quantity responsible for the energy exchange in dynamic experiments, whereas $\tilde{G}''$ gives information about the dissipated power. Due to the fact that the described dynamic measurements do not deliver the same amount of information as creep or stress relaxation measurements, they are not only performed at one single frequency ω, but in ranges over up to four orders of magnitude [28]. To even enlarge this still limited range, these experiments are carried out at different temperatures, which further completes the knowledge of the viscoelastic behavior of the specimen. The measurements carried out at different temperatures, each across a broad

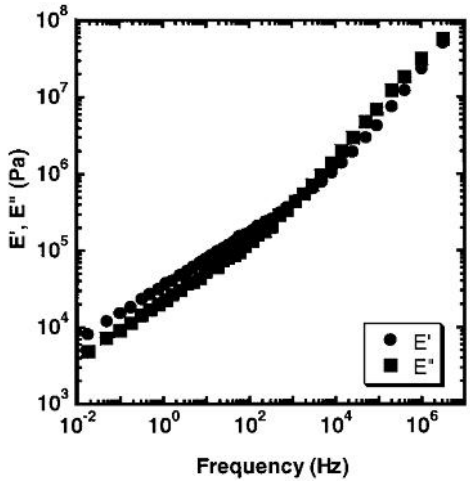

Figure 2.4: Rheological data for poly(ethylhexylacrylate) (PEHA): E' denotes the storage modulus, E'' denotes the loss modulus. Time-temperature superposition was applied to obtain a master curve. The image is taken from [30].

frequency range, are then combined using a temperature-dependent shift factor to obtain the so-called master curve [29]. Exemplary master curves for storage and loss moduli are shown in figure 2.4. The data was collected for the homopolymer poly(ethylhexylacrylate), a standard component in model PSAs, with a parallel plate shear rheometer using a spectrum of temperatures and frequencies which were then combined via time-temperature superposition to obtain the master curves [30].

2.1.4. Tack test, failure mechanisms

The most important property of an adhesive is the ability to form bonds of a desired strength between different kinds of materials. In particular the class of PSAs is capable of joining very different materials such as paper, wood or metal [3, 10]. To test the performance of an adhesive many mechanical tests are used, which mimic certain applications of the adhesive to account for e.g. mechanical deformation. Well established examples are the rolling-ball-test [31, 32], rolling cylinder test [33], peel-test [34, 35], Johnson-Kendall-Roberts method [36], the tack [3, 37, 38] and the loop tack test [39] and finally the finger [40] and the shear adhesion test [41]. For adhesion measurements on the nano scale the atomic force microscope (AFM) is the method of choice [42, 43] which is sensitive even to friction and rupture of single polymer chains [44]. For scientific approaches and systematic investigations the probe tack test offers several advantages which make this method superior to others and which will be explained in the following. In a tack test (see figure 2.5) a cylindrical probe of radius r is pressed onto an adhesive layer of thickness h for a given time period t and thus creates a nominal stress σ_N (figure 2.5b). Subsequently, the punch is retracted at a constant rate v and the necessary force F is recorded as a function of the distance to the sample surface d (figure 2.5c). The outcome of such a tack experiment is the corresponding tensile stress σ_{zz} as a function of the distance d. For

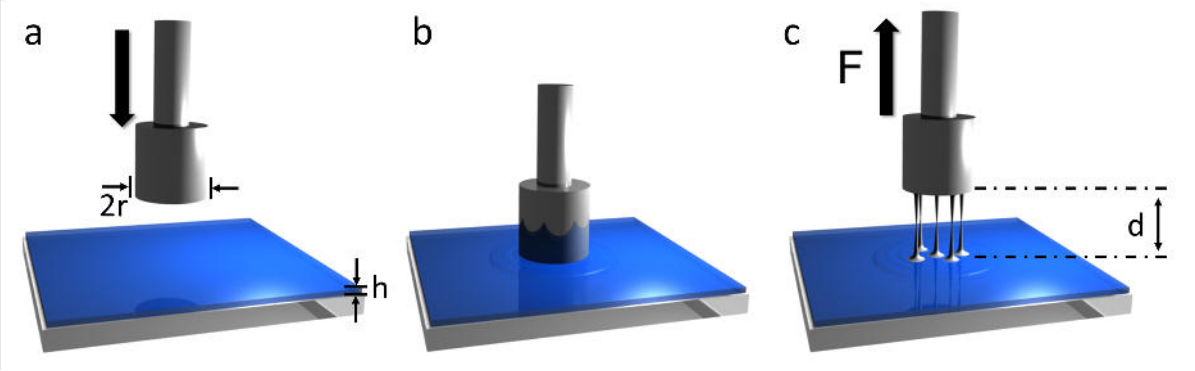

Figure 2.5.: Principle of a tack measurement: a) The punch with radius r approaches the PSA film (thickness h). b) The punch and the PSA are kept in contact by applying a pressure for a certain time. c) The punch is retracted and a force-distance curve is recorded.

probing the PSA different punch tip geometries are possible, e.g. spherical or flat ended [45]. The spherical punch provides better reproducible results by a reduced sensitivity to alignment and is therefore mostly used in industry. The geometry used in this work is the flat-ended cylinder, which results in a homogeneous stress distribution in the PSA and consequently a homogeneous debonding. Furthermore, this work is focussed also on the near-surface region of the PSA, up to 100 nm in depth. To be able to probe regions of this depth and smaller, a flat-ended punch is crucial due to its high surface sensitivity. For an unambiguous interpretation of the obtained tack results it is required that the bond between the PSA and its substrate is stronger than the bond between PSA and punch probe, so that only the surface-near region of the PSA is probed in the experiment.
The stress field in the adhesive layer below the punch is a function of the ratio $\alpha = r/h$, which is referred to as the confinement [46]. This stress field can only be calculated via finite element methods [45]. For large values of α however, the pressure distribution $p(r)$ is found to be parabolic [47]

$$p(r) = -\sigma_{zz}(r) = p_0 - 2\lambda\sigma_N \left(1 - \frac{r^2}{a^2}\right), \tag{2.20}$$

with r being the radial distance from the symmetry axis, p_0 the external (usually atmospheric) pressure, $\lambda = (h + d)/h$ the extension ratio, σ_{zz} the normal and σ_N the nominal tensile stress. σ_N is derived from the tensile load P by $\sigma_N \equiv P/(\pi r^2)$. For an incompressible elastic solid the nominal stress reads

$$\sigma_N = \frac{8Gd}{\pi r}. \tag{2.21}$$

For even a slight deviation from incompressibility the stress field below the probe punch becomes rather flat [45]. This is experimentally evidenced by the fact that in case cavitation occurs, it is observed simultaneously over the whole surface of the probe [48].

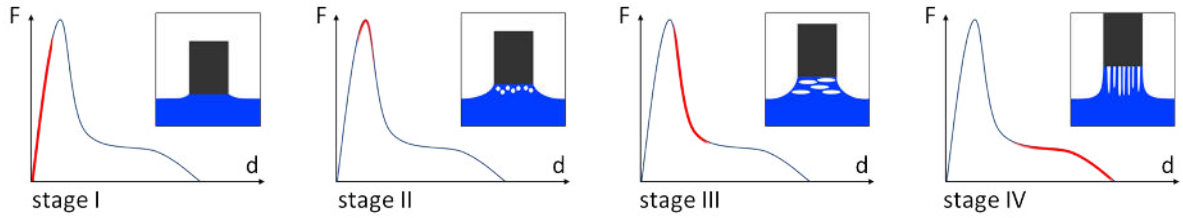

Figure 2.6.: Four-stage model by Creton [49]: The red lines highlight different time periods at characteristic distances of punch and PSA during a typical tack experiment (blue line). Each inset corresponds to the respective period and schematically shows the present stage of cavitation.

The performance of an adhesive is governed by its resistance against separation of adhesive and adherent. In the case of PSAs this separation process is accompanied by the mechanisms of cavitation and fibrillation which will be explained in the following. During debonding small voids inside the PSA appear (cavities), which grow and get elongated until the material between them forms only thin fibers (fibrils). The complete separation process of PSAs has been phenomenologically described by Creton [49] who divided the debonding in four different stages (see figure 2.6): In the beginning of the separation (stage I) the adhesive gets homogeneously deformed while no cavities are present. During this stage the force F increases rapidly. Around the force maximum of the tack curve first voids appear in the bulk of the adhesive (stage II), close to the interface to the punch [48]. During the fast decay of the force F the cavities grow laterally (stage III) until they grow vertically for larger distances d (stage IV). The material between the vertically elongated cavities is now continuously elongated until these fibrils successively rupture and the force F finally drops to zero.

A theoretical description of the cavity growth assumes a single spherical void of radius R_c^0 (stage II), filled with an ideal gas [50]. The surrounding material of this void is considered to be inelastic, infinite and incompressible, having a surface tension γ. The Laplace-pressure represents the pressure difference between inside and outside the void and reads $-2\gamma/R_c^0$ in this case [50]. The outside pressure is identical to the applied pressure p, whereas the pressure inside the void deviates from the initial pressure p_0 and follows from the ideal gas equation. Under the assumption that the spherical shape is maintained (which strictly only holds within the early stage II) the pressure reads [50]

$$p = \frac{p_0}{\lambda_R^3} - \frac{2\gamma}{\lambda_R R_c^0}, \tag{2.22}$$

where L_R represents to the ratio of extension of the void. Closer to reality is the assumption of an elastic medium. An additional elastic inflation pressure p_{el} needs to be accounted for to maintain the elastic deformation of the surrounding material. This leads

to the model of the so-called neo-Hookean material, which is the simplest constitutive model describing the elasticity of rubber at finite strains [50] and leads to

$$p = \frac{p_0}{\lambda_R^3} - \frac{2\gamma}{\lambda_R R_c^0} - E\frac{1}{6}\left(5 - \frac{4}{\lambda_R} - \frac{1}{\lambda_R^4}\right), \tag{2.23}$$

E being the Young's modulus. This approach to tackle the tack experiment theoretically is however very limited. It is for instance not applicable to the vertical growth of cavities and does not account for plastic deformation or flow. It ignores the fact that voids can merge and is limited to small strains and is not including failure mechanisms at large strains. The theory behind this experiment has of course already been taken to higher complexity also using different approaches [50, 51, 52]. A complete theoretical description however, is still not achieved.

Depending on many influencing factors, e.g. surface energies, confinement, roughness, Young's modulus, etc. different failure mechanisms of the adhesive bond may occur [30]. First of all it is important to note that the failure of an adhesive bond can be twofold in nature. The first possibility is cohesive failure, where the failure occurs in the adhesive layer itself. In the second case, the adhesive failure, the interface of adhesive and adherent is the origin of the failure [27].

During the debonding in tack experiments on PSAs, three different kinds of failure mechanisms have been reported [53] (see figure 2.7a): Cavitation as a way of failure has already been explained above. Under certain circumstances also external and internal crack propagation can be observed. External cracks originate from defects at the edge of the probe and are always vertically located at the adhesive-adherent interface. Internal cracks on the other hand do not touch the outer rim of the punch. Figure 2.7b shows a deformation map developed by Creton et al. which allows for prediction of the failure mechanism of a certain punch-PSA combination [53]. Three regions can be seen, corresponding to cavitation, external crack propagation and internal crack propagation. The occurrence of one or the other mechanism depends for one on the ratio of probe radius and adhesive layer thickness $= a/h$, referred to as confinement. Moreover, the quantity represented by the y-axis in figure 2.7, $\mathcal{G}_0/Ea$, plays a major role, where E represents the Young's modulus, a the punch radius and $\mathcal{G}_0$ the critical energy release rate. $\mathcal{G}_0$ is an interfacial parameter, sensitive to the adhesion between punch and PSA. Although this map allows in principle for predictions, in practice however, they are difficult to derive because in most cases $\mathcal{G}_0$ is unknown and not easy to deduce [53].

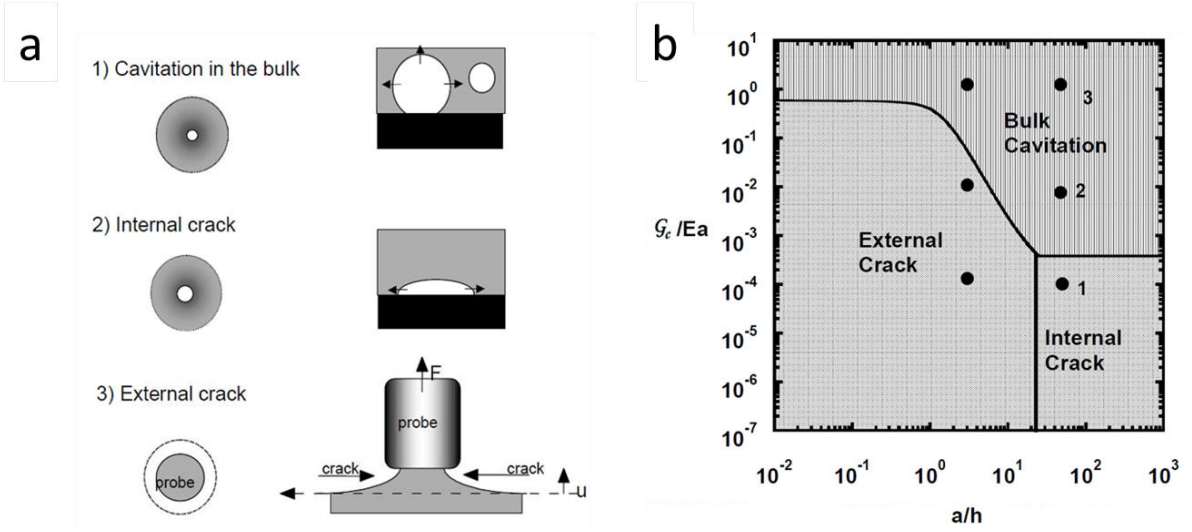

Figure 2.7.: a) Illustration of the initial failure mechanism of a PSA layer. b) Deformation map showing three distinct regions, each for one of the three failure mechanism. The images are taken from [27].

2.2. Polymer and solvent

Most systems investigated in this work consist of more than one component, i.a. combined in so-called statistical copolymers. In this section the architecture of statistical copolymers is described, followed by a short introduction of the theory of solubility.

2.2.1. Statistical copolymers

Polymers are macromolecules comprising of a large number of repeated subunits, so-called monomers, which are chemically linked by covalent bonds. The architecture of such a polymer chain can be arbitrarily complex [54]. The simplest example is the linear chain, which is also the architecture of the polymers investigated in this work. Polymers consisting of more than one kind of monomer are called copolymers [55]. The sequence of the different monomers determines a further categorization. Alternating blocks of monomers of kind A and kind B are called block-copolymers.
For PSA applications the statistical copolymer plays an important role, in which two kinds of monomers are distributed statistically along the chain [56]. Figure 2.8 shows a schematic of a linear statistical copolymer. Another important parameter describing the polymer is its degree of polymerization, i.e. the number N of monomers which comprise the polymer [55]. Closely linked is the molecular weight M. For polymers two more quantities are of utmost importance: The number average molar mass M_n and the weight

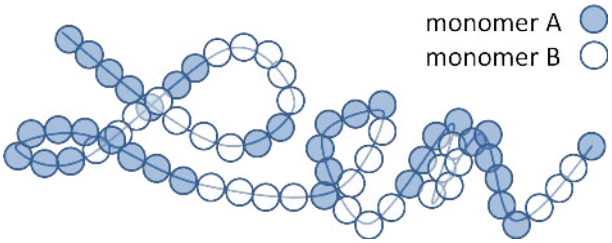

Figure 2.8: Schematic of a statistical copolymer comprising of two kinds of monomers A and B which are distributed statistically along the chain.

average molar mass M_w:

$$M_n = \int_0^\infty p(M) M dM, \tag{2.24}$$

$$M_w = \frac{\int_0^\infty p(M) M^2 dM}{\int_0^\infty p(M) M dM}, \tag{2.25}$$

where $p(M)$ denotes the distribution function of molar masses of the chains [55]. These two quantities lead to the polydispersity index (PDI):

$$PDI = \frac{M_w}{M_n} \geq 1. \tag{2.26}$$

In reality a polymer never reaches a $PDI = 1$, but always exhibits a certain polydispersity ($PDI > 1$). The chemical reactions during the synthesis of a statistical copolymer lead to several implications adding to the complexity of a theoretical treatment. Ideally, the monomers A and B should be randomly distributed along the chain. The reactions in which the monomers bond during the synthesis are in practice not equally likely. This means, that the probability of an establishment of an A-A bond differs from an A-B and a B-B bond. The conditional probability p_{KL} ($K, L \in \{A, B\}$) describes the likelihood of a monomer of type L following a monomer of kind K [57].

2.2.2. Solubility

Due to the fact that many polymeric coating techniques are solution based, the solubility of polymer and solvent is an important issue. Different approaches exist to quantify the respective solubilities, e.g. the Kaouri-Butanol number, the solubility grade, the aromatic characterization or the Hildebrand solubility parameter [58]. More complex quantifications are the Hildebrand number, the hydrogen bonding value or the Hansen parameter [59].

For low polarities, which mostly occur in this thesis, the Hildebrand parameter is found to be essential to understand the reorganization in the PSA films. In general, the dissolution of a polymer in a given solvent only occurs if the Gibbs free energy G is decreased upon mixing. The change in Gibbs free energy ΔG_{mix} reads

$$\Delta G_{mix} = \Delta H_{mix} - T \Delta S_{mix}, \tag{2.27}$$

T being the temperature, ΔH_{mix} the change in enthalpy and ΔS_{mix} the change in entropy [60]. Clearly ΔS_{mix} is always positive in mixing processes, which leads to the conclusion that the sign and magnitude of ΔH_{mix} is responsible for the solubility of the system. To obtain a good solution, the polymer chains need to be surrounded by solvent molecules. The polymers and solvents used in this work interact mainly via van der Waals forces. Therefore, it is advantageous to find similar attractive forces between polymer-polymer and polymer-solvent. Using this approach Hildebrand [61] and Scatchard [62] derived ΔH_{mix} to be

$$\Delta H_{mix} = V_{mix} \left(\sqrt{\frac{\Delta E_1^v}{V_1}} - \sqrt{\frac{\Delta E_2^v}{V_2}} \right)^2 \Phi_1 \Phi_2, \tag{2.28}$$

where V_{mix} is the volume of the mixture, ΔE_i^v are the energy changes upon isothermal vaporization at infinite volume, V_i the molar volumes and Φ_i the volume fractions of the involved polymer ($i = 1$) and solvent ($i = 2$). The Hildebrand solubility parameters $\mathfrak{D}_i$ represent a measure of the strength of attraction between the molecules of a material and are defined by

$$\mathfrak{D}_i = \sqrt{\frac{\Delta E_i^v}{V_i}} \; (i = 1, 2), \tag{2.29}$$

with ΔE_i^v representing the respective cohesive energy densities [60]. Using these parameters, equation 2.28 simplifies to

$$\Delta H_{mix} = (\mathfrak{D}_1 - \mathfrak{D}_2)^2 \, V_{mix} \Phi_1 \Phi_2 \geq 0. \tag{2.30}$$

With this it is obvious that in order to minimize ΔH_{mix}, and thus also ΔG_{mix}, polymer and solvent must exhibit similar Hildebrand parameters. A more detailed description can be found in [61, 60].

2.3. Scattering methods

Due to the fact that also the inner structure of a polymer film majorly determines its function and performance in applications, it is of utmost importance to obtain a detailed and reliable picture of the structural composition of the sample of interest. Microscopic real space techniques like atomic force microscopy (AFM), scanning transmission microscopy (STM) or transmission electron microscopy (TEM) are, if combined, able to draw such a coherent picture. However, to obtain information about the film volume, these methods require destructive means like slicing or cutting the sample. Moreover, only small areas of the sample can be probed. Therefore, elastic scattering techniques are in many cases a superior approach. A large footprint of the beam on the sample ensures results with a much higher statistical relevance, while still providing structural resolution on the

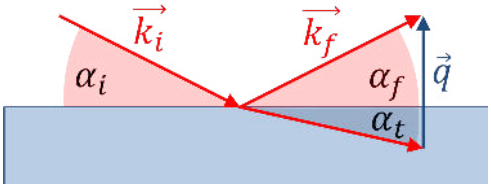

Figure 2.9: Specular reflection of x-rays at an interface ($\alpha_i = \alpha_f$), $\vec{q}$ denotes the momentum transfer.

nanoscale. Moreover, x-ray and neutron scattering are non-destructive and are also capable of probing the bulk of the sample. In this section the theoretical background for x-ray and neutron reflectivity (XRR and NR) as well as grazing incidence small angle x-ray and neutron scattering (GISAXS and GISANS) is introduced. XRR and NR yield vertical composition profiles, while GISAXS and GISANS also provide information about lateral structures.

2.3.1. X-ray reflectivity (XRR)

In XRR the intensity of a specularly reflected x-ray beam is monitored as a function of the angle of incidence α_i. The basic geometry is depicted in figure 2.9. For monochromatic measurements this angle corresponds to the z-component of the scattering vector $\vec{q}$, given that x- and y-components are zero:

$$q_z = (\vec{k_f} - \vec{k_i})_z = \frac{4\pi}{\lambda} \sin(\alpha_i). \tag{2.31}$$

X-rays interact with the electrons in the atomic shells. The index of refraction can be deduced [63] to be

$$n(\vec{r}) = 1 - \delta(\vec{r}) + i\beta(\vec{r}), \tag{2.32}$$

already including the terms for dispersion δ and absorption β:

$$\delta(\vec{r}) = \frac{\lambda^2}{2\pi} r_e \rho(\vec{r}) \sum_{j=1}^{N} \frac{f_j^0 + f_j'(E)}{Z}, \tag{2.33}$$

$$\beta(\vec{r}) = \frac{\lambda^2}{2\pi} r_e \rho(\vec{r}) \sum_{j=1}^{N} \frac{f_j''(E)}{Z} = \frac{\lambda}{4\pi} \mu(\vec{r}), \tag{2.34}$$

where λ denotes the wavelength, $r_e = e^2/(4\pi\epsilon_0 mc^2)$ the classical electron radius, $\rho(\vec{r})$ the electron density. The quantities f_j^0, f_j', f_j'' are tabulated and $\vec{q}$-dependent scattering factors [64], while $Z = \sum_j Z_j$ is the total number of electrons. The quantity $\mu(\vec{r})$ represents the linear absorption coefficient. It is important to note that for x-rays δ is always smaller than 1, which leads to the fact that total external reflection occurs for angles smaller than the critical angle α_c of the material. Throughout this work angles are measured with respect to the interface, not to the surface normal as it is common for optics in the

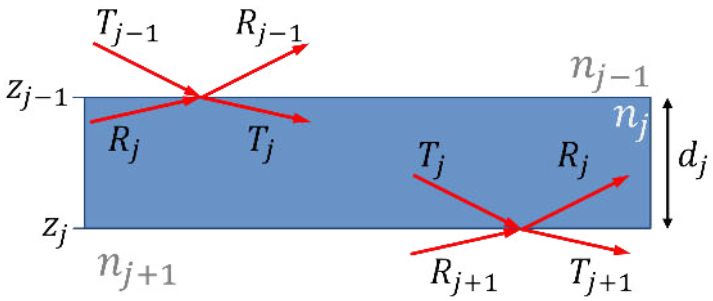

Figure 2.10: Nomenclature for the Parratt algorithm: transmitted and reflected beams are shown at two exemplary interfaces of a multilayer.

visible range. In figure 2.9 the reflection geometry for specular reflection is depicted. The direction of the transmitted beam α_t can be calculated following Snell's law of refraction. The intensities are directly proportional to the squared amplitude ratios with respect to the incoming beam and are referred to as Fresnel reflection and transmission coefficients r^F and t^F, respectively [63]:

$$r^F = \frac{\sin(\alpha_i) - \sqrt{n^2 - \cos^2(\alpha_i)}}{\sin(\alpha_i) + \sqrt{n^2 - \cos^2(\alpha_i)}}, \tag{2.35}$$

$$t^F = \frac{2\sin(\alpha_i)}{\sin(\alpha_i) + \sqrt{n^2 - \cos^2(\alpha_i)}}. \tag{2.36}$$

The reflectivity is defined as $R_F = |r^F|^2$ and reads [63]

$$R_F = \frac{(\alpha_i - p_+)^2 + p_-^2}{(\alpha_i + p_+)^2 + p_-^2}\,, \text{with} \tag{2.37}$$

$$p_\pm^2 = \frac{1}{2}\left(\sqrt{(\alpha_i^2 - \alpha_c^2)^2 + 4\beta^2} \pm (\alpha_i^2 - \alpha_c^2)\right). \tag{2.38}$$

In practice, at least two interfaces need to be taken into account because each polymer sample is supported by a substrate, e.g. silicon. Moreover, internal layer structures can be present in the sample which also increases the necessary number of layers and therefore the number of interfaces. The beam passing through several layers also suffers from absorption. A schematic sketch of reflection on such a multilayer is shown in figure 2.10. The interfaces are located at the positions $z_j, j \in [0, N]$, where z_0 denotes the sample surface.

The incoming beam has an amplitude of $T_1 = 1$. Within each layer j the quantity $\vec{k}_{i,j}$ denotes the wavevector and T_j represents the amplitude of the transmitted wave. The quantities $\vec{k}_{f,j}$ and R_j correspond to the wave after the reflection at position z_j. The starting assumption for the calculation of the reflectivity R_1 of the complete multilayer is $R_{N+1} = 0$ at the interface to the substrate. The first successful calculation of the full reflectivity was performed by Abelés using a matrix formalism [65]. Parratt developed an equivalent, however numerically more efficient recursive formalism [66]: Given a known

ratio of reflectivity and transmittivity, $X_{j+1} = R_{j+1}/T_{j+1}$, for a layer $j+1$, this ratio can be deduced for layer j using equation 2.39:

$$X_j = \frac{R_j}{T_j} = \exp(-2ik_{z,j}z_j)\frac{r_{j,j+1} + X_{j+1}\exp(2ik_{z,j+1}z_j)}{1 + r_{j,j+1}X_{j+1}\exp(2ik_{z,j+1}z_j)}, \tag{2.39}$$

with

$$r_{j,j+1} = (k_{z,j} - k_{z,j+1}) \,/\, (k_{z,j} + k_{z,j+1}) \tag{2.40}$$

being the Fresnel reflection coefficient of interface j, and $k_{z,j} = k\left(n_j^2 - \cos(\alpha_i)^2\right)^{1/2}$ being the z-component of the wavevector in layer j. The starting point for the calculation is $X_{N+1} = R_{N+1} = 0$ from which all X_j can iteratively be determined. The total reflectivity therefore becomes $R_{total} = |X_1^2|^2 = |R_1^2|^2$. In real systems each interface suffers from a certain roughness which smoothens the transition of refractive index. The average roughness σ_{avg} and the root mean squared (rms) roughness σ_{rms} of interface j are defined by [67]:

$$\sigma_{avg} = \frac{1}{N_{\sigma_j}} \sum_{k=1}^{N_{\sigma_j}} \left| z_j^k - z_j \right| \tag{2.41}$$

$$\sigma_{rms} = \sqrt{\frac{1}{N_{\sigma_j}} \sum_{k=1}^{N_{\sigma_j}} \left(z_j^k - z_j \right)^2}. \tag{2.42}$$

An error function $erf(z) = \int_0^z \exp -t^2 dt$ was introduced by Névot and Croce for the transition from a layer j to a layer $j+1$ [68]:

$$n_j(z) = \frac{n_j + n_{j+1}}{2} - \frac{n_j + n_{j+1}}{2} erf\left(\frac{z - z_j}{\sqrt{2}\sigma_{rms}}\right). \tag{2.43}$$

The error function is implemented in the *Motofit*-package used in this work for fitting reflectivity data [69]. To include roughness into the described model, the Fresnel reflection coefficients (eq. 2.40) are corrected by an additional factor. The resulting coefficients read

$$r_{j,j+1}^{corr} = r_{j,j+1} \exp -2k_{z,j}k_{z,j+1} \left(\sigma_{rms}\right)^2, \tag{2.44}$$

where the exponential function is called Névot-Croce factor. This approach holds for values of roughness up to the layer thickness. Several programs are available to perform simulation and fitting of reflectivity data, the most prominent representatives are *Parratt32* [70], *Reflfit* [71], *GenX* [72] and the *Motofit*-package [69] for *IGOR pro*. The latter is used in this work. In Figure 2.11a the reflectivity for an exemplary 20 nm thick layer of homogeneous PMMA on SiO_2 is calculated for three different (rms-) roughness values, assuming a constant background of 10^{-6}. It can easily be seen, that for a perfectly flat surface the characteristic oscillations, the so-called Kiessig-fringes [73], are visible up to high

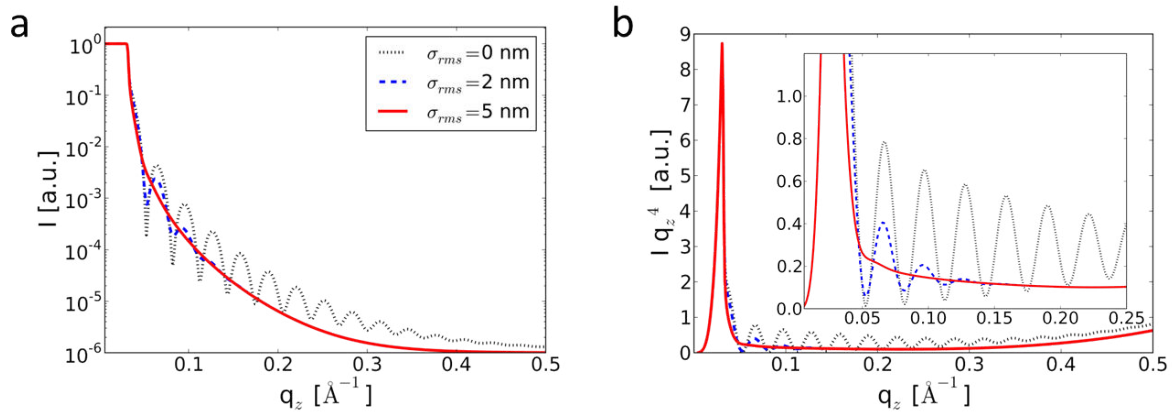

Figure 2.11.: a) XRR simulations for a homogeneous PMMA film on SiO_2. Three different values for the surface rms-roughness are used: σ_{rms} =0 nm, 2 nm and 5 nm. b)The same XRR simulations plotted in the Fresnel-normalized representation. The inset shows a zoom-in for better visibility of the low q_z region.

q_z-values. The higher the interfacial roughness the more these fringes get damped. From the q_z-spacing of the fringes, the film thickness can be estimated via $d \approx 2\pi/\Delta q_z$. From a Taylor expansion of $R_F(\alpha_i)$ (see eq. 2.37) it follows that for $\alpha_i > 3\alpha_c$ the reflectivity of a flat interface to an infinitely thick layer can be written as [63]

$$R_F = \left(\frac{\alpha_c}{2\alpha_i}\right)^4. \tag{2.45}$$

This directly translates into a dependency of $R_F \propto q_z^{-4}$ which is utilized in the so-called Fresnel-normalized representation of reflectivity data: The reflected intensity R_F is multiplied by the factor q_z^4 to remove the generic decay of the reflectivity. Figure 2.11b shows the same simulations of 20 nm PMMA on SiO_2 in the Fresnel-normalized representation. It becomes clear that in this representation features close to the edge of total reflection become more pronounced, which were hidden in the steep decay before. Therefore this representation is mostly chosen in this work.

2.3.2. Neutron reflectivity (NR)

In contrast to x-rays which interact with the shell-electrons, the uncharged neutrons interact with the atomic nuclei. Nonetheless, the same formalism is able to treat both kinds of scattering, XRR and neutron reflectivity (NR), identically. The different interactions are accounted for in a different definition of the scattering length density for neutrons, whereas the refractive index (as derived from the Helmholtz equation [64]) is unchanged:

$$n_n = 1 - \delta_N + i\beta_n. \tag{2.46}$$

The dispersion and absorption for neutrons read:

$$\delta_n = \frac{\lambda^2}{2\pi} N b, \tag{2.47}$$

$$\beta_n = \frac{\lambda}{4\pi} N \alpha_a, \tag{2.48}$$

with the number density of atoms N, the coherent scattering amplitude of a bound atom b and the absorption cross section for neutrons α_a. Hence, the SLD for neutrons is

$$SLD_n = Nb. \tag{2.49}$$

For neutrons δ_n is on the order of 10^{-6} and β of 10^{-12} [63], which is why in literature the absorption is often considered to be negligible and therefore omitted [74]. The big advantage of neutrons compared to x-rays, especially in the field of soft matter, is the possibility to adjust the scattering contrast in the sample to the specific needs: By exchanging hydrogen by deuterium in the synthesis of the polymer the contrast can be tuned, due to the large difference in SLD of ${}^1H$ and ${}^2D$ [75].

2.3.3. Grazing incidence small angle x-ray scattering (GISAXS)

The scattering techniques described so far measure the specular reflectivity, in which only q_z is accessible. They are not able to probe the sample laterally, which is why these methods can only be applied to layered structures [76]. Lateral structures can originate e.g. from phase separation in polymer blend films [77] or from nano-structuring [78, 79]. The diffuse scattering signal contains information about the size, shape and distance of also laterally distributed structures. Grazing incidence small angle x-ray scattering (GISAXS) is able to access this diffuse scattering [80, 81] and is a well established technique, especially in soft matter [82, 83]. The theoretical background of GISAXS is explained in this section, while further details can be found in [64, 84, 85]. The experimental realization is described in section 3.8. The scattering geometry is depicted in figure 2.12. The x-ray beam impinges on the sample under a shallow angle α_i, which is typically smaller than 1°. The scattered beam is defined by the two angles $\alpha_i + \alpha_f$ in the plane of the incoming beam and Ψ in plane of the sample surface. A 2d detector captures the scattered intensity at a typical distance of 2-3 m from the sample position (measured from the center of the sample). The full scattering vector is given by [86]

$$\vec{q} = \frac{2\pi}{\lambda} \begin{bmatrix} \cos(\alpha_f)\cos(\psi) - \cos(\alpha_i) \\ \cos(\alpha_f)\sin(\psi) \\ \sin(\alpha_f) + \sin(\alpha_i) \end{bmatrix}. \tag{2.50}$$

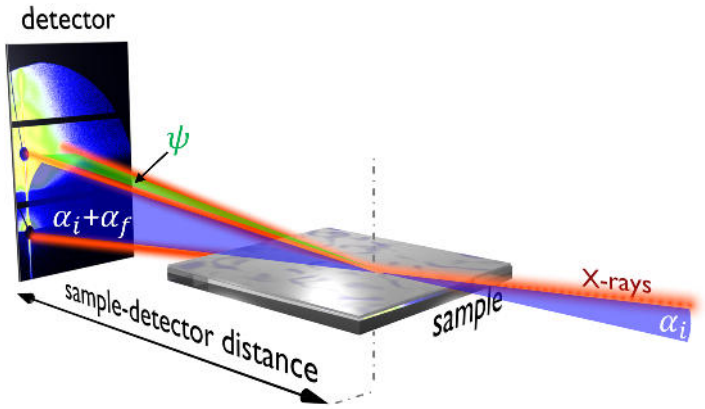

Figure 2.12: Scattering geometry for GISAXS: The x-ray beam impinges on the sample under a shallow angle α_i. The scattered beam is defined by the two angles $\alpha_i + \alpha_f$ (in the plane of the incident beam) and Ψ (in the plane of the sample surface). The scattered intensity is captured on a 2d detector in a distance of typically 2-3 m from the sample.

The GISAXS data in this work is analyzed within the framework of the distorted-wave Born approximation (DWBA) [82, 87]. It is based on a quantum-mechanical perturbation theory of first order, in which the scattering from a layered sample with perfectly flat interfaces represents the unperturbed case. Interfacial roughness can be included via a corresponding disturbance [88, 89]. The DWBA exhibits four different terms corresponding to four different scattering events: (1) scattering in the bulk material, (2) reflection at the substrate and subsequent scattering in the bulk, (3) scattering in the bulk followed by reflection at the substrate, and finally (4) succeeding reflection at the surface, scattering in the bulk and another reflection at the substrate. The coherent interference of these terms leads to the effective form factor. In this work, only cylindrical form factors are assumed. The structure factor is described by a one-dimensional paracrystalline lattice. In this approach the cylinders are arranged periodically, exhibiting a short-range order which deteriorates for longer ranges. Due to the fact that the scattering objects in reality are not monodisperse in size, in this work a so-called local monodisperse approximation accounts for differences in object size. Finally, only scattering from an isolated area is considered, offering the capability to decouple height and radii of the scattering sub-structures. Therefore, the total scattered intensity is described by the sum of the individual intensities scattered from the isolated domains of monodisperse sub-structures. The differential cross section based on the DWBA reads

$$\frac{d\sigma}{d\Omega} = \frac{A_{ill}\pi^2}{\lambda^4}\left(1-n^2\right)^2 \left|t_i^F\right|^2 \left|t_f^F\right|^2 P_{diff}\left(\vec{q}\right), \tag{2.51}$$

A_{ill} being the illuminated sample area, t_i^F and t_f^F the Fresnel transmission functions of incident and scattered beam and $P_{diff}(\vec{q})$ the diffuse scattering factor. At either $\alpha_i = \alpha_c$ or $\alpha_f = \alpha_c$ the transmission functions show a maximum, hence the diffuse scattering is strongly enhanced in this case. The corresponding intensity maximum is the so-called Yoneda peak [90]. The diffuse scattering factor $P_{diff}(\vec{q})$ of the sub-structures in the sample

is mainly governed by the size and number of objects, the corresponding form factor $F(\vec{q})$ which is the Fourier transform of the electron density distribution of the objects and their spatial distribution which is reflected by the structure factor $S(\vec{q})$. For N identical objects with a certain size, $F(\vec{q})$ and $S(\vec{q})$ being the corresponding form and structure factors, $P_{diff}(\vec{q})$ can be approximated by

$$P_{diff}(\vec{q}) \approx NF(\vec{q})S(\vec{q}). \tag{2.52}$$

Throughout this work this effective surface approximation is used to extract information about lateral structures in the q_y-direction [85].

Scattering depth

For incident angles smaller than the critical angle of the investigated material, the evanescent waves only penetrate the film to a certain depth. The penetration depth is defined as the depth at which the intensity has dropped to $1/e$ of its initial intensity. On the way back to the surface, the wave gets damped again. This escape-depth also needs to be considered. Both penetration and escape depth can be combined in the so-called scattering depth Λ [91], which reads

$$\Lambda = \frac{\lambda}{\sqrt{2\pi}} \frac{1}{l_i + l_f}, \tag{2.53}$$

with

$$l_{i,f} = \sqrt{(\sin^2(\alpha_c) - \sin^2(\alpha_{i,f})) + \sqrt{(\sin^2 \alpha_{i,f} - \sin^2 \alpha_c)^2 + \left(\frac{\mu\lambda}{2\pi}\right)^2}}. \tag{2.54}$$

For very small incident angles below the critical angle of the material the scattering depth for x-rays is typically around 50 Å. At the critical angle $\alpha_i = \alpha_c$ the scattering depth increases drastically, reaching a plateau. The height of this plateau depends on the absorption of the investigated material. By tuning the incident angle of the x-ray beam the scattering depth can be adjusted to the specific needs to get information from desired depths of the sample.

2.3.4. Grazing incidence small angle neutron scattering (GISANS)

Grazing incidence small angle neutron scattering (GISANS) features the same measurement geometry as GISAXS. The only difference is the use of a neutron beam, consequently accompanied by different materials involved in the beamline setup and different sizes for the optics [92]. The scattering process itself can in general be described using the same

formulae. Neutrons, however, exhibit a rest mass and therefore are subject to gravity. The implications of gravity are dealt with in this section. Moreover, the scattering depth of neutrons looks quite different for time-of-flight measurements, which is also explained in the following section.

Gravity effects

In contrast to x-rays, neutrons have a rest mass m_n. Therefore, neutrons of different wavelength λ travel at different speed in the neutron beam. Measuring the time-of-flight (TOF) of the neutron from a known starting point to the location of detection, the wavelength of a neutron can be calculated. The details about the experimental realization of TOF-GISANS are discussed in section 3.9. Due to their mass, neutrons are influenced by gravity. They drop on their way from the last slit of the neutron optics to the sample, as well as on their way to the detector. The deBroglie-wavelength of neutrons with momentum $p(v_n)$ reads

$$\lambda = \frac{h}{p(v_n)}, \tag{2.55}$$

with Planck's constant h and the velocity-dependent neutron momentum $p(v_n)$. Neutrons with high λ are rather slow and therefore longer under the influence of gravity, ergo they fall a longer distance during the travel to the detector. This has in principle two consequences: the angle of incidence α_i varies slightly with λ ($\alpha_{i,real} = a\lambda^2 - b\lambda + c$) and the position of the direct beam on the detector drops with increasing λ.

Scattering depth

In 2.3.3 it was shown that x-rays exhibit a limited scattering depth Λ, which is determined by the wavelength λ, the incident angle α_i, the exit angle α_f and the refractive index of the probed material n. The scattering depth Λ of neutrons can be obtained using the same formalism as for x-rays. In case of a monochromatic neutron beam and a varying angle of incidence, both the scattering depth and the Fresnel transmission exhibit the same behavior as known from x-rays. The use of a wavelength band in the TOF-mode provides means to probe a broad q-range without changing the angle of incidence. For the information depth however, this has some implications. Figure 2.13a shows the scattering depth Λ along with the Fresnel transmission T_F as a function of incident angle α_i around the critical angle α_c. With T_F reaching a plateau of $T_F = 1$ for $\alpha_i >> \alpha_c$ also the scattering depth Λ levels off. This behavior is well known for x-rays [91]. Performing the same calculations (see equation 2.53) using a fixed α_i while setting λ as variable, a different behavior is observed, which is shown in Figure 2.13b. For small λ the Fresnel transmission

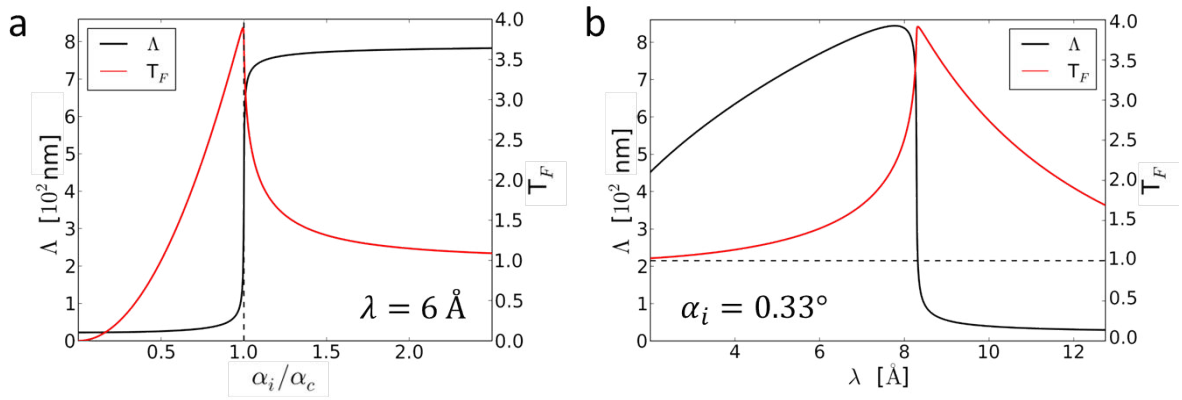

Figure 2.13.: a) Scattering depth Λ (black line) together with the Fresnel transmission T_F (red line), calculated for a wavelength of $\lambda = 6\,\text{Å}$ as a function of incident angle α_i around the critical angle α_c. b) The scattering depth Λ (black line) together with the Fresnel transmission T_F (red line), calculated for a fixed incident angle $\alpha_i = 0.33°$ as a function of wavelength λ.

drops to 1 as expected. The scattering depth Λ however, shows a well-pronounced maximum and a continuous drop towards smaller λ. Figure 2.14 shows the scattering depth Λ as a function of wavelength λ for a set of deviations from the exit angle α_c (Figure 2.14a) and deviations from the linear attenuation coefficient μ (Figure 2.14b). It can easily be seen that the drop of scattering depth with decreasing λ gets less pronounced for exit angles higher than the critical angle $\alpha_f > \alpha_c$. The drop of Λ is even more pronounced for angles smaller than α_c. Moreover, it is obvious that the scattering depth Λ drops for an increasing linear attenuation coefficient μ and increases for a decreased μ at shorter wavelengths. This non-monotonic behavior of the scattering depth Λ with varying wavelength λ needs to be taken into account in the interpretation of the measured data. Care has to be taken due to the fact that for a given λ the contributions from different depths need to be weighted according to the shape of the wavelength dependent scattering depth $\Lambda(\lambda)$. However, in practice, the steep transition between surface sensitivity and bulk sensitivity is smeared out depending of the wavelength resolution $\Delta\lambda/\lambda$ provided by the instrumental settings.

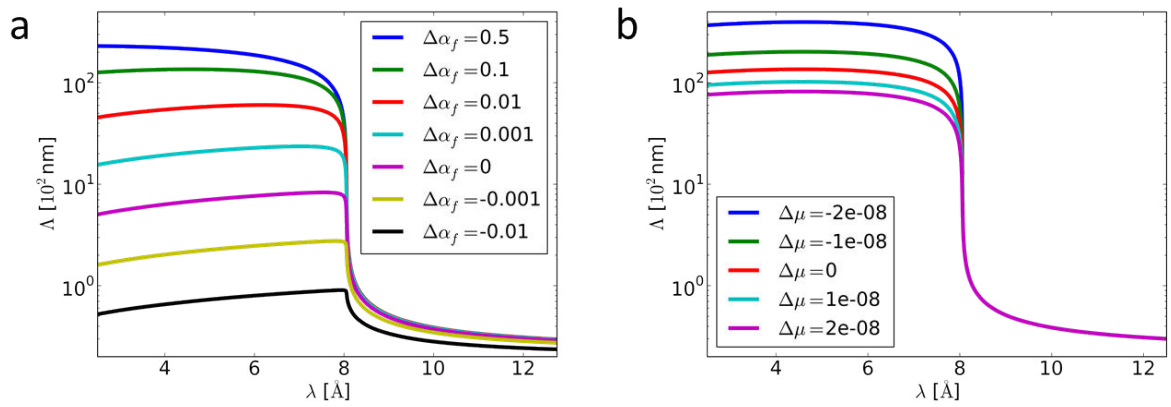

Figure 2.14.: Scattering depth Λ as a function of wavelength λ for different sets of varying parameters: a) $\Lambda(\lambda)$ evolves towards a plateau for higher exit angles α_f. b) As expected, higher linear absorption coefficients reduce the plateau of Λ_{max} and vice versa. For this plot $\Delta\alpha_f = 0.1$ was chosen.

3. Characterization methods

Different methods are used in this work to investigate the structure and adhesive properties of polymer films. The quality of the solution cast PSA films as well as of the prepared polymer punch probes for the tack measurements is controlled by optical microscopy. Moreover, using optical microscopy the bonding/debonding of adhesive and adherent is followed during the tack-tests. Topological information of the investigated polymer films is obtained by atomic force microscopy (AFM). The adhesive performance of the PSA films is investigated via tack-tests. Surface energies are derived using contact angle measurements and the Owens-Wendt method (see section 2.1.2), while film thickness is measured by white light interferometry (WLI). Scattering techniques such as XRR, NR, GISAXS and GISANS aim for the morphology determination of the samples.

3.1. Optical microscopy

An optical microscope is integrated in the tack apparatus to follow the bonding and debonding processes at the probe-PSA interface (see section 3.3) with a sampling rate of 58 Hz. As a result, cavity formation and growth are monitored. The PSA films themselves are transparent and homogeneous, therefore optical microscopy is not well suited for more detailed structural characterizations. The characterization of the polymer punches is carried out with an Axiolab A microscope (*Carl Zeiss*) in combination with a S621CU CCD camera (*PixeLINK*).

3.2. Atomic force microscopy (AFM)

The working principle of an AFM is schematically shown in figure 3.1. A piezo-driven cantilever oscillates slightly above its resonance frequency and is approached to the sample surface. As soon as the tip starts to interact with the surface this frequency changes. Using a segmented photodiode which monitors the deflection of a reflected laser beam from the back of the cantilever, a computer converts this variation of frequency into topographic

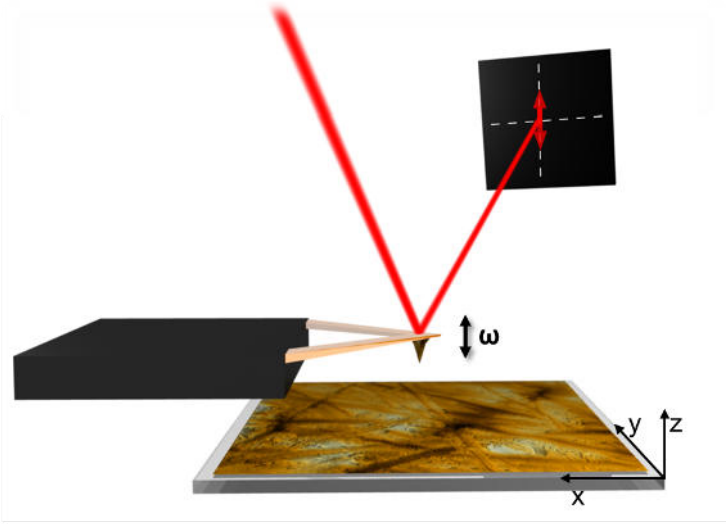

Figure 3.1: Atomic force microscopy setup. A segmented photodiode recognizes changes in the oscillation frequency of the cantilever. These changes are translated into a topographic map of the surface.

information. The tip is moved across the area of interest in x- and y- direction to map the surface of the sample. A more detailed description can be found in [93, 94]. For the measurements carried out in this thesis different AFMs were used: **AFM-1:** Agilent 5500 (*Agilent Technologies*) with a non-contact silicon tip, exhibiting a resonance frequency of 150 kHz and a spring constant of 6 N/m. **AFM-2:** AutoProbe CP-R (*TM Microscopes, Veeco Metrology Group*), with a tip having an eigen-frequency between 70 and 80 kHz and a spring constant of 2.1 N/m. **AFM-3:** JSPM-5200 (*Joel*) using a tip with a resonance at 210 kHz and a spring constant of 7.5 N/m.

The raw data obtained from the different AFMs is corrected by subtraction of a polynomial background which originates from the piezo-movement during scanning using the software *Gwyddion*.

3.3. Tack-test

The adhesive performance of the samples is investigated using the tack-test, which was already described in section 2.1.4. All measurements are carried out on a custom-designed apparatus (shown in figure 3.2) at a controlled room temperature of 18°C. The tack-tester consists of an actuator (*DC-Mike Physik Instrumente M-235.2DD*) (1) which moves the probe punch (2) up and down (in this illustration: a polymer punch attached to a steel punch). The punch is fixed on a *FGP XF-3030* force-sensor (3). The position of the punch can be measured using a *Kaman KD-2440* distance sensor (4). The sample (5) is fixed to a translation stage via four clamps preventing any movement during the measurement. The alignment of punch and sample can be adjusted by three screws (6), acting as a tripod. To be able to monitor the bonding and debonding of punch probe and adhesive

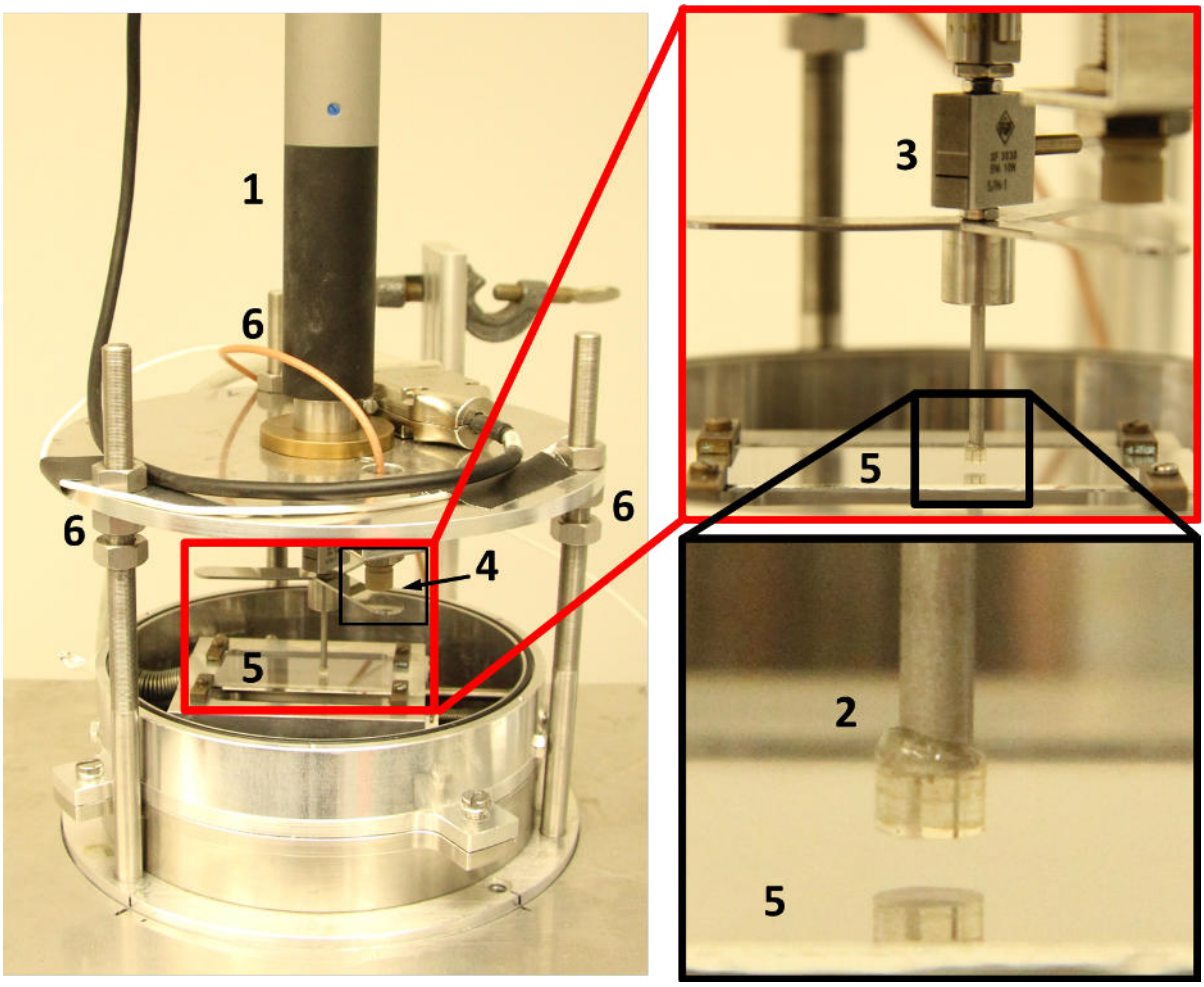

Figure 3.2.: Photograph of the custom-design tack apparatus. The two close-ups on the right show the combination of force-sensor, distance-sensor and probe punch, as well as the probe punch (here: polymer punch attached to a steel pin) and the sample in more detail.

- and also for the purpose of alignment - a CCD camera films the contact area of punch and sample from below (not shown in the image). The whole setup is controlled by a *TestPoint* program, which also records the force-distance curves. The experimental setup as well as the controlling software was designed by Dr. V. Körstgens.
For experiments requiring control over the relative humidity, a custom-designed cell was constructed, which is shown without main lid in figure 3.2 and schematically in figure 3.3. The atmosphere is controlled by the substances put in the trench at the bottom of the cell, which is made of stainless steel for its chemical stability against salt solutions. The window in the bottom center allows for an observation of the bonding and debonding processes. A translation stage holds the sample, which enables multiple measurements on the same sample, each at a fresh spot of the sample. The sample stage also has a cooling/heating option, which in this work was not used because the air-conditioning in the lab already

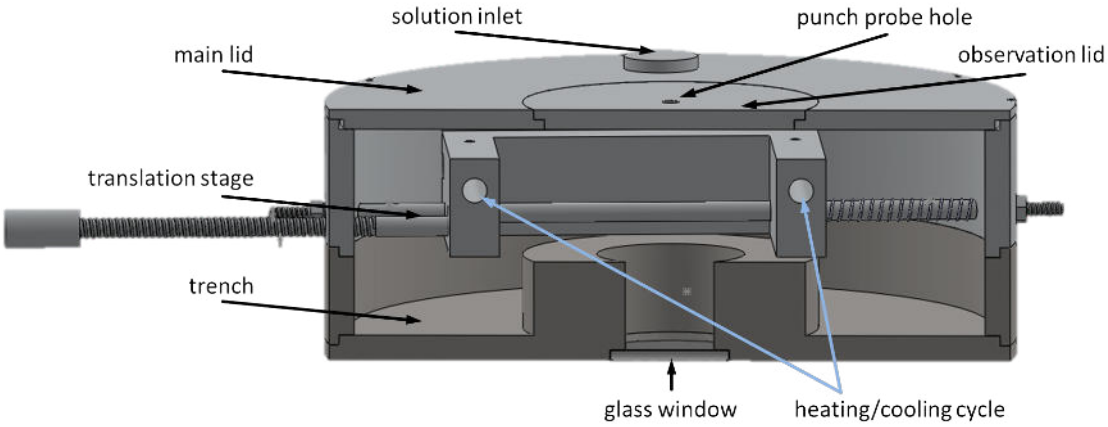

Figure 3.3.: Sketch of the humidity cell for the probe tack-test: A stainless steel trench at the bottom stores the substance providing the desired atmosphere. The sample is mounted on a translation stage and the punch probe contacts the sample through a small hole in the main lid. Solution inlets allow for changing the relative humidity also while the cell is closed. The observation lid is made of plexiglass. The bonding and debonding can be observed through a window in the bottom of the cell.

provided a constant temperature. Through a small hole in the observation lid the punch approached the sample. Figure 3.4 shows the relative humidity (RH) in the cell as a function of time, measured with an integrated combined temperature and humidity sensor (*Sensirion* SHT-71). After 30 min only minor changes in the RH can be seen, thus, this time is chosen as the starting point for the experiments. If not stated differently, for all measurements an approaching velocity of 100 μm/s and a retraction speed of 100 μm/s are used. The punch probe position is held constant for a dwell time of 10 s after a force

Figure 3.4: Temporal evolution of the relative humidity (RH) in the humidity cell for the tack test after closing the main lid for different atmospheres. The different RHs are realized using silica gel, a saturated solution of LiCl in water, ambient air, water based saturated solutions of $Mg(NO_3)_26H_2O$ and NaCl and finally H_2O (from bottom to top). The dashed vertical line marks the starting time for the measurements.

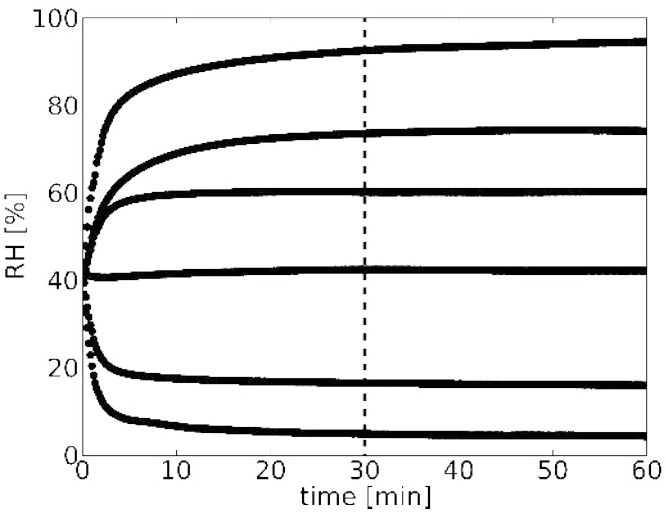

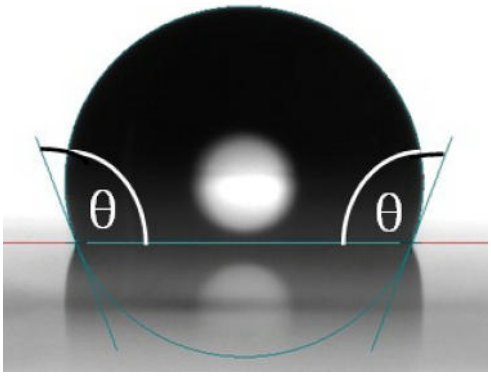

Figure 3.5: Typical image during relaxation of a droplet on a surface. An elliptical contour is fitted to the droplet shape and the baseline is set. For each frame of the recorded movie the left and right contact angles are automatically detected.

threshold of $|F_{threshold}| = 1$ N is reached. Two different kinds of punch probes are used: metal punches and polymer punches. The metal punch probes are cleaned with a soft dust-free tissue (Kimberly-Clark) soaked in toluene before each measurement to remove possible PSA residues and other contaminants. For tack measurements performed on PSAs, the sample is moved via the translation stage to provide a fresh spot for each measurement. At least eight repetitions are carried out per measurement to guarantee sufficient statistics. Where applicable, the resulting values in this thesis represent the mean values and their standard deviations.

3.4. Contact angle measurements

The surface energy or surface tension strongly affects the bonding process in adhesive applications [95]. Therefore, the surface tension γ of both adhesive and adherent is of utmost importance and is determined in this work via contact angle measurements. The corresponding theoretical background is explained in section 2.1.2.
The contact angle measurements in this work are carried out under ambient conditions at a constant temperature of 20°C on a dataphysics Contact Angle System OCA. A computer-controlled syringe deposits a sessile droplet ($V_{droplet} = 2$ μL) onto the sample. After retraction of the syringe, the droplet is filmed from the side using a pre-aligned camera with large magnification and a frame rate of 15 frames per second. Figure 3.5 shows a typical frame. The evolution of the droplet shape is recorded for a time period of at least 70 s. The obtained sequence is analyzed with the dataphysics SCA20 software. In each frame an ellipsoidal contour is fitted to the droplet shape and the left and right contact angle are automatically recognized. Finally, the mean value Θ is extracted. The volume of the droplet is chosen to be small enough to neglect influences of gravity on the droplet shape and to justify the assumption of an ellipsoidal contour [96].
The six different test liquids (see section 2.1.2) are chosen to span a broad range of polarities and are listed in table 3.1 along with their respective dispersive γ^d and polar

Table 3.1.: Surface tensions of the used test liquids with dispersive and polar contributions, taken from [97].

liquid	$\gamma^d \left[\frac{mN}{m}\right]$	$\gamma^p \left[\frac{mN}{m}\right]$	polarity
paraffin oil	29.5	0	0
diiodomethane	47.4	2.6	0.0549
ethylene glycol	29.0	19.0	0.655
formamide	23.5	33.4	1.42
glycerol	21.2	41.5	1.96
water	19.9	52.2	2.62

γ^p contributions of the surface tension [97]. Due to the fact that the droplets do not reach equilibrium instantly, the contact angles Θ are determined as a function of time t. A continuous decay of Θ saturating at a certain value is observed for all liquids. Evaporation of the liquids limits the time window for the extraction of Θ [98]. Following [99] the used fitting function for the decay reads

$$\Theta(t) = \Theta_f + (180^\circ - \Theta_f) \exp\left(-k_\Theta (t - t_0)^{m_\Theta}\right). \tag{3.1}$$

This function is defined for $t \geq t_0$, t_0 being the moment at which the droplet contacts the substrate. At $t = t_0$ the contact angle of the liquid on the sample is $\Theta = 180^\circ$. The quantities $\Theta_f, k_\Theta, m_\Theta$ and t_0 are fitting parameters. It is important to note that k_Θ and m_Θ account for interaction kinetics of droplet and sample. To improve statistics, the measurement of $\Theta(t)$ was repeated at least 6 times. In the following, Θ_f denotes the statistical average, while the errorbars are the calculated corresponding standard deviations.

3.5. White light interferometry (WLI)

A fast and reliable technique to obtain the film thickness of non-absorbing polymer films is white light interferometry (WLI), which features a broad range of accessible thicknesses from tens of nanometers to several hundred micrometers [100]. In this method the reflectance of the investigated polymer film is measured with a white beam. The incident beam impinges on the sample under a constant angle of 90° and the reflectance at an exit angle of 90° is measured as a function of the wavelength. The measurements are carried out using a Filmmetrics Inc. F20 Thin-Film Measurement System which is connected to a sample chamber (60 mm × 60 mm). The spot size of the light beam is adjustable within a range of 0.5 to 10 mm, the usable wavelength band ranges from 340 to 1100 nm. This

measurement needs a strong reflection from the substrate, which is why the corresponding samples are prepared on silicon wafers instead of microscopy glass slides. The obtained data is fitted using the software *FILMeasure 6*, provided by the device manufacturer.

3.6. X-ray reflectivity (XRR)

The XRR measurements in this work are carried out on two different reflectometers. The first reflectometer is a *Siemens D5000 Diffraktometer* (denoted XRR-1), operated at room temperature. The sample is mounted on a vacuum chuck which is rotated along with the detector in a way to maintain the $\Theta - 2\Theta$ condition for specular reflection during scanning across the desired angular range. The x-ray beam has a width of 12 mm and a wavelength of 0.154 nm, corresponding to the Cu-K_α line provided by the copper x-ray tube. The beam is further defined by a collimation system consisting of several slits and a tantalum knife edge at the sample position. This knife edge avoides over-illumination at small angles of incidence and further collimates the beam. Absorbers avoid a saturation of the scintillation detector at high intensities. The typical duration of a single measurement is 8 h.
The second reflectometer is a *Bruker D8 ADVANCE* (denoted XRR-2) which is also equipped with a copper tube. This machine features a Goebel mirror which both monochromizes and focuses and hence increases the intensity of the beam. Therefore, shorter measurement times of about 4 h are possible. The fact that in this instrument both the x-ray tube and the detector are moved in a coupled $\Theta/2\Theta$ mode while the sample is not moved at all, allows for a facilitated implementation of a custom designed temperature controlled humidity cell.
To be able to provide the exact same conditions during the XRR measurements as compared to during sample preparation and eventual post-treatments, a sample environment is constructed and implemented in XRR-2. Figure 3.6 shows the architecture of this temperature-controlled humidity cell. Two teflon reservoirs next to the sample store the substance of choice for installing the desired atmosphere. Kapton windows seal the cell while allowing x-rays to pass through. The temperature control is realized by a cooling/heating liquid which circulates through the optional bottom disc. A *Lauda RC 6 CS* allows for temperatures from -35 °C to 150 °C. The temperature is always kept at 18 °C. In this work the influence of different relative humidities (RH) on the tackiness of PSAs is investigated, therefore the time for full saturation of the atmosphere after sealing the cell is of importance. The RH inside the cell after insertion of the desired salt solution (see section 4.4) as a function of time, starting after closing the cell, is shown in figure 3.7. After 30 min only minor changes of the RH are evident, which is why this time was

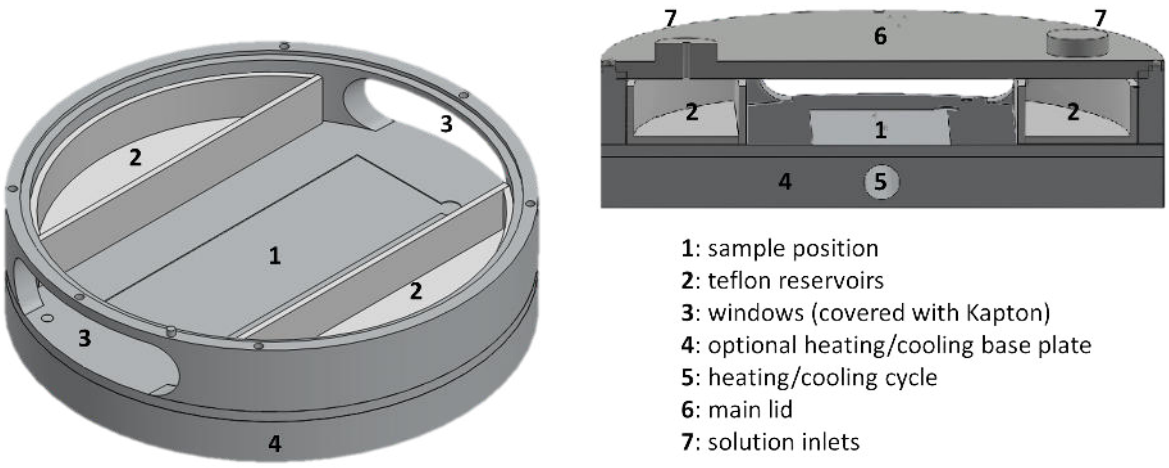

Figure 3.6.: Sketch of the temperature-controlled humidity cell for XRR. Two Teflon reservoirs (2) next to the sample position (1) store the liquid (e.g. water or salt solution) which provides the desired atmosphere. These reservoirs can also be filled while the cell is sealed by using the inlets (7) in the main lid (6). Cooling/heating liquid circulates (5) through the supporting bottom disc (4). Kapton widows (3) allow x-rays to pass through.

chosen as the starting point of each measurement (marked by the dashed vertical line in figure 3.7). Figure 3.8a shows a typical XRR measurement using the humidity cell, which exhibits additional broad scattering originating from the Kapton windows. Before fitting the data is corrected for this effect, which can be seen in figure 3.8b. For this correction a Gaussian peak was fitted to the scattering contributions from the Kapton windows and subtracted from the reflectivity. As described in section 2.3.1, the reflectivity data was fitted using the software *Motofit* [69]. The resulting SLD profile is translated into a dis-

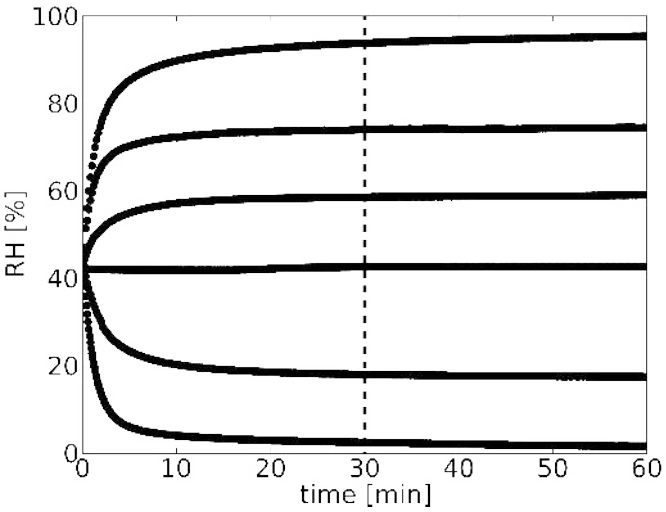

Figure 3.7: Temporal evolution of the relative humidity (RH) in the humidity cell for XRR after sealing for different atmospheres. The RHs are realized using silica gel, a saturated solution of LiCl in water, ambient air, water based saturated solutions of $Mg(NO_3)_26H_2O$, NaCl and H_2O (from bottom to top). the dashed vertical line marks the starting time for the measurements.

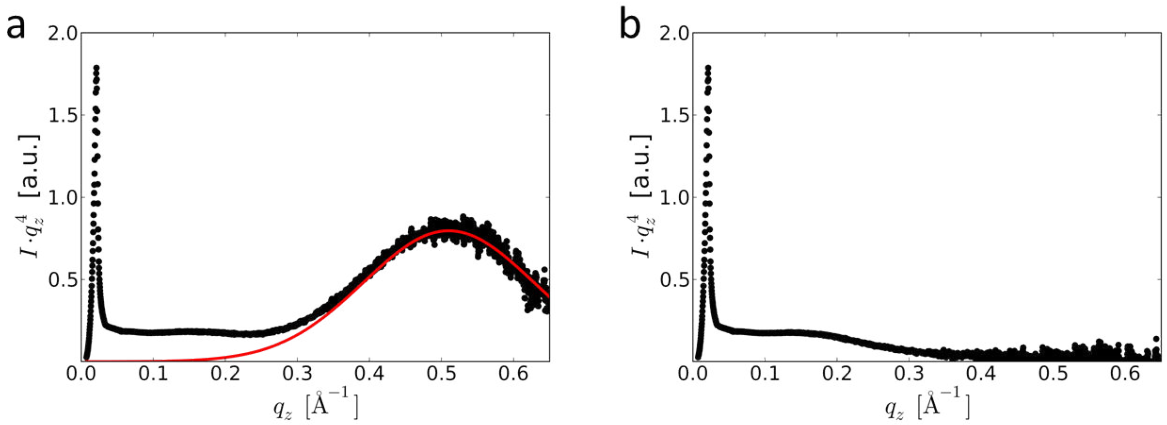

Figure 3.8.: a) Typical XRR measurement obtained with the humidity cell exhibiting additional scattering which originates from the Kapton windows. b) XRR data after removal of the Kapton contributions.

persion profile using equation 2.33. Due to the fact that the dispersion is proportional to the electron density and that only two components are involved, the dispersion profile reflects the depth-resolved composition of the sample. The dispersion at every position in the profile is a linear combination of the dispersion values of the involved components, δ(PEHA) and δ(PMMA). Therefore, the concentration of PMMA at a depth z of the extracted dispersion profile δ(z) can be calculated by

$$c_{PMMA} = \frac{\delta(z) - \delta(PEHA)}{\delta(PMMA) - \delta(PEHA)}. \tag{3.2}$$

In this work the composition profiles are often shown in a grayscale color code, in which the color white represents pure PEHA and black pure PMMA. The RGB colors for compositions in-between are assigned by $(255 \cdot c_{PMMA}(z), 255 \cdot c_{PMMA}(z), 255 \cdot c_{PMMA}(z))$ to the corresponding depth z. Figure 3.9 shows an exemplary dispersion profile for a freshly prepared P(EHA-stat-20MMA) film along with the composition in gray-scale coding in the inset.

3.7. Neutron reflectivity (NR)

The neutron reflectivity (NR) measurements were performed at two different beamlines. One of them was the AMOR beamline at the Swiss Spallation Neutron Source, Paul Scherrer Institut (SINQ at PSI, Switzerland). The instrument was operated in TOF mode (see section 2.3.4). A double chopper system provided pulses with a wavelength band ranging from 1.5 to 13 Å. Recalling equation 2.31, it becomes obvious that a

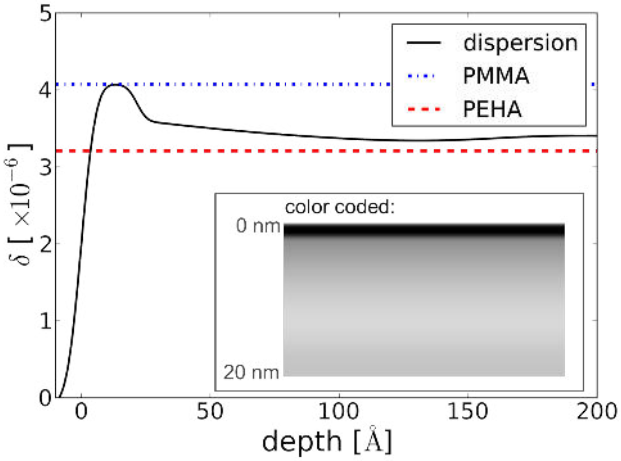

Figure 3.9: Dispersion profile of the near-surface region of a freshly prepared P(EHA-stat-20MMA) film (main plot). The dashed lines in blue and red represent the dispersion values for pure PMMA and PEHA, respectively. This profile is translated to a more intuitive color coded compositional map (inset). The color black represents pure PMMA, the color white pure PEHA, while the colors in-between show the corresponding compositions.

reflectivity measurement carried out in TOF mode under one single angle of incidence α_i already covers a certain q_z-range. To obtain a full reflectivity curve however, two angles $\alpha_{i,1} = 0.35°$ and $\alpha_{i,2} = 0.9°$ were necessary. Further details about the beamline can be found in [101, 102].

The second neutron reflectometer used in this work was the instrument FIGARO at the Institut Laue-Langevin (ILL) in Grenoble (France), which is also operated in TOF mode. The wavelength band ranged from 2 to 30 Å. The used angles were $\alpha_{i,1} = 0.62°$ and $\alpha_{i,2} = 3.78°$ to cover the desired q_z-range. An important feature of FIGARO is the possibility to bend the beam to change the angle of incidence, i.a. the sample remains horizontal. This possibility is a prerequisite for the investigation of liquid samples like polymer solutions. Further details about the latter instrument can be found in [103].

3.8. Grazing incidence small angle x-ray scattering (GISAXS)

All GISAXS measurements were carried out at the P03 beamline of the PETRA III storage ring (DESY, Hamburg) [104, 105]. The theoretical background is explained in section 2.3.3, the geometry of the setup is shown in figure 2.12. A monochromatic x-ray beam with a typical size of 22×12 μm^2 with a wavelength of $\lambda = 0.0954$ nm was used. A shallow angle of incidence of $\alpha_i = 0.507°$ was chosen, which is above the critical angle of all involved materials, to allow for a complete penetration of the sample.

The diffusely scattered intensity was monitored with a two-dimensional (2d) noise-free

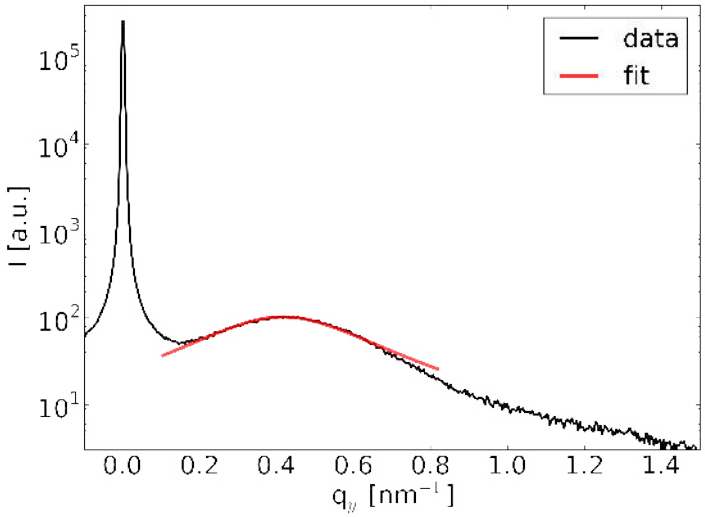

Figure 3.10: Exemplary horizontal cut from a measurement during sputtering gold on a PEHA template. The peak at around $q_y = 0.45$ nm^{-1} is fitted with a Lorentzian distribution.

Pilatus 300k detector (*DECTRIS*, Baden, Switzerland), composed of 487 × 619 pixels with a pixel size of 172 × 172 μm^2 at a sample-detector distance (SDD) of 2011 mm. A circular beam-stop protected the detector from over-illumination at the position of the specularly reflected beam. Having a read-out time of roughly 5 ms the detector was used for time-resolved measurements with a resolution of 0.15 s. The recorded intensity is presented using a false color code in logarithmic scale.

To extract information about lateral structures in the sample, horizontal line cuts, also referred to as out-of-plane cuts, were extracted along Ψ at an exit angle equal to the critical angle of the material of interest. To improve statistics while maintaining the high time-resolution, an average over 30 pixels in vertical direction was used. The cuts are analyzed using the software DPDAK [106], which allows for batch processing of the large number of recorded frames during in-situ measurements. As described in section 6.2, intensity peaks at large q_y values appear and move towards smaller q_y with ongoing experimental time. These peaks are fitted with a Lorentzian distribution, from which peak position, height and width are extracted time dependently. Figure 3.10 shows an exemplary horizontal cut from sputtering gold on a PEHA template along with the corresponding Lorentzian fit.

3.9. Grazing incidence small angle neutron scattering (GISANS)

Neutrons provide means to probe soft matter to higher depths as compared to x-rays and allow also for specific adjustment of the contrast in the sample by partial deuteration [75].

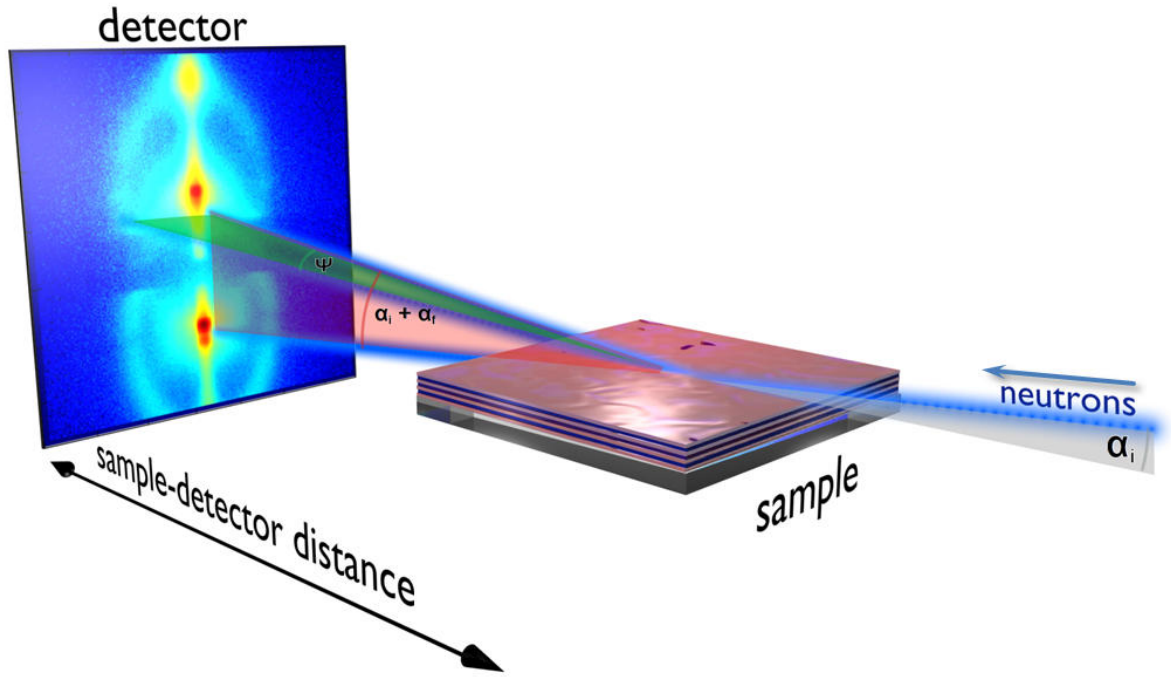

Figure 3.11.: Scattering geometry for GISANS and GISAXS: Neutrons/x-rays impinge on the surface of the sample under an angle α_i. The scattered beam is defined by the two angles $\alpha_i + \alpha_f$ in the plane of the incoming beam and Ψ in the plane of the surface of the sample. The scattered intensity is captured with a 2d detector at a distance of typically 10 m (GISANS)/2-3 m (GISAXS). The detector image shown corresponds to a GISANS measurement.

The measurement geometry is very similar to the GISAXS setup, both are schematically shown in figure 3.11. All GISANS measurements in this work were carried out at the REFSANS instrument (MLZ, FRM2, Garching) [107, 108]. This instrument is operated in the TOF-mode, realized by a set of choppers providing a pulsed beam. The period of time during which both chopper disks are open defines a certain wavelength band. The chopperdisks are closed long enough to ensure that no frame-overlap between subsequent pulses can occur. The used wavelength band ranged from $\lambda = 2.25$ Å – 11.75 Å and the angle of incidence α_i was chosen to be closely around 0.33° or 0.4°, depending on the sample. Small deviations from the incident angle arise from the wavelength-dependent effect of gravity and are taken into account in the analysis. Apart from gravity effects the incident angle was kept constant throughout the measurements. At a distance of 10.52 m from the sample a 2d He^3-detector with a pixel size of 1.378×1.378 mm^2 recorded the scattered intensity. Each counting event in the detector is recorded with a time- and a space-stamp, which makes it possible after the measurement to slice the obtained data into slabs of desired λ-resolution.

The impinging neutrons penetrate the polymer film to very high depths compared to x-rays (see section 2.3.4). The depth, in which the scattered intensity drops below a fraction of 1/e compared to the initial intensity is called penetration depth. On the way back to the surface, the intensity get again damped, which leads to an upper depth-limit for information extraction, called the scattering depth Λ. While details can be found in [91], it is important to note that Λ strongly varies with λ, when keeping the incident angle constant. This dependency together with the simultaneous use of multiple wavelengths in a TOF-GISANS experiment allows a depth-dependent structural investigation.
From the resulting 2d patterns vertical and horizontal line cuts are extracted. From the vertical line cuts information about the Yoneda positions is obtained, while the horizontal line cuts provide information about the lateral structures. These out-of-plane line cuts are fitted using a model based on the effective surface approximation as described in section 2.3.3.

4. Sample preparation

The different kinds of polymers which are investigated in this work are introduced in this chapter. Also, the routines for the different substrate cleanings and the polymer film deposition techniques are addressed. The preparation of the probe punches for the tack measurements is described for both metal and polymer punch probes in the last section of this chapter.

4.1. Investigated polymers

The homopolymers composed of the monomers which build up the PSAs in this work are poly(ethylhexylacrylate) (PEHA) and poly(methylmethacrylate) (PMMA). Investigations aiming at properties of these single constituents are crucial for the interpretation of results obtained from experiments with the PSA itself. PEHA was synthesized by *BASF SE* while PMMA was purchased from *Polymer Standards Service*. Another batch of PMMA (denoted PMMA*) was provided by *KAO, Japan*. Important properties of these polymers are listed in table 4.1. The molecular weight M_w and the polydispersity PDI are not available for the homopolymer PEHA provided by BASF. However, a so-called K-value is provided in table 4.1, which increases with increasing M_w and is used internally at BASF. Moreover, several copolymers were investigated in this work (important quantities are listed in table 4.2). The class of PSAs was represented by a statistical copolymer consisting of ethylhexylacrylate (EHA) and methylmethacrylate (MMA). A composition of 80wt.% of the soft and sticky EHA and 20wt.% of the glassy MMA is used throughout this work. This composition is very close to the general optimum ratio for a

Table 4.1.: Homopolymers and corresponding properties.

Homopolymer	T_g [109]	ρ	M_w	PDI
PEHA	ca. 188 K	ca. 0.887 g/cm^3	K = 39.6*	n.a.
PMMA	ca. 378 K	ca. 1.18 g/cm^3	204.0 kg/mol	1.06
PMMA*	ca. 378 K	ca. 1.18 g/cm^3	110.0 kg/mol	2.6

Table 4.2.: Copolymers and corresponding properties.

Copolymer	Ratio	M_w	PDI
P(EHA-stat-20MMA)	80/20	248.0 kg/mol	4
P(tBA-stat-20MMA)	80/20	150.0 kg/mol	2.46
P(EHA-stat-20dMMA)	80/20	209.5 kg/mol	4.65
$P(dS\text{-}b\text{-}nBMA)_{50:50}$	50/50	124.0 kg/mol	1.08
$P(dS\text{-}b\text{-}nBMA)_{35:65}$	35/65	166.4 kg/mol	1.17

PSA [110]. This polymer was synthesized by *BASF SE* via radical solution polymerization [111]. For neutron experiments the same kind of polymer was synthesized by *Specific Polymers*, having the MMA-blocks fully deuterated for enhanced scattering contrast. To investigate the structure formation in block-copolymer films upon drying (see chapter 7) two different block-copolymers are used, purchased from *Polymer Standards Service*. The first, poly(styrene-d8-b-n-butylmethacrylate) ($P(dS\text{-}b\text{-}nBMA)_{50:50}$) has a molecular weight of $M_w = 124000\,\mathrm{g/mol}$ and a block ratio of 50:50. The second is the same kind of block-copolymer except for a different composition of 35:65 and a molecular weight of $M_w = 166400\,\mathrm{g/mol}$ ($P(dS\text{-}b\text{-}nBMA)_{35:65}$). The styrene blocks in both polymers are fully deuterated. If not stated differently, all polymers were dissolved in toluene (*Roth*). After mixing of polymer and solvent the solutions were kept on a shaker (*IKA-VIBRAX-VXR*) for at least 12h at room temperature to ensure a complete dissolution of the polymer.

4.2. Substrate cleaning

For polymer thin films the substrate supporting the films plays an important role. Its surface roughness and chemistry can severely affect the inner morphology of the polymer film [112, 113]. Detailed information about the wide range of silicon wafer cleaning routines can be found in literature [114, 115, 116, 117, 118]. Silicon wafers with a roughness of $R_{rms} < 4$ Å were used for the interface investigations in this work. An exemplary XRR measurement of a silicon wafer revealing a roughness of 3.4 Å is shown in figure 4.1. To address the effect of surface chemistry on the inner morphology different cleaning procedures have been applied, an acidic and a basic treatment. For investigations which focus only on the PSA surface properties, rather thick films ($\approx 50\ \mu$m) were prepared via solution casting (see chapter 4.3). For this purpose the substrates were just rinsed with isopropanol (*Roth*) and dried with compressed oilfree nitrogen, also to remove dust particles. Due to the high film thickness in this special case the substrate-adhesive interface

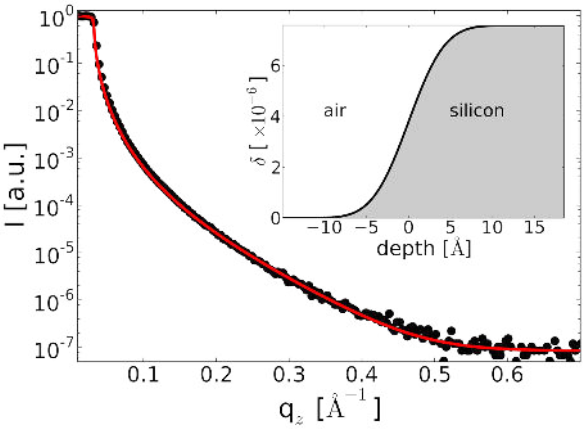

Figure 4.1: X-ray reflectivity measurement of a bare silicon wafer (black symbols) along with the corresponding fit (red line). In inset shows the dispersion profile obtained for a surface roughness of 3.4 Å.

is decoupled from the investigated surface, meaning that the substrate does not affect the surface morphology.

Acid cleaning

One cleaning routine used in this work was acid cleaning. This procedure follows in principle a method developed by Müller-Buschbaum [117], which has proven to remove residues of polishing paste used by the silicon manufacturer (*SiMat*) and provides a reproducible silicon oxide layer. The silicon substrates were treated with an acid bath consisting of 54 ml deionized water (DI H_2O), 84 ml 30% hydrogen peroxide (H_2O_2) (*Roth*) and 198 ml 95-97% sulfuric acid (H_2SO_4) (*Roth*) for 15 min at 80 °C. Afterwards they were rinsed with DI H_2O and dried in a flow of oil free nitrogen. This procedure is referred to as acidic cleaning. The ingredients of the acid bath are also listed in table 4.3.

Base cleaning

The second procedure for substrate cleaning in this work was a 3-step basic cleaning routine. According to [119] the silicon substrates were first stored in a dichloromethane bath (CH_2Cl_2) (*Roth*) for 30 min at 46 °C, followed by an intermediate treatment in a bath of DI H_2O for 20 min at room temperature. Finally the substrates were put in a

Table 4.3.: Ingredients of the acid cleaning solution

Chemical	Amount	Time	Temperature
DI H_2O	54 ml		
H_2O_2 (30%)	84 ml	15 min	80 °C
H_2SO_4 (95-97%)	198 ml		

Table 4.4.: Ingredients of the 3-step base cleaning solutions

chemical	amount	time	temperature
CH_2Cl_2		30 min	46 °C
DI H_2O		20 min	25 °C
DI H_2O	350 ml		
NH_3 (32%)	30 ml	2 h	65 °C
H_2O_2 (30%)	30 ml		

solution of 350 ml DI H_2O, 30 ml 32% ammonia (NH_3) (*Roth*) and 30 ml 30% H_2O_2 (*Roth*) for 2 h at 65 °C. The substrates were finally rinsed with DI H_2O and dried with a flow of oil free nitrogen. This procedure is referred to as basic cleaning. This cleaning routine is also summarized in table 4.4.

4.3. Deposition methods

Spin coating

Spin coating is used to obtain thin films in the range from a few Angstroms to several hundred nanometers. This technique is applied to obtain very homogeneous polymer films on silicon as templates for sputtering experiments in chapter 6. For this purpose a *Süss Microtec Lithography Delta 6 RC TT* spin coater was used. A vacuum chuck fixed the acid cleaned silicon substrates to the rotating disk of the apparatus. Speed of rotation, spinning duration, acceleration and deceleration rates were adjustable. The polymer solution was dispensed on the substrate (figure 4.2a) until full coverage was reached. Then the lid of the spin coater was immediately closed and the spinning was initiated (figure 4.2b). During the rotation excess solution is spun off the substrate while the solvent evaporates. This leads to very homogeneous dry thin films (figure 4.2c). The precise spin coating parameters used in this work are listed in table (4.5). Using the initial solution concentration c, the molecular weight of the polymer M_w and the speed of rotation the final film thickness d can be calculated by equation (4.1) [120], where A_p

Table 4.5.: Spin coating parameters

speed of rotation	1971 rpm
duration	30 s
acceleration level	9

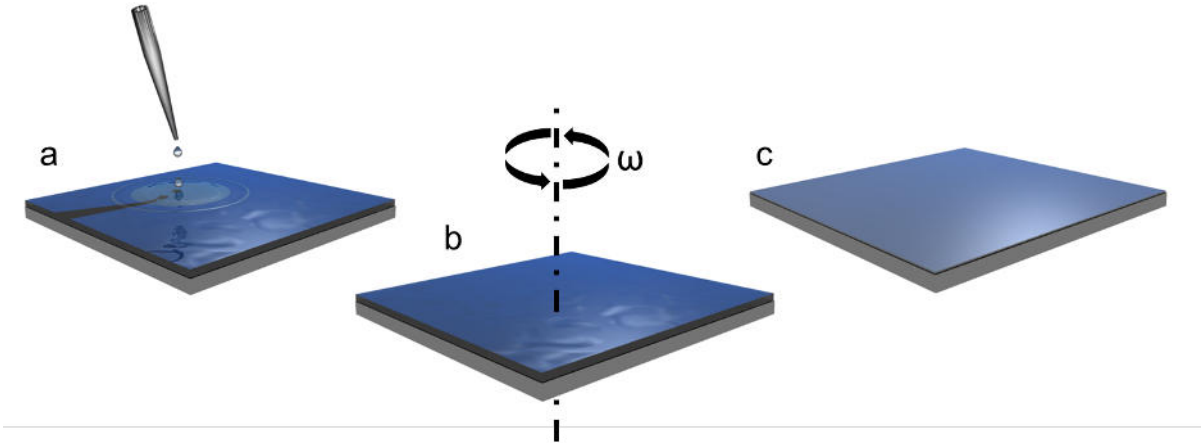

Figure 4.2.: Spin coating: a) The solution is dispensed on the substrate. b) After full surface coverage is reached the rotation is initialized. c) During the spinning excess solution is spun off the substrate while the solvent evaporates. A homogeneous dry thin film is obtained.

denotes a parameter which depends on the experimental conditions.

$$d = cA_p\omega^{-0.5}M_w^{0.25} \tag{4.1}$$

Solution Casting

Solution casting is a solvent based method to create homogeneous adhesive layers and especially suited for the preparation of films with a thickness in the micrometer range. In order to join two not perfectly flat but rather rough materials in an adhesive application the thickness of the PSA has to exceed each surface roughness involved. Therefore, PSAs are usually applied with a thickness larger than achievable by spin coating. Furthermore, from the industrial point of view the upscaling of this technique is tremendously easier as compared to spin coating. The reproducibility of the investigated samples and their high quality is of utmost importance to later come to unambiguous conclusions. Therefore the process of solution casting was carried out under very controlled conditions in an air conditioned lab with a constant temperature of $T = 18°C$. The polymers were all dissolved in toluene. The obtained solution (see 4.1) was dispensed on a glass substrate (*Roth*, 76 mm x 26 mm x 1 mm) which was carefully aligned before in a desiccator (*Schott Duran*, volume $V = 0.7$ L) using a self-aligning vertical laser spirit level (*Stanley FatMax PB3*). After the whole substrate was covered with the solution (figure 4.3a) the lid of the desiccator was closed and the sample dried for 24 h until a dry film with the desired thickness was obtained (figure 4.3b). This state is referred to as fresh sample in this thesis and all times measures for the sample age start from this point at $t = 0$. To control

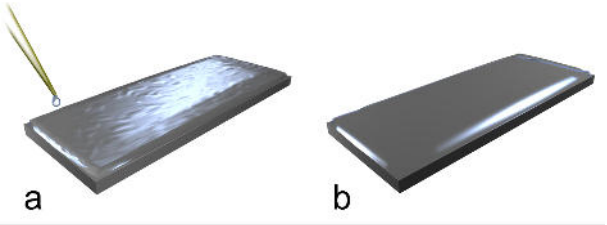

Figure 4.3: Solution casting: a) The solution is dispensed on the substrate. b) After 24 h a homogeneous dry PSA film is obtained.

the film thickness d of the resulting PSA film the solution concentration was varied. The necessary concentration was calculated depending on the substrate size A using the following equation:

$$c = \frac{d_{desired}\rho_{polymer}A}{V_{solvent}}, \tag{4.2}$$

with $\rho_{polymer}$ being the polymer density, A the substrate surface area and $V_{solvent}$ the volume of solvent. For all XRR and tack measurements a film thickness of about 50 μm was achieved with a concentration of c = 94.5 g/L of P(EHA-stat-20MMA) in toluene. The thickness values for other samples are provided in the corresponding chapters.

Sputter deposition

Sputtering is a well established technique to grow thin metal films on different substrates. Metal is also deposited on polymers via sputtering i.a. in optical, electrical or magnetic applications [121, 122, 123, 124, 125]. The working principle of this technique is explained in the following. As can be seen from figure 4.4 a plasma (in this work an Argon plasma) is ignited between the target and the substrate. An additional voltage is applied to accelerate the Ar^+-ions towards the target material (in this thesis: aluminum and gold). The result is a bombardment of the target with Ar^+-ions which due to conservation of momentum causes the ejection of target atoms. These atoms can then attach to the substrate and form islands or layers. Control over the sputtering process is gained via the pressure in the plasma p and the sputtering power P. The sputter chamber used in this work was provided by *DESY, Hamburg* and implemented in the beamline *P03*. It was operated at a pressure of $p = 1.5 \cdot 10^{-2}$ mbar and a power of $P = 100$ W. Once atoms are ejected from the target material and impinge on the substrate they can either adsorb to the surface or desorb again. The probability of adsorption is given by the condensation coefficient (cc) [126]. The limiting cases are $cc = 0$ for no adsorption at all and $cc = 1$ in case every incoming atom adsorbs to the substrate. These two extreme cases are illustrated in figure 4.5.

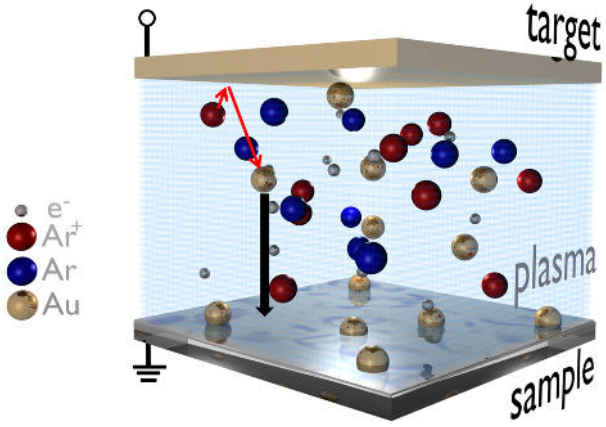

Figure 4.4: Principle of sputtering: In an Argon plasma the target (e.g. gold) is bombarded by accelerated Ar^+-ions. Gold atoms are ejected from the surface via momentum transfer, attach to the substrate (e.g. a polymer film) and eventually build up a layer.

4.4. PSA post-treatments

In order to tailor the near-surface composition of P(EHA-stat-20MMA) the films were post-treated using different atmospheres. This approach has been successfully applied in the past [99]. To provide a completely unpolar environment the PSA samples were kept under nitrogen atmosphere in a glovebox for different periods of time. In order to install atmospheres of different polarity saturated salt solutions were used. In this well established approach different kinds of salt are added to water, exceeding their respective solubility limits [127, 128]. For pure water, 100% relative humidity (RH) directly above the water is provided. The ions present in the salt solutions however, hinder evaporation of the polar water molecules, leading to a reduced relative humidity [129]. Therefore, the desired RH can be adjusted by the choice of the type of salt. Table 4.6 shows the kinds of salt used in this work along with the corresponding theoretical RHs for a temperature of 18°C [130]. The table also includes silica gel and water for the lowest (< 2 %) and highest realized RHs, respectively. The samples post-treated using polar atmospheres were kept in closed desiccators (*Schott Duran*, V= 0.7 L), in which 60 mL of salt solution was stored in the reservoir right below the sample. The duration of this treatment was

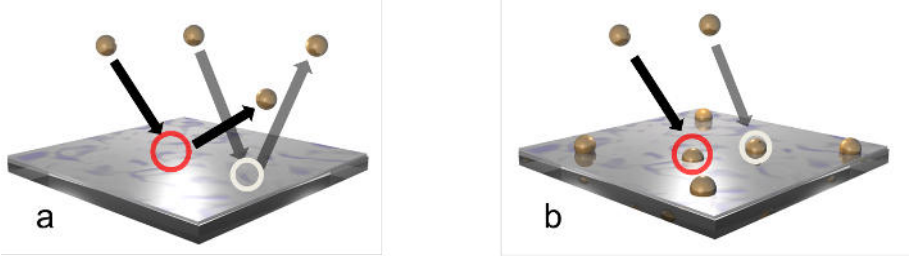

Figure 4.5.: The condensation coefficient (cc) is a measure of the probability for incoming atoms to adsorb to the surface. For $cc = 0$ all atoms immediately desorb after arriving at the surface (a), for $cc = 1$ all of the incoming atoms adsorb (b).

Table 4.6.: Chemicals used for adjusting the polarity of the atmosphere along with the corresponding theoretical resulting relative humidities, taken from [130].

chemical	relative humidity (RH)
silica gel	<2 %
LiCl	12 %
$Mg(NO_3)_26H_2O$	56 %
NaCl	75 %
H_2O	100 %

24 h. The salt solutions were prepared well in advance to make sure to have exceeded the solubility limits. Consequently, a certain amount of salt remained undissolved. The complete sample post-treatment was carried out at a controlled temperature of 18°C.

4.5. Punch preparation

For the tack measurements two different kinds of punch probes were used. The punch probes made of different metals were polished by the *TUM Crystal lab* using polishing pastes of different grain size purchased from *Struers*. To increase the punch roughness in the case of stainless steel, common sand paper was used. As probe materials stainless steel, aluminum, titanium and gold were used. To characterize the resulting surfaces atomic force microscopy (AFM) was used to map their topographies. These measurements were carried out under standard room conditions with AFM-3 in tapping mode (see figures 4.6a-e). Table 4.7 summarizes the used metal punch materials along with the obtained roughness values σ_{rms}. Also polymeric punch probes were used to investigate the phenomenon of crack-healing (see chapter 5.6). The preparation was carried out as follows. The polymer was put in a copper mold ontop of a acid cleaned and silanized

Table 4.7.: Probe punch materials and σ_{rms} values obtained from AFM.

Material	σ_{rms}
stainless steel (V2A-a)	1.7 ±0.2 nm
stainless steel (V2A-b)	6.4 ±0.3 nm
stainless steel (V2A-c)	105 ±2 nm
aluminum	8.3 ±0.1 nm
gold	11.6 ±0.3 nm
PMMA	0.34 ±0.07 nm

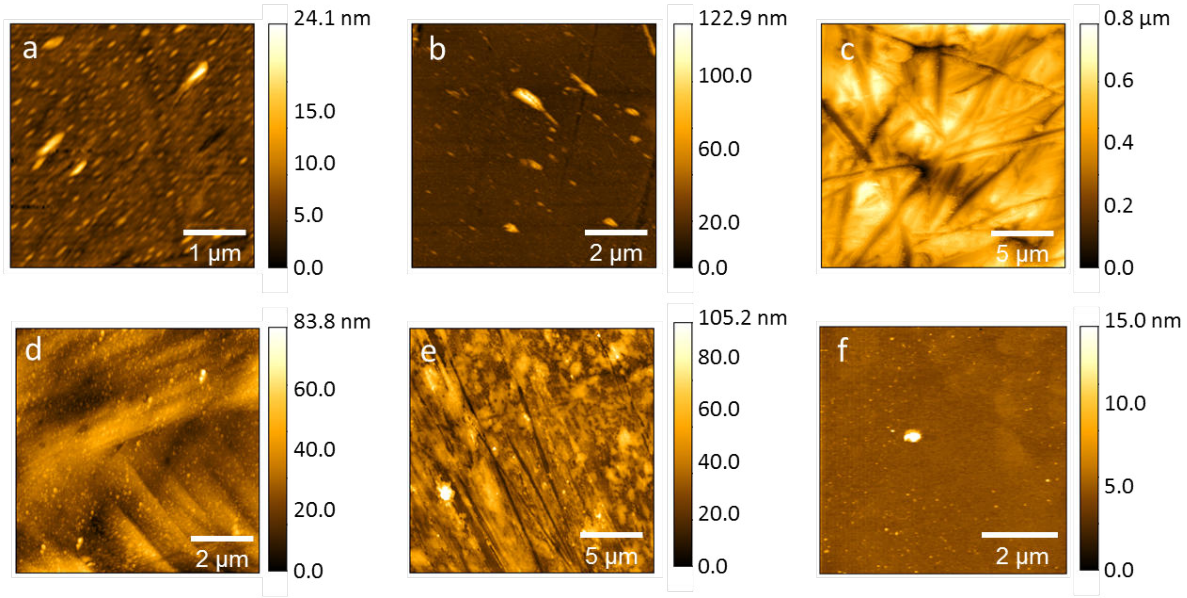

Figure 4.6.: AFM topography images of the punch probe surfaces: a) stainless steel (V2A-a), b) stainless steel (V2A-b), c) stainless steel (V2A-c), d) aluminum, e) gold, f) PMMA.

silicon substrate (see figure 4.7). For the silanization the substrates along with 20 μL of trichloro(1H,1H,2H,2H-perfluorooctyl)silane (TCPS) (*Sigma-Aldrich*) were put in a desiccator which was evacuated using a water jet vacuum pump. After 30 min of evacuation the connection to the vacuum pump was closed and the samples remained in the TCPS atmosphere for another 30 min. In order to guarantee a monolayer of TCPS the silicon samples were heated up subsequently to 150 °C for 1 h on a heating plate (*IKA RCT basic*). The silanization was necessary to reduce the surface energy of the silicon substrates and therefore facilitated the nondestructive withdrawal of the punches from the casting mold. Furthermore the adhesion between polymer and silicon was reduced [131]. The casting mold consisted of a copper block (4×4 cm^2) which was put on top of the silanized silicon and sandwiched in between two steel plates (7×7 cm^2, not shown in the image). Steel pins fitting exactly inside the holes of the mold allowed the application of pressure on the polymer. The filled casting mold was put in a vacuum oven (*nüve EV018*) which was heated to 190°C while vacuum was applied. After keeping the casting mold at the specified temperature for 2 h the vacuum oven was vented. The steel pins were pushed into the holes of the mold, compressing the polymer. A weight of 500 g was subsequently put on all pins. The oven was again evacuated but not heated anymore. Over the course of at least 16 h the casting mold cooled down to ambient temperature. Finally the polymer punches are slowly pushed out of the mold using the steel pins, avoiding excessive stress. The polymer punches were then glued onto unpolished steel punches which were mounted in the tack device using epoxy glue (*UHU Endfest 300*). During the drying of

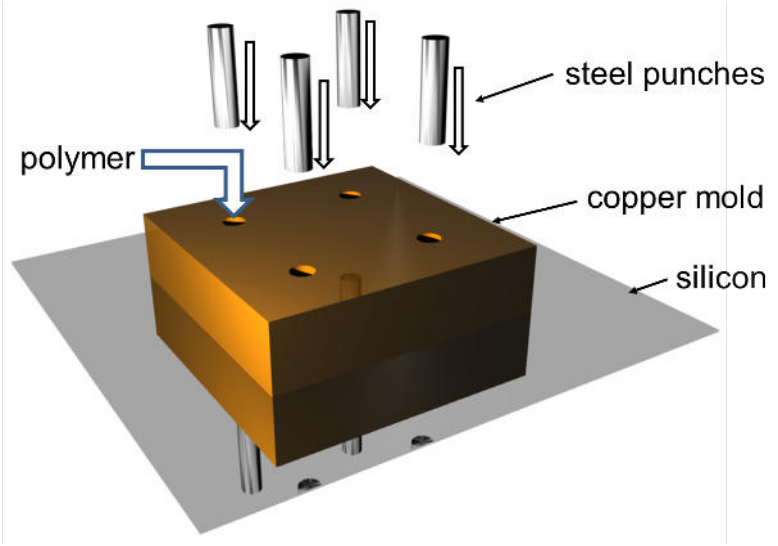

Figure 4.7: Melting of polymers for polymer punch probe: The solid polymer is deposited into the holes of the copper mold. Additionally, pressure is applied from the top. After cooling down cylindrical polymer punch probes with a very low surface roughness are obtained.

the epoxy glue the punch was pressed onto a glass substrate in the tack apparatus for 18 h, which facilitated the later alignment of punch and sample. The surface roughness of the PMMA punch is determined via AFM to be 0.34 ± 0.07 nm, shown in figure 4.6f. To characterize the surface on a larger scale the PMMA punch is investigated by optical microscopy, shown in figure 4.8. A smooth and clean surface is evident.

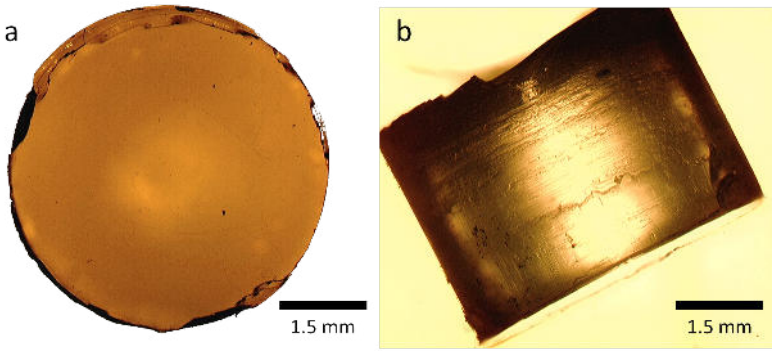

Figure 4.8.: Optical microscopy images of a PMMA punch: The surface (a) appears smooth and without major defects. The outer rim shows inevitable cracks originating from the removal of the punch from the mold. From the side-view image (b) taken with a slight tilt of the punch, the surface (lower right) appears also very smooth and no skewness or waviness is evident.

5. Inner structure and adhesion of the investigated PSAs

The functionality of polymer films is in many cases based on their inner structure. In organic photovoltaics, for instance, the choice of solvent severely affects the morphology of the active layer which, in turn, influences the efficiency of the resulting solar cells [132]. Also, in other fields like polymers in biosensors, a strong structure-function relationship is reported [133, 134]. Especially for pressure sensitive adhesives the performance is strongly linked to their inner structure [135, 99, 136]. This inner structure can be affected e.g. by addition of tackifier resins and other additives to adjust the viscoelastic properties of the PSA [7, 137, 138, 139]. The segregation behavior of copolymers consisting of the monomers EHA and MMA depends strongly on the segmental length distribution of the statistical copolymer and also the polymerization method [110, 140]. The possibilities reach from strong segregation, which is unusable for PSA applications [141], to very homogeneous samples which, depending on the compositional ratio, can also lead to poor adhesive performance [142, 143].
In this chapter the near-interface composition of P(EHA-stat-20MMA) and P(EHA-stat-20dMMA), being model systems for PSAs, is investigated. In the first section the topography of P(EHA-stat-20MMA) is probed with AFM. Subsequently, the inner structure, especially close to the surface and the adhesive-adherent interface, is investigated with time-of-flight grazing incidence small angle neutron scattering (TOF-GISANS) using the partially deuterated model system P(EHA-stat-20dMMA). The reorganization of the near-surface composition of P(EHA-stat-20MMA) exposed to environments of different polarity is addressed in section 5.3. Furthermore, the implications of the specific near-surface composition in terms of tack performance and observed failure mechanisms is detailed. Section 5.4 shows the effects of surface treatments of silicon adherents on the adhesive-adherent interface composition in the PSA, probed by neutron reflectivity. In section 5.5, the reorganization of the near-surface composition of P(EHA-stat-20dMMA) upon treatments with different relative humidities is followed in-situ by neutron reflectivity (NR). Finally, section 5.6 presents an investigation of the autoadhesion of PMMA under different relative humidity accessed via tack tests.

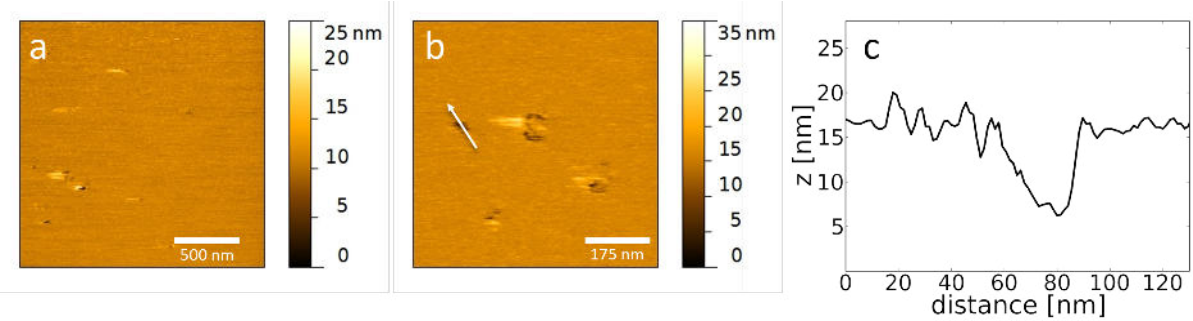

Figure 5.1.: Topography of a freshly cast P(EHA-stat-20MMA) film using a scan range of a) 2×2 μm^2 and b) 700×700 nm^2. Figure c) shows a line cut along the white arrow indicated in b).

Some results of this chapter were obtained together with Manuel Koller and Ferdinand Jarisch and are published in their respective Bachelor's theses [144, 145]. Parts of the results of this chapter are published in articles [146, 147].

5.1. Topography of solution cast P(EHA-stat-20MMA) films

The use of AFM to probe the surface topography of the investigated PSA film gives valuable information about possible phase separation and the homogeneity of the surface of the statistical copolymer. If a prominent phase separation would be present, the assumption of homogeneous layers in the interpretation of reflectivity data would be not valid. The measurements presented in this section were carried out on AFM-1. Figure 5.1a,b shows AFM topography images of a freshly prepared P(EHA-stat-20MMA) film at two different magnifications along with a line cut across one of the defects (figure 5.1c). The obtained root-mean-square roughness of the surface $\sigma_{rms} = 0.58\,nm$ (larger defects excluded) is considered to be the upper limit for the actual roughness, because the measurement was carried out with very low damping to avoid sticking. The dark areas show a depth of $\delta z \approx 10\,nm$ and represent small defects in the PSA surface. The scanning direction was from right to left which explains the white parts at the left rims of the defects in the images. In these areas the AFM tip slightly touched the surface when leaving the small cavities. This caused stronger interaction between tip and adhesive, leading to an increased retraction of the tip. The performed AFM measurements show very flat and homogeneous PSA film surfaces even at higher resolution. No evidence for the presence of lateral structures at the surface is found.

5.2. Inner structure of solution cast P(EHA-stat-20dMMA) films

Polymer films can exhibit different morphologies at the surface compared to the bulk and the interface to the substrate. AFM measurements alone are therefore not sufficient for complete structural investigations. Another drawback of AFM measurements is the limited probed surface area. Moreover, for the case of PSAs, the adhesive-adherent interface is of utmost importance for the performance of the adhesive bond. This interface is difficult to access non-destructively. Methods utilizing ultrasonic waves and dielectric spectroscopy have been applied in the past to get information about the durability and the integrity of adhesive bonds [148, 149, 150]. Meanwhile, also scattering methods are well established tools for structural investigations. In this section the structures at the surface, in the bulk and at the adhesive-adherent interface of the model PSA P(EHA-stat-20dMMA) are investigated by TOF-GISANS. These measurements are carried out at the instrument REFSANS at MLZ (FRM2, Garching). The angle of incidence is chosen to be $\alpha_i = 0.33°$ and a wavelength band from 2.25 Å to 11.75 Å is used. The counting time for every sample is 24 h. For the film preparation a concentration of 16.57 g/L is used for solution casting to obtain adhesive films with a thickness of 15 ± 2 μm. Thick silicon wafers with a size of $5 \times 8 \times 1.5$ cm^3 act as adherents, one acid cleaned, the other basic cleaned (see section 4.2). The different substrate treatments influence the interactions between the adherent and the EHA and dMMA components in the copolymer. Altered interfacial energies can favor an enrichment of one or the other component at the interface to the substrate [147]. A preferential enrichment can lead to seeds of one component which could be able to enhance the phase separation at the interface to the adherent.

Surface and near-surface structure

To probe surface and bulk of the investigated PSA films, the neutrons impinge directly on the free surface of the adhesive layer. Due to the large thickness of the polymer layer, the surface is decoupled from the adhesive-adherent interface. Therefore, the surface investigations were only carried out for the sample on the acid cleaned silicon substrate. Figure 5.2a-c shows three exemplary 2d GISANS data, corresponding to wavelength values of 3 Å, 7 Å and 11 Å. Due to the low all-over scattered intensity, a rather broad wavelength band width of $\Delta\lambda = 2$ Å is integrated to improve statistics. The very low count rate already indicates the absence of well pronounced structures in the PSA film. Each 2d data shows a strong specular reflected peak. The direct beam is shielded by a beam stop to protect the detector from too high intensities. In figure 5.2a two distinct Yoneda peaks are visible,

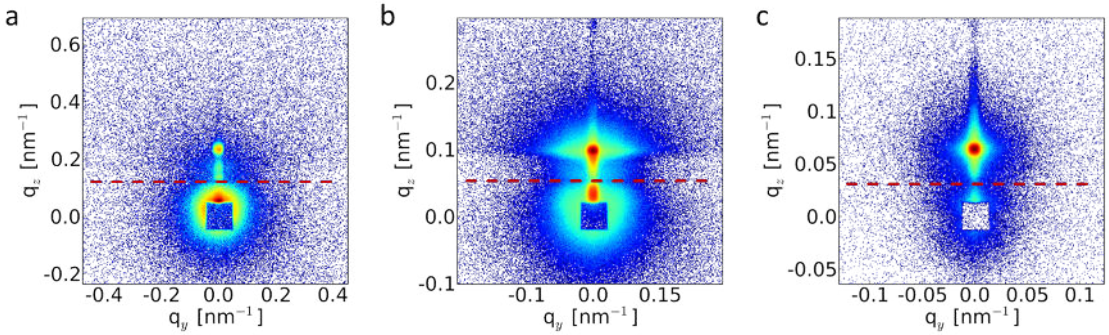

Figure 5.2.: Selected 2d TOF-GISANS data of P(EHA-stat-20dMMA) probed at the adhesive-air interface. For better statistics each data set integrates a wavelength bandwidth of $\Delta\lambda = 2$Å around a) 3 Å b) 7 Å and c) 11 Å. The direct beam is shielded with a beamstop. The dashed lines separate the transmitted from the reflected signal.

which shift towards the specular peak with increasing wavelength (see figure 5.2b) and finally disappear in the high intensity of the specular reflection (see figure 5.2c). In order to extract quantitative information, vertical line cuts are taken at $q_y = 0$ nm^{-1} using a higher resolution in λ-slicing of $\Delta\lambda = 0.5$ Å. Figure 5.3 shows the obtained line cuts. The red bar marks the position of the specular reflection. Also the identified Yoneda positions are indicated for PEHA (red markers) and for P(EHA-stat-20dMMA) (blue markers). The obtained Yoneda positions for PEHA and P(EHA-stat-20dMMA) are compared to the theoretical values in figure 5.4. An excellent agreement is evident which allows to extrapolate the Yoneda positions also to regions where they are not observable anymore

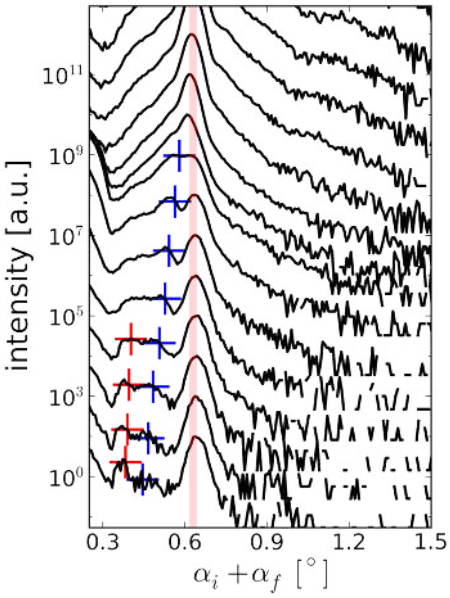

Figure 5.3: Vertical line cuts of the 2d GISANS data taken at $q_y = 0$ nm^{-1}, shifted along the y-axis for clarity. The crosshairs indicate the Yoneda peaks of PEHA (red markers) and P(EHA-stat-dMMA) (blue markers). The position of the specular peak is marked by a vertical red bar.

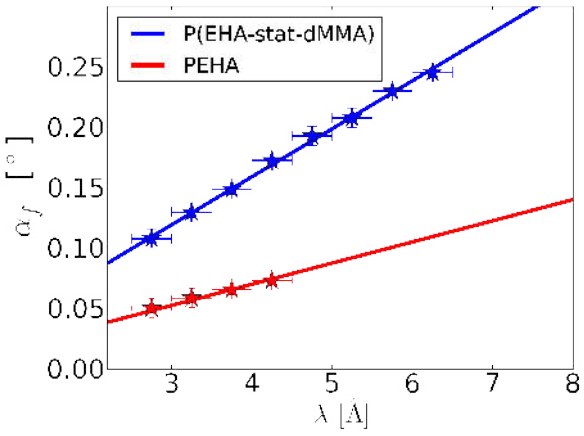

Figure 5.4: Comparison of theoretical and measured Yoneda positions for PEHA (red stars) and P(EHA-stat-dMMA) (blue stars) as a function of λ.

because of the intense specular peak. Quantitative information about lateral structures in the PSA film are accessed via horizontal line cuts taken at the wavelength-dependent Yoneda position of the material of interest, in this case PEHA and P(EHA-stat-20dMMA). Figure 5.5 shows a set of these cuts taken at the Yoneda positions of PEHA, covering a wavelength range from 4.25 Å to 9.75 Å. The corresponding fits to the data are also provided in figure 5.5 (red lines). These fits are based on a model which comprises a form factor of cylindrically shaped objects, distributed on a 1d paracrystal [151]. All line cuts exhibit a broad intensity shoulder, which corresponds to object sizes of $\approx 25 - 35$ nm for small λ and ≈ 40 nm for large λ, as identified from the fitting. As already explained in section 2.3.4, the scattering depth Λ strongly depends on the wavelength λ. Therefore, Λ is calculated for the used setup and shown in figure 5.6a (black line) along with the

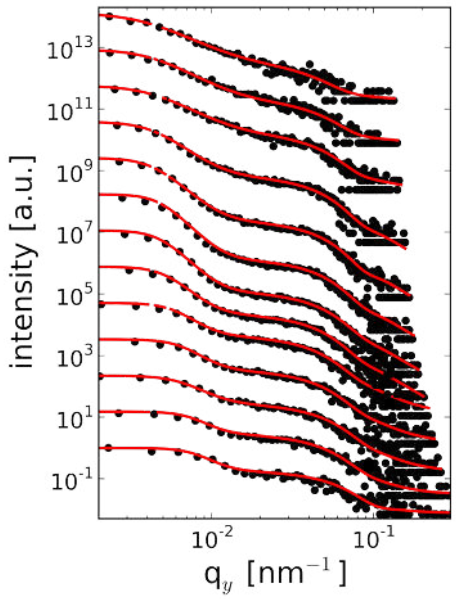

Figure 5.5: Exemplary set of horizontal line cuts taken at the Yoneda position of PEHA (black dots) along with the corresponding fits (red lines) as explained in the text. The curves are shifted along the y-axis for clarity. The wavelength ranges from 4.25 Å to 9.75 Å from bottom to top in steps of 0.5Å.

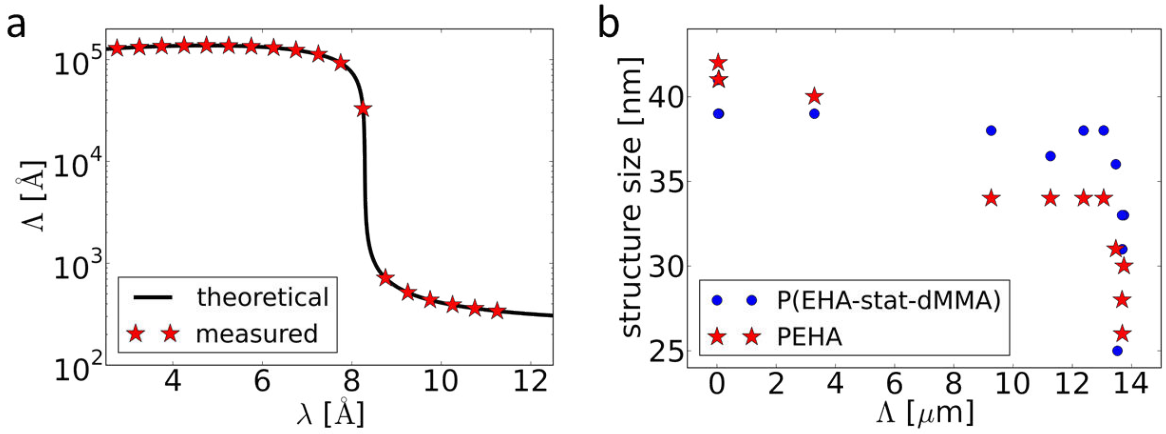

Figure 5.6.: a) Scattering depth Λ as a function of wavelength λ (black line). Each wavelength of the performed GISANS slices is marked by a red star. b) Structure sizes obtained from fitting of the horizontal line cuts as function of information depth for PEHA (red stars) and P(EHA-stat-dMMA) (blue dots).

positions of the used wavelength slices (red stars). The steep increase in Λ with decreasing λ is clearly visible. Combining the calculated scattering depth Λ and the structure sizes obtained from fitting the horizontal line cuts, each structure size can be correlated with a certain scattering depth, which is shown in figure 5.6b. The structure sizes found for PEHA and P(EHA-stat-20dMMA) show a similar trend. At the sample surface the largest sizes with $\approx 38-40$ nm are observed. With increasing Λ (deeper in the bulk) these sizes shrink to ≈ 25 nm. It has to be noted, that the bulk measurements also probe the PSA surface and the near-surface region. Therefore, the probed volume gets bigger with decreasing λ and consequently averaged information is obtained. Due to the similarity of structure sizes for both PEHA and P(EHA-stat-20dMMA) these sizes are attributed to defects in the PSA film rather than to a phase separation phenomenon. Furthermore, the density of these defects is negligibly low, since only very weak signals were obtained after a 24 h measurement. Also, in another study, these samples have shown enrichment layers of the copolmyer components in vertical direction which exhibit purities that can not be reached in presence of a significant amount of defects like voids or holes [147].

Adhesive-adherent interface

One of the strengths of TOF-GISANS is the ability to access buried interfaces non-destructively. This ability is used to probe the adhesive-adherent interfaces of P(EHA-stat-20dMMA) and two differently cleaned silicon wafers. For this purpose the samples

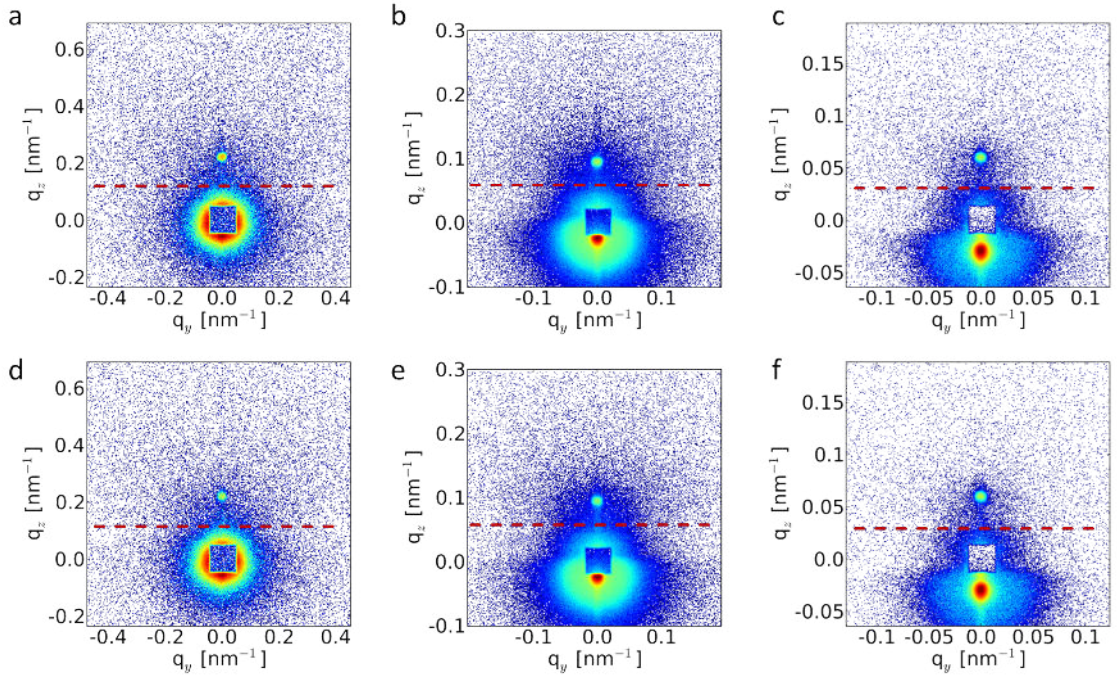

Figure 5.7.: Selected 2d TOF-GISANS data probed at the adhesive-adherent interface for both acid (a-c) and base (d-f) substrate cleaning. For better statistics each data set integrates a wavelength bandwidth of $\Delta\lambda$ = 2Å around a,d) 3 Å b,e) 7 Å and c,f) 11 Å. The direct beam is shielded with a beamstop. The dashed lines separate the transmitted from the reflected signal.

are put into the beam upside-down. The neutrons enter the thick silicon wafer through its side, impinge on the adhesive-adherent interface and leave through the other side of the silicon. Figure 5.7a-c shows exemplary 2d GISANS data obtained for the acid cleaned sample, while figure 5.7d-f shows the data recorded for the basic cleaned sample. In all images no Yoneda peak is visible between the direct beam position and the specularly reflected beam position, which is due to the sequence in which the neutrons pass through the involved SLDs. Already from the 2d data it is possible to state that no prominent structures are present. However, to get a more detailed impression, horizontal line cuts are performed in the region between the direct beam (located under the beam stop) and the specular peak, trying to avoid the tails of both peaks. A typical line cut is shown for the acid cleaned sample at a wavelength of λ = 4.75 Å in figure 5.8a (black dots). The origin of the visible intensity shoulder becomes obvious when comparing this cut to a cut from a measurement without the sample in the neutron beam, taken at the same position on the detector (figure 5.8a, red stars). From this comparison it is clear that the alleged lateral structure originates from the shape of the direct beam. This strong influence of the direct beam becomes even more visible in the vertical cuts of measurements with

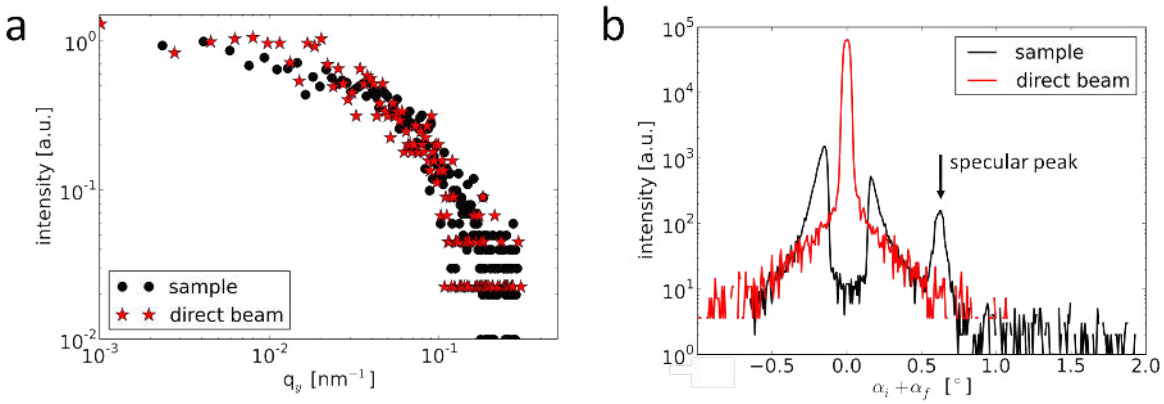

Figure 5.8.: a) Exemplary horizontal line cut from the acid cleaned sample taken at the Yoneda position of PEHA at a wavelength of 4.75 Å (black dots) compared to a horizontal line cut taken at the same angle for a direct beam measurement (red stars). b) Exemplary vertical line cuts taken at $q_y = 0$ nm^{-1} with the sample mounted (black line) and without the sample (red line).

and without the sample, which is shown in figure 5.8b. It becomes obvious that the tail of the direct beam (red line) reaches up to the position of the specular reflected beam in the actual measurement with the sample in the beam (black line). Therefore, at the adhesive-adherent interface no lateral structures are detected.
This absence of lateral structures makes reflectivity methods the techniques of choice for the investigation of enrichment layers of one or the other component of the statistical copolymer under study at and close to interfaces.

5.3. Tuning of the near-surface composition of P(EHA-stat-20MMA)

Adhesion of PSAs is based on van der Waals interactions, which are in theory strongest for molecules at the very top surface. In practice, the adherent penetrates this very surface of the adhesive due to its own roughness. As a consequence, not only the PSA surface is important for proper adhesion but also the near-surface region of the PSA film. This near-surface composition of P(EHA-stat-20MMA) was investigated by Diethert et al. using x-ray reflectometry (XRR) [136, 13]. They addressed the influence of aging of the adhesive under ambient conditions as well as the use of different solvents during sample preparation. Moreover, they showed that an additional treatment of the PSA film with various different relative humidities not only alters the near-surface composition

but also the tack performance [99]. The ability to tune the performance of one and the same PSA can be essential to tailor a specific near-surface composition which is suited best for a desired application. In this section the temporal evolution of an EHA enrichment in the near-surface region of P(EHA-stat-20MMA) under the influence of a completely unpolar nitrogen atmosphere is investigated with XRR. Subsequently, the MMA enrichment close to and at the surface under atmospheres of different polarity is addressed. This is realized using a custom designed temperature controlled humidity cell for XRR. Moreover, the tackiness of these humidity post-treated PSA films is investigated using a custom-designed humidity cell for tack measurements. The different observed failure mechanisms are addressed in the second part of section 5.3.3.

5.3.1. Surface enrichment of EHA

In this section the reorganization of the near-surface composition of P(EHA-stat-20MMA) films upon exposure to a nitrogen atmosphere, representing an apolar and inert gas, is investigated. The homogeneity of the PSA surface was already ensured via AFM measurements in section 5.1, which is an important prerequisite for an unambiguous interpretation of XRR measurements. Moreover, GISANS investigations performed on the very similar PSA P(EHA-stat-20dMMA) proved the lateral homogeneity of the adhesive films (see section 5.2). The vertical inner composition is accessed via XRR measured for samples which are aged under nitrogen for different times.
This aging investigation consists of a fresh sample and polymer films which are kept under nitrogen for 0, 4, 5, 10 and 12 days. Shorter times for the aging process are not selected to avoid complications related to a possible reorganization in the sample during the XRR measurement which lasted 8 h. After this post-treatment of the PSA films XRR measurements are carried out on XRR-1. Figure 5.9 shows the resulting reflectivity curves (black dots) along with the corresponding fits (red lines). The aging time increases from bottom to top. The reflectivity shown in the Fresnel normalized representation shows already significant changes in the low q_z-region for the different storage times under nitrogen. The dispersion profiles obtained from fitting the data are shown in figure 5.10a-e. The fresh film (figure 5.10a) shows an enrichment layer of MMA in the top 2.5 nm of the adhesive which decays smoothly to the bulk, which is finally reached in a depth of 20 nm. As already observed in earlier studies [99] this MMA enrichment establishes during the drying process and owes to the fact that PMMA is slightly better soluble in toluene than PEHA. The involved solubility parameters are $\mathfrak{D}_{PMMA} = 18.27\,\mathrm{MPa}^{1/2}$, $\mathfrak{D}_{PEHA} = 18.37\,\mathrm{MPa}^{1/2}$ and $\mathfrak{D}_{toluene} = 18.2\,\mathrm{MPa}^{1/2}$ [152]. Upon solvent evaporation toluene drags MMA segments of the copolymer along towards the surface. After four days (figure 5.10b) changes in the

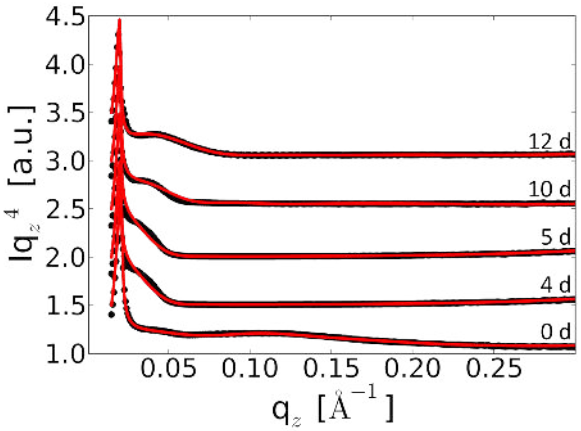

Figure 5.9: XRR measurements in the Fresnel representation (black dots) along with the corresponding fits (red lines) for samples aged under nitrogen atmosphere for 0 d, 4 d, 5 d, 10 d, 12 d (time increases from bottom to top). The curves are shifted along the y-axis for clarity.

dispersion profile are clearly evident. The former sharp enrichment layer of MMA has broadened to approximately 5 nm and diffused to a higher depth. A subsequent slightly EHA-enriched layer can be seen in the dispersion profile before the composition reaches the bulk value. Storing the adhesive film for 5 days under nitrogen further changes the resulting dispersion profile (figure 5.10c). The slightly enriched EHA layer, which could be seen after 4 days, has broadened, while the MMA-rich layer has also increased its vertical dimension to roughly 10 nm. Subsequently, the dispersion fades towards the bulk for higher depths. The dispersion profile of the sample aged for 10 days in nitrogen atmosphere still reveals ongoing changes (figure 5.10d). A broad and damped MMA enrichment can be seen at a depth of approximately 6.5 nm. Without further major oscillations the bulk dispersion is reached slowly with increasing depth. After 12 days an approximately 2 nm thick EHA enrichment layer has formed at the very surface of the polymer film (figure 5.10e). Due to the high purity of the EHA layer, the subsequent MMA-rich layer appears contracted and shifted towards the surface.

The enrichment of EHA at the very surface of the P(EHA-stat-20MMA) film originates not only from the lower surface energy of PEHA compared to PMMA ($\gamma_{PEHA} = 30\frac{\mathrm{mN}}{\mathrm{m}}$, $\gamma_{PMMA} = 38.5\frac{\mathrm{mN}}{\mathrm{m}}$ [153, 154]). In earlier studies aging of this sample system under ambient conditions resulted also in EHA enrichment layers at the surface, but not nearly as pure and not as fast as found in the present work [136]. In former investigations the EHA migration to the top was attributed to the minimization of the surface free energy. Therefore, this reorganization of the near-surface composition towards an EHA enrichment on-top is attributed to the interactions with the surrounding nitrogen atmosphere. The oscillatory nature of the composition profiles can be explained by the fact that the film consists of a statistical copolymer, meaning that the chain segments of the two components (EHA and MMA) are covalently linked. As a consequence, an enrichment layer of one component is followed by an enrichment of the other. However, this alternating se-

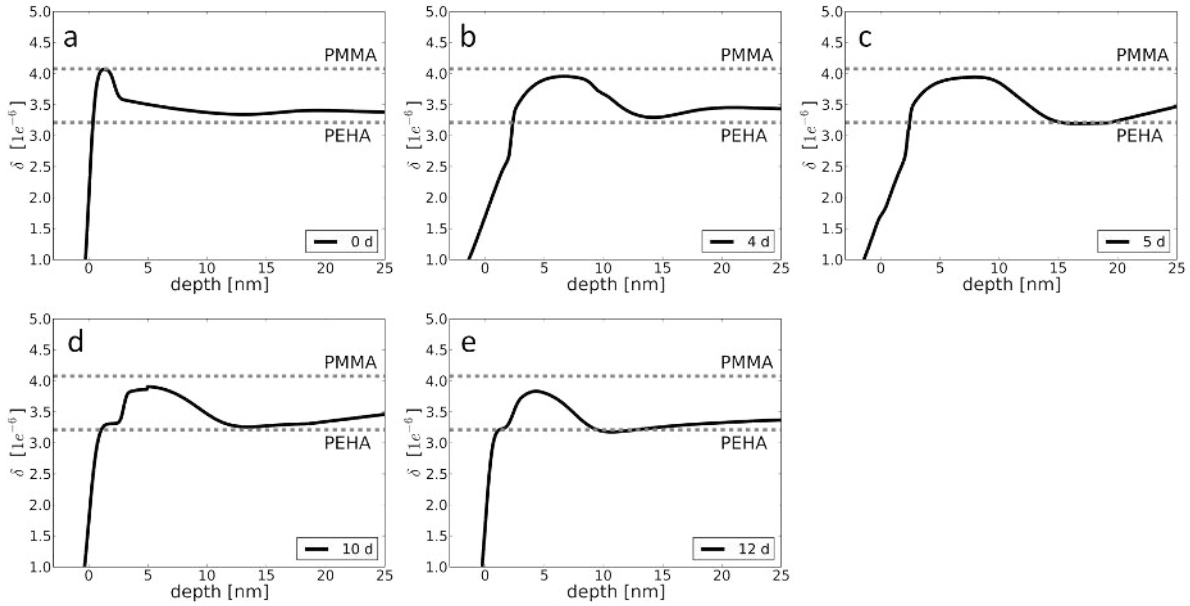

Figure 5.10.: Dispersion profiles of the near-surface region of the PSA for the different aging times: a) 0 d, b) 4 d, c) 5 d, d) 10 d and e) 12 d. The dashed lines indicate the dispersion of pure PMMA and PEHA, respectively.

quence of both types of monomers is not necessarily observed, because due to the limited scattering depth of x-rays the sample is considered to be semi-infinite, thus no conservation of mass is expected.

The dispersion profiles obtained from fitting the reflectivity data for the different aging times can also be converted to a color coded representation, shown in figure 5.11a-e. The color white represents pure EHA, black represents pure MMA. From the dispersion profile the colors in between these limiting cases are calculated as a linear combination as explained in section 3.6. A complete inversion of the near-surface composition profile is obtained within 12 days by a nitrogen treatment from a 2.5 nm enrichment layer of MMA to an EHA-rich layer of 2 nm.

5.3.2. Surface enrichment of MMA

In this section adhesive films prepared from the model copolymer P(EHA-stat-20MMA) are post-production treated with atmospheres of different relative humidity (RH). The resulting samples are investigated concerning their near-surface composition using XRR measurements. The measurements were carried out using the temperature and humidity controlled sample environment which is in detail described in section 3.6. For the post-production treatment the samples were stored after drying in desiccators under different RH for 24 hours. The RH series comprises of $< 2\%$, 18%, 59%, 75% and 96%

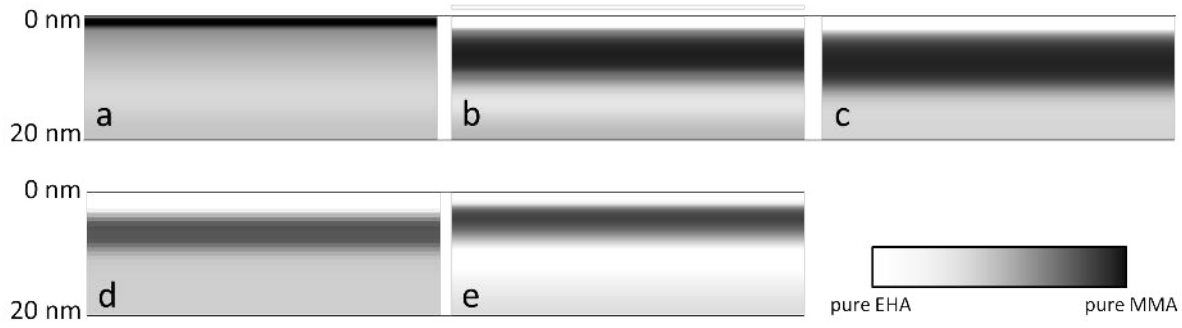

Figure 5.11.: Gray scale coded composition profiles for different storage times of the PSA under nitrogen: a) 0 d, b) 4 d, c) 5 d, d) 10 d, e) 12 d. The color white represents pure EHA, the color black stands for pure MMA. The different shades of gray represent mixtures of both components.

RH. The resulting reflectivity curves are shown in figure 5.12 (black dots) along with the corresponding fits (red lines) in the Fresnel-normalized representation. All obtained XRR curves exhibit distinct modulations in the low q_z-range, which already indicate the presence of non-homogeneous composition profiles. With increasing RH also the scattering at low q_z values increases, which reflects an enhancement of refractive index contrast in the vertical direction. The dispersion profiles, the obtained fits are based on, are presented in figure 5.13a-e. The dashed horizontal lines indicate the dispersion values for pure PMMA and PEHA, respectively. The sample post-treated at a RH of $< 2\%$ already shows an enrichment of the glassy minority component MMA (figure 5.13a). Such an enrichment has already been observed experimentally [146, 147, 13] and also predicted theoretically for similar systems [155]. This enrichment originates from the higher solubility of the MMA chain segments compared to EHA segments in toluene. During solution casting

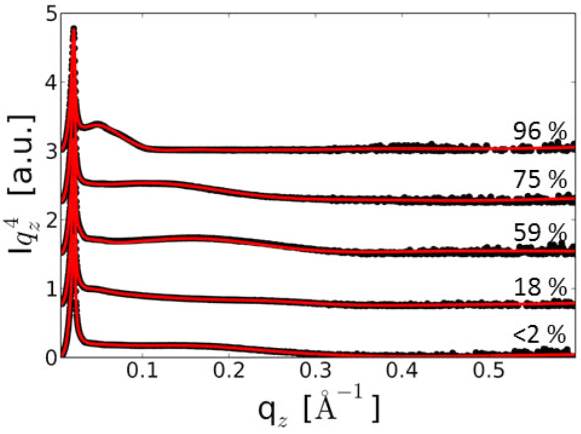

Figure 5.12: XRR measurements in the Fresnel representation (black dots) along with the corresponding fits (red lines) for samples aged under different RH of $< 2\%$, 18%, 59%, 75% and 96%, as indicated in the graph. The curves are shifted along the y-axis for clarity.

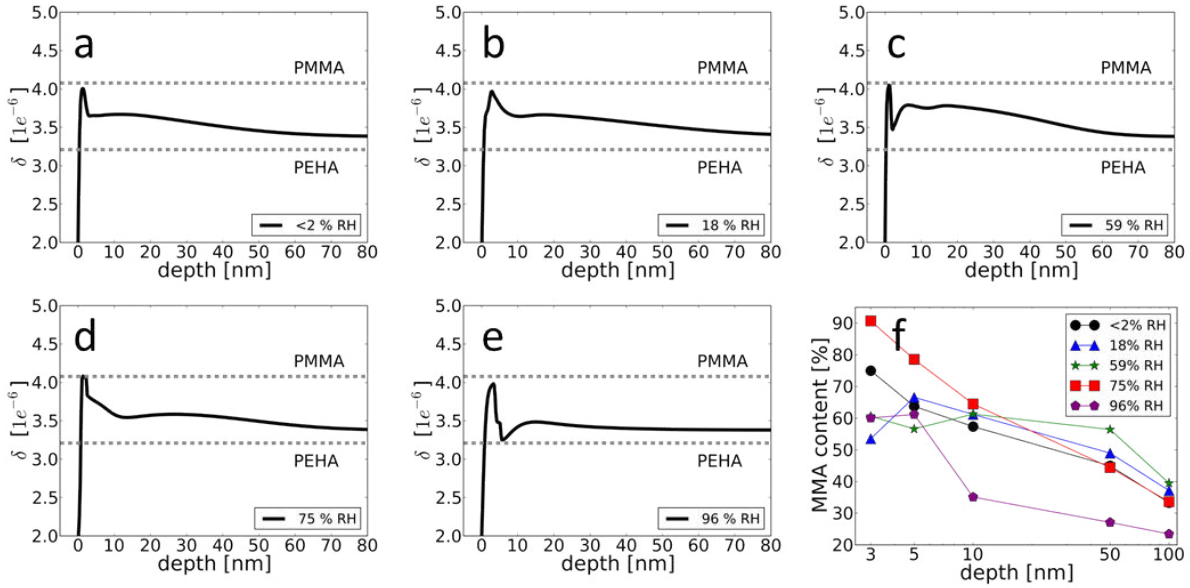

Figure 5.13.: Dispersion profiles of the near-surface region of P(EHA-stat-20MMA) films under different RHs: a) < 2% RH, b) 18% RH, c) 59% RH, d) 75% RH, e) 96% RH. The dashed horizontal lines in each plot mark the dispersion of pure PMMA and pure PEHA, respectively. f) Integrated MMA content in the near-surface region for different RHs as a function of integration depth.

the solvent evaporates and preferentially drags the MMA segments along towards the surface. At an increased RH (18% RH, see figure 5.13b) the MMA surface enrichment broadens. For 59% RH (figure 5.13c) again a more sharp and pure enrichment layer of the minority component MMA is observed close to the surface. Two weaker maxima follow, which get broader with increasing depth. These weaker maxima apparently migrate to smaller depth for 75% RH (figure 5.13d). The composition of the sample treated with 96% RH (figure 5.13e) shows again a very sharp and clear enrichment of MMA, necessarily followed by an EHA enrichment, because both components are covalently linked in the statistical copolymer. All extracted dispersion profiles share the weak decay to the mean bulk composition for larger depths from the surface.

Figure 5.13f shows the depth dependence of the integrated relative MMA content for the different RHs. It is striking that the MMA content drops only monotonically for the samples treated with < 2% and 75%. For 96% RH only a weak maximum is observed at a very shallow depth. The other curves show clear maxima at certain depths. The reason for this is found in the driving force for the rearrangement of the near-surface composition. PMMA has been found to have a polarity of 0.357 [156], while the polarity of PEHA is 0.026 [99], which is much smaller. The sample treated with the lowest RH of < 2% is dry and already close to equilibrium after a total time of 48 h. Also the PSA kept

under 96% RH has almost equilibrated due to the strong interaction of the strongly polar environment with the MMA segments in the PSA film. The sample stored at 75% RH, however, exhibits a larger MMA enrichment close to the surface compared to 96% RH. This can be partly explained by residual solvent in the adhesive after the first 24 h. Under 75% RH it is easier for the solvent to escape than under 96% RH, because water vapor is known to slow down the solvent evaporation [99]. Therefore, the toluene can still drag MMA chain segments along to the surface. The adhesive films stored under RHs of 18% and 59% show states in-between the lowest and the highest RH. The fact that P(EHA-stat-20MMA) is a two-component system allows for translating the dispersion profiles into composition profiles of MMA and EHA. When integrating these composition profiles the MMA enrichment at shallow depths appears low, which leads to the maxima/plateaus in figure 5.13f for 18% and 59% RH. The MMA enrichment in general decreases with depth, tending asymptotically towards the bulk content of 20%, which is still not reached at a depth of 100 nm. These integrated MMA contents show that the influence of a polar environment can influence the inner structure of PSAs to rather high depths. The resulting implications for the adhesive performance of the differently post-production treated samples are addressed in the following section.

5.3.3. Tackiness and failure mechanisms

The influence of different relative humidity (RH) on the adhesive performance of P(EHA-stat-20MMA) is investigated using tack-tests. To be able to provide constant temperature and constant RH throughout the post-production treatments and also during the tack measurements, a custom-designed sample environment is used (see section3.3). The RH series comprises of 5%, 16%, 42%, 60%, 75%, 95% RH, as measured with an integrated humidity sensor. To prove the necessity of such full control over the RH during tack-tests, sets of measurements with and without the use of the cell are compared. Each set comprises of at least 8 subsequent measurements with a constant time in between of $\Delta t = 5$ min. Figure 5.14 shows the obtained stress maxima σ_{max} for the three RH values 5%, 42% and 95% as a function of time. The dashed lines are guides to the eye. Clearly, the temporal evolution of σ_{max} differs for both setups. In case of no humidity cell is used, the post-production treated samples are exposed to ambient RH during the tack-tests. The stress maximum σ_{max} increases for the sample post-treated with 5% RH, stays constant for a post-treatment at 42% RH and decreases for the sample stored under 95% RH. In case the humidity cell is used and therefore a constant RH is provided, these trends vanish. The observed trends show that σ_{max} changes towards the values obtained for the sample which was post-production treated at the ambient RH of 42%. For this sample no trends

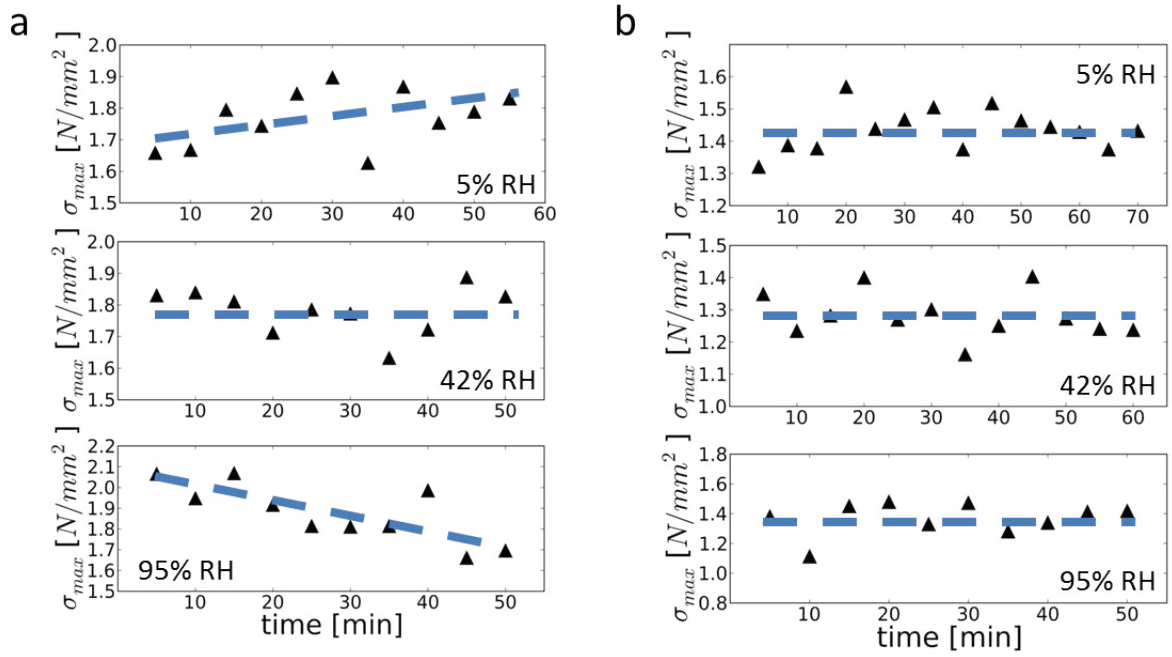

Figure 5.14.: Comparison of the temporal evolution of σ_{max} with (a) and without (b) the humidity cell for three exemplary RH values of 5%, 42% and 95%. The dashed lines are guides to the eye.

are observed, also without the cell. Therefore, by choosing a time interval of $\Delta t = 5$ min between each measurement the adaption of the near-surface region of the PSA to ambient conditions can be resolved in a tack-test. Due to the need for longer metal punches for the implementation of the humidity cell in the tack device, the two setups with and without the cell (figure 5.14a, b) are using two different stainless steel punch probes. The punch for the setup without the humidity cell exhibits a roughness of 1.7 nm, while the longer punch for the use in the cell has a roughness of 6.4 nm. This difference explains the generally lower stress maxima in the latter case. It is important to note that without identifying this temporal evolution the extracted quantities like mean stress maxima σ_{max} and mean tack energies E_{tack} would suffer from unrealistically large error-bars. By the use of the humidity cell this temporal reorganization can be avoided. Hence, all further measurements involving humid atmospheres are carried out in the humidity cell.

The recorded stress-strain curves under different RH exhibit in general all the typical shape of a non-crosslinked PSA: A sharp stress peak at small strains is followed by a low stress plateau at higher strains. However, they substantially differ in detail. While for the different RHs below 75% common cavitation and fibrillation is found, a transition of the failure mechanism is observed at around 75% RH. Figure 5.15a-c shows three exemplary stress-strain curves for the three observed failure mechanisms along with optical micro-

graphs of the adhesive-punch interfaces in the corresponding insets. It can clearly be seen that at 75% RH cavitation coexists with internal crack propagation (figure 5.15a, b). Not only the optical micrographs show differences, but also the stress-strain curves. Different values of the stress maximum σ_{max} and the tack energy E_{tack} result, accompanied by a very abrupt rupture of the adhesive bond in the case of internal crack propagation. Taking the optical micrographs into account, it is clear that at 75% RH both failure mechanisms coexist, even within one detachment (figure 5.15b). At high RH such as 95% RH (figure 5.15c) only external crack propagation is observed. This process is very fast and thus unfortunately not resolved with the CCD camera used. The adhesive bond ruptures already at significantly lower strains.

Comparing to the map of failure mechanisms introduced by Creton et al. [157] (see figure 2.7b) it is obvious that the quantities which determine the failure mechanism of a PSA bond are the critical energy release rate G_c and the Young's modulus. The observation of different failure mechanisms at different RHs shows that the near-surface composition of the PSA plays an important role in combination with the used punch. By the use of the humidity cell a constant RH is provided also for the steel punch probe, which is why the surface energy of steel needs to be included in the considerations. Adsorption of water from the atmosphere to the stainless steel changes the interfacial properties and hence G_c. At the same time the Young's modulus of PMMA is reported to decrease with increasing RH [158], which means that enrichment layers of MMA near the surface can also alter the mean Young's modulus. Hence, by adjusting the RH the map of failure mechanisms (see figure 2.7b) is scanned along its y-axis, because the confinement (punch diameter divided by the film thickness) is kept constant.

Despite the fact that different failure mechanisms are observed, still stress maxima and tack energies can be extracted. Figure 5.16 shows these quantities measured with a punch roughness of 6.4 nm. Clearly, σ_{max} drops from the first to the second investigated RH to a minimum. The stress maximum then stays rather constant with increasing RH until a sudden increase to the global maximum at 60% RH is observed. For higher RHs the values of the stress maximum drop further, regardless of the failure mechanism. At 75% RH two different failure mechanisms coexist. The internal crack propagation (red triangles) shows a higher σ_{max} than obtained for cavitation (black dots). For 95% RH and external crack propagation the stress maximum stays on a low level (blue stars).

In earlier experiments Diethert et al. have found MMA enrichment layers in P(EHA-stat-20MMA) near the surface as well [99]. They showed that the amount of MMA near the surface increases monotonically with RH, while also stress maximum and tack energy continuously grow with RH. This behavior is attributed to the enrichment of the glassy MMA close to the surface, which disables the PSA to adapt to the roughness of the punch

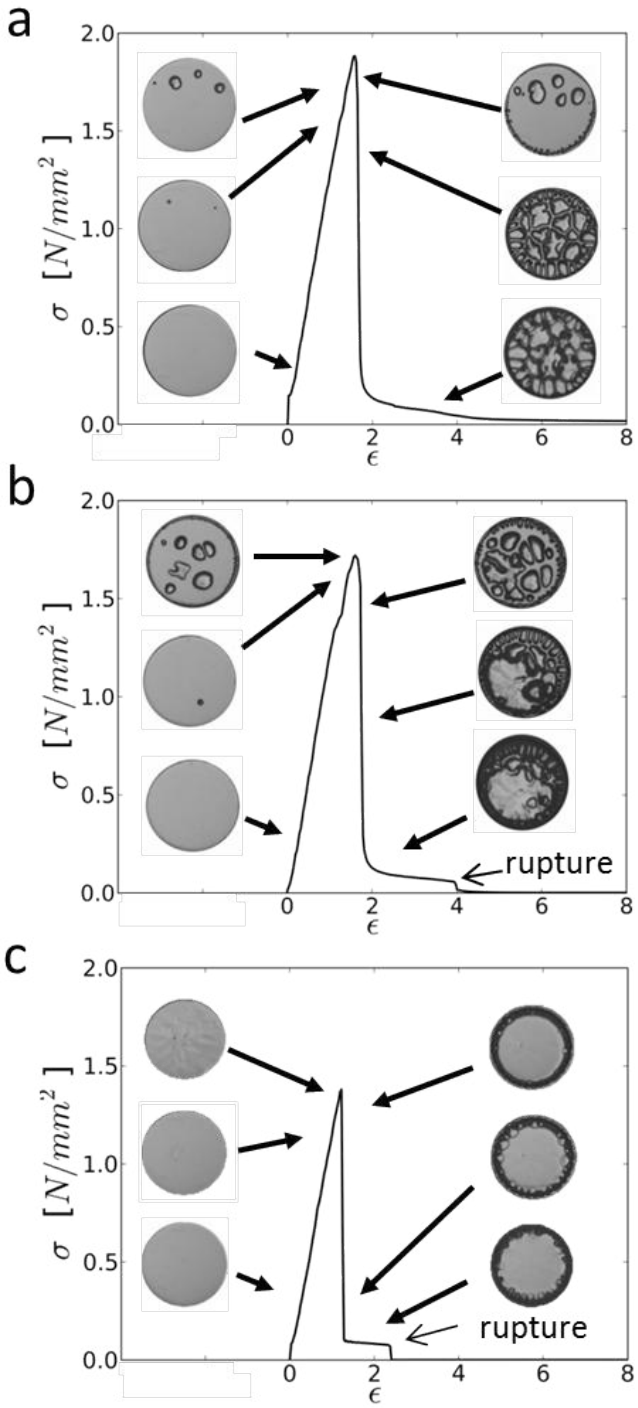

Figure 5.15: Exemplary stress-strain curves for a measurement conducted at 75% RH (a,b). The optical micrographs of the adhesive-punch interface show that at 75% RH two failure mechanisms coexist. In the first case the bond rupture occurs via cavitation and fibrillation (a), the second case represents a failure by internal crack propagation (b). Evident is the early and sudden rupture of the bond in b. Even within one detachment a coexistence of cavitation/fibrillation and internal crack propagation can occur, visible in the micrographs of the contact area in b. For tack experiments conducted under 95% RH external crack propagation is observed (c). The adhesive bond ruptures suddenly at even lower strains as compared to b.

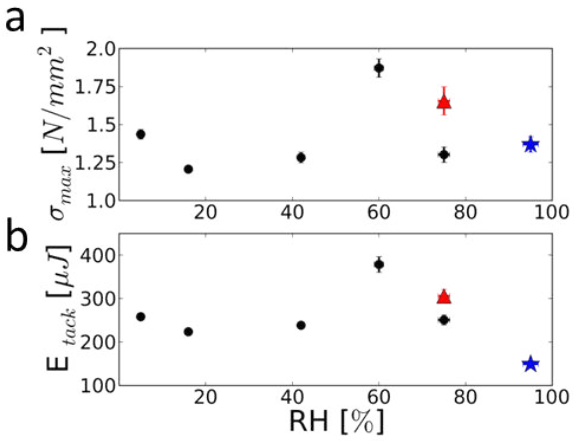

Figure 5.16: a) Stress maxima as function of RH measured with a punch exhibiting a surface roughness of 6.4 nm. The black dots mark failure via cavitation and fibrillation, the red triangles represent internal crack propagation and the blue stars denote external crack propagation. b) Tack energies as function of RH, using the same color and symbol coding.

as good as before. Consequently, the effective contact area of punch and PSA is smaller, which results in a higher pressure. In contrast to these earlier studies, a more complex behavior is observed in the present work, which can be explained by the use of the humidity cell. Due to the fact that constant RHs are provided during the tack measurements, the changes in the Young's modulus of the enriched component MMA in the near-surface region need to be taken into account as well. The Young's modulus of PMMA is known to soften with increasing RH exhibiting the steepest drop at around 60% RH [158]. For tack measurements at RHs up to 60% the Young's modulus stays rather constant for PMMA. The XRR measurements in section 5.3.2 have shown a slightly increased roughness at the surface of the PSA films, which lowers the tack performance for these films at RHs from 16% to 75%. At 60% RH, where a global maximum of σ_{max} is present, more MMA has enriched near the surface as compared to lower RHs. Its Young's modulus is still on a high level. At RH values higher than 60% σ_{max} drops significantly due to the softening of Young's modulus [158].

The determined tack energies follow a similar trend. Nonetheless, at 60% RH the difference in E_{tack} for the two failure mechanisms is not as pronounced, due to the earlier rupture of the bond for internal crack propagation (see figure 5.15b). For 95% RH the tack energy drops to a global minimum, because of the even earlier complete rupture of the bond (see figure 5.15c).

This complex behavior is affected by competing effects: An increase of RH is known to enrich MMA near the surface, which in turn improves the tack performance concerning higher values of σ_{max} and E_{tack}. However, an increase in RH also reduces the Young's modulus of PMMA, which in turn reduces these improvements of the tack performance by decreasing σ_{max} and E_{tack}. Furthermore, surfaces with high surfacial energies (in this case stainless steel) are known to adsorb water vapor [14], which is also expected to lower the tack performance, due to a reduction of interfacial tension and consequently a reduction

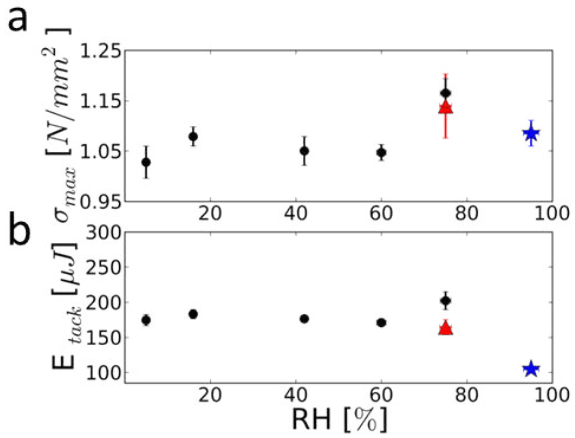

Figure 5.17: a) Stress maxima as function of RH measured with a punch with a surface roughness of 105 nm. The black dots mark failure via cavitation and fibrillation, the red triangles represent internal crack propagation and the blue stars denote external crack propagation. b) Tack energies as function of RH, using the same color and symbol coding.

of the Dupre work [18].

To obtain a more detailed picture of the influence of RH on the tack performance, the influence of punch roughness on this complex behavior is investigated. A stainless steel punch with an increased roughness of 105 nm is used. The identical experiments as in the case of the lower punch roughness are performed. The different failure mechanisms are observed at the same RHs, irrespective of the punch roughness. The extracted σ_{max} and E_{tack} from the RH series are shown in figure 5.17. The same general trends are visible as in case of the low punch roughness, but significantly weaker pronounced. This damping of the trends can be explained by the increased punch roughness. The rougher the punch, the further it penetrates into the adhesive film. XRR measurements in the previous section have shown, that the RH post-production treatment alters the composition of the surfaces and the near-surface region of the PSA strongly in depths up to approximately 20 nm (see section 5.3.2). At larger depths of up to about 100 nm still a weak effect of the RH on the composition profile is found (see section 5.3.2). The punch roughness of 105 nm is significantly larger compared to the heavily influenced region of the PSA film (20 nm), leading to a penetration of the punch into less affected regions of the PSA film. As a consequence, the rougher the punch is, the less sensitive it is concerning changes at and close to the surface. Hence, the features in figure 5.17 are damped because the large punch roughness reduces its sensitivity in the tack measurement. In turn, the most sensitive tack measurements can be performed with very smooth punch surfaces.

Hence, the results from tack measurements under different RHs using stainless steel punches of different roughness agree well with the findings from XRR concerning the near-surface composition in section 5.3.2.

5.4. Tuning of the adhesive-adherent interface composition

As shown in section 5.3 the near-surface composition of the investigated statistical copolymer P(EHA-stat-20MMA) reorganizes depending on the surrounding atmosphere. This rearrangement also affects the tack performance as shown in section 5.3.3 and is already reported in earlier studies [99, 136]. This knowledge is of importance not only for the application of a PSA after a certain storage time but also offers a possibility to tune the adhesive properties of one and the same PSA to the specific needs at hand, e.g. for low-tack applications. Nonetheless, it is even more important to investigate the behavior of the polymer at the adhesive-adherent interface to be able to predict the strength and durability of the established bond. The polymer near-interface composition can change in a similar fashion due to the present interactions installed by the surface chemistry of the adherent. The goal of this section is to shed light on this buried interface. Neutron reflectivity (NR) is used to access the adhesive-adherent interface of the partially deuterated model PSA P(EHA-stat-20dMMA) prepared on differently cleaned silicon substrates. The NR experiments were carried out the instrument AMOR (PSI, Switzerland).
Silicon is used as a model adherent and is subject to two different surface cleanings to install different surface energies. Silicon is very well-suited for reflectivity measurements due to its very small surface roughness, which allows for decoupling the effects of surface chemistry and surface roughness affecting the near-interface composition of the PSA film. Two different cleaning procedures are applied to the substrates, an acid and a basic treatment (see section 4.2). The different surface polarities are expected to selectively attract one or the other constituent of the statistical copolymer due to the different polarities of the chain segments. The polarity of PEHA is 0.026 [99], which is significantly lower than the polarity of PMMA of 0.357 [156]. To make sure to only measure static samples the PSA films are pre-aged for 4 days before the NR measurements. Furthermore a heating of the samples at $80°C$ results in identical reflectivity curves as obtained before heating, which is why the samples are considered to be equilibrated. To decouple the top interface from the bottom interface, films with a thickness of $15 \pm 2\mu$m are prepared. NR measurements of the polymer-air interface of both samples show the exact same reflectivity (figure 5.18), meaning that the adhesive film is thick enough not to superimpose information from both interfaces. Therefore, also a cross-influencing of the two interfaces is avoided. Furthermore, this measurement proves the excellent reproducibility of the sample preparation routine. The critical edge of silicon ($q_{c,Si} = 0.01\,\text{Å}^{-1}$) is not visible, which means that the scattering depth in this neutron experiment is smaller than the film thickness. The inset in figure 5.18 shows the SLD profile for both samples, obtained

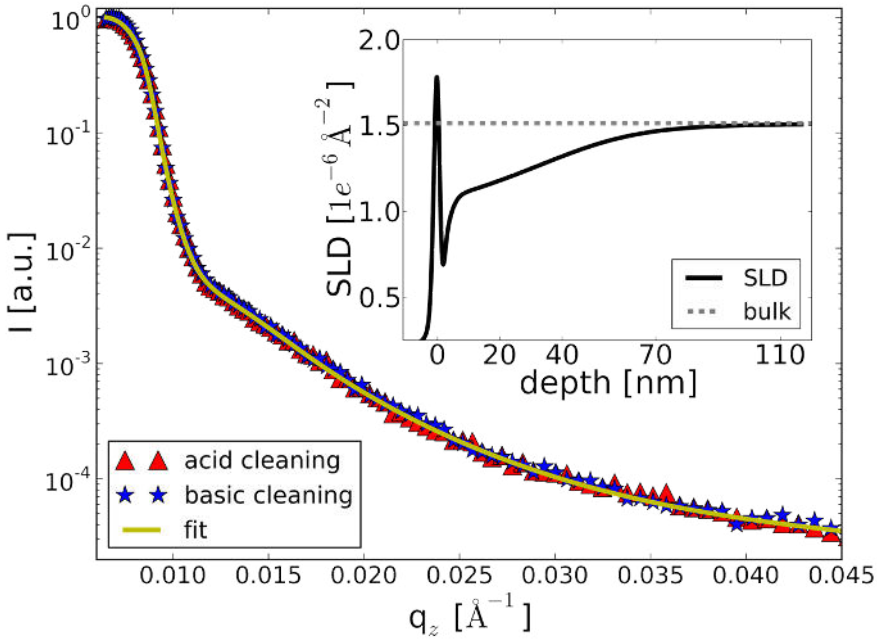

Figure 5.18.: NR measurements of P(EHA-stat-d20MMA) on acid (red triangles) and basic (blue stars) cleaned silicon. The yellow line represents the best fit for both curves. The SLD profile obtained from the fitting is shown in the inset (black line). The bulk SLD of the PSA is also indicated in the inset (dashed line).

from fitting the reflectivity. The dashed line marks the SLD of the bulk adhesive. As already observed in section 5.3 for a similar system, a dMMA enrichment forms at the very surface due to its better solubility in toluene. Upon solvent evaporation this copolymer component gets dragged along to the surface and after 4 days still forms an enrichment layer of $\approx 1.3\,\mathrm{nm}$. The subsequent EHA-rich layer originates from the fact that dMMA and EHA chain segments are covalently bonded and a dMMA enrichment therefore has to be followed by an EHA-rich layer. Nonetheless, due to the high sample thickness this interface is considered semi-infinite, meaning no conservation of mass is expected. The bulk SLD of the PSA of $1.5 \times 10^{-6}\,\mathrm{Å}^{-2}$ is reached after $\approx 100\,\mathrm{nm}$.
To address the buried interface of adhesive and adherent the sample is put into the beam upside down. In this geometry the neutrons enter the thick silicon wafer through its side, get reflected at the silicon-polymer interface and exit again through the side of the silicon block. Figure 5.19 shows the NR data along with the corresponding fits (black lines) for the buried interfaces of acid and basic cleaned adherents (red triangle and blue stars, respectively). It is obvious that no critical edge is present, which means that only subtle enrichment layers of dMMA can have established. Otherwise, the critical edge of dMMA would appear due to its higher SLD compared to silicon ($\mathrm{SLD}_{dMMA} = 6.40 \times 10^{-6}\,\mathrm{Å}^{-2}$,

$SLD_{silicon} = 2.07 \times 10^{-6}\,\text{Å}^{-2}$). The decay of both curves differs significantly. In the case of acid cleaning only weak features appear in the measurement, while in the case of the basic treatment a prominent shoulder is present at $q_z \approx 0.015\,\text{Å}^{-1}$. As a consequence, the SLD profiles, shown in the inset of figure 5.19, reveal very different interfacial compositions. The red line represents the SLD profile of the acid cleaned sample while the blue line shows the profile of the basic cleaned sample. The dashed line indicates the SLD of the bulk PSA. For the basic cleaned silicon a sharp dMMA enrichment layer is found with

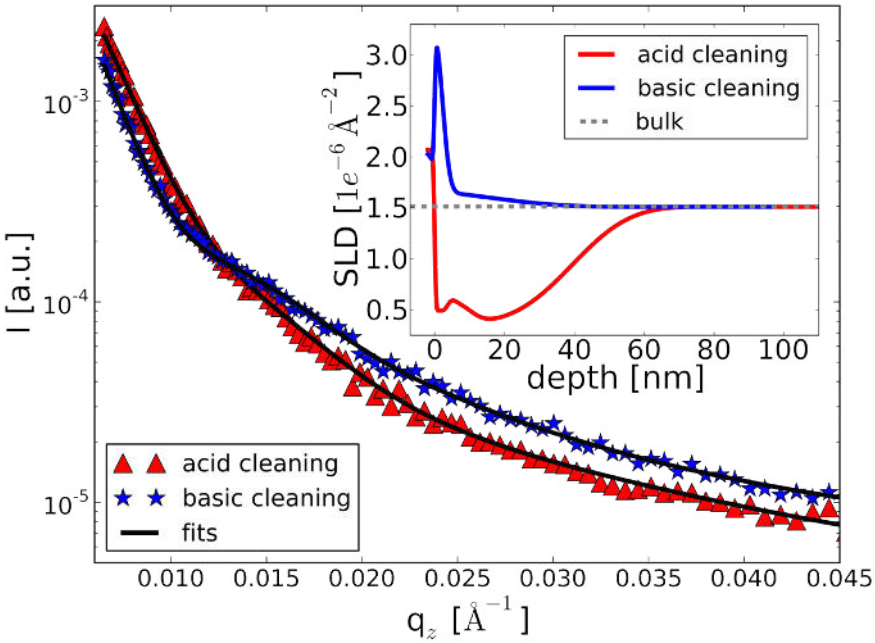

Figure 5.19.: NR measurements of P(EHA-stat-d20MMA) on acid (red triangles) and basic (blue stars) cleaned silicon at the buried interface. The black lines represent the best fits to the data. The inset shows the corresponding SLD profiles for the acid cleaned sample (red line) and the basic cleaned sample (blue line). The dashed line indicates the SLD of the bulk material.

a thickness of $\approx 2.4\,\text{nm}$ representing a mixing ratio the two copolymer components of EHA:dMMA = 0.55 : 0.45. The bulk ratio for comparison is EHA:dMMA = 0.80 : 0.20. After this layer the SLD slowly decays towards the bulk. On acidic cleaned silicon the situation appears differently. In this case a broad EHA enrichment starts at the silicon surface with a maximum ratio of EHA:dMMA = 0.97 : 0.03 and extends over $\approx 70\,\text{nm}$. After this highly EHA enriched region the SLD increases slowly reaching the bulk value in a depth of $\approx 70\,\text{nm}$.

For better visualization the obtained SLD profiles are converted to color coded composition profiles (according to section 3.6) in figure 5.20. Pure EHA is represented by white

while dMMA is shown in black. Again, the individual profiles differ significantly in all three cases. For the sharp enrichment layers close to the surface which occur for the

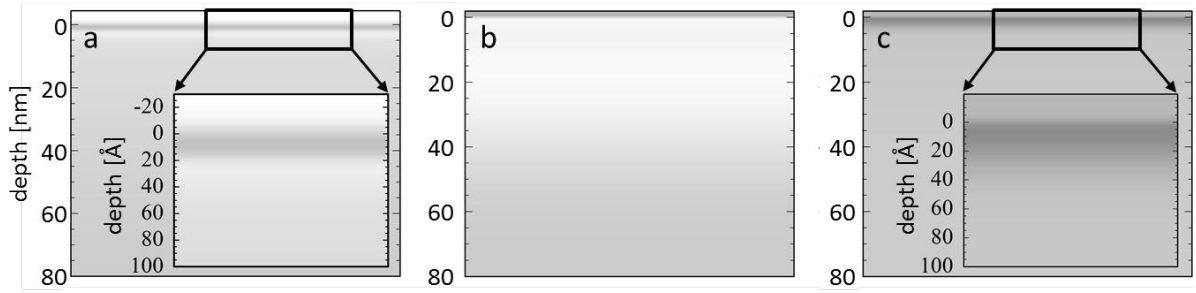

Figure 5.20.: Gray scale coded composition profiles of the adhesive-air interface (a) and the adhesive-adherent interfaces (b, c). The acidic treated buried interface is shown in b, the profile of the base treated sample in c. For the cases of very sharp enrichment layers close to the surface, a zoom-in is provided in the inset for better visibility of the detailed composition profile.

adhesive-air interface (figure 5.20a) and for the basic treated sample (figure 5.20c), zoom-ins are provided as insets for a better visibility of the detailed profile.
The composition of the model PSA P(EHA-stat-20dMMA) close to the buried adhesive-adherent interface reveals a high sensitivity to the surface treatment of the adherent. While acid cleaning results in a more hydrophobic surface attracting the less polar EHA segments, basic cleaning provides a more hydrophobic surface. The hydrophobic surface attracts the more polar dMMA chain segments. Even on the same adherent, using different treatments, different near-interface compositions can be installed to serve the desired needs.

5.5. Vertical structure evolution in films of P(EHA-stat-20dMMA)

The reorganization of the near-surface composition of the model PSA P(EHA-stat-20MMA) and also the corresponding implications for the adhesive behavior have already been addressed, both within in this chapter and in literature [99, 136, 146, 147, 13]. All of these studies have in common that the rearrangements of the near-surface compositions were investigated ex-situ by XRR. This method however, is (on the lab-scale) not capable of in-situ measurements due to insufficient flux which causes an inadequately low time resolution. Neutron reflectivity however, can provide the necessary resolution in time for in-situ experiments, especially at high-flux neutron research facilities like the reactor at

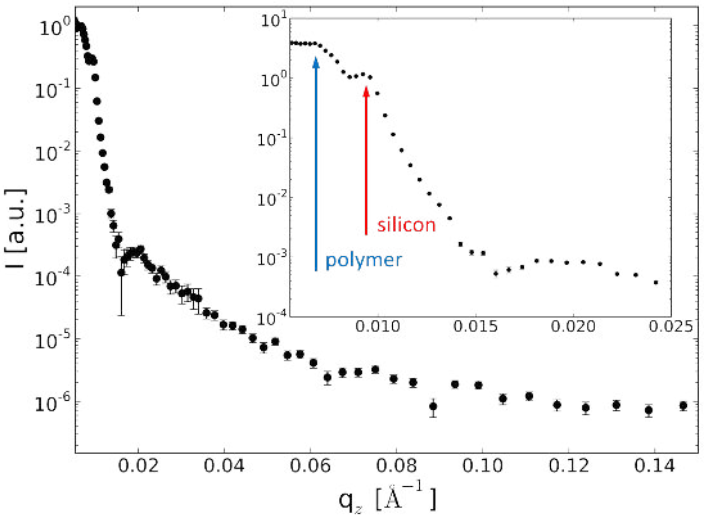

Figure 5.21: Reflectivity of the dry film of P(EHA-stat-20dMMA) before RH treatments. The inset shows an average of the first four measurements at $\alpha_i = 0.624$ from the in-situ experiment. Clearly visible are the critical edges of polymer and silicon substrate.

ILL, Grenoble [159, 160, 161]. Moreover, instruments which are operated in TOF-mode are even more beneficial for in-situ experiments, because a broad (although limited) q_z-range is probed at the same time. In NR curves measured monochromatically with varying incident and exit angles every data point is recorded at a different time. Therefore the reflectivity of dynamic processes obtained from monochromatic NR can appear compromised. An example for successful in-situ NR measurements is the determination of the near-surface solvent concentration profiles in PSA films during soluting casting [162].

As already shown in section 5.3, the near-surface composition of the model PSA P(EHA-stat-20MMA) changes during the course of a 24 h RH treatment. To follow this reorganization in-situ the very similar partially deuterated statistical copolymer P(EHA-20dMMA) is investigated. This polymer consists of 80% EHA and 20% deuterated MMA. For the in-situ NR measurement a custom-designed sample chamber is constructed. Four closed compartments of equal size, each with entrance and exit aluminum windows, store four simultaneously cast polymer films. The troughs beneath each sample store silica gel, solutions of MgCl and NaCl in D_2O and finally pure D_2O and to install RHs of $< 2\%$, 33%, 75% and 100%, respectively. After insertion of the substances providing the desired RH the sample chamber is closed and the measurement is started. The four different samples are probed subsequently in a loop by moving the sample chamber in between two subsequent measurements relative to the beam. The custom-designed sample environment was integrated into the FIGARO beamline at ILL, Grenoble, operated in TOF-mode. The resulting time resolution for each sample is $\Delta t = 6$ min. The whole process of reorganization is followed for 24 hours at an incident angle of $\alpha_{i,1} = 0.624$ °. Before adjusting the RHs in the different compartments as well as after the 24 h-measurement full reflectivity curves are measured using a second angle of incidence of $\alpha_{i,2} = 3.78$ °. For the sake of the

time resolution during the reorganization only one angle of incidence is used during the in-situ experiment. As explained in sections 5.3.1 and 5.3.2 the near-surface composition

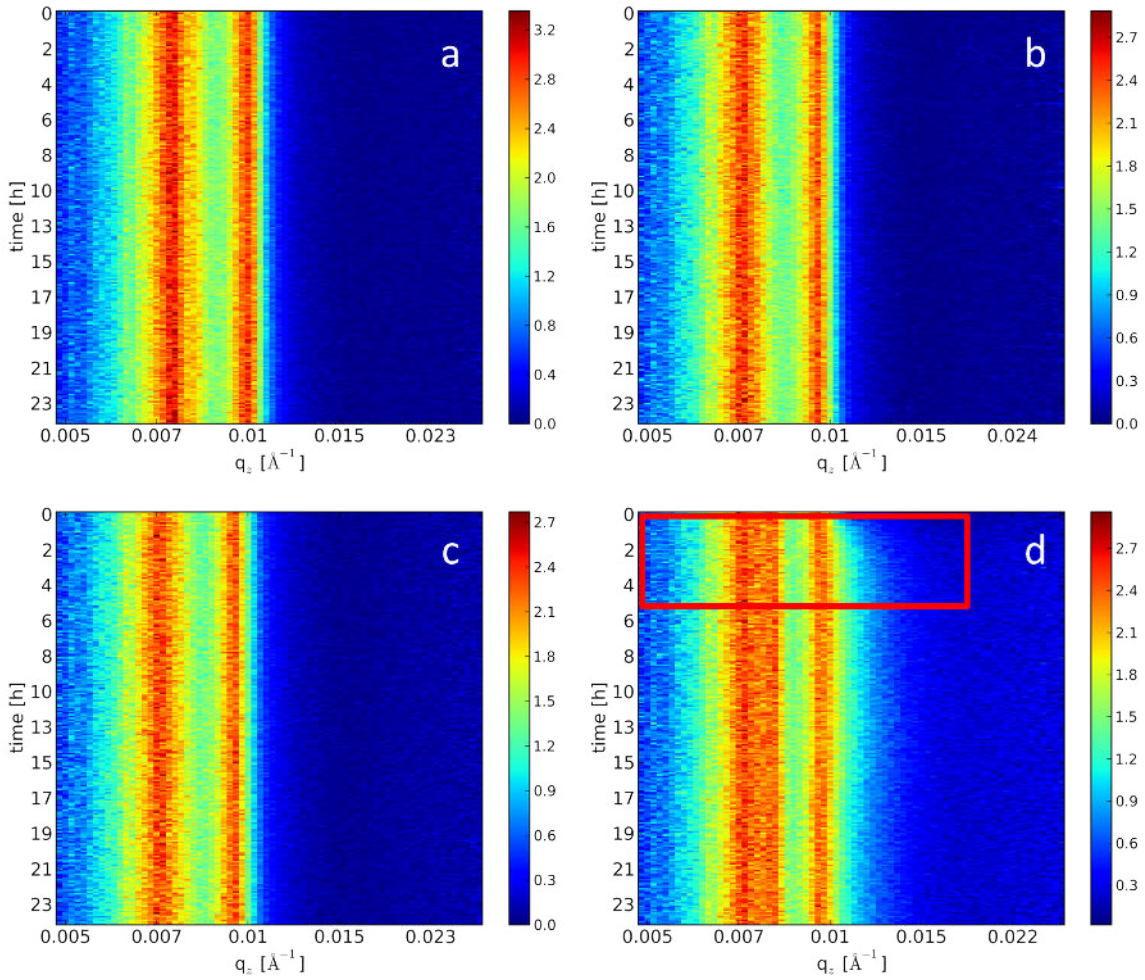

Figure 5.22.: Temporal evolution of the reflectivity of P(EHA-stat-20dMMA) stored at a) < 2% RH, b) 33% RH, c) 75% RH and d) 100% RH. Surprisingly, the only significant changes occur under 100% RH within the first 5 hours (marked by the red box).

can be determined under the assumption of a semi-infinite interface. This assumption holds as long as the film thickness exceeds the scattering depth. Therefore, a conservation of mass is not necessarily observed in the former studies. For a more precise picture of the near-surface composition of the PSA this conservation of mass can be included. For this purpose, both the surface and the interface to the substrate need to be measured simultaneously. Thus, the PSA films are prepared with a thickness of $5 \pm 1\mu$m.
Figure 5.21 shows the reflectivity of the dry film of P(EHA-stat-20dMMA). This curve represents the starting point for the tuning of the near-surface composition. Clearly, the two critical edges of the bulk polymer and of silicon are visible in the inset of figure 5.21,

which shows the average of four subsequent measurements at $\alpha_i = 0.624$. The temporal evolution of the four differently treated samples is shown in figure 5.22a-d in the Fresnel-normalized representation. Surprisingly, only the sample stored under 100% RH exhibits significant changes, which also happen quite early within the first 5 h. Due to the fact that no changes are visible during the treatments with relative humidities of <2%, 33% and 75% and for times larger than t = 6 h for 100% RH, the corresponding frames can be combined for improved statistics. Figure 5.23a shows the integrated reflectivity curves. It can be seen, that the highest RH leads to a decreased slope of the NR curve. The evolution of the NR under the highest RH is shown in figure 5.23b. The colored symbols represent single frames during the reorganization for t < 6 h, the black symbols represent an integration of all curves from t = 6 h on. Evident is a decreasing slope directly after the critical edge of silicon at $q_z = 0.01$ Å^{-1}. To extract precise information about

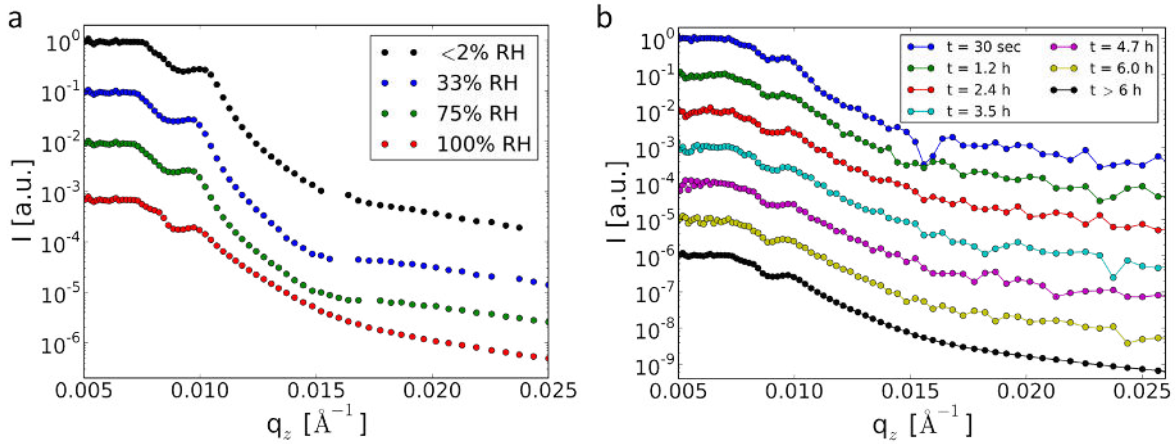

Figure 5.23.: a) Integrated NR curves for P(EHA-stat-d20MMA) stored under <2%, 33%, 75% and 100% RH. For the highest RH only times larger t = 6 h are integrated. b) Temporal evolution of the NR data under 100% RH within the first 6 h. The time increases from top to bottom, each curve represents one single frame. The black symbols represent an integration of all frames for t > 6 h.

the statics before and after the different treatments, a fitting of the reflectivity curves is necessary. Moreover, quantitative information about the kinetics in the samples during the exposure to different RHs would be accessible. This task however, is not easy to tackle. Calculating the reflectivity of a layer with a thickness in the micrometer range while maintaining a resolution of a few Ångstroms is not feasible with common software and standard computational means. The fact that the *Motofit* package, which is used in this work, uses equidistant slices, prevents the simulation of these thick polymer films. Also the fitting tools Parratt32 [70] and Reflfit [71] are found to be incapable of simulating such thick layers with a sufficiently high resolution. The solution to this challenge could

be to calculate the reflectivity using non-equidistant slicing of the layer model. In more detail, the resolution of the SLD profile at the interfaces should be as high as necessary to resolve the details of the near-interface composition, which is typically achieved by slices of 1 Å. In the region of the broad layer of homogeneous bulk material a coarser slicing is acceptable to reduce the computational effort. A possible approach could be the use of the software GenX [72] which is based on Python and allows for a direct manipulation of the reflectivity calculation algorithm.

5.6. Autoadhesion of PMMA

As already mentioned, pressure sensitive adhesives form bonds via van der Waals interactions. However, this section focuses on diffusive adhesion, observed in auto-adhesion experiments using specimens made of the glassy poly(methyl methacrylate). In this kind of experiment two polymer work pieces made of the same material are brought into close contact. During contact the polymer chains from both sides diffuse into the opposing specimen. For the separation of both work pieces after a certain contact time, a certain force is necessary, owing to diffusive adhesion. Autoadhesion allows i.a. for self-healing of grazes and cracks in polymers. Wool et al. have reported a theory describing the nanoscopic origins of crack-healing in polymeric material [163], which has been successfully applied in interface investigations [164, 165, 166, 167].
In this section the autoadhesion of PMMA* (for more details see section 4.1) is investigated in tack tests under different relative humidity. The measurements are carried out at room temperature, which is well below the glass transition temperature of PMMA* ($T_{g,PMMA*}$ = 378 K [109]). All experiments in this section are conducted using punch probes made of PMMA* which are prepared following the routine explained in section 4.5. The counterpart of the punch is a solution cast PMMA* film with a thickness of $40 \pm 3\,\mu$m. In the tack tests the maximum fracture stress of the adhesive bond between the polymer punch probe and the polymer film is determined as a function of contact time. By providing two different relative humidities the influence of water vapor on autoadhesion is revealed.

5.6.1. Autoadhesion under high humidity

Tack measurements are performed using a PMMA* punch probe (prepared as explained in section 4.5) under a relative humidity of 95% using the humidity cell for tack tests (see section 3.3). In the tack test the punch approaches the polymer film until a stress

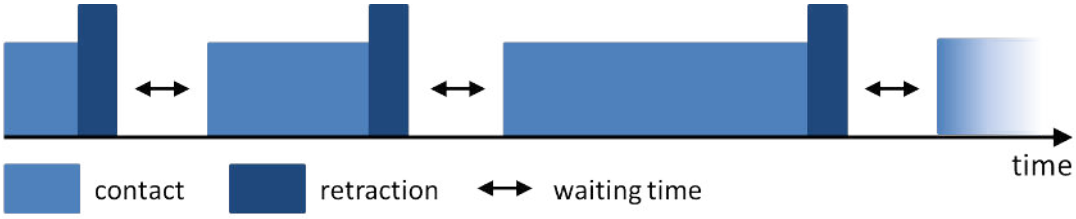

Figure 5.24.: Schematic of the measurement routine: The contact time of polymer punch and polymer film is increased for each measurement within one cycle. In between two subsequent measurements a constant waiting time of 10 min is set. The next cycle starts again from the shortest contact time.

threshold of 1.0 MPa is reached. At this threshold the movement of the punch stops and its position is maintained for a chosen contact time. The contact times are varied from 1 s to 6 h. After the contact time has passed the punch is retracted again and a force-distance curve is measured. Between two subsequent measurements with increasing contact time a waiting time of 10 min is set. This measurement routine is depicted schematically in figure 5.24. One measurement cycle consists of a set of increasing contact times, before the next cycle starts again with the shortest contact time.

Figure 5.25 shows the stress-distance-curves for a set of different contact times, which are each shifted along the y-axis by a relative offset of 20 kPa for clarity. Clearly, in all curves only a stress peak is evident without any stress plateau at larger distances. This behavior indicates a sudden rupture without contributions from peeling effects. Moreover, it is obvious that the maximum fracture stress increases with increasing contact time. Furthermore, the distance at which the bond ruptures increases as well, which originates from the bending of the glass slide which supports the polymer film. The stronger the

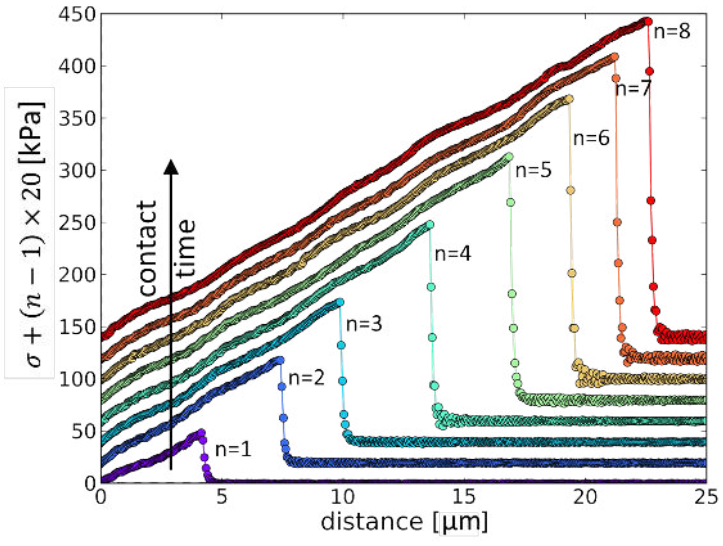

Figure 5.25: Stress-distance curves for increasing contact times of t_c = 10 s, 60 s, 3 min, 10 min, 40 min, 120 min, 240 min and 360 min. The contact time increases from bottom to top. For clarity, the symbols are connected by lines and the curves are shifted by a relative offset of 20 kPa.

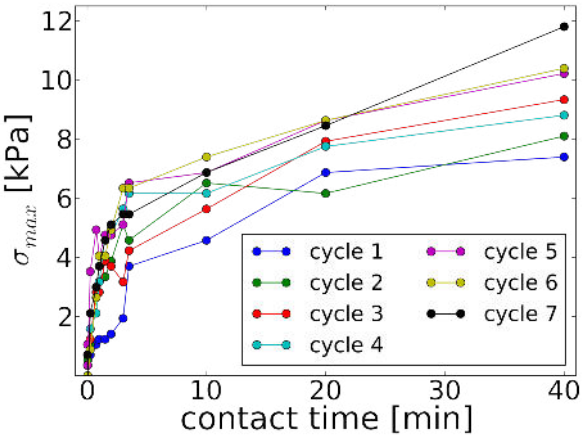

Figure 5.26: Stress maxima as a function of contact time for the first seven cycles. The symbols are connected by lines for clarity.

adhesive bond, the more the glass slide is bent, and hence, the distance at which the bond fails increases. The use of this kind of supporting glass slide has an important advantage concerning the time resolution: The failure of the adhesive bond between the two glassy polymers takes place without fibrillation. It is a very fast process and the corresponding distance the punch travels during debonding is also very short. This distance in principle reflects the interpenetration depth X to which the polymer chains have already diffused to during the contact time. This interpenetration depth X is typically in the nanometer range. Therefore, using a completely inflexible support for the polymer film, the observation of the stress peak would be compromised because both time and spatial resolution of the tack apparatus is not sufficient. A faintly flexible support of the polymer film shifts the locus of bond rupture towards larger distances, which are well resolvable with the used setup.

From each tack measurement a stress maximum σ_{max} is extracted. Figure 5.26 shows σ_{max} as a function of contact time for the first seven cycles with contact times from 1 s to 40 min. The systematic uncertainty is smaller than the symbol size. A statistical uncertainty is not included due to the fact that a trend towards higher stress maxima is visible from cycle to cycle.

This trend becomes even more pronounced for the subsequent cycles which also cover a larger range of contact times, shown in figure 5.27a. After a steep increase of σ_{max} at short contact times, it tends towards a plateau for larger contact times. A dramatic increase of σ_{max} with increasing contact time is observed throughout all cycles. In order to reveal a possible diffusive origin of this behavior, the stress maxima are shown as a function of $t^{1/4}$ according to Wool's theory [163] in figure 5.27b. While exhibiting a linear behavior for the earlier cycles, the curvature of the measured data increases for later cycles. As soon as a stress threshold of $\sigma_{threshold} = 180$ kPa is reached (indicated by a dashed horizontal line in figure 5.27b) a change in curvature exhibiting a decreasing slope is evident.

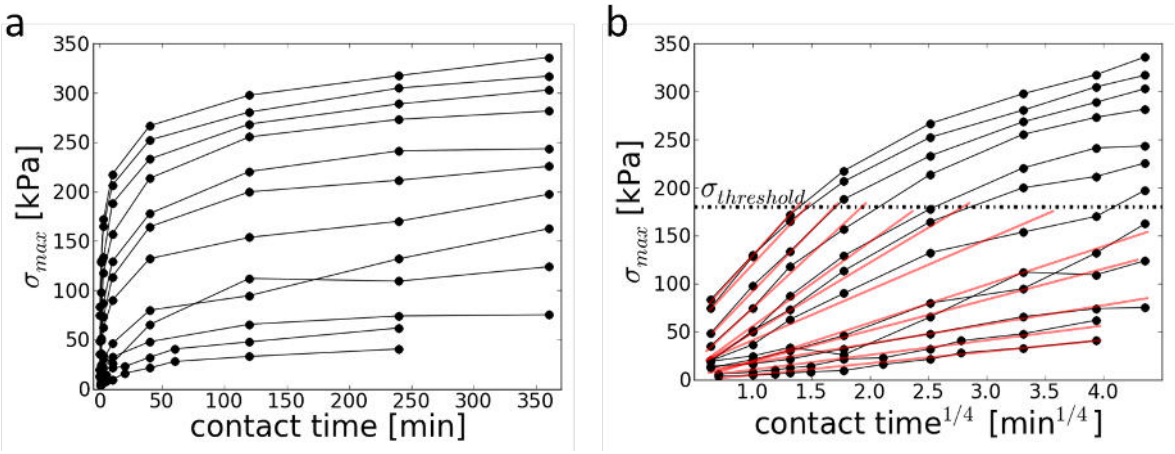

Figure 5.27.: Stress maxima σ_{max} as a function of contact time (a). The cycle number increases from bottom to top. To reveal a possible diffusive behavior according to Wool's theory [163], σ_{max} is presented also as a function of (contact time)$^{1/4}$ (b). The red lines indicate the linear regime.

During the contact time the surfaces of punch and polymer film adapt to each other, which increases the wetting and consequently aids the diffusion. This inelastic adaption persists throughout the different cycles, leading to continuously increasing stress maxima and steeper slopes from cycle to cycle, as indicated by the red lines in figure 5.27b. The improved interdiffusion leading to larger σ_{max} also harms the surface during the bond rupture. The caused damage to the surfaces deteriorates the wetting, which in turn lowers σ_{max}. This effect is visible only for stress maxima larger than $\sigma_{max} \approx 180$ kPa.
In crack healing t_∞ denotes the time at which the crack has healed. Accordingly, the full strength of the adhesive bond in a tack test is reached at t_∞. The applied pressure p in the tack experiment promotes the wetting, but should be reduced for the diffusion stage due to a $t_\infty \propto e^p$ dependency, found by Wool et al. [163]. This demand is partly met under high humidity because on the one hand the glass transition T_g is reduced [168] and on the other hand the Youngs modulus is lowered [158]. These effects lead to an enhanced stress relaxation in the polymer during contact of punch and polymer film and improve diffusion, hence lead to larger stress maxima σ_{max}. According to Wool's theory, the total fracture stress $\sigma_{tot}(t)$ is a function of the contact time and a sum of an instantaneous van der Waals contribution σ_0 and a diffusive contribution $\sigma_d(t)$, $\sigma_{tot}(t) = \sigma_0 + \sigma_d(t)$ [163]. The diffusive part reads $\sigma_d(t) = k\,(t_c)^{1/4}$, k being a constant. This relation holds under the assumption of a direct proportionality of fracture stress σ_{max} and interdiffusion depth X, $\sigma_{max} \propto X$. The fact that the glass transition temperature T_g of PMMA is lowered under high humidity also affects the bond formation, because a lower T_g improves both the wetting and also the diffusion due to a higher chain segment mobility. Furthermore,

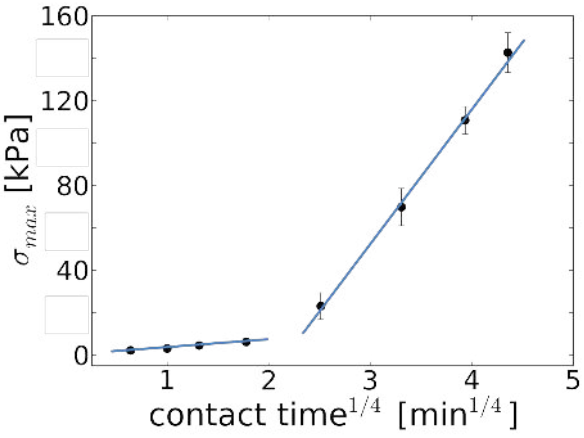

Figure 5.28: Fracture stress σ_{max} as a function of the fourth square root of the contact time. The linear behavior indicates a instant van der Waals bonding at short contact times and a diffusive origin of the adhesive bond for longer contact times (blue lines).

it has to be noted that computer simulations have shown an accumulation of chain ends close the the surface of a polymer bulk material [169], which also facilitates the interdiffusion.
It can be stated that the high relative humidity allows for an inelastic adaption of both polymer surfaces, which drastically improves wetting and thereby also enhances the diffusive adhesion.

5.6.2. Autoadhesion under low humidity

The autoadhesion of PMMA* is investigated also under a low relative humidity of 5% following the same routine as explained above. The low humidity is realized with silica gel in the humidity cell. Under these conditions the trends visible for high humidity have vanished. Figure 5.28 shows the mean stress maxima and standard deviations of six consecutive cycles as a function of contact time.

Under dry conditions the polymer surfaces are more rigid, which hinders the inelastic adaption of both surfaces upon contact. Therefore, no increase of the stress maxima from cycle to cycle is observed. The hindered adaption of the surfaces leads to a retardation of increased stress maxima in the tack experiments, which is evident from figure 5.28. The two different slopes (indicated by blue lines in figure 5.28) indicate that for contact times longer than 40 min the adaption is sufficient for diffusion to take place more effectively, leading to a higher slope. According to Wool's theory [163], for short contact times the measured adhesion is governed by instantaneous van der Waals interactions. For longer contact times, diffusion from both sides of the interface takes place, up to an interdiffusion depth X. Also under dry conditions the applied pressure in a tack experiment improves the wetting. However, due to the higher rigidity of the polymer as compared to the case of a RH of 95%, the stress relaxation in the polymer during contact of punch and polymer

film is less pronounced. Moreover, at low RH the glass transition T_g is also not reduces, which is also hinders diffusion. Consequently, the diffusion at a relative humidity of 5% is compromised and hence, lower stress maxima σ_{max} are obtained.

5.7. Summary

To get a first impression of the morphology of the investigated model PSA, AFM measurements are carried out and reveal homogeneous and smooth PSA film topographies without indications of phase separation. This is an important finding, as for other PSA systems phase separation has been observed by AFM [170, 171]. Furthermore, the observed homogeneous surface causes also a homogeneous tack performance irrespective of the location on the PSA film.

A well-established technique to address the near-surface region of PSAs is reflectometry [99, 146, 13]. However, this technique is unambiguously only applicable to vertically stacked layers without lateral structures. The absence of significant lateral structures and the presence of negligible defects of P(EHA-stat-20dMMA) at the surface as well as at the adhesive-adherent interface is shown by TOF-GISANS measurements. Due to the high scattering depth of neutrons, they are a powerful probe for buried interfaces, especially for the investigation of adhesive bonds.

To tune the tackiness of the model PSA P(EHA-stat-20MMA) Diethert et al. have shown that post-production treatments under diffferent relative humidity (RH) have significant impact on the adhesive performance of the PSA [99]. The polar environment was found to drag MMA segments to the surface, improving the tackiness. In the present work XRR measurements show that a treatment of the adhesive films with a non-polar nitrogen atmosphere is able to invert the near-surface composition profile. As a result, an EHA-enrichment forms at the PSA surface within 12 days. An inversion of the surface composition that fast has not been observed before, while exhibiting such a high level of purity of the enrichment layers.

The implementation of custom-designed temperature-controlled humidity cells for XRR and tack-tests allows for a precise control over external parameters influencing the near-surface composition and the tack performance of the PSA films. The RH is kept constant throughout post-production treatment and measurement. The composition profiles obtained from XRR agree well with literature [99]: Polar environments drag MMA components towards the surface. Tack measurements under constant RH however, reveal the three different failure mechanisms described by Creton et al. [157]. Cavitation, internal and external crack propagation are observed for the first time depending on the RH. Tack measurements using different punch probe roughnesses further confirm this finding.

Moreover, without the use of the humidity cell for the tack test, temporal trends of the stress maxima and tack energies are observed. This behavior is related to an adaption of the PSA near-surface region to the ambient environment. These findings show the importance of full control over all parameters during tack- and XRR experiments. Moreover, by changing the RH a way for creating maps of failure mechanisms for a desired adhesive-adherent combination is introduced.

The interface of adhesive and adherent is of utmost importance for the durability and strength of an adhesive bond. Similar to the reorganization observed close to and at the PSA surface, the near-interface composition of P(EHA-stat-20dMMA) close to the adherent is found by NR to be non-homogeneous. Acid and basic cleaning routines install hydrophilic and hydrophobic surfaces of the silicon adherent [172]. The interactions between the polymer chain segments and the different adherent surfaces lead to inverse composition profiles. In the case of acid cleaning the less polar EHA enriches close to the adherent. Basic cleaning enriches the more polar dMMA component close to the adherent. These results show that the surface chemistry can strongly influence the near-interface composition of PSAs even in contact with the same adherent material and offers a way of tuning this composition to the specific needs. Moreover, these findings prove the applicability of NR for adhesion science, where the methods for non-destructive investigations of adhesive bonds are so far very limited to e.g. ultrasonic waves and dielectric spectroscopy [148, 149, 150].

The vertical near-surface composition profile is investigated by in-situ neutron reflectivity during reorganization upon a treatment with relative humidity. The approach to investigate films exhibiting a thickness of 5 ± 1 μm offers the possibility to include the conservation of mass as an additional fitting constraint during the analysis of the NR data. These thick films however, can not be simulated with common fitting software like e.g. *Motofit*. A non-equidistant resolution of the SLD profile needs to be used to provide sufficient resolution to resolve the near-interface compositions while saving computational efforts in the homogeneous bulk region in the middle of the polymer film. Only the highest RH of 100% leads to significant changes in the reflectivity. Moreover, these changes happen already within the first 5 hours.

Tack experiments focusing on the auto adhesion of PMMA under high and low relative humidity reveal drastic differences. Under a RH of 95% a continuous increase of the maximum stress σ_{max} is observed from measurement cycle to measurement cycle, which is explained by an ongoing inelastic adaption of the polymer surfaces. After a fracture stress threshold of 180 MPa is reached, this adaption of both surfaces is deteriorated by the damage done to the surface during the rupture of the bond. In tack tests conducted at a RH of 5% the ongoing inelastic adaption of the involved surfaces is missing and hence

is traced back to the effect of the relative humidity on the glass transition temperature T_g and on the Young's modulus of the polymer. Moreover, a retarded diffusion is observed for low RH owing to the missing surface adaption in this case of low RH.

6. Metal-adhesive interactions

A common application for adhesives is the bonding of metal components [173, 174, 175, 176]. An adhesive bond between a metal and a pressure sensitive adhesive can in principle be installed in different ways. First, the PSA can be directly solution cast on the desired adherent (see section 4.3). If the adhesive film is already on a supporting substrate, it can be applied to the adherent under already small pressure [177]. This approach is chosen to invesitgate the interactions between P(EHA-stat-20MMA) and different kinds of metal adherents in the first part of this chapter. Parts of the results in this chapter were obtained together with Gökhan Gümüssoy and are published in his Master's thesis [178]. Another approach is the metal film formation directly on the polymer, which is important for instance in food packaging, where diffusion barriers are formed on polymeric foils via evaporation or sputtering [179, 180]. In the second part of this chapter, the interactions between metal and PSA are investigated on a nanoscopic scale using in-situ GISAXS measurements during sputter deposition of aluminum and gold on the PSA and its homopolymer components. Due to the fact that such sputter experiments are carried out under high vacuum, the target metal is always pristine and not oxidized. The fact that metal atoms are deposited on the polymers also rules out contaminations of the metal which would alter the surface tension. The chapter is finally concluded with a short summary.

6.1. Adhesion of metals on P(EHA-stat-20MMA)

The use of PSAs also in combinations with metal, e.g. for noise damping in aircrafts [181] raises the need of reliable predictions on strength and durability of the established bonds. Commonly known is the strong influence of surface tension of adhesive and adherent on adhesive joints [182]. After determination of the involved surface tensions in the first part of this section, macroscopic tack tests are performed using punch probes made of the different metals. The statistical copolymer P(EHA-stat-20MMA) is chosen as a model system for PSAs.

Table 6.1.: Surface tensions of the investigated materials along with dispersive and polar contributions.

sample	roughness [nm]	$\gamma^d \left[\frac{mN}{m}\right]$	$\gamma^p \left[\frac{mN}{m}\right]$	$\gamma \left[\frac{mN}{m}\right]$
aluminum	8.3 ± 0.1	24.6 ± 0.2	3.8 ± 0.1	28.4 ± 0.3
stainless steel	1.7 ± 0.2	23.1 ± 1.4	12.5 ± 1.3	35.6 ± 2.7
titania	6.4 ± 0.8	22.0 ± 0.9	28.1 ± 0.8	50.2 ± 1.7

6.1.1. Surface energies

As already mentioned in section 2.1.2 proper wetting is a prerequisite for the establishment of an adhesion bond. Therefore, the involved surface tensions are investigated in this section. In previous studies Diethert et al. have determined the surface energy of P(EHA-stat-dMMA) to be $\gamma_{PSA} = 33.1 \pm 0.3$ mN/m with the corresponding dispersive and polar contributions $\gamma^d_{PSA} = 30.5 \pm 0.8$ mN/m and $\gamma^p_{PSA} = 2.6 \pm 0.6$ mN/m [99]. In this work, the influence of the punch probe material is investigated. Therefore, the surface tensions of the polished metal punches is derived according to section 2.1.2. Figure 6.1 shows the contact angle evolution for all six test liquids used along with the corresponding fits (see section 2.1.2) exemplarily for the measurements carried out on aluminum. The other contact angle measurements are shifted to the appendix A. For each liquid at least ten repetitions were conducted to improve statistics. From the fitting the final contact angle Θ_f is extracted and used for the Owens-Wendt calculations as described in section 2.1.2. Figure 6.2 shows the results for aluminum, stainless steel and titania. Clearly deviations from the theoretically predicted linear dependency are visible in each plot. One reason is for instance, that the test liquids are subject to evaporation to different extents, because the measurements are not conducted in saturated atmospheres for all the liquids. The error bars in the Owens-Wendt plots are calculated via the standard equation for the propagation of uncertainty. The resulting surface tensions along with the dispersive and polar contributions are listed in table 6.1. The surface tensions increase from aluminum ($\gamma = 28.4 \pm 0.3 \left[\frac{mN}{m}\right]$) to stainless steel ($\gamma = 35.6 \pm 2.7 \left[\frac{mN}{m}\right]$) and finally titania ($\gamma = 50.2 \pm 1.7 \left[\frac{mN}{m}\right]$). The most significant difference is found in the polar part, which ranges from $\gamma^p_{aluminum} = 3.8 \pm 0.1 \left[\frac{mN}{m}\right]$ to $\gamma^p_{titania} = 28.1 \pm 0.8 \left[\frac{mN}{m}\right]$. Surface tensions are in general very sensitive to contaminations, which is why they can be strongly affected e.g. by the polishing process [183, 184]. The metals used for this investigation are therefore thoroughly cleaned in an ultrasonic bath with acetone, ethanol, isopropanol and also toluene to avoid any changes in the surface tensions during later cleaning steps. However, compared to literature the obtained surface tensions are in agreement with literature

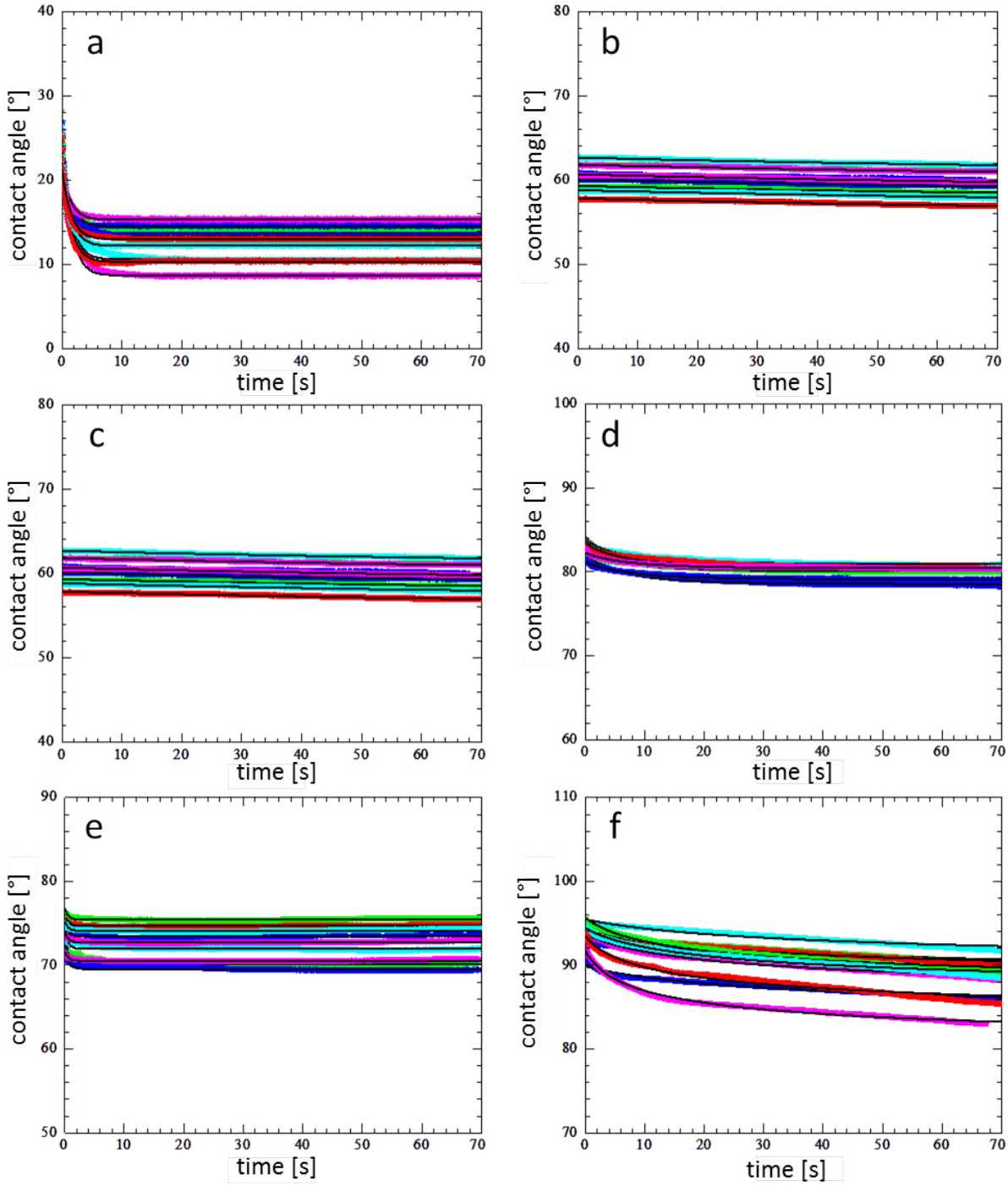

Figure 6.1.: Time dependent contact angles of the different test liquids: a) paraffin oil, b) diiodomethane, c) ethylene glycol, d) formamide, e) glycerol and f) water on aluminum.

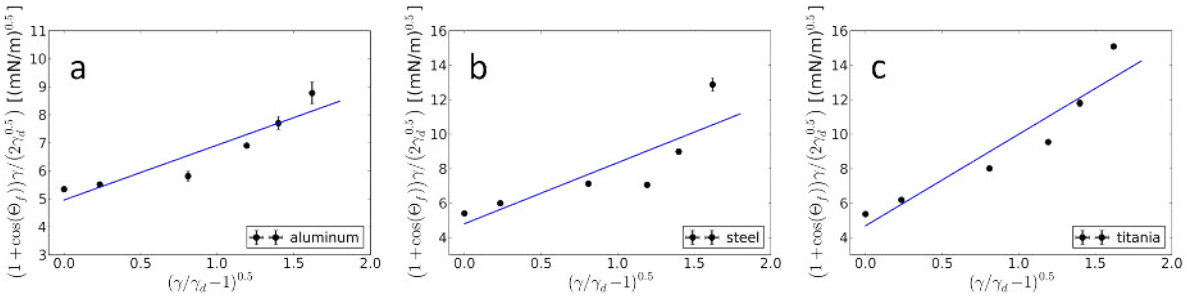

Figure 6.2.: Owens-Wendt plots for a) aluminum, b) stainless steel and c) titania. The blue lines are linear fits to the data.

($\gamma_{aluminum} = 50 - 170\left[\frac{mN}{m}\right]$, $\gamma_{stainlesssteel} = 34 - 278\left[\frac{mN}{m}\right]$, $\gamma_{titania} = 46 \pm 1.08\left[\frac{mN}{m}\right]$), taking the strong influence of the surface treatment into account [183, 185, 186, 187].

6.1.2. Tack performance

To see the influence of different metals on the adhesive performance tack-tests were conducted at a constant room temperature of 18 °C. Four different types of metal punches were prepared and polished by the in-house *TUM crystal lab* as described in section 4.5: aluminum, stainless steel, titania and gold. Figure 6.3 shows all tack measurements for the investigated materials. The corresponding insets show representative images of the corresponding adherent-adhesive interfaces during the debonding process. From these images it is already obvious that the number and shape of the cavities differ. Moreover, from the stress-strain curves it can be seen that the values for maximum stress σ_{max} and tack energy E_{tack}, which is shown in more detail in figure 6.4, differ for all metals. Clearly, both σ_{max} and E_{tack} decrease with increasing surface tension, which is surprising at first glance, because commonly low surface tensions lead to poor tackiness due to improper wetting. This can only partly be explained by the increase of punch roughness from aluminum to gold, as obtained from AFM (see section 4.5). The main reason is the similarity of surface tensions of stainless steel and aluminum compared to the surface tension of the PSA (see table 6.1). Toyama et al. showed, that the largest stress maxima occur for the case in which adherent and adhesive exhibit very similar surface tensions [188]. The more the surface tension differs from the surface tension of the PSA γ_{PSA}, the smaller σ_{max} is. Bulk gold has a reported surface tension of 1.7-2 N/m [189], which by far exceeds the values obtained for the other adherents in this work. As already mentioned in section 6.1.1 the surface treatment can drastically alter the surface tension. Furthermore, materials exhibiting high surface tension tend to adsorb water molecules from the atmosphere which also reduces the effective surface tension [190] and therefore can reduce the tack

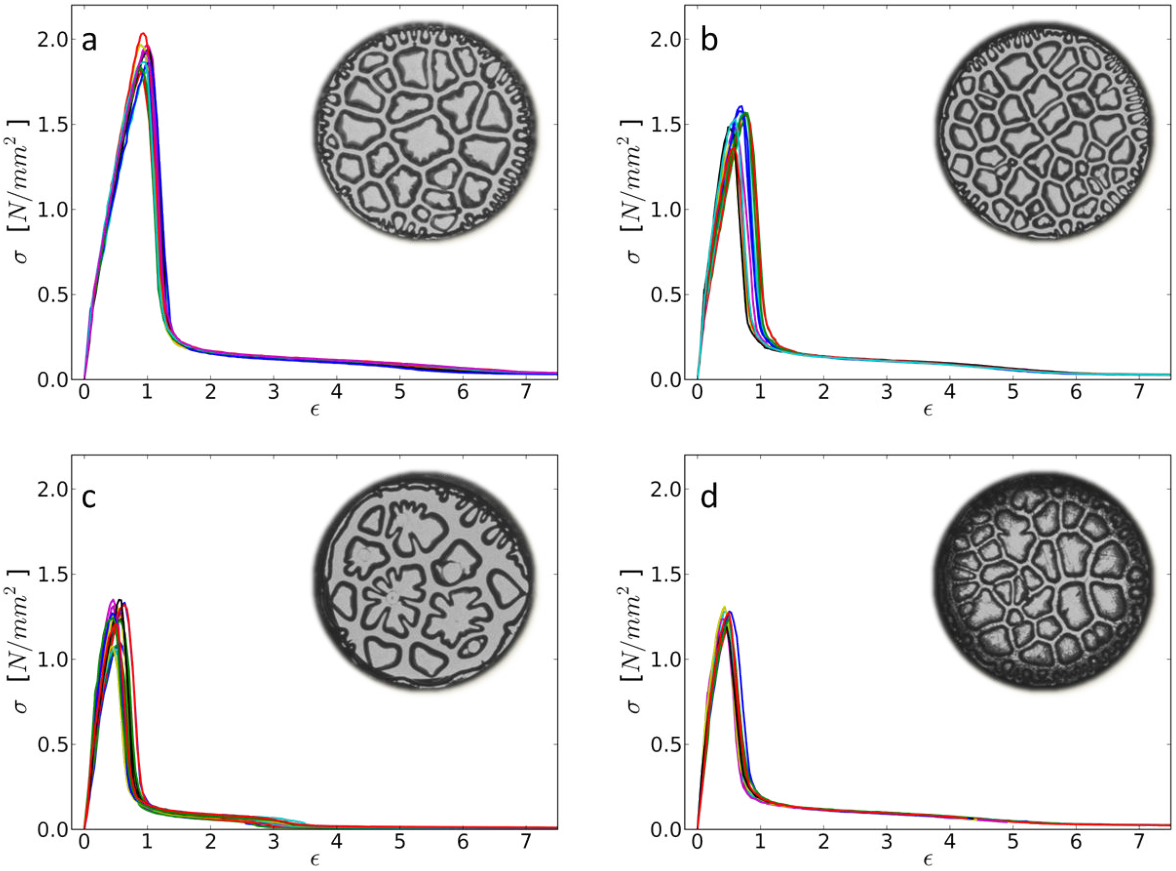

Figure 6.3.: 10 exemplary stress-strain curves (shown in by different colors) obtained from tack measurements using punch-probes made of a) aluminum, b) stainless steel, c) titania and d) gold. The insets show representative images of the corresponding adherent-adhesive interfaces during cavitation.

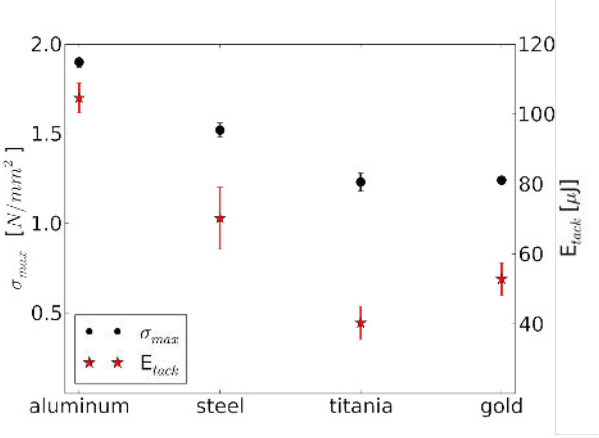

Figure 6.4: Maximum stress σ_{max} values for the different metal punch probes along with the obtained values for the corresponding tack energies E_{tack}.

performance.
The representative images of the adhesive-metal interfaces during debonding in figure 6.3 reveal a noteworthy detail. For aluminum, steel and gold the cavity shape is rather smooth and round, whereas for titania clearly finger-like structures occur. The round shape of cavities can be traced back to the minimization of surface tension. The finger-like cavities are the result of a so-called Saffman-Taylor instability [191] and are usually expected to be more pronounced for the smoother punch probes [192]. It has to be noted that the metal surfaces are handled under ambient conditions and are therefore oxidized. As a result, these surfaces are chemically passivated and consequently PSA and metals do not form chemical bonds. Hence, the influence of the kind of metal on adhesion is reduced to the influence of the metal-oxides on adhesion. Finally it can be stated that the surface tensions of the involved metal adherents as well as their roughness contribute most to the resulting tack performance.

6.2. Metal film formation upon sputtering

The growth of the metal layer on the polymer substrate depends strongly on the metal-polymer interactions [193]. Due to the fact that the sputtering process is carried out under vacuum, the interactions of pure metal and polymer can be addressed, differently to experiments under ambient conditions, where metals usually quickly oxidize. The final metal film architecture strongly depends on many different parameters such as the involved surface free energies, the deposition conditions (i.a. deposition rate, working pressure) or the surface morphology of the used substrate. The ability to tune the growth of metal domains and finally films on the nanoscale affects many fields of interest, e.g. in optical, electrical or magnetic applications [121, 122, 123, 124, 125]. In most cases block-co-polymers have been used as structure directing templates. To isolate effects like the influence of the glass transition temperature of the substrate material, it is beneficial to investigate the interplay of metals and homopolymers. The nucleation and growth of thin films have been treated both experimentally and theoretically [194, 195, 196], however most studies aim at metal-on-metal growth. In general, among the three main mechanisms observed in metal film growth is the Volmer-Weber growth, which describes the formation and growth of islands rather than smooth layers and is found usually for noble metals with poor wetting behavior [197, 80, 198]. The layer-by-layer growth (Frank-Van der Merwe growth) is favored in case of good wetting [199, 200], while also a combination of these mechanisms has been reported (Stranski-Kastranov growth) [200]. Despite the fact that the tuning of metal structures on polymer surfaces on the nano-scale is of utmost importance for many fields of interest, only little fundamental knowledge is available

[201]. In this work two different target materials are chosen for the sputter deposition, which differ vastly in surface tension (see section 6.1.1): Aluminum and gold. Three different kinds of polymer films act as substrates, exhibiting different glass transition temperatures. The glass transition plays an important role, not only because it can affect the surface mobility of the metal on the polymer. Also, at temperatures above the glass transition a significant incorporation of metal clusters in the polymer template has been reported, which also changes the metal film growth kinetics [197, 202]. GISAXS provides the high time resolution and high statistics necessary for an in-situ monitoring of the metal film growth on polymer films. In this work the statistical copolymer P(EHA-stat-20MMA) as well as its constituents PEHA and PMMA are used as polymeric templates the metal is sputtered on. The two homopolymers drastically differ in glass transition temperature ($T_{g,PEHA}$ = 188 K, $T_{g,PMMA}$ = 378 K [109]), which makes them promising candidates to address the influence of T_g on the early stages of metal film growth. It has to be noted that it is not possible to exclude the influence of chemical selectivity in the interpretation of the results of this investigation. Nonetheless, this effect is expected to play a minor role in this experiment. Polymer films comprising of the copolymer are subject to ongoing rearrangements (see chapter 5) provided a sufficiently large film thickness. In very thin films, however, these processes based on diffusion are assumed to be in comparison suppressed because of the stronger confinement [203]. The polymer films in this section exhibit a film thickness of 200 nm and are considered to be comparably very thin. The polymer films comprised of P(EHA-stat-20MMA) as well as its homopolymer components PEHA and PMMA. The focus of this in-situ experiment is set to the very early stages of metal film growth, because in later stages when the film mostly grows vertically, metal-metal interactions dominate the process. In this work DC sputtering was performed at an Argon pressure of 1.5×10^{-2} mbar and a power of 100 W using a sputtering chamber provided by DESY, Hamburg. In this section the film formation of aluminum on the three polymer templates is addressed, followed by the investigation of the metal film growth using gold as target material. Insights into growth kinetics are provided and a growth model is proposed.

6.2.1. Aluminum deposition

Aluminum represents a rather reactive target material, which was shown by Dannetun et al. [204]. It is commonly used in organic solar cells forming the electrical contacts [205, 206, 207]. Therefore, the growth of aluminum on polymer templates during sputter deposition has already been investigated [208], however not with respect to the influence of the glass transition temperature of the involved polymers. During the continuous

sputtering the samples were illuminated by the x-ray beam for 1.000 s with read-out brakes of 0.005 s inbetween. This yields a very high time-resolution in combination with still good statistics. Figure 6.5 shows selected 2d GISAXS data recorded during the in-situ sputter experiment using the templates PEHA (a-e), PMMA (f-k) and P(EHA-stat-20MMA) (l-q). The general evolution is very similar for all three templates. The bare polymer film shows no lateral structure at all (Fig. 6.5a,f,l). With ongoing sputtering time, a peak in intensity arises at high q_y values and moves to smaller q_y while getting more intense (Fig. 6.5b-e, g-k, m-q). This peak originates from the aluminum deposited on the polymer film. With ongoing sputtering the morphology of the aluminum on the template changes, resulting in different 2d scattering patterns. The general behavior is found to be similar for all polymer templates. The circular halo in all detector images is due to a shadow effect originating from the exit window of the sputter chamber and not related to the samples. To get a more detailed understanding of the structure evolution for each polymer template, figure 6.6 shows q_y-cuts as a function of time for PEHA (figure 6.6a), PMMA (6.6b) and P(EHA-stat-20MMA) (6.6c). It is obvious that on PMMA the peak is more intense already at earlier times, compared to the PEHA template. For a more quantitative analysis the horizontal cuts are fitted using a Lorenzian function. Three parameters can be extracted: the peak position, peak width and peak height. From the peak position a characteristic length $\Lambda = 2\pi/q_y$ is extracted. The time-dependent characteristic length Λ for each polymer template is shown in figure 6.7 on a double logarithmic scale. All three curves exhibit a steep drop in Λ in the beginning. However, the minima of Λ appear at different times for the different templates. While Λ_{min} for PEHA appears rather early ($t_{min,PEHA} = 460$ s), it moves to later times for PMMA ($t_{min,PMMA} = 1150$ s) and even further for the statistical copolymer P(EHA-stat-20MMA). On this template the minimum cannot be resolved within the observed time frame ($t_{min,P(EHA-stat-20MMA} \geq 1820$ s) due to constraints from the synchrotron experiment. The initial drop of the characteristic length which is present for all templates and has not been reported so far, can be explained by the decreasing distance of scattering centers. When the aluminum adatoms stick to the polymer, they have a certain mobility on the surface and therefore can merge to bigger objects or act as seeds attracting other adatoms. With ongoing metal deposition more of these objects occur on the surface, hence their distance (characteristic length Λ) shrinks. During the continuous sputtering these agglomerates also grow, which decreases their mobility until their positions stay constant. Once the mean distance between the structures has reached Λ_{min}, the aluminum objects start to feel each others vicinity and their growth starts to be constricted. After reaching a certain size, the diffusion of the aluminum agglomerates slows down and finally stops. Newly arriving adatoms stick to these already existing and immobilized particles. A common approach to identify known

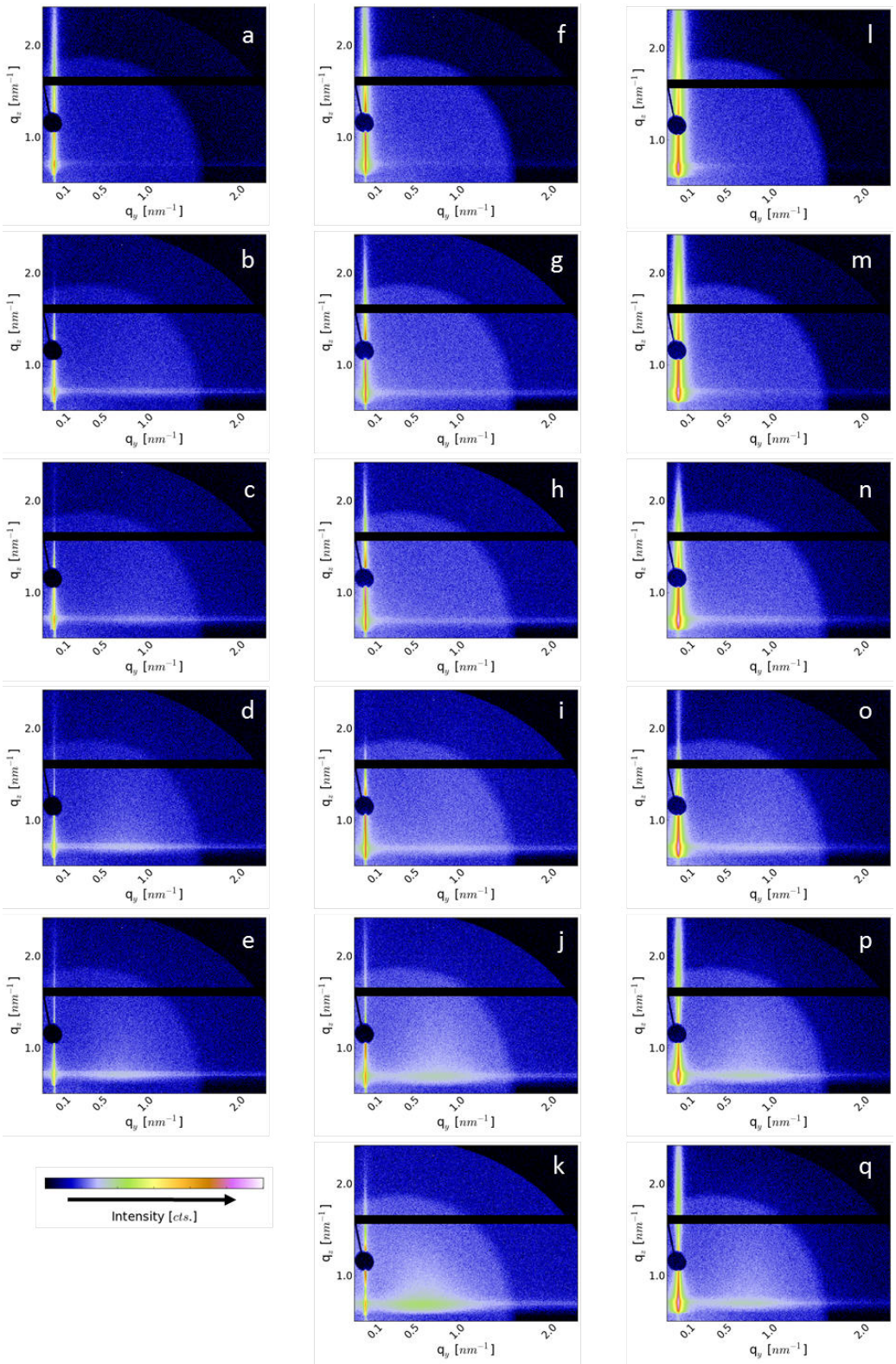

Figure 6.5.: 2d GISAXS data obtained after different sputtering times using the PEHA template (a-e: 1 s, 7.5 min, 10 min, 17 min, 21 min), the PMMA template (f-k: 1 s, 7.5 min, 10 min, 17 min, 25 min, 40 min) and the P(EHA-stat-20MMA) template (l-q: 1 s, 7.5 min, 10 min, 17 min, 25 min, 30 min).

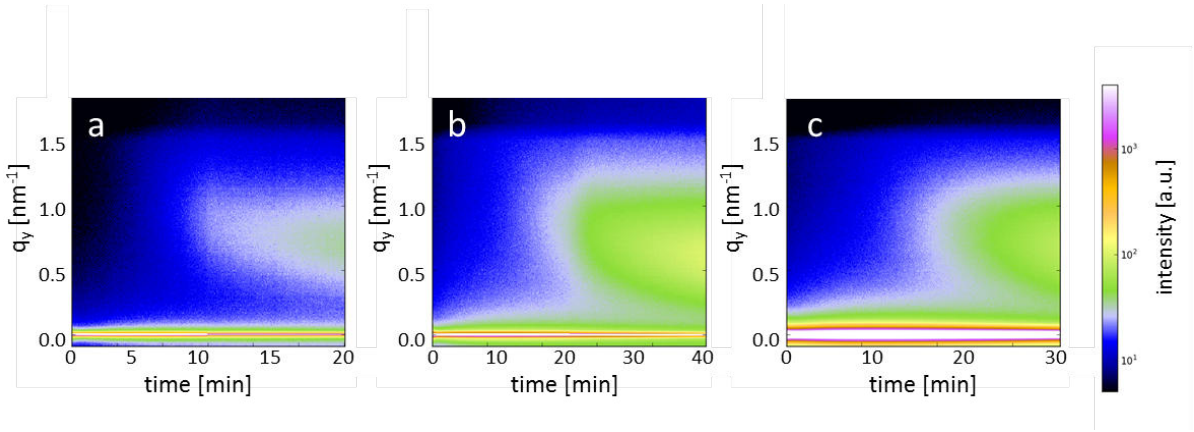

Figure 6.6.: Mapping composed of horizontal line cuts as a function of time for the investigated polymer templates: a) PEHA, b) PMMA, c) P(EHA-stat-20MMA).

growth mechanisms is the determination of the exponent of a power-law fit to the data as reported in literature [209]. By fitting the regions directly after Λ_{min} is reached, scaling laws $\Lambda \propto t^{\alpha}$ can be extracted. The fits are included in figure 6.7 (red lines) along with the corresponding exponents α_1. Exponents of $\alpha_{1,PEHA} = 0.28$ and $\alpha_{1,PMMA} = 0.36$ are found for PEHA and PMMA, respectively. These exponents are in good agreement with values from literature, identifying this growth regime as adsorptive growth without coalescence [201, 210]. The difference of α_1 on both templates can be explained by a higher mobility of aluminum on PMMA. The lower T_g of PEHA can lead to diffusion of metal also into the film, whereas on the glassy PMMA the metal atoms stay on the polymer surface. As a consequence, the diffusion of aluminum on PMMA is rather two-dimensional, whereas on PEHA it can be assumed to be also in vertical direction into the polymer film [197, 202]. The regime for aluminum-on-aluminum growth is not observed in the investigated time ranges. The values of Λ_{min} are very similar for all three templates and are in the range of 7-9 nm. This indicates that the aluminum objects have a similar size. The density of the

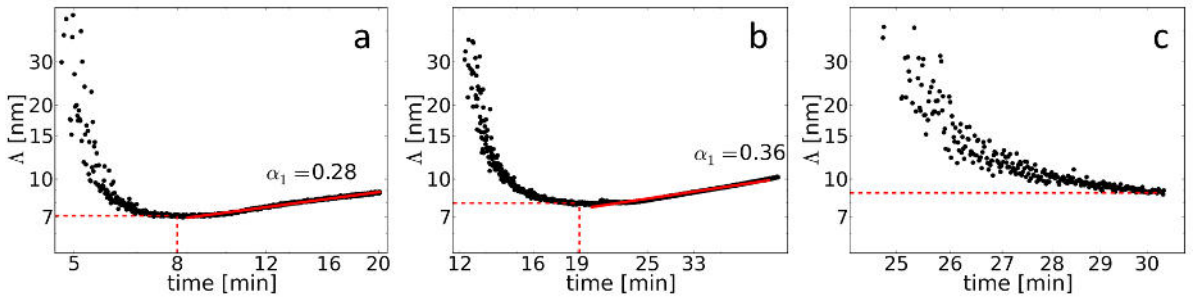

Figure 6.7.: Time dependent characteristic length Λ for all three templates: a) PEHA, b) PMMA and c) P(EHA-stat-20MMA).

objects on the surface is similar as well at the corresponding times. The time when Λ_{min} is reached, however, differs significantly. The decay of Λ from 30 nm to 7 nm happens within $\Delta t_{PEHA} \approx 3$ min for PEHA, whereas it takes $\Delta t_{PMMA} \approx 6$ min, and therefore much longer for aluminum on PMMA. In contrast, for the co-polymer this minimum is not resolved within the present experiment. The faster decay, hence the small Δt_{PEHA} can be explained by a higher condensation coefficient of the adatoms on PEHA compared to PMMA: $cc_{PEHA} > cc_{PMMA}$. This can be explained by the lower T_g of PEHA, which at room temperature is soft and sticky ($T_{g,PEHA} \ll T_{ambient}$), while PMMA is glassy at room temperature ($T_{g,PMMA} \gg T_{ambient}$). Therefore, the glass transition temperature of the polymer template is shown to have a direct impact on the condensation coefficient. It has to be noted, that the surface of the statistical copolymer is not expected to be a homogeneous mixture of both constituents of the copolymer. In fact, enrichment layers of one or the other component are expected to form close to the surface and the interface to the substrate, as observed for similar systems in chapter 5.

6.2.2. Gold deposition

In this section gold is chosen as target material. Being a noble and inert metal it represents the counterpart to aluminum in the previous section. The sputtering conditions are the same as in section 6.2.1. The illumination time per frame was set to 0.100 s with a read-out brake of 0.005 s. Figure 6.8 shows the time evolution of the 2d GISAXS data for sputtering gold on PEHA, PMMA and P(EHA-stat-20MMA). Similarly to the case of aluminum, a weak peak arises at high q_y values on all templates. For gold, however, it moves faster to smaller q_y and exhibits higher intensity. Moreover, this peak is also accompanied by additional peaks which emerge at higher q_z values and also move towards smaller values. To extract quantitative information vertical and horizontal line cuts are taken for every recorded frame, as explained in section 3.8. Figure 6.9a shows a set of exemplary vertical line cuts for the later stages of the deposition on PEHA. To avoid the beamstop, the line cuts were taken at $q_y = 0.015$ nm^{-1} rather than at $q_y = 0$ nm^{-1}. With increasing time of the sputter deposition, intensity oscillations start to evolve. These fringes exhibit a decreasing spacing with time because of the increase in gold layer thickness. By taking the positions of two consecutive extrema, the thickness d of the gold layer can be estimated for each point in time by $d = 2\pi/\Delta q_z$. The use of this formula at $q_y ! = 0$ nm^{-1} may result in small deviations from the mean layer thickness, because the corresponding q_y value leads to an average thickness of islands of the corresponding size, rather than a mean thickness of the whole layer. The results are shown in figure 6.9b. Clearly visible is a transition of growth rate at around $t^* \approx 450$ s.

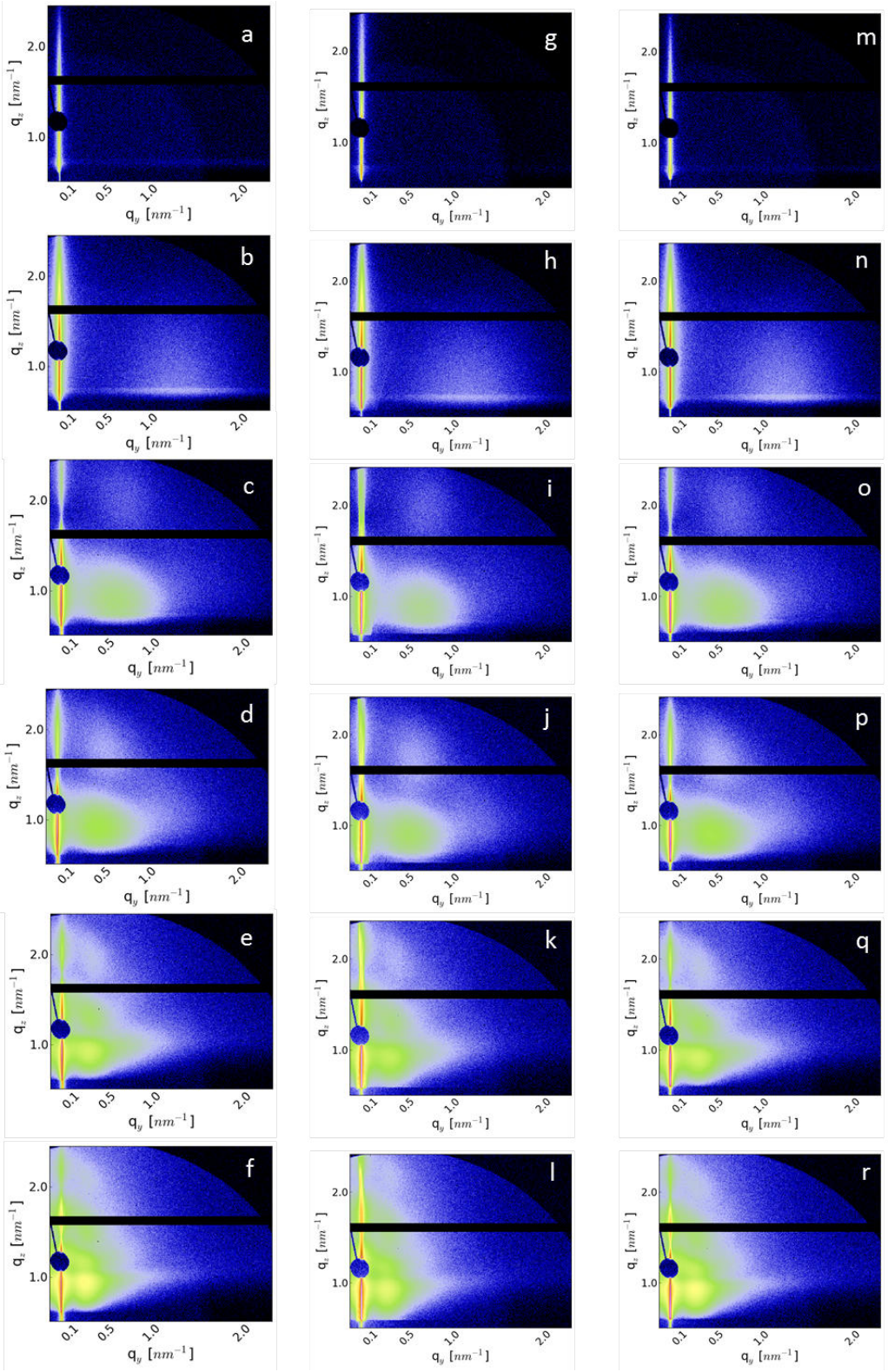

Figure 6.8.: 2d GISAXS data obtained after different sputtering times (t = 5 s, 60 s, 2.5 min, 3.5 min, 7 min, 10 min) using the templates PEHA (a-f), PMMA (g-l) and P(EHA-stat-20MMA) (m-r).

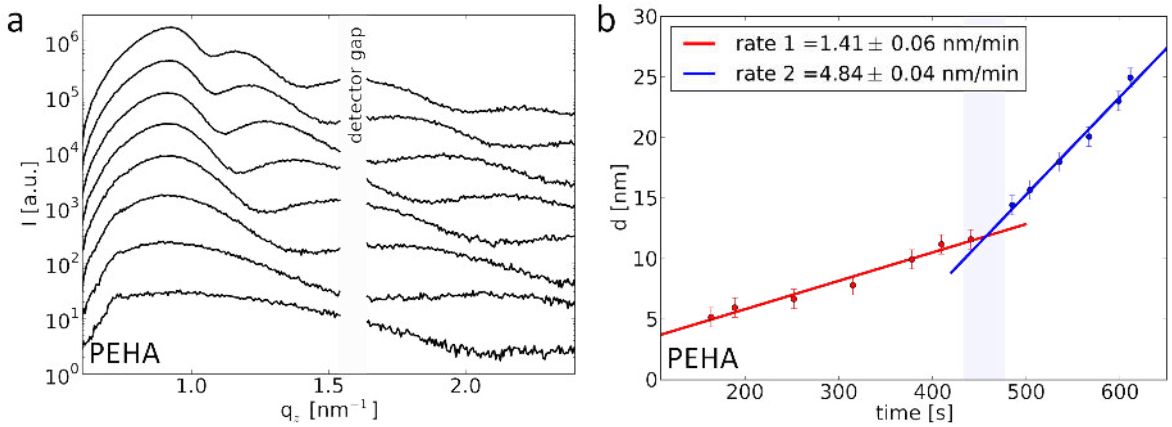

Figure 6.9.: a) Exemplary vertical line cuts from the 2d GISAXS data at $q_y = 0.015$ nm^{-1} for different times. From bottom to top the time increases from t = 170 s to t = 611 s in steps of Δt = 63 s. The curves are shifted along the y-axis for clarity. b) Thickness of the gold layer as a function of time, obtained from the fringe spacings. Clearly visible is the transition to the gold-on-gold growth at $t \approx 450$ s (indicated by blue vertical bar).

In the first regime (red symbols) the gold growth rate is lower than in the second regime (blue symbols). The reason for this transition is that at time t* the polymer surface is completely covered with gold. From this moment on, the gold-on-gold growth begins, which has a higher condensation coefficient of $cc_{gold-on-gold} = 1$. Before a full coverage is reached, the growth rate is reduced, because the metal structures still mostly grow laterally, which is also why the obtained film thickness represents a mean thickness of the gold islands on the surface. This analysis is also applied to the other two polymer templates, which is shown in figure 6.10 and already give a grasp of the influence of T_g. The fitted lines to the extracted film thickness values for different times show the same slopes $\delta_{gold-on-gold} \approx 4.87$ nm/min in the second regime for all polymer templates, which is due to the fact that after a full surface coverage with gold the growth is independent of the now buried polymer substrate. In the first regime however, differences are clearly visible: the growth rate for gold on PEHA $\delta_{PEHA} = 1.41$ nm/min is significantly higher than on PMMA $\delta_{PMMA} = 1.06$ nm/min. On the co-polymer an intermediate rate of $\delta_{P(EHA-stat-20MMA)} = 1.31$ nm/min is observed. This can be explained by the lower T_g of PEHA. The fact that this polymer is soft and sticky at room temperature leads to a higher condensation coefficient cc_{PEHA} compared to the glassy PMMA and the corresponding cc_{PMMA}. In the copolymer both types of polymers are covalently bonded with a ratio of 80:20. Under the simplified assumption of a homogeneous mixture of both homopolymers forming the surface of the statistical copolymer, an expected growth rate of $\delta_{mix} = 1.34$ nm/min is calculated. This value is close to the experimentally observed one, which might

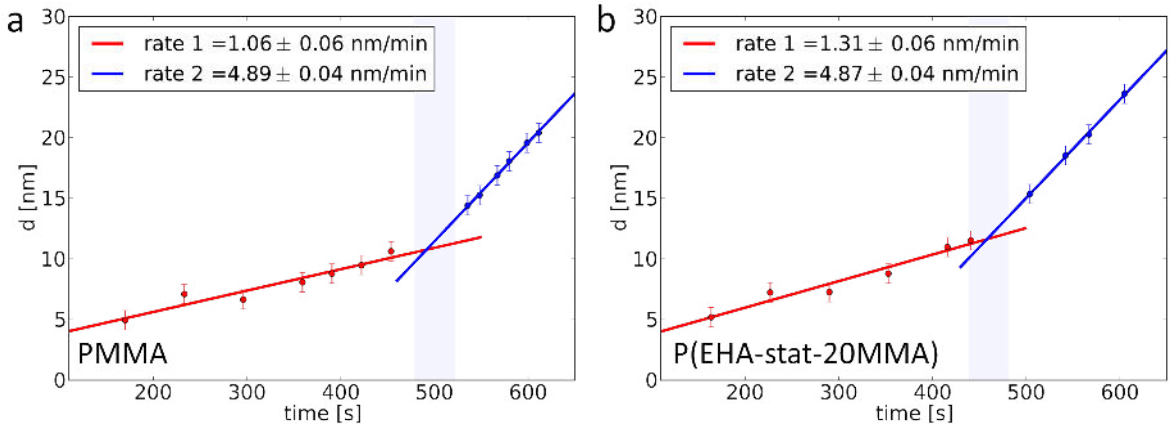

Figure 6.10.: Thickness of the gold layer on a) PMMA and b) P(EHA-stat-20MMA) as a function of time. Both show a low growth rate in the first regime, followed by the gold-on-gold growth in the second regime.

indicate that this simplified approach is accurate. Comparing the values of the threshold-thickness at the transition, it is noteworthy that also in this case a trend is visible: The gold-on-gold regime starts from ≈ 12 nm, 10 nm and 11 nm for PEHA, PMMA and P(EHA-stat-20MMA), respectively. Also the time of rate transition t* differs slightly, PEHA resulting in the earliest transition, PMMA in the latest. Information about the lateral structure evolution is obtained by fitting the emerging peak at high q_y with a Lorentz-distribution, as explained in section 3.8, for every time frame. From the fitting the parameters peak position, full width at half maximum (FWHM) and peak height are extracted time-dependently. From the peak position the values of the time-dependent characteristic length Λ for all three polymer substrates are determined, as shown in figure 6.11a-c on a double logarithmic scale. Similar to aluminum the curves start with a steep decay, representing the fast decrease of center-to-center distance of the gold particles on the surface. The minimum $\Lambda_{min} \approx 4.1$ nm (red dashed lines) is almost equal for all three templates. To reach this minimum, however, it takes a longer time (measured from the first appearance of the peak) on PEHA ($t_{min,PEHA} = 26.6$ s) than on PMMA ($t_{min,PMMA} = 11.3$ s). The position in time of the minimum on P(EHA-stat-20MMA) shows a value in-between the ones found for the homopolymers $t_{min,P(EHA-stat-20MMA)} = 13.6$ s, which is already intuitive. After a steep increase of Λ all three curves show a plateau $\Lambda_{plateau} = 21 - 22.5$ nm starting at t= 400 s (blue dashed lines). An exemplary zoom-in into the late times for PEHA reveals the transition to the gold-on-gold growth: At around $t^* = 450$ s (green dash-dotted line) a change in curvature is clearly visible on the linear scale, which is in accordance with the findings from the growth rates. By fitting distinct regions of the double logarithmic plots, scaling laws $\Lambda \propto t^{\alpha_i}$ can be extracted. The fits are

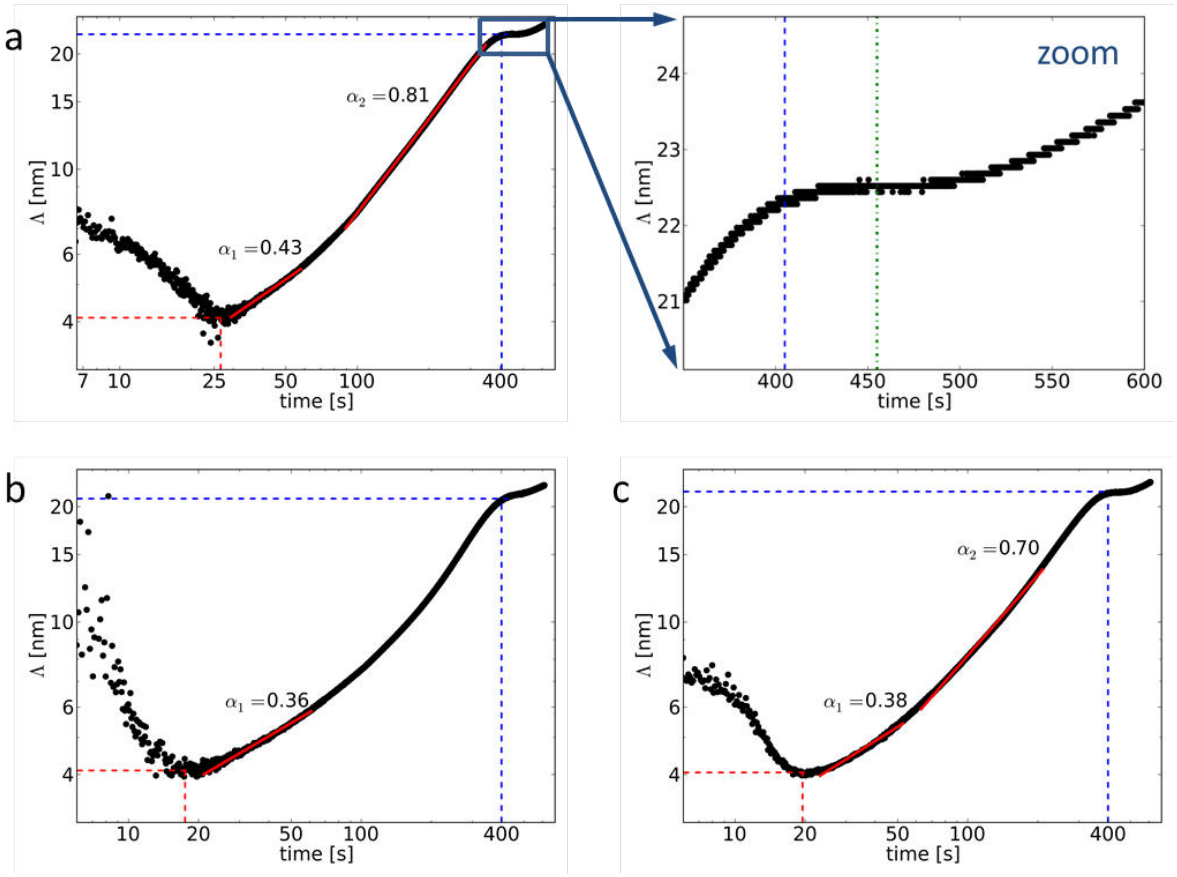

Figure 6.11.: Time dependent characteristic length Λ for all three templates: a) PEHA, b) PMMA and c) P(EHA-stat-20MMA). All curves show a similar behavior: Λ decreases fast until reaching a global minimum before it increases again, until at t ≈ 400 s the regime of gold-on-gold growth is reached. Fits to distinct regions (red lines) reveal power law behaviors with different exponents α_i.

shown in figure 6.11 (red lines) along with the corresponding exponents α_i. Directly after Λ_{min} is reached, a growth regime begins which exhibits an exponent of $\alpha_1 = 0.36 - 0.43$ on all templates. These exponents are in good agreement with values from literature for adsorptive growth without coalescence [201, 210], which can be explained by the fact that after reaching a certain size, the diffusion of the gold agglomerates slows down and eventually stops. Newly arriving adatoms stick to these existing and immobilized particles, which is the dominating growth mechanism at this stage. For later times exponents of $\alpha_{2,PEHA} = 0.81$ and $\alpha_{2,P(EHA-stat-20MMA)} = 0.70$ are found on PEHA and the statistical copolymer P(EHA-stat-20MMA), respectively. These values are in good accordance with values observed for growth regimes which are dominated by coalescence [201]. With ongoing gold deposition in this regime the gaps between the clusters are filled. Taking the condensation coefficient of gold-on-gold $cc_{gold-on-gold} = 1$ into account, it becomes

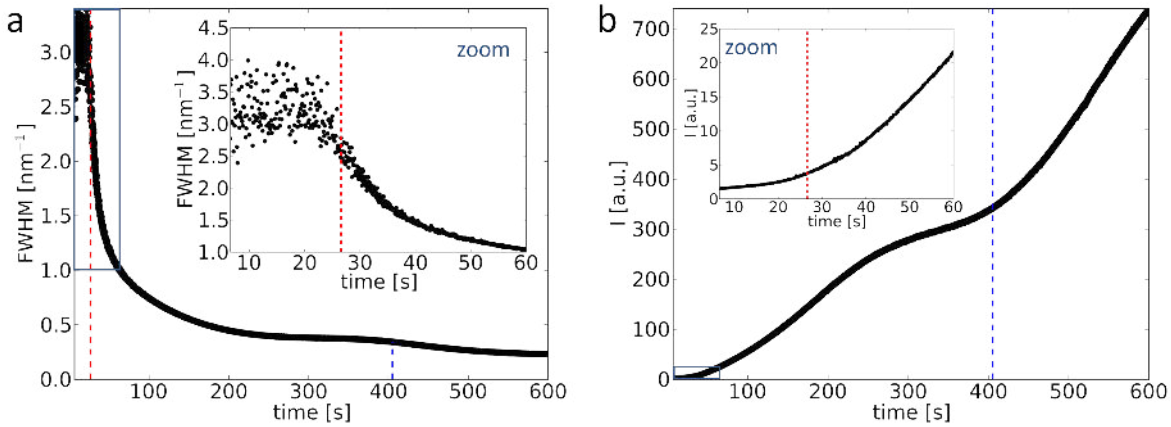

Figure 6.12.: a) Evolution of the FWHM with time for the PEHA template. The inset shows a zoom-in for small times t. b) Evolution of the peak height with time along with a zoom-in of the early times for the PEHA template.

clear that with increasing cluster size, hence increasing surface area of gold, the growth accelerates. This is also the reason why there is no distinct power-law-regime observed for PMMA, where the regimes overlap. At the times around t $\approx$ 400 s, a plateau of Λ is reached. Meanwhile, all gaps in-between the gold clusters are successively filled, hence their distance does not change anymore. Once a homogeneous gold surface is obtained, the gold-on-gold growth starts as shown above, at around t* $\approx$ 450 s. In this regime again lateral structures form, but the kinetics are not related anymore to the polymer underneath but to the behavior of gold-on-gold growth. The temporal evolution of the FWHM and the peak height for the PEHA template are plotted in figure 6.12a and b, respectively. For small times the FWHM scatters rather strongly around $\approx$ 3.25 nm^{-1} before a very steep drop occurs after t = 26.6 s (red dashed line), which is exactly the same time the minimum in Λ occurs. This shows that during the decay of Λ at early times, the polydispersity of the particle shape on the surface is rather constant because they still can grow rather freely. Reaching a certain threshold-distance, the structures start to feel the vicinity of one another which confines the growth. Hence, the objects get more monodisperse and the FWHM starts to level off. At t = 400 s, an intermediate plateau decays further, which means that the shapes of the objects still get more and more similar. The transition to the gold-on-gold growth does not emerge in this plot. This early behavior of the FWHM has not been resolved before. Figure 6.12b shows the evolution of the peak height with time. At the time t = 26.6 s no transition is visible (see inset), but at around t= 400 s (the onset of $\Lambda_{plateau}$) a change in slope can be seen. The extraction of information from the peak height-plot is not unambiguous. An increase of intensity can reflect either an increase of deposited amount of gold or changes in object

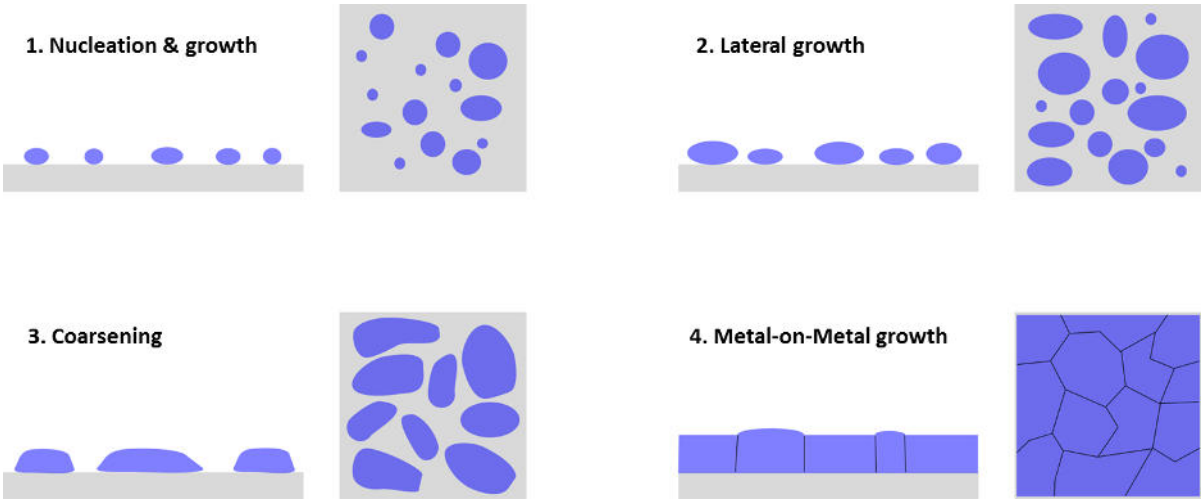

Figure 6.13.: Growth model for metal on polymer templates comprising of four stages: 1) In the beginning the mean distances between the scattering objects are still big, only a small amount of metal has been deposited. With ongoing sputtering more scattering centers occur, hence their mean distance decreases. 2) The objects grow laterally, therefore their mean distance increases. 3) Clusters merge, which results in a further increase of Λ. 4) As soon as full surface coverage is reached, the metal-on-metal growth begins.

shape leading to an increase of intensity in the respective positions on the detector. Also a combination of both cases is possible.

6.2.3. Growth model

The information about the vertical and lateral structure evolution found for aluminum and gold allows for the proposition of a growth model, which is schematically shown in figure 6.13. This model consists of four steps:

1. Nucleation and growth:

Once a metal adatom sticks to the polymer surface and does not desorb back into the plasma, it acts as a seed to which further adatoms can stick to. Hence, in the beginning the number of seeds increases with ongoing gold deposition. These small agglomerates grow in all dimensions, because the condensation cefficient for metal-on-metal is equal to 1, while it is smaller for the adsorption of metal on different materials [126]. Due to this island growth also the distance between these condensation nuclei, Λ, decreases.

2. Lateral growth:

As soon as the metal objects start to feel the presence of their neighbor objects, their diffusion is slowed down and eventually stopped. Their growth is also constricted by the surrounding objects, hence they become more monodisperse. The threshold limits for the

mean distance are found to be $\Lambda_{min,Al} = 7 - 9$ nm and $\Lambda_{min,Au} = 4$ nm. After reaching this critical mean distance the particles start to diffuse and merge, building up clusters, hence Λ increases. The obtained scaling exponents $\alpha_1 = 0.36 - 0.43$ are in good agreement with literature for adsorptive growth without coalescence [201, 210].

3. Coarsening:

With ongoing sputter deposition of gold, the gaps and voids between the clusters are filled, thus they merge, which further increases Λ. The observed scaling exponents of $\alpha_2 = 0.7 - 0.81$ indicate that coalescence is the dominant process in this regime [201].

4. Metal-on-metal growth:

When the polymer surface is finally fully covered with metal, the metal-on-metal growth begins. This growth is independent of the subjacent polymer template.

6.3. Summary

Interactions of metals and adhesives have been investigated on macroscopic and nanoscopic length scales. Tack experiments show a dependency of adhesive performance from the involved surface energies of metal and the adhesive. Similar surface energies for adhesive and adherent metal have been found to yield the strongest bonds, which is in agreement with literature [188]. However, also higher roughness of the metal probes decreases the tack performance, which has also been shown by Peykova et al. [12]. The growth of aluminum and gold layers on different polymer templates during sputter deposition is followed in-situ using GISAXS measurements. In this work the focus lies on the very early stages of film formation, where a Volmer-Weber growth with its characteristic 3d cluster formation is surprisingly found for both metals on all templates. The polymer substrates comprise of thin films of PEHA, PMMA and P(EHA-stat-20MMA), representing two homopolymers with very different glass transition temperatures and the statistical copolymer, consisting of the latter. Volmer-Weber growth reflects in general a non-wetting behavior which is well known for gold [201], but is surprisingly found to be also present for the less noble aluminum, where so far a layer-by-layer growth was observed for sputter deposition on the conductive polymer P3HT [208]. Finally a growth model is proposed applying to both metals which consists of the four stages nucleation and growth, lateral growth, coarsening and metal-on-metal growth. Similar kinetics have been already reported for metal deposition on both organic and inorganic solids, as for example P3HT or silicon [210, 201, 211]. The very early phases observed in this work however, have not been reported so far. These very early processes determine the growth mechanism as well as the resulting morphology of metal nanostructures on the polymer template. The observation of structures at these

early times is of utmost importance for a fundamental understanding of the evolution of metal structures on polymer templates.

7. Structure formation of block-copolymers during drying

As already mentioned, the functionality of polymer films in applications is majorly based on their inner structure and morphology. Block copolymers, for instance, are used in many fields like drug delivery [212, 213, 214], sensors [215, 216, 217] or electronics, e.g. in the production of nanowires [218, 219]. These polymers are used i.a. as structure directing templates for the active layers in hybrid solar cells [220, 221] or in structuring of metal nanoparticles [222, 223]. Hence, the fundamentals of the structure formation in these systems is of high interest also from a scientific point of view.

In this chapter the structure formation of two different block copolymers is addressed. The polymers investigated are poly(styrene-d8-b-n-butylmethacrylate) (P(dS-b-BMA)) with different weight ratios of 50:50 ($P(dS\text{-}b\text{-}nBMA)_{50:50}$) and 35:65 ($P(dS\text{-}b\text{-}nBMA)_{35:65}$). In the first section 7.1.1 the structure formation in solution cast films is monitored in-situ by neutron reflectivity (NR) during drying of the polymer films. The used solvent toluene acts as a good solvent for both blocks of both copolymers. Moreover, by using deuterated toluene additional contrast is employed which allows for an observation of the solvent evaporation kinetics, which is detailed in section 7.1.2. Finally, the dry films obtained after solution casting are further investigated by time-of-flight grazing incidence small angle neutron scattering (TOF-GISANS) in section 7.1.3.

Moreover, the structure formation in films of $P(dS\text{-}b\text{-}nBMA)_{35:65}$ cast from deuterated dimethylformamide (DMF), acting as a bad solvent for both blocks, as well as the solvent evaporation is followed by in-situ NR in section 7.2.1. To also shed light on the lateral structure evolution upon drying, for the first time in-situ TOF-GISANS measurements are performed on the drying polymer solutions of both polymers dissolved in DMF at the liquid-air interface, shown in section 7.2.2. In section 7.2.3 the TOF mode of the GISANS measurements is utilized for the first time to extract reflectivity data from the temporal evolution of the wavelength dependent specularly reflected intensity. This approach allows for extraction of the solvent evaporation kinetics of the involved sample systems.

7.1. P(dS-b-nBMA) in toluene

In the following section the structure formation of two block copolymers is followed in-situ during solution casting with time-of-flight neutron reflectivity (TOF-NR) at the horizontal neutron reflectometer FIGARO, ILL (Grenoble, France). The copolymers are poly(styrene-d8-b-n-butylmethacrylate) (P(dS-b-BMA)) with weight ratios of the two blocks of 35:65 (referred to as P(dS-b-nBMA)$_{35:65}$) and 50:50 (referred to as P(dS-b-nBMA)$_{50:50}$), respectively. Solutions of the polymers in protonated toluene and fully deuterated toluene are dispensed on acidic precleaned silicon wafers which are aligned perfectly horizontal. The sample environment consists of a closed aluminum box (30 cm $\times$ 30 cm $\times$ 15 cm) with aluminum foil windows, allowing for the neutrons to pass through the box. The closed sample chamber slows down the solvent evaporation and therefore guarantees homogeneous dry films. Silicagel beneath the sample ensures a relative humidity of <2%. All measurements are conducted at room temperature. The in-situ NR measurements are carried out under an angle of incidence of $\alpha_{i,1} = 0.624°$. The finally dry samples are furthermore measured under a larger angle of incidence $\alpha_{i,2} = 3.78°$ to cover a larger q_z-range. The use of only one angle of incidence during the in-situ measurements allows for a high time resolution of 30 s, because a changing of the setup to $\alpha_{i,2}$ and back to $\alpha_{i,1}$ with all involved motor movements is avoided.

7.1.1. Structure formation followed by in-situ neutron reflectivity

To get a first overview, the final measurement over the full q_z-range of P(dS-b-nBMA) with a weight ratio of 50:50, cast from deuterated toluene, is shown in figure 7.1. Strong Bragg peaks are clearly evident. Due to the thickness of the polymer film of $5 \pm 1\,\mu$m no Kiessig fringes are observed. The large number of possible parameters for modelling the film in simulations makes it difficult to obtain a satisfying fit to the data. Among these parameters are the purity, number and interfacial roughness of the consecutive layers, which also may change with depth. A fit which reproduces the Bragg positions is shown in figure 7.1 along with the corresponding SLD profile in the inset. However, close to the top and bottom interfaces the SLD profile shows deviations from a regularly repeated structure. Nonetheless, a layer spacing of 306 Å leads to Bragg peaks at the correct positions. This model uses only eight repetitions of layers with a high purity of deuterated styrene (up to 100 % dPS) followed by a less pure layer of nBMA (23% nBMA), indicating perforated lamellae, to reproduce the correct Bragg peak positions (SLD(dPS) $= 5.99 \times 10^{-6}\,\text{Å}^{-2}$, SLD(nBMA)$= 0.554 \times 10^{-6}\,\text{Å}^{-2}$). In order to identify the different Bragg peaks, the Fresnel normalized representation of the reflectivity data is chosen for

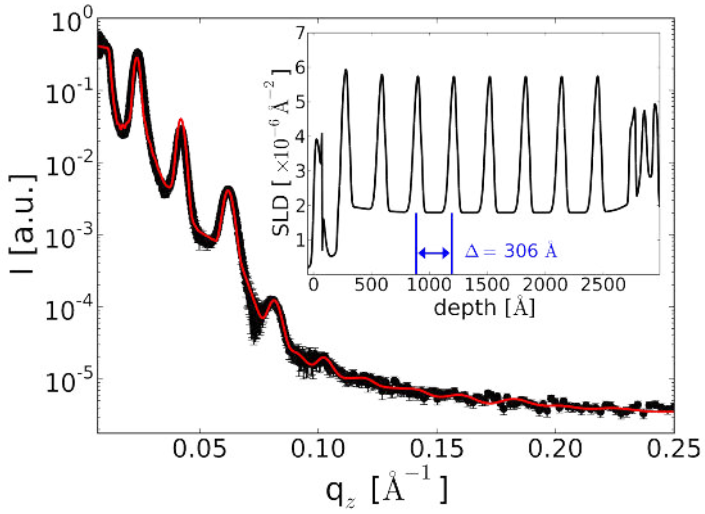

Figure 7.1: Neutron reflectivity of the dry film of P(dS-b-nBMA) with a block ratio of 50:50 (black dots), exhibiting strong Bragg peaks. The fit (red line) is based on the SLD profile, shown in the inset.

both kinds of block copolymer, $P(dS\text{-}b\text{-}nBMA)_{50:50}$ and $P(dS\text{-}b\text{-}nBMA)_{35:65}$, as shown in figure 7.2a and b, respectively. Both block copolymer films are cast from deuterated toluene. The solid red vertical lines indicate the positions of the critical edges, while the differently colored dashed lines mark the positions of the Bragg peaks. Busch et al. have introduced a modified Bragg equation which accounts for refraction and reflection effects [224, 225]. It reads:

$$\alpha_f = \pm\sqrt{\alpha_{c,p}(\lambda)^2 + \left[\frac{m\lambda}{D} \pm \sqrt{\alpha_i^2 - \alpha_{c,p}(\lambda)^2}\right]^2}. \tag{7.1}$$

In this equation $\alpha_{c,p}(\lambda) = \lambda\sqrt{SLD_{polymer}/\pi}$ denotes the critical angle of the polymer, m the order of the Bragg peak, D the layer spacing and α_i the angle of incidence. Being derived for GISAXS and GISANS experiments, this modified Bragg equation is also applicable for NR measurements. Figures 7.2c,d show the Bragg peak positions in α_f as a function of wavelength λ, calculated using equation 7.1 in differently colored dashed lines, corresponding to the different orders m. In reflectometry experiments usually only the specular reflection is measured ($\alpha_i = \alpha_f$). Therefore, in this plot the Bragg peaks are expected to be located on the line of specular reflection (solid gray line). The q_z position of each Bragg peak in the measured data corresponds to a certain wavelength λ via $q_z = 4\pi/\lambda sin(\alpha)$. The Bragg positions in q_z direction are determined from the measured data and transferred to the corresponding λ. By adjusting the spacing D all orders m are brought into agreement with the measured positions, located on the specular line. This agreement is found for a spacing $D = 306 \pm 0.5$Å for $P(dS\text{-}b\text{-}nBMA)_{50:50}$ and for $D = 287 \pm 0.5$Å for $P(dS\text{-}b\text{-}nBMA)_{35:65}$. From the volume ratio of $P(dS\text{-}b\text{-}nBMA)_{50:50}$ being 50% dPS and 50% nBMA, lamellae can be expected inside the dry film [226]. Moreover, the phase diagram for P(dS-b-nBMA) presented by Fischer et al. also predicts the

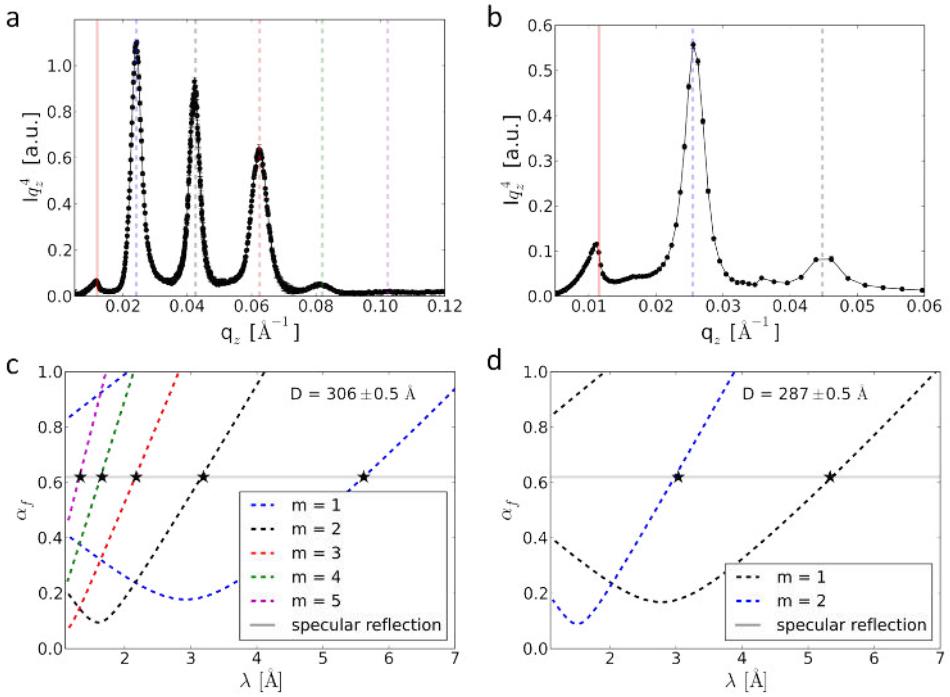

Figure 7.2.: Fresnel normalized representation of the NR measurement of the dry samples of P(dS-b-nBMA)$_{50:50}$ (a) and P(dS-b-nBMA)$_{35:65}$ (b). The red vertical lines indicate the positions of the critical edges, respectively. The differently colored dashed vertical lines indicate the Bragg peak positions. Using the modified Bragg equation 7.1, the spacing for both samples is obtained by fitting the theoretical Bragg positions to the observed positions (c, d).

same structures [227]. The highest observed order is $m = 5$. The volume ratio of P(dS-b-nBMA)$_{35:65}$ of 35% dPS and 65% nBMA suggests cylinders or rods of dPS in a matrix of nBMA [226]. For this sample the highest observed Bragg order is $m = 2$.
The in-situ drying of P(dS-b-nBMA)$_{50:50}$ films cast from fully deuterated toluene and protonated toluene are shown in figure 7.3a, b, respectively, in a mapping composed of Fresnel normalized NR curves as a function of time. In both samples the same behavior is observed. Bragg peaks emerge after $\approx$ 2 h at low q_z values and asymptotically move towards constant values at larger q_z positions. From the results of the dry sample, the visible Bragg orders are already identified as $m = 1, 2$ and, very weak at high q_z values, $m = 3$. The relative positions of the peaks stay constant throughout the experiment, which is a strong indication that the structure stays the same, just the spatial dimensions change. Due to the multiplication of the intensity I with q_z^4 in the Fresnel representation, the critical edges are barely visible in figure 7.3a,b. For further analysis the first two Bragg peaks are fitted with Gaussian functions for all reflectivity curves. Using equation 7.1 the temporal evolution of the lamellar spacing D is obtained from the fitted peak

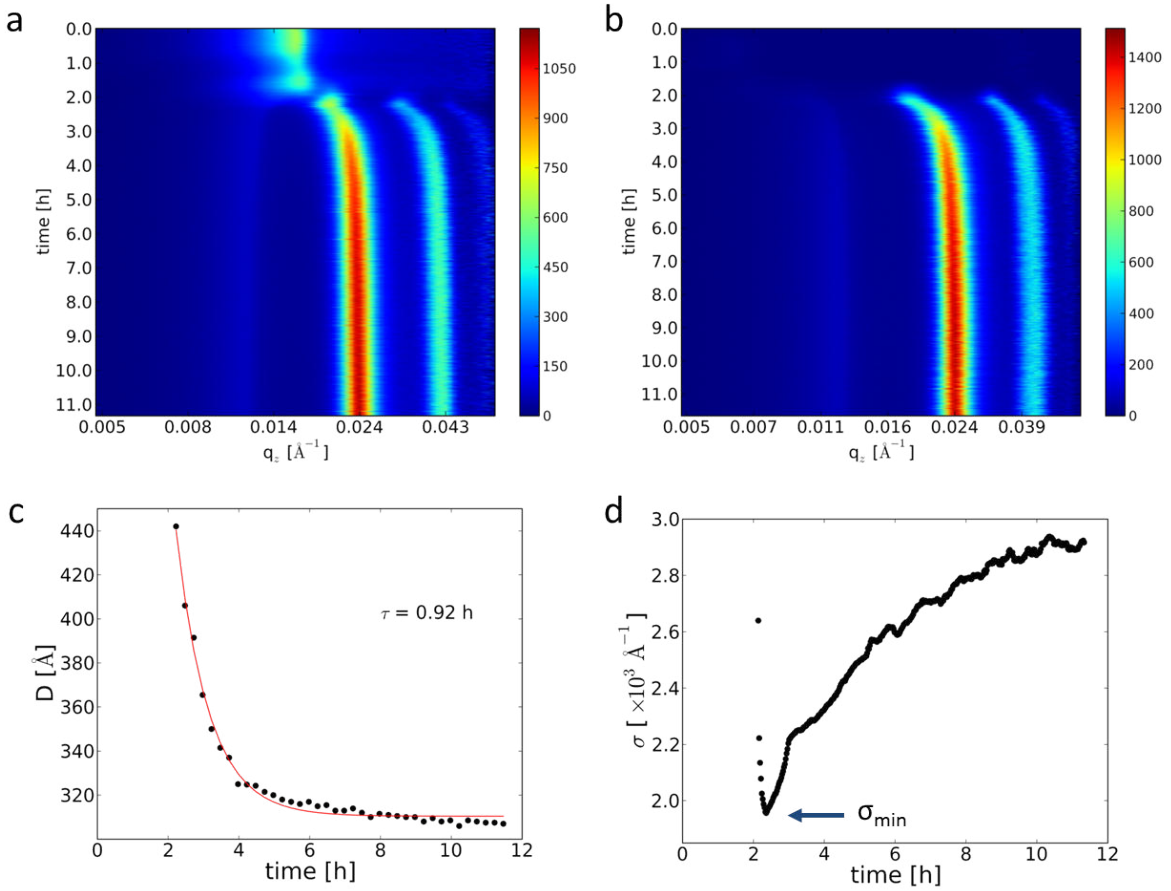

Figure 7.3.: Mapping composed of Fresnel normalized representations of the NR in-situ measurements of P(dS-b-nBMA)$_{50:50}$ cast from deuterated toluene (a) and from protonated toluene (b) as a function of time. In both plots the Bragg peaks with $m = 1$ appear at low q_z move asymptotic towards $q_z = 0.024$ Å^{-1}. Bragg orders $m = 1, 2$ are clearly visible, $m = 3$ is only very weakly pronounced.

positions of the peaks $m = 1$ and $m = 2$, which is shown in figure 7.3c. It has to be noted that during the first 2 hours no Bragg peaks are visible. The spacing D decreases rapidly starting from $D \approx 440$ Å at t = 2 h to $D \approx 330$ Å at t = 4 h. The shrinkage decelerates continuously with time, reaching a lamellar spacing of $D \approx 310$ Å after a time of t = 11 h. This spacing further shrinks until $D = 306 \pm 0.5$ Å for the final dry film, as shown above. Fitting an exponential decay to the spacing evolution reveals a time constant $\tau = 0.92$ h. From fitting the Bragg peaks with a Gaussian function, also the peak width σ is extracted as a function of time, shown in figure 7.3d. It can be seen that the width rapidly drops to a minimum at t = 2.3 h. At this time t the lamellae are oriented most uniformly. With ongoing time the peak width increases and starts to level off after $t \approx 10$ h. The broadening of the Bragg peaks indicates that the uniform orientation of the lamellae deteriorates

during the ongoing drying, reaching a maximum width after t = 10 h.

The in-situ NR of the drying process of the P(dS-b-nBMA)$_{35:65}$ films cast from deuter-

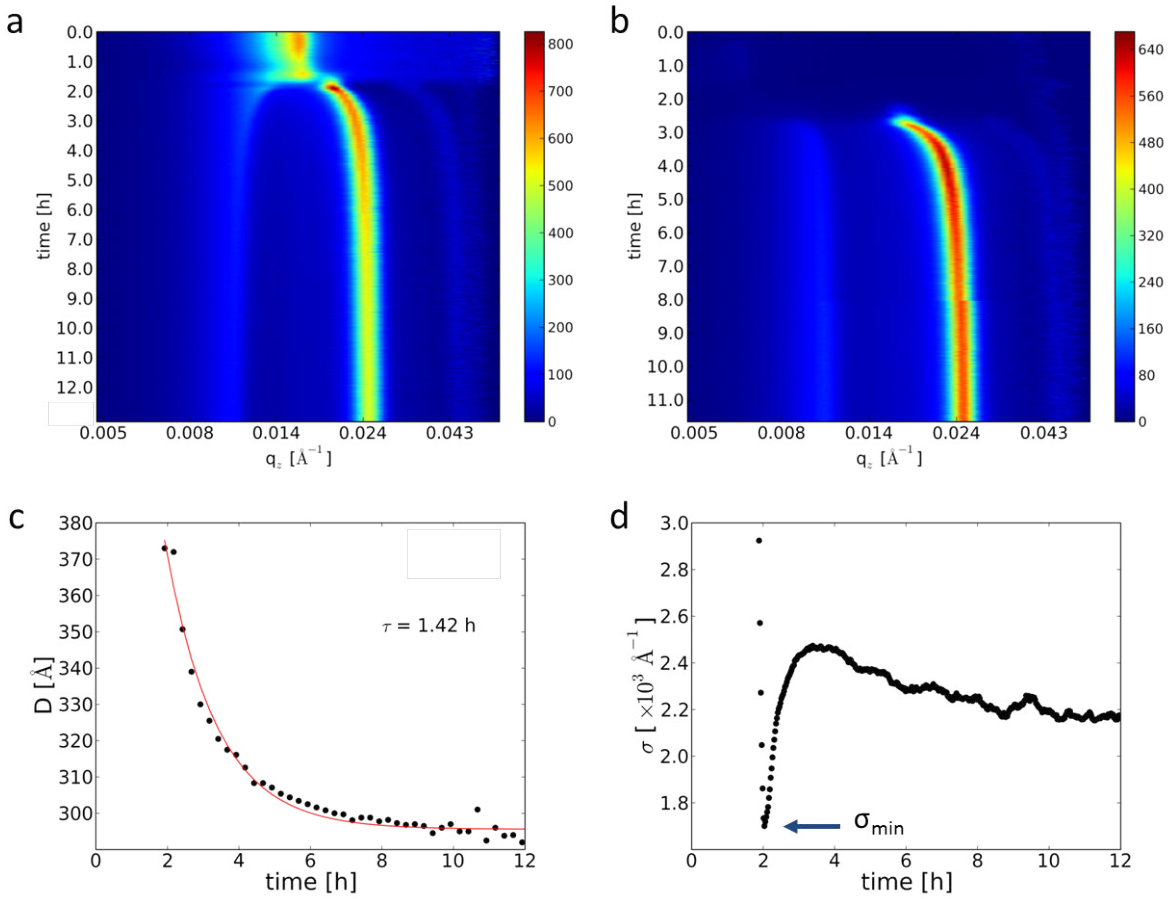

Figure 7.4.: Mapping composed of Fresnel normalized representations of the NR in-situ measurements of P(dS-b-nBMA)$_{35:65}$ cast from deuterated toluene (a) and from protonated toluene (b) as a function of time. In both plots the Bragg peaks with $m = 1$ appear at low q_z move asymptotic towards $q_z = 0.024$ Å^{-1}.

ated and protonated toluene are shown in the Fresnel normalization in figure 7.4a and b, respectively. From the analysis of the dry sample it is obvious that the strongest peak originates from the Bragg peak order $m = 1$. Following the same procedure as for the P(dS-b-nBMA)$_{50:50}$ samples and using equation 7.1, the spacing D is derived for the block copolymer cast from deuterated toluene, shown in figure 7.4c. Obviously, the first structure is visible at a time t = 2 h. The spacing D decreases more slowly as compared to P(dS-b-nBMA)$_{50:50}$ from 370 Å in the beginning to 293 Å after t = 12 h (τ = 1.42 h). The spacing obtained for the final dry film in this case is $D = 287 \pm 0.5$ Å, shown above. This small deviation originates from the fact that for the determination of the spacing in the in-situ measurement only one single peak ($m = 1$) is accessible, while for the dry

film the observed two orders $m = 1, 2$ increase the precision of the D determination. Moreover, a slow ongoing spacing shrinkage might be responsible for this small deviation. The widths σ_i for the P(dS-b-nBMA)$_{35:65}$ samples, cast from protonated and deuterated toluene, share the same behaviour, shown for the case of deuterated toluene in figure 7.4d. A rapid decay of σ to a minimum width at t = 2 h is followed by a steep increase, which levels off at $\approx$ 3.8 h. With ongoing time t the peak width σ continuously decreases again, which indicates an ongoing improvement of order in the block copolymer film.
For both block copolymers the corresponding structure in the drying films is apparently maintained throughout the drying process, while the spacings D decrease to $D = 306 \pm 0.5$Å for P(dS-b-nBMA)$_{50:50}$ and to $D = 287 \pm 0.5$Å for P(dS-b-nBMA)$_{35:65}$. The spacing D decreases slightly faster for the 50:50 block copolymer compared to the copolymer with a volume ratio of 35:65, as can be seen from the extracted time constants of $\tau_{50:50} = 0.92$ h and $\tau_{35:65} = 1.42$ h. In contrast to other approaches, in which the focus is on the tuning of the final structure of the polymer film, e.g. by solvent vapor annealing [228, 229], the present study reveals the structure formation upon drying of the polymer solution. By understanding the fundamental mechanisms driving the self-assembly and by tuning external parameters, e.g. via electrical fields [230], these post-production treatments can be avoided.

7.1.2. Solvent loss during drying

To investigate, whether the different kinetics of structure formation in P(dS-b-nBMA)$_{50:50}$ and P(dS-b-nBMA)$_{35:65}$ correlate with the solvent evaporation during solution casting, the temporal evolution of the critical edges of the reflectivity curves are examined more closely. The position of the critical edge is mostly governed by the bulk SLD of the material present within the accessible scattering depth. The freshly dispensed solution of polymer and deuterated toluene exhibits a critical edge at the theoretical position of deuterated toluene, which has the highest SLD involved (SLD$_{dDMF} = 5.84 \times 10^{-6}$ Å^{-2}). With ongoing time the solvent evaporates, thus the mean SLD decreases and the critical edge moves towards lower q$_z$ values. To track the position of the critical edge as a function of time, again the Fresnel normalized representation is chosen, in which the critical edge transforms into a peak (see also the solid red lines in figures 7.2a, b). For better illustration figure 7.5 shows the reflectivity in the region around the critical edge for four different curves starting at time t = 30 s with intervals of Δt = 50 min in between in the Fresnel normalized representation. The semi-transparent solid vertical lines mark the positions of the critical edges at the corresponding times. The shift from larger q$_z$ to smaller q$_z$ values is clearly visible. Moreover, it is apparent that the underlying kinetics are not

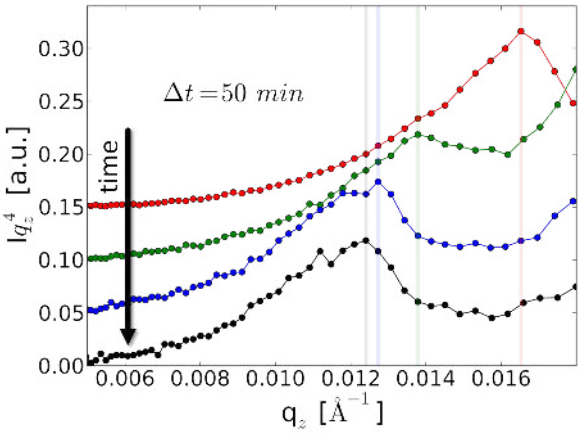

Figure 7.5: Reflectivity curves in the Fresnel normalized representation in the region around the critical edge. The starting time is t = 30 s (red symbols), the time intervals in between are Δt = 50 min. The different colors correspond to the different times. The semi-transparent solid lines mark the positions of the corresponding critical edges. The time increases from top to bottom. The curves are shifted along the y-axis for clarity.

entirely linear. The mean SLD within the accessed scattering depth can be obtained via the relation $q_c = \sqrt{16\pi SLD}$. The solvent volume content c_{tol} can be extracted by

$$c_{tol} = \frac{q_c^2/(16\pi) - SLD_{bulk}}{SLD_{tol} - SLD_{bulk}} \tag{7.2}$$

with SLD_{bulk} being the mean SLD of the block copolymer, SLD_{tol} the SLD of the deuterated toluene and q_c the position of the critical edge, as extracted from the measured data. By tracking the critical edge position as a function of time the solvent evaporation can be analyzed. To be able to compare the solvent evaporation observed for the two different polymers a common time axis is necessary. Therefore, the time at which the critical edge is no longer at the position of pure deuterated toluene is chosen as t = 0. The time dependent solvent loss 1-c_{tol} is shown in figure 7.6a for both block copolymers P(dS-b-nBMA)$_{50:50}$ (red dots) and P(dS-b-nBMA)$_{35:65}$ (blue stars) along with a zoom-in into the early times, shown in the inset. Clearly, the sample with a volume ratio of 50:50 reaches 1-c_{tol} = 1 faster than the sample with the volume ratio of 35:65. This behavior already explains the slower decrease in spacing and the decay of the Bragg peak width σ observed for P(dS-b-nBMA)$_{35:65}$. Due to a slower solvent evaporation, the structure in the film has more time to evolve towards an equilibrium before getting frozen-in in the dry film. On a linear scale also a slightly step-like evaporation behavior is apparent. On a double-logarithmic scale, shown in figure 7.6b, different regimes of solvent evaporation can be identified. For P(dS-b-nBMA)$_{50:50}$ (red dots) only one distinct regime is observed which follows $\propto t^{1.09\pm0.1}$ and therefore is identified as a common case II diffusion ($\propto t$). The block copolymer P(dS-b-nBMA)$_{35:65}$ (blue stars) exhibits a different behavior. In this case, two regimes are observed, the first with a time dependence $\propto t^{0.95\pm0.1}$, the second with a time dependence $\propto t^{0.25\pm0.13}$. Therefore, the first regime corresponds also to a case II diffusion ($\propto t$), whereas at later times an anomalous sub-diffusional behavior is observed due to hindered evaporation of the solvent. Diethert et al. have also observed

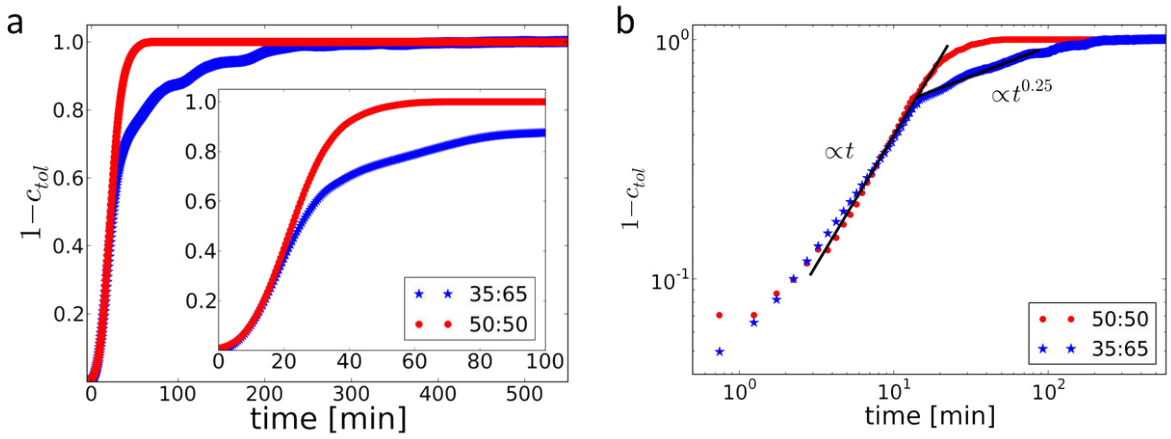

Figure 7.6.: a) Solvent loss 1-c_{tol}(t) for both block copolymers P(dS-b-nBMA)$_{50:50}$ (red dots) and P(dS-b-nBMA)$_{35:65}$ (blue stars). The inset shows a zoom-in into the early times. b) Solvent loss 1-c_{tol}(t) on a double logarithmic plot. Regimes with different diffusion kinetics are evident, as indicated by the linear fits (black lines) and the corresponding exponents.

a case II behavior in the early stages of toluene evaporation from a statistical copolymer solution [162]. Surprisingly, they found an increased solvent evaporation in the second regime. This can be explained by the nature of the statistical copolymer which represents a model system for the class of pressure sensitive adhesives and hence comprises a soft and sticky component with a glass transition T_g well below room temperature. In the present case, the block copolymers are both glassy in their dry states at room temperature. This leads to a decreased mobility at the surface for both polymer and solvent and hence, hinders further solvent evaporation.

7.1.3. Dry state investigated by TOF-GISANS

To obtain information also about the lateral structures in both types of solution cast block copolymer films, TOF-GISANS measurements are performed at the instrument REFSANS (MLZ, FRM2, Garching). An angle of incidence of $\alpha_i = 0.5°$ is chosen along with a sample-detector distance SDD of 10.5 m. Figure 7.7a-j shows GISANS data obtained for the wavelengths $\lambda = 2.25$ to 6.75 Å in steps of $\Delta\lambda = 0.5$ Å.

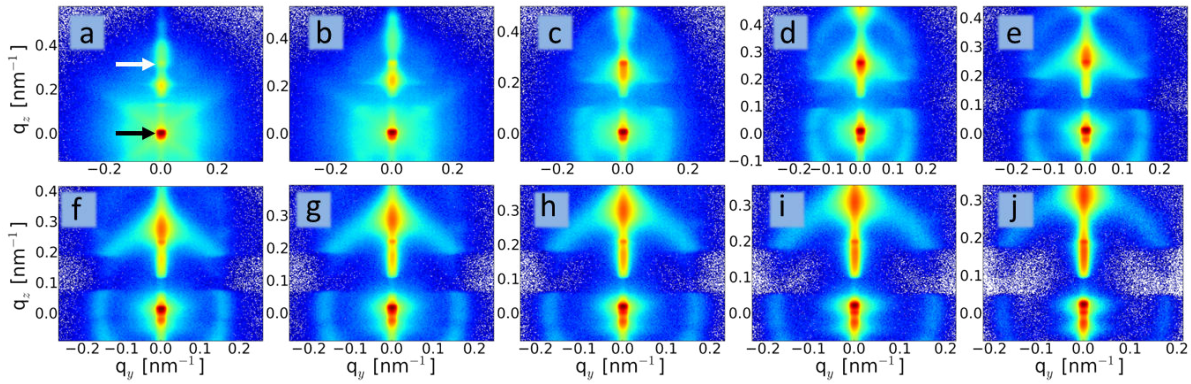

Figure 7.7.: TOF-GISANS data of the P(dS-b-nBMA)$_{50:50}$ film obtained for the wavelengths 2.25 to 6.75 Å in steps of $\Delta\lambda = 0.5$ Å(a-j). The black arrow indicates the direct beam position, the white arrow indicates the specularly reflected beam position.

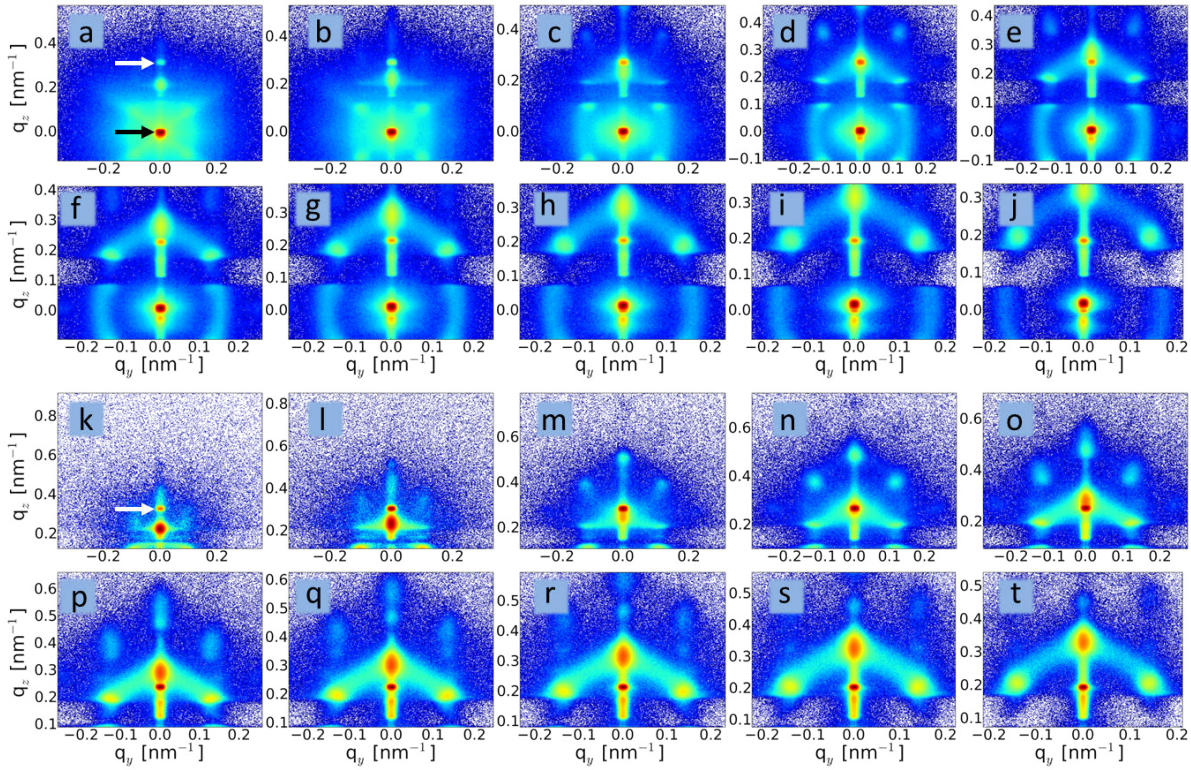

Figure 7.8.: TOF-GISANS data of the P(dS-b-nBMA)$_{35:65}$ film obtained for the wavelengths 2.25 to 6.75 Å in steps of $\Delta\lambda = 0.5$ Å(a-j). The black arrow indicates the direct beam position, the white arrow indicates the specularly reflected beam position. To cover a larger q_z-range, the same measurement is repeated with the detector at an increased height (k-t).

In figure 7.7a the white arrow denotes the specularly reflected beam position, the black arrow indicates the direct beam position. From figure 7.7c on, a distinct ring is evident

originating from different orientations of lamellar domains. In vertical direction at q_y=0 nm^{-1} several intensity maxima are visible for all wavelengths, which move to higher q_z with increasing wavelength.
The 2d data obtained for the measurement of $P(dS\text{-}b\text{-}nBMA)_{35:65}$, shown in figure 7.8a-j, not only exhibit distinct intensity maxima in vertical direction at $q_y = 0$ nm^{-1}, but also off-centered ones. Moreover, also for this sample a ring-shape of increased intensity is observed (figure 7.8d-j). Also for this sample the positions of the direct and the specularly reflected beam are exemplarily indicated in figure 7.8a by a black and a white arrow, repectively. In order to cover a larger q_z-range, the 2d detector was moved to a higher position for a second measurement, shown in figure 7.8k-t. The white arrow in figure 7.8a indicates the specularly reflected beam position.

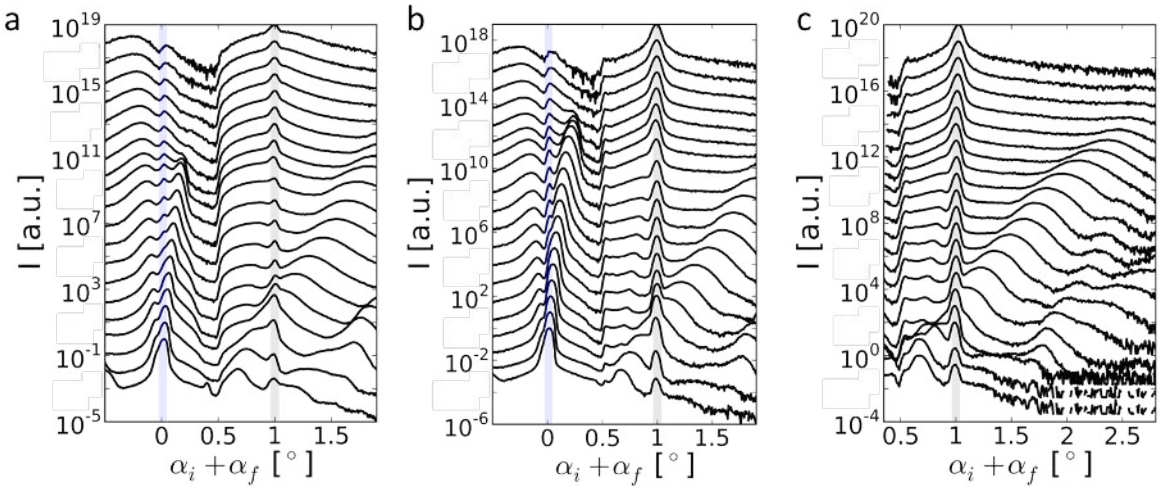

Figure 7.9.: Vertical line cuts taken from the 2d GISANS data at $q_y = 0$ nm^{-1} for the $P(dS\text{-}b\text{-}nBMA)_{50:50}$ film (a), the $P(dS\text{-}b\text{-}nBMA)_{35:65}$ film (b) and the $P(dS\text{-}b\text{-}nBMA)_{35:65}$ film with a higher detector position (c). The wavelength increases from bottom to top (2.25 to 6.75 Å, $\Delta\lambda = 0.5$ Å). The semi-transparent blue solid vertical line denotes the direct beam position, the semi-transparent solid black line indicates the specularly reflected beam position.

To be able to distinguish between Yoneda and Bragg peaks which are present in vertical direction in figures 7.7 and 7.8 at $q_y = 0$ nm^{-1}, vertical line cuts are taken at $q_y = 0$ nm^{-1} for all measurements, shown in figure 7.9a-c. Every line cut corresponds to a certain wavelength λ. Therefore, for every wavelength λ a set of peak positions can be extracted from each line cut.

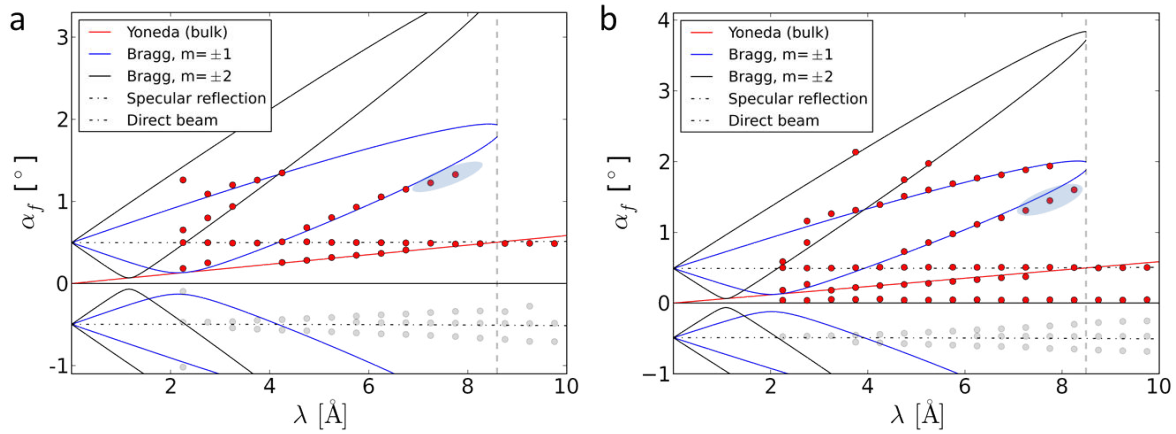

Figure 7.10.: Peak identification using the modified Bragg equation (equation 7.1) for P(dS-b-nBMA)$_{50:50}$ (a) and P(dS-b-nBMA)$_{35:65}$ (b). The semi-transparent blue areas mark deviations from the bulk spacing at the copolymer surface. The gray symbols indicate peaks of unknown origin.

Figure 7.10a,b shows these peak positions relative to the sample surface as a function of wavelength λ. The positions of the direct and the specularly reflected beam are indicated by horizontal dashed lines. The red line represents the wavelength dependent theoretical Yoneda position of the bulk material. The modified Bragg positions calculated using equation 7.1 are represented by blue and black lines for $m = \pm 1$ and $m = \pm 2$, respectively. By adjusting the spacing D a good agreement between observed peak positions and the theoretical Bragg positions is achieved with a spacing of $D = 275 \pm 0.5$ Å for P(dS-b-nBMA)$_{50:50}$ and $D = 260 \pm 0.5$ Å for P(dS-b-nBMA)$_{35:65}$. For longer wavelengths, which are more surface sensitive, the observed Bragg peak positions deviate slightly from the theory, indicating a slightly different spacing D at the surface, as indicated by the semi-transparent blue areas in figure 7.10. The discrepancy between the obtained values for D from TOF-GISANS ($D_{50:50,GISANS} = 275 \pm 0.5$ Å, $D_{35:65,GISANS} = 260 \pm 0.5$ Å) and from NR ($D_{50:50,NR} = 306 \pm 0.5$ Å, $D_{35:65,NR} = 287 \pm 0.5$ Å) in section 7.1.1 can be explained by a very slow rearrangement which is still going on in both samples, which aged for six months between the NR and the TOF-GISANS measurements at ambient conditions at a temperature of 18°C.

7.2. P(dS-b-nBMA) in dimethylformamide

To follow the structure formation upon drying of a solution of P(dS-b-nBMA)$_{35:65}$ in a bad solvent, in-situ NR measurements are performed at the TOF beamline FIGARO

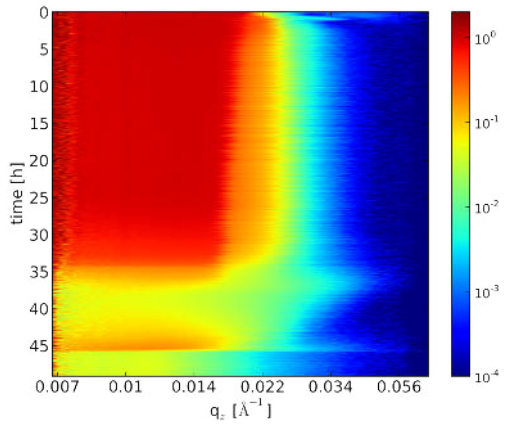

Figure 7.11: Mapping composed of the NR measurements recorded during drying of the solution of $P(dS\text{-}b\text{-}nBMA)_{35:65}$ in deuterated DMF as a function of time.

at ILL (Grenoble, France). Deuterated dimethylformamide (DMF) is chosen as a bad solvent. It is slightly worse for the PS block than for the PnBMA block, thereby aiming at a micellar structure in the dried block copolymer film. The involved Hildebrand solubility parameters are reported to be $\mathfrak{D}_{H,PS} = 18.4\,\mathrm{MPa}^{1/2}$ for polystyrene (PS) [231], $\mathfrak{D}_{H,PBMA} = 18.65\,\mathrm{MPa}^{1/2}$ for poly(butyl methacrylate) (PBMA) [232] and $\mathfrak{D}_{H,DMF} = 24.7\,\mathrm{MPa}^{1/2}$ for the solvent DMF [59]. The same experimental setup as described in section 7.1.1 is used. In between two subsequent measurements the height of the sample is realigned every time to account for the thickness changes upon solvent loss.

7.2.1. Structure formation and solvent loss followed by in-situ neutron reflectivity

Figure 7.11 shows a mapping composed of the NR in-situ measurements as a function of time in the common representation with a logarithmic color scaling, as indicated by the color scale bar. Compared to the results from section 7.1.1, where strong Bragg peaks emerged, no prominent structure is observed in the case of DMF being used as a solvent. The critical edge of the NR curves moves towards smaller q_z with ongoing time due to the evaporation of the deuterated solvent. Moreover, after t $\approx$ 34 h the intensity at the plateau of total reflection decreases until it starts to rise again at t = 40 h until t $\approx$ 46 h. Finally, a very rapid and sharp drop in intensity is evident. For better illustration a set of NR curves is shown in figure 7.12a-f, corresponding to the times t = 0, 30, 35, 39, 45 and 47 h. The differently colored vertical solid lines mark the positions of the critical edges of the involved materials, as indicated in the plots. The freshly dispensed solution exhibits only the critical edge of the deuterated solvent (see figure 7.12a). With ongoing time, the position of the critical edge moves towards smaller values of q_z and the intensity of the plateau of total external reflection decreases (see figure 7.12b). Moreover,

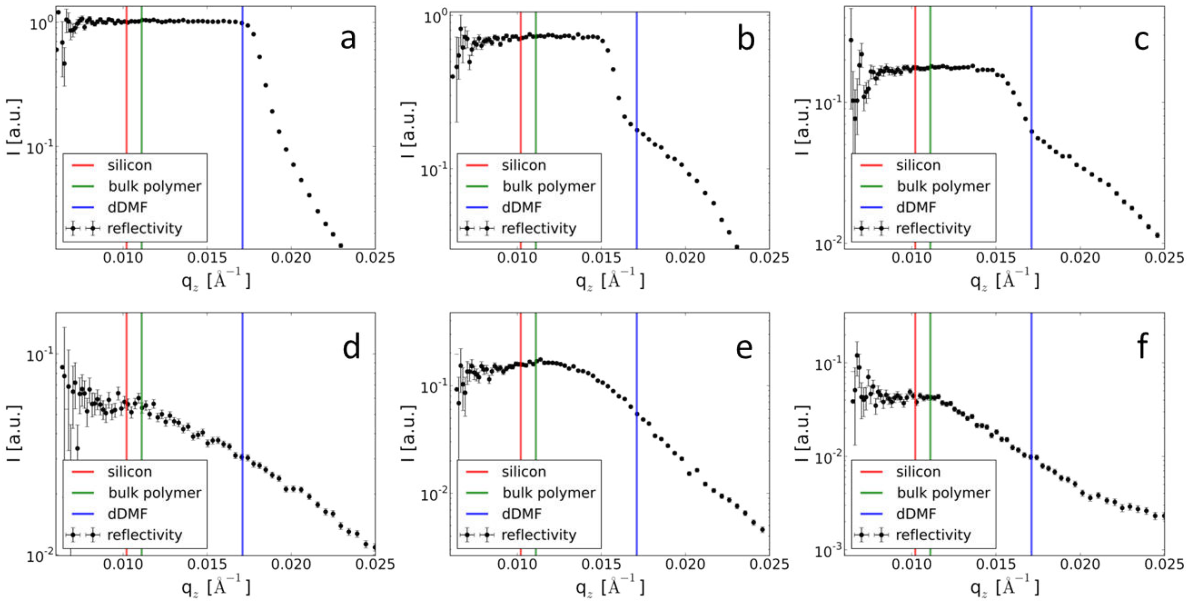

Figure 7.12.: Selected NR curves during drying at times 0 h (a), 30 h (b), 35 h (c), 39 h (d), 45 h (e), 47 h (f). The vertical lines indicate the positions of the critical edges of the involved materials.

a shoulder in intensity at $q_z \approx 0.020$ Å^{-1} is a clear indication of an inhomogeneous SLD profile within the accessed scattering depth. For t = 35 h (see figure 7.12c) this shoulder in intensity stays at the same q_z position, however, the intensity of the plateau region drops further. After 39 h the typical shape of a reflectivity curve is lost (figure 7.12d). The plateau of total external reflection partly forms again after 45 h accompanied by an increase of the plateau intensity (figure 7.12e). However, the structure previously visible at $q_z = 0.020$ Å^{-1} has vanished. At t = 47 h the plateau intensity has dropped again and a rather round shaped critical edge is apparent slightly beyond the critical edge of the bulk polymer. The difference in q_z of the theoretical position (marked by the green vertical line) and the actual critical edge indicates the presence of residual solvent in the polymer film.

To follow the intensity at the plateau of total external reflection as a function of time the q_z-region between 0.006 Å^{-1} and 0.010 Å^{-1} is integrated for every NR curve. The limits of this q_z range are chosen to avoid the large uncertainties at very small q_z and to stay below the critical edge of silicon. The result is shown in figure 7.13 (black symbols). The intensity stays rather constant until t ≈ 25 h, before it decreases rapidly to a minimum at t = 39 h. Surprisingly, the intensity increases again to a maximum at ≈ 45.5 h and finally drops to a constant low level. The first drop in intensity, starting at t = 25 h, can be explained by a rapidly increasing surface roughness of the block copolymer film. Due to the fact that the final sample still has residual solvent incorporated in the film,

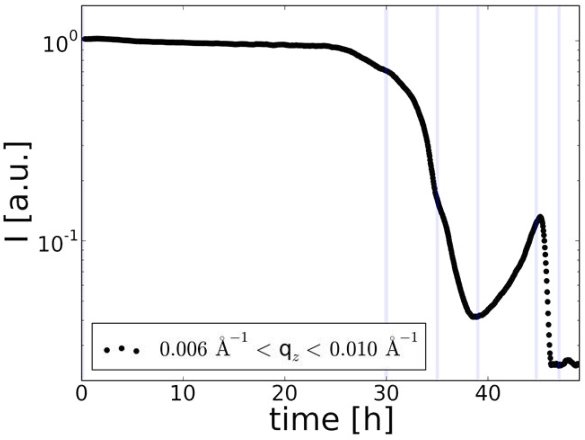

Figure 7.13: Integrated intensity in the region of the plateau of total external reflection in the range between 0.006 Å^{-1} and the critical edge of silicon at 0.010 Å^{-1}. The blue vertical lines indicate the points in time at which the selected NR in figure 7.12 are shown.

the polymer chains can still rearrange, which leads to a temporary smoothening of the surface, hence an increased intensity at the plateau of total external reflection.
By tracking the position of the critical edge as a function of time, the solvent evaporation kinetics in the early stages during drying are accessible (see also section 7.1.2). Figure 7.14 shows the solvent loss as a function of time on a double logarithmic scale. A step-like evaporation behavior is observed with three different diffusion regimes in between. After a slow beginning a regime of almost case II diffusion $\propto t^{0.90}$ is observed. After a phase of constant solvent content with a duration of $\Delta t \approx 20$ min, a sub-diffusional behavior $\propto t^{0.76}$ is evident, followed by another phase of constant solvent content with a larger duration of $\Delta t \approx 200$ min. After a third regime of further slowed-down subdiffusion $\propto t^{0.6}$, a long plateau is reached, which extends towards the collapse of the specular reflection (see figure 7.12d).
At later times the specular reflectivity is lost (see figure 7.12d), which is why the position of the critical edge can not be extracted, anymore. For the final state at t = 47 h a

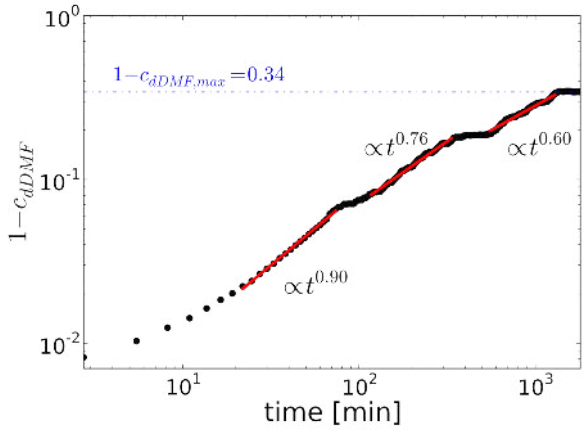

Figure 7.14: Time dependent solvent loss $1 - c_{dDMF}(t)$ on a double logarithmic scale. A step-like profile is obvious with three different diffusion regimes in between. A significant amount of solvent remains in the P(dS-b-nBMA)$_{35:65}$ film.

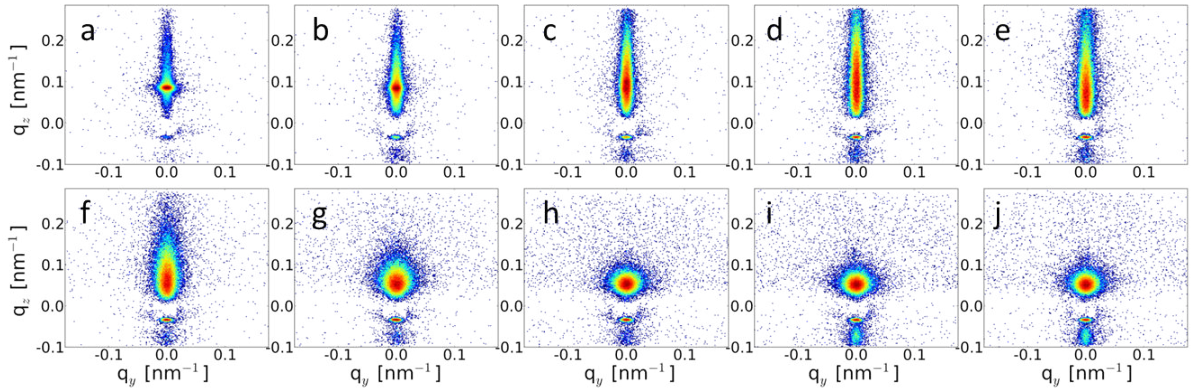

Figure 7.15.: 2d TOF-GISANS data at a wavelength $\lambda = 10.17\,\text{Å}$ during drying at times t = 20, 45, 48, 50, 51, 52, 53, 54, 55 and 60 h (a-j).

critical edge at $q_z = 0.0118\ \text{Å}^{-1}$ is extracted. The corresponding solvent volume content is calculated to be 9.5 %.

7.2.2. Structure formation followed by in-situ TOF-GISANS

As already shown in the previous section the evaporation of DMF is a rather slow process. The loss of the specular reflection after t ≈ 39 h shows that NR is not the ideal tool to investigate the structure formation of this system. TOF-GISANS as a method capable of capturing also the diffuse scattering is well-suited for this task. By sealing the sample environment the time scales for drying of the polymer solution are further streched. These long time scales offer the possibility to follow the structure formation with in-situ TOF-GISANS. The following measurements are performed at the instrument REFSANS (MLZ, FRM2, Garching). The possibility of the beamline setup to bend the beam is utilized to be able to follow the drying of the liquid polymer solution on a silicon wafer. Every 60 min the height of the sample surface is realigned to account for thickness changes due to solvent evaporation. The drying of P(dS-b-nBMA)$_{35:65}$ and P(dS-b-nBMA)$_{50:50}$ cast from deuterated DMF is followed over a period of 65 h. An anti-vibration stage damped possible external vibrations. As already shown in sections 2.3.4 and 5.2 the scattering depth Λ is a function of the wavelength λ. Therefore, in the following two exemplary wavelengths $\lambda = 10.17\,\text{Å}$ and $\lambda = 5.58\,\text{Å}$ are chosen as representatives for surface and bulk sensitivity, respectively. Figure 7.15a-j shows the 2d TOF-GISANS data obtained after 20, 45, 48, 50, 51, 52, 53, 54, 55 and 60 h for the surface sensitive wavelength $\lambda = 10.17\,\text{Å}$. In the beginning only the specular peak is visible with a narrow halo which extends mostly towards larger q_z values (figure 7.15a). With ongoing time this halo stays narrow, but the specular peak broadens successively in q_z direction (figure 7.15b-e). From

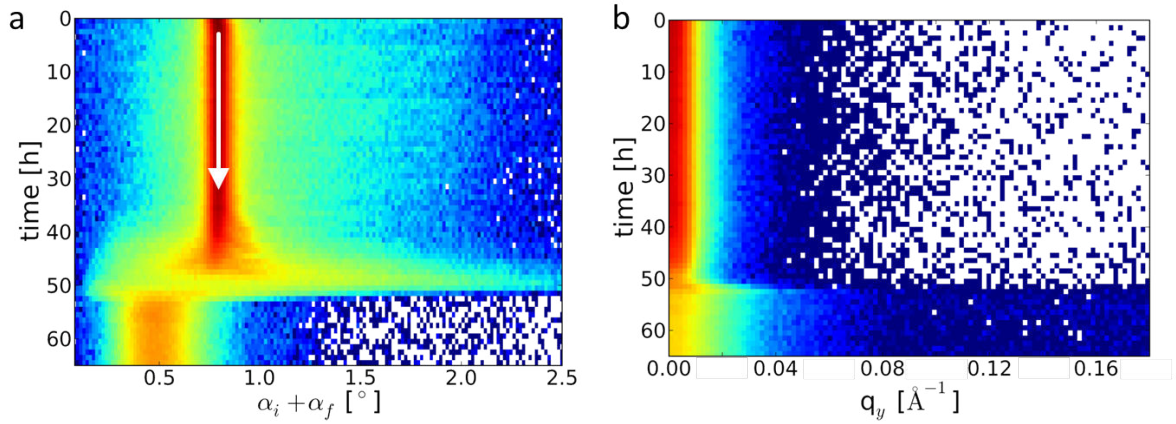

Figure 7.16.: a) Mapping composed of vertical line cuts taken at $q_y = 0$ nm^{-1} as a function of time. The white arrow indicates the position of the specularly reflected beam. b) Mapping composed of horizontal line cuts taken at the Yoneda position of the polymer as a function of time. For improved statistics the intensities left and right from $q_y = 0$ nm^{-1} are averaged.

t = 52 h on, the peak shifts towards the Yoneda peak of the polymer (figure 7.15f-j). The shape of the peak changes from an elongated droplet shape to a more circular shape, while the specular peak completely vanishes. This behavior indicates a strong roughening of the polymer surface. The diffuse scattering slightly increases with time, but no prominent structure is evident for this surface sensitive wavelength $\lambda = 10.17$ Å.

To better visualize the changes in the scattering patterns, vertical line cuts at $q_y = 0$ nm^{-1} are taken as a function of time, shown in figure 7.16a. The white arrow denotes the specularly reflected beam position. From t ≈ 35 h on, first changes appear. The peak width at the specular position broadens and the peak intensity drops drastically at t = 48 h, until no specular peak is present, anymore. At t = 50 h a broad peak appears at the Yoneda position of P(dS-b-nBMA)$_{35:65}$ and stays at the same position throughout the experiment. Horizontal line cuts, taken at the Yoneda position of P(dS-b-nBMA)$_{35:65}$, are shown in a time dependent mapping in figure 7.16b. To improve statistics, the diffuse scattering left and right from $q_y = 0$ nm^{-1} is averaged, using the symmetry of the 2d TOF-GISANS data. Until t ≈ 48 h the line cuts do not exhibit significant changes. From t ≈ 48 h on the intensity around $q_y = 0$ nm^{-1} drops and the corresponding peak width decreases at first before an immediate increase sets on. At t = 53 h the peak width has reached its maximum and slightly decreases again with ongoing time t.

To probe the bulk material the wavelength $\lambda = 5.58$ Å is chosen. Figure 7.17a-j shows the 2d TOF-GISANS data obtained at the same times as above. A different behavior is evident. In the beginning only the specular peak is visible and a narrow halo around it which extends in the q_z direction (figure 7.17a). With ongoing time the specular peak

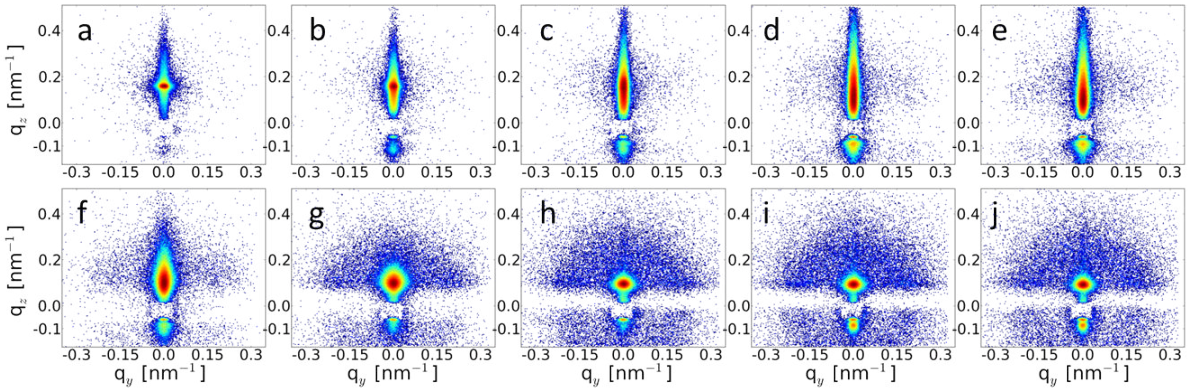

Figure 7.17.: 2d TOF-GISANS data at a wavelength $\lambda = 5.58$ Å during drying at times t = 20, 45, 48, 50, 51, 52, 53, 54, 55 and 60 h (a-j).

broadens in q_z direction (figure 7.17a-e) and the highest peak intensity moves to smaller q_z. Moreover, the scattering in q_y direction gets more intense (figure 7.17d-e). After 52 h (figure 7.17f) two off-centered peaks emerge, which get more intense with time. Also a diffuse ring-like shape develops with time (figure 7.17g-j). Again, vertical and horizontal line cuts are extracted, shown in figure 7.18a and b, respectively. A similar picture as for $\lambda = 10.17$ Å is obtained for the vertical line cut evolution. However, within the first 10 h the tail of the specularly reflected beam stretches towards larger angles $\alpha_i + \alpha_f \approx 1.5°$ and stays constant until t $\approx$ 45 h.

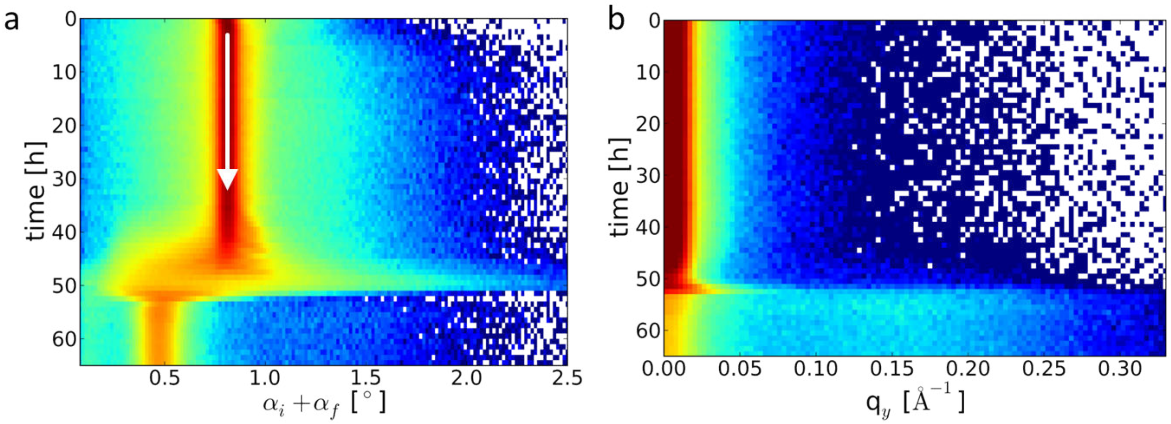

Figure 7.18.: a) Mapping composed of vertical line cuts taken at $q_y = 0$ nm^{-1} as a function of time. The white arrow indicates the position of the specularly reflected beam. b) Mapping composed of horizontal line cuts taken at the Yoneda position of the polymer as a function of time. For improved statistics the intensities left and right from $q_y = 0$ nm^{-1} are averaged.

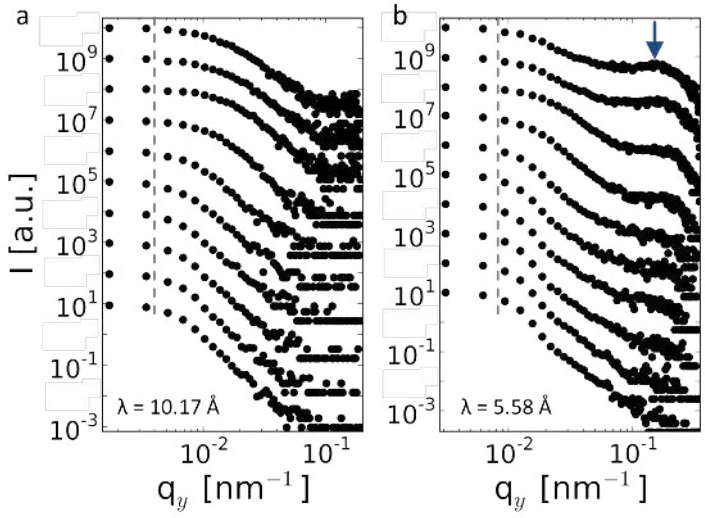

Figure 7.19: Horizontal line cuts for the wavelengths $\lambda = 10.17\,\text{Å}$ (a) and $\lambda = 5.58\,\text{Å}$ (b). The curves are shifted along the y-axis for clarity, the time increases from bottom to top (t = 20, 45, 48, 50, 51, 52, 53, 54, 55 and 60 h). The surface sensitive wavelength does not exhibit significant lateral structures (a), whereas the bulk sensitive wavelength shows an emerging peak at $q_y \approx 0.15\ \text{nm}^{-1}$ (b), indicated by an arrow. The dashed lines represent the resolution limits.

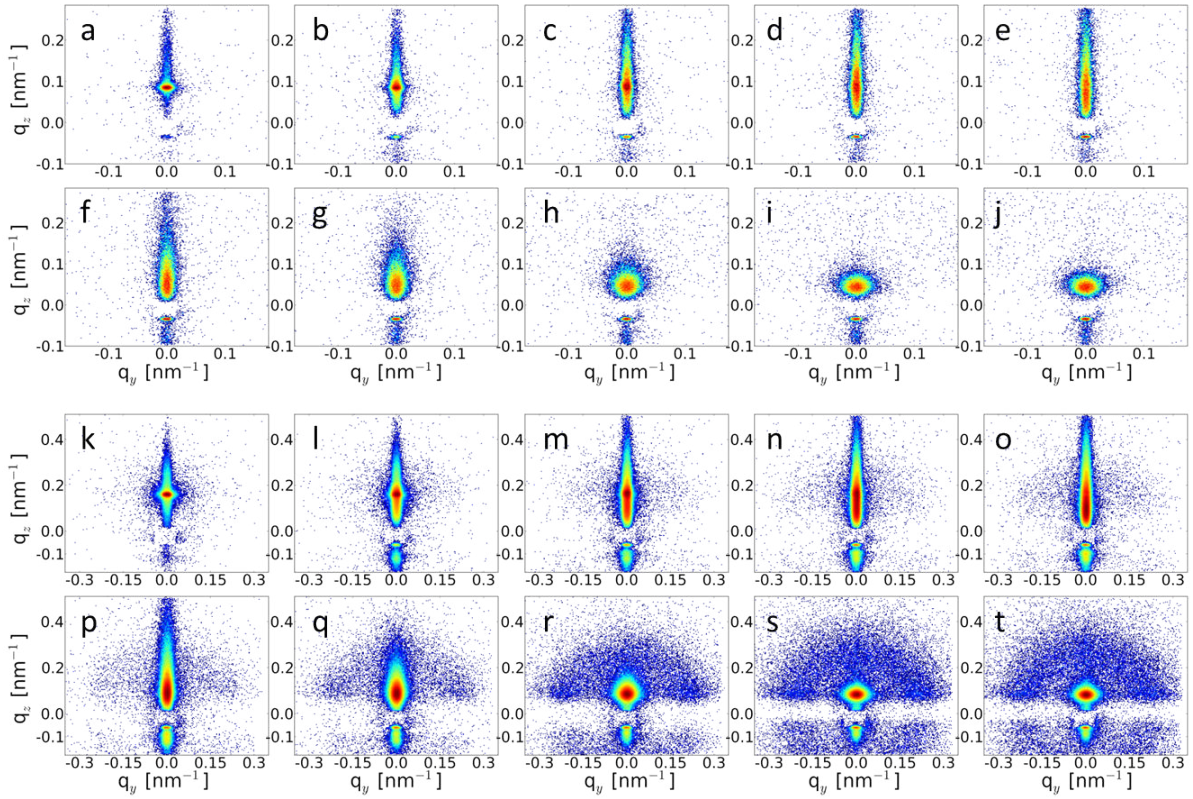

Figure 7.20.: 2d TOF-GISANS data at the wavelengths $\lambda = 10.17\,\text{Å}$ (a-j) and $\lambda = 5.58\,\text{Å}$(k-t) during drying at times t = 20, 40, 43, 44, 45, 46, 47, 48, 49 and 54 h.

From this time on the specular peak exhibits decreasing intensity, while the Yoneda peak of $\text{P(dS-b-nBMA)}_{35:65}$ emerges. At t = 53 h the specular peak has vanished and

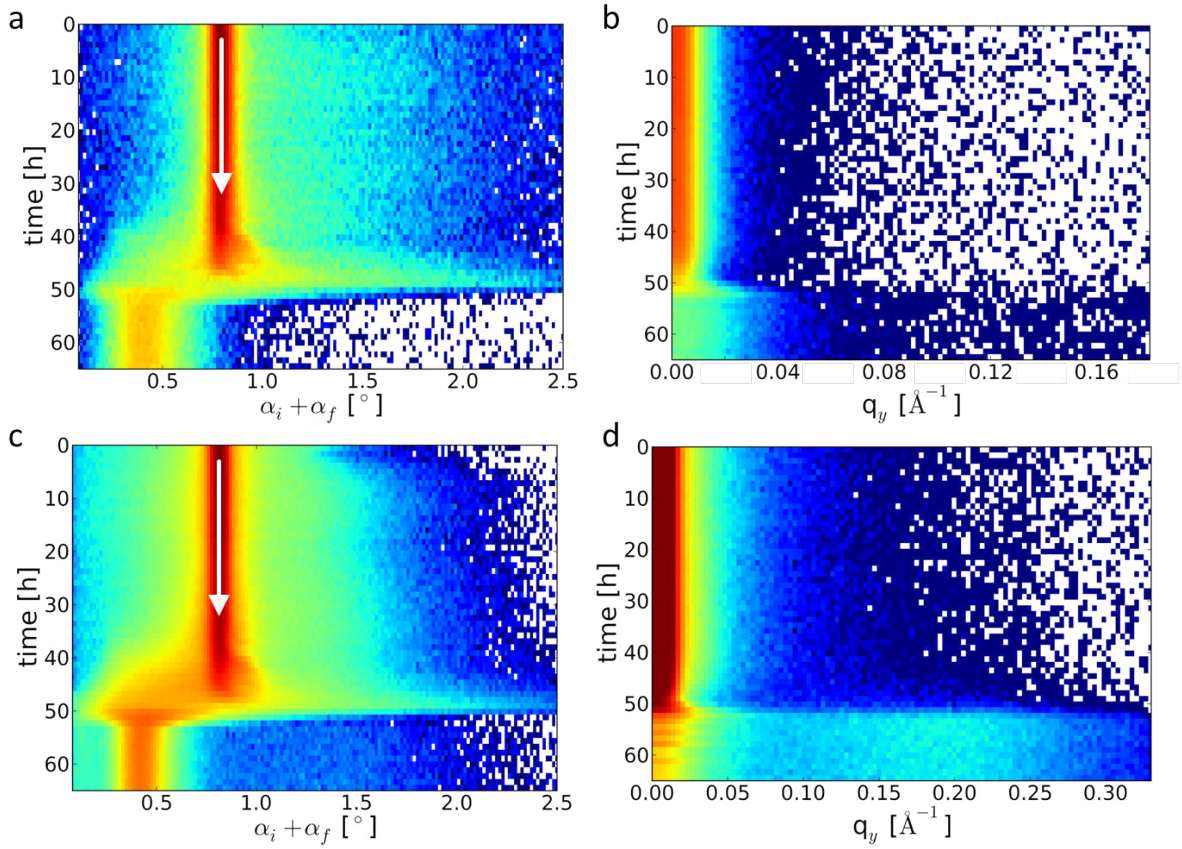

Figure 7.21.: a) Mapping composed of vertical line cuts taken at $q_y = 0$ nm^{-1} as a function of time during drying of P(dS-b-nBMA)$_{50:50}$. The white arrow indicates the position of the specularly reflected beam. b) Mapping composed of horizontal line cuts taken at the Yoneda position of the polymer as a function of time. For improved statistics the intensities left and right from $q_y = 0$ nm^{-1} are averaged.

the Yoneda peak width has decreased to its final width. Figure 7.18b shows the time dependent horizontal line cuts. No significant changes are present until t $\approx$ 48 h, when the width of the peak at $q_y = 0$ nm^{-1} quickly decreases, followed by a sudden increase at t = 52 h. This width decreases again, accompanied by a drastic drop in intensity. Moreover, diffuse scattering extending up to q_y =0.25 nm^{-1} with a peak at $q_y \approx 0.15$ nm^{-1} is present from t = 53 h on.

The vanishing specularly reflected beam for both wavelengths is a clear indication of a prominent surface roughening upon drying, which can also explain the collapse of the neutron reflectivity in section 7.2.1, where the specular reflection is also lost.

To get a more quantitative understanding of the lateral structure evolution in the P(dS-b-nBMA)$_{35:65}$ film cast from DMF, the horizontal line cuts which correspond to the 2d TOF-GISANS data at $\lambda = 10.17$ Å and $\lambda = 5.58$ Å in figures 7.16 and 7.18 are shown in

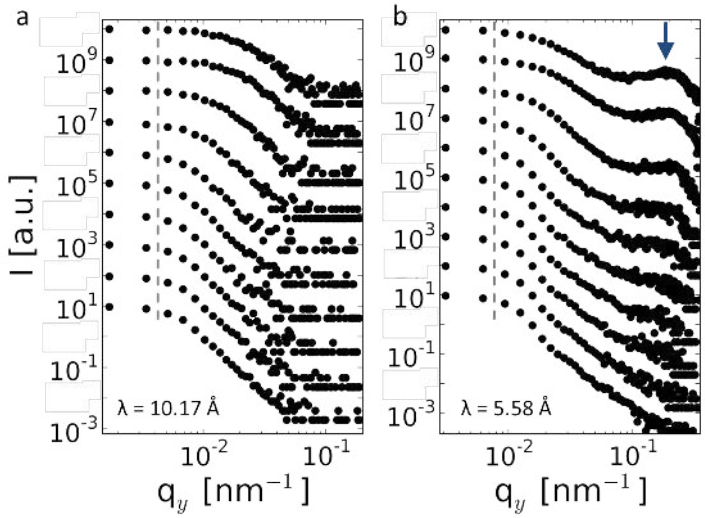

Figure 7.22: Horizontal line cuts during drying of P(dS-b-nBMA)$_{50:50}$ at the wavelengths $\lambda = 10.17$ Å (a) and $\lambda = 5.58$ Å (b). The curves are shifted along the y-axis for clarity, the time increases from bottom to top (t = 20, 40, 43, 44, 45, 46, 47, 48, 49 and 54 h). The surface sensitive wavelength does not exhibit significant lateral structures (a), whereas the bulk sensitive wavelength shows an emerging peak at q_y = 0.20 nm^{-1} (b), indicated by an arrow. The dashed lines represent the resolution limits.

figure 7.19a and b, respectively, in the common double-logarithmic representation. For the surface sensitive wavelength $\lambda = 10.17$ Å no lateral structure is resolved (figure 7.19a). However, the bulk sensitive wavelength $\lambda = 5.58$ Å reveals a prominent peak at q_y = 0.15 nm^{-1} from t = 51 h on, which corresponds to a characteristic size of 42±0.2 nm. This peak exhibits an increasing intensity with ongoing time, whereas its positions stays rather constant.

To investigate the influence of the volume ratio of the two blocks in the copolymer on the structure formation, the same experiment is conducted with P(dS-b-nBMA)$_{50:50}$. Figure 7.20a-j shows the surface sensitive 2d TOF-GISANS data ($\lambda = 10.17$ Å), whereas figure 7.20k-t shows the bulk sensitive data ($\lambda = 5.58$ Å). The data in figure 7.20 correspond to the times t = 20, 40, 43, 44, 45, 46, 47, 48, 49 and 54 h. Both series appear very similar to the TOF-GISANS data obtained for P(dS-b-nBMA)$_{35:65}$. Also the time dependent line cuts in both directions, shown in figure 7.21a-d do not show drastic differences. However, subtle differences are present. The changes in both types of line cuts appear slightly earlier compared to the case of P(dS-b-nBMA)$_{35:65}$. Moreover, the peak in the horizontal line cuts for $\lambda = 5.58$ Å (figure 7.22b) at times larger than t = 50 h appears at a larger q_y position of $q_y \approx 0.20$ nm^{-1}.

More detailed information about the lateral structures in the drying film of P(dS-b-nBMA)$_{50:50}$ is extracted from the common representation of the horizontal line cuts, shown in figure 7.22a and b for $\lambda = 10.17$ Å and 5.58 Å, respectively. As in the case of P(dS-b-nBMA)$_{35:65}$ the surface sensitive measurement does not show any prominent

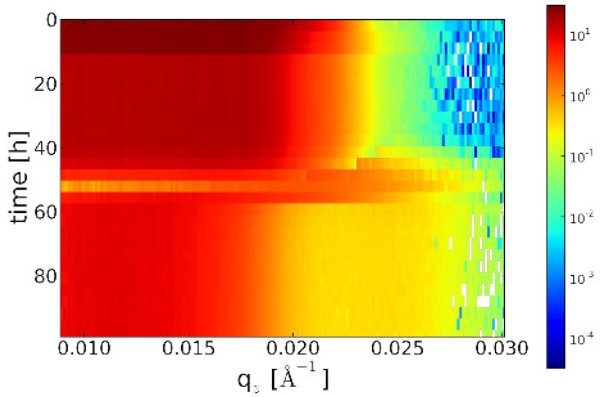

Figure 7.23: Mapping composed of the reflectivity calculated from the intensity at the specularly reflected beam of the 2d TOF-GISANS data versus time.

features (figure 7.22a). However, the bulk sensitve wavelength $\lambda = 5.58$ Å reveals prominent peaks at $q_y = 0.20$ nm^{-1} from t = 44 h on, which corresponds to a characteristic size of 31.4 ±0.2 nm, which is smaller than 42 ± 0.2 nm as obtained for P(dS-b-nBMA)$_{35:65}$.

7.2.3. TOF-GISANS goes reflectivity

As already mentioned above, TOF-GISANS uses a wavelength band. Therefore, the slicing in wavelength λ and the corresponding uncertainty $\Delta\lambda/\lambda$ can be chosen in a way to have a high resolution in λ, while maintaining sufficient statistics. This λ - resolution translates into a depth-resolution due to the wavelength dependent scattering depth Λ (see also section 2.3.4). The TOF-mode in GISANS can furthermore be utilized to extract the specular reflectivity, just like in a NR experiment. By taking the intensity in the specularly reflected beam in the 2d GISANS data for every wavelength slice, a NR curve can be extracted. As a consequence, the width of the wavelength band together with the chosen angle of incidence α_i determine the accessible q_z-range. In the present in-situ experiment of a drying polymer solution, the evaporation of the solvent can be tracked as well. Figure 7.23 shows evolution of the calculated reflectivity as a function of time. Similar to above, the critical edge moves to lower q_z values upon evaporation of the deuterated solvent. At t ≈ 50 h, the intensity of the plateau of total external reflection loses both in intensity and also its characteristic shape. With ongoing time, the sample has reached a stable state at t ≈ 60 h.

For a more detailed view, selected NR curves are shown in figure 7.24a-f for the times t = 1 h, 3 h, 20 h, 30 h, 50 h and 70 h. Despite the lower time-resolution as compared to a measurement conducted at a dedicated reflectivity setup, similar trends are clearly visible. In the beginning (figure 7.24a), the critical edge of the deuterated solvent is the dominating feature. Moreover, a shoulder in intensity at $q_z \approx 0.021$ Å^{-1} already indicates a non-homogeneous SLD-profile within the still liquid sample. With ongoing time (figure

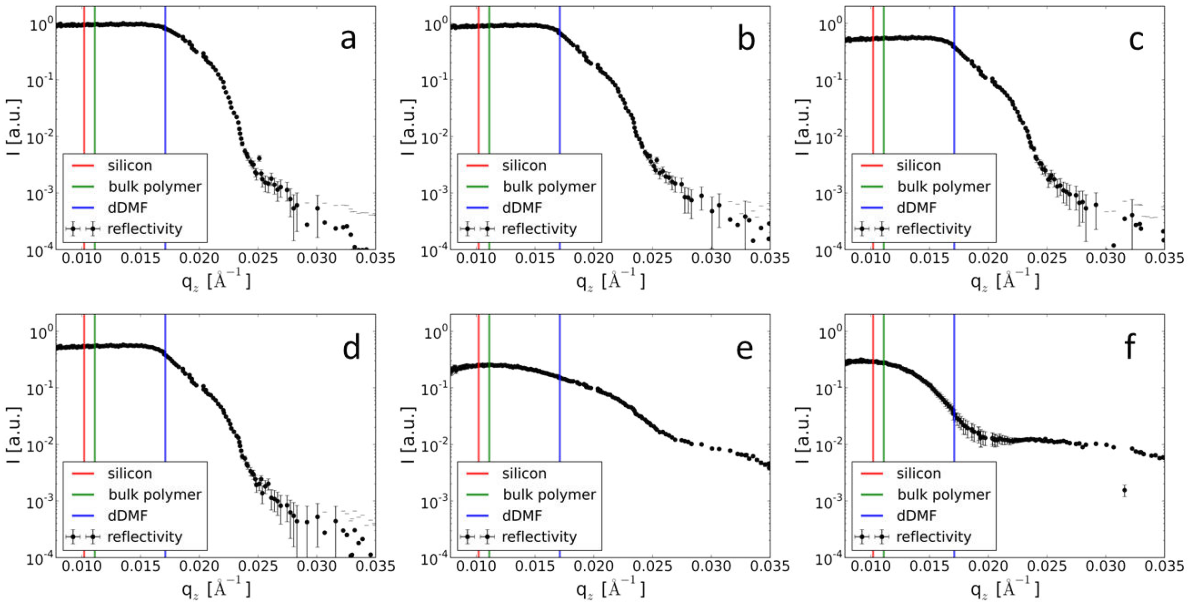

Figure 7.24.: Reflectivity curves calculated from the specular peak position of the 2d GISANS data at times t = 1 h, 3 h, 20 h, 30 h, 50 h, 70 h (a-f). The vertical lines indicate the positions of the critical edges of the materials in the sample.

7.24b-d) this shoulder gets more pronounces, while the total intensity of the plateau of total external reflection drops. At t = 50 h the reflectivity has lost its characteristic shape and has dropped further in intensity. The specular reflectivity seems to have recovered for later stages, e.g. at t = 70 h (figure 7.24f). At this stage, the reflectivity curve exhibits a very round shape, most likely due to the large roughness of the dry polymer film. However, inner structure is clearly visible in form of a broad oscillation with its center at $q_z \approx 0.027\,\text{Å}^{-1}$.

While fitting of the reflectivity data is crucial for extraction of exact quantitative results, the observed behavior is very similar to the results from section 7.2.1. This experiment demonstrates, that TOF-GISANS can be well utilized to extract also the specular reflectivity. Especially in case of in-situ experiments involving changes in the vicinity of the critical edge, this approach can help to track, for instance, solvent loss. This simultaneous use of TOF-GISANS to extract depth-resolved structure formation during drying of a block copolymer solution while also extracting the reflectivity to identify changes at the low q_z-region, has not been reported so far.

7.3. Summary

This chapter details the kinetics of structural evolution during drying of solutions of symmetric (weight ratio 50:50) and asymmetric (weight ratio 35:65) compositions of the diblock copolymer poly(styrene-d8-b-n-butylmethacrylate) (denoted P(dS-b-nBMA)$_{50:50}$ and P(dS-b-nBMA)$_{35:65}$, respectively) in good and bad solvents. The chosen compositions are reported to lead to lamellar (in case of a ratio of 50:50) and cylindrical/rodlike (in case of a ratio of 35:65) structures, respectively [226]. Toluene acts as good solvent for both blocks, and leads to well established Bragg peaks originating from the polymer self assembly with observed orders up to $m = 5$ in the dry state. By in-situ NR measurements a shrinkage of the spacing D is observed, being fast in the beginning and continuously slowing down. Despite the changing spatial dimensions, the structure stays from its first appearance on, as is obvious from the agreement of the theoretical positions of the higher Bragg orders m and the observed positions from the measurements. The final Bragg spacings are found to be $D_{50:50} = 306 \pm 0.5\,\text{Å}$ for the block ratio of 50:50 and $D_{35:65} = 287 \pm 0.5\,\text{Å}$ for the block ratio of 35:65.
Furthermore, the position of the critical edge q_c, present in all in-situ NR measurements, is tracked as a function of time during the evaporation of the deuterated toluene. From the time dependent position of q_c a corresponding solvent volume content is determined. Moreover, the solvent loss is calculated and two distinct evaporation regimes are observed. For P(dS-b-nBMA)$_{50:50}$ only one regime is present, exhibiting the typical behavior of a case II diffusion as indicated by the linear behavior. In case of P(dS-b-nBMA)$_{35:65}$ in the beginning also a case II behavior is observed, while at later times a retarded evaporation is evident. Due to the identical chemistry of both sample systems, this difference is traced back to a hindered evaporation of the solvent caused by the structure in the polymer film. TOF-GISANS measurements performed on the dry samples furthermore prove the existence of highly ordered domains and agree well with the assumption of lamellar/cylindrical structures. Superimposed ring-shaped scattering patterns reveal also deviations from a perfect alignment of all domains. By using a modified Bragg equation [225] the higher order Bragg peaks are identified along with the fitted spacings of $D = 275 \pm 0.5\,\text{Å}$ for P(dS-b-nBMA)$_{50:50}$ and $D = 260 \pm 0.5\,\text{Å}$ for P(dS-b-nBMA)$_{35:65}$.
Deuterated dimethylformamide (DMF) is chosen as bad solvent. Structure formation as well as solvent loss is monitored with in-situ NR. A broad shoulder in intensity at $q_z \approx 0.020\,\text{Å}$ appears, which is a clear indication of an inhomogeneous SLD profile. With ongoing time a strong surface roughening leads to a collapse of the specular reflection. At later times the surface smoothens again, before worsening to the final state. The time dependent solvent loss of the early stages of drying reveal three regimes in a step-like process. A case II diffusion in the beginning changes to subdiffusional behavior at later

times, where the evaporation is hindered by the established structures in the film.
The long time scales of drying allow for the first in-situ TOF-GISANS investigation of a liquid-air interface. It is shown, that the lateral structures occur earlier for P(dS-b-nBMA)$_{50:50}$ than for P(dS-b-nBMA)$_{35:65}$. This means that also for the bad solvent the cylindrical structure hinders the solvent evaporation. Moreover, the resulting values of the characteristic length obtained from the horizontal line cuts reveal larger structures for P(dS-b-nBMA)$_{35:65}$ (42 ± 0.2 nm) than for P(dS-b-nBMA)$_{50:50}$ (31.4 ± 0.2 nm). These sizes are larger than the ones observed in the TOF-GISANS measurements of the dry samples cast from toluene, which is due to the worse solubility of both blocks in DMF.
Finally, for the first time the time-of-flight mode of a in-situ GISANS measurement was utilized to calculate the corresponding time-resolved reflectivity from the specularly reflected intensity for each wavelength. With this approach, e.g. solvent evaporation kinetics can be extracted simultaneously to a common GISANS measurement.

8. Conclusion and outlook

The inner structure of a model system of pressure sensitive adhesives (PSAs) is investigated by atomic force microscopy (AFM) and several scattering techniques. AFM and time-of-flight grazing incidence neutron small angle scattering (TOF-GISANS) prove the absence of significant lateral structures at the surface, in the bulk and at the interface to the adherent of the investigated PSA films, which are based on statistical copolymers. X-ray and neutron reflectivity (XRR, NR) reveal the chemical composition of the PSA in the near-surface region as well as at the adhesive-adherent interface. Compositional deviations from the bulk material are found in depths of up to approximately 100 nm. The results from tack-tests addressing the macroscopic adhesive performance of a stainless steel punch and the model PSA, also performed with punch probes of different surface roughness, agree well with the findings from XRR and NR. It is successfully shown that at and near the surface of the solution cast PSA films, the components of the PSA can be selectively enriched by providing an appropriate atmosphere. High relative humidity is found to lead to an enrichment of the more polar methyl methacrylate (MMA), while a completely unpolar nitrogen atmosphere leads to an enrichment of ethylhexylacrylate (EHA). An enrichment of MMA at the surface is found to increase the maximum stress in tack tests.

The possibility to access buried interfaces is utilized to investigate the adhesive-adherent interface of the PSA film on silicon by NR. It is shown that a tuning of the hydrophilicity of the silicon by different cleaning routines can selectively attract one or the other component of the PSA. This finding provides means to tune also the adhesive strength of a given adhesive-adherent combination just by tuning the surface chemistry. Thus, the successful utilization of neutron scattering, to access the buried adhesive-adherent interface, enriches the field of adhesion science by a powerful and non-destructive method to probe adhesive bonds.

The successful implementation of a temperature-controlled humidity cell for tack experiments reveals different failure mechanisms of the adhesive bond between stainless steel and the PSA at different relative humidities (RH). For low RH cavitation and fibrillation is observed, while at higher RH internal crack propagation dominates, before at very high RH external crack propagation takes over completely. This RH dependency of the failure

mechanism is found to be independent from the surface roughness.
Furthermore, the reorganization of the chemical composition in solution cast PSAs is followed in-situ with NR during post-production treatments with different RH. While only the highest RH leads to significant changes in the composition, a detailed analysis remains difficult due to the large thickness. This large thickness on the other hand allows for an important constraint for fitting: the conservation of mass, because the whole PSA is probed, including the interface to the adherent.
In PSAs the dominating adhesive forces are usually van der Waals forces. However, if adhesive and adherent are both polymers and, more specifically, the same polymer, diffusive adhesion can be observed. In the present thesis tack experiments are performed with punch probes and films made of poly(methyl methacrylate) (PMMA). The adhesive performance strongly depends on the contact time. Furthermore, large differences are revealed for experiments carried out under humid and dry conditions. At high RH the fracture stress increases continuously with repetition of the measurement, indicating an inelastic adaption of both surfaces which leads to improved wetting and hence, improved diffusive adhesion. At low RH however, this surface adaption effect is lost. The maximum stress increases nonetheless with contact time.
A common industrial application of adhesive bonding includes the joining of metals. In the present thesis different metals are subject to tack tests in combination with the model PSA. Surface energy and surface roughness, as well as the surrounding atmosphere during the tack test are found to be the dominating parameters influencing the adhesive performance. The interactions between metal and adhesive are also successfully investigated by in-situ grazing incidence small angle x-ray scattering (GISAXS) during metal film growth on PSA and homopolymer layers. It is found that the glass transition temperature T_g plays an important role in the early stages of film formation concerning the growth rate of the metal film. While on the soft and sticky poly(ethylhexylacrylate) (PEHA) the growth rate is higher, the growth is slower on the glassy PMMA. This behavior is found for aluminum and gold, despite their different reactivity. Moreover, a Volmer-Weber growth is found for both kinds of metals on all used polymers.
The structure formation of diblock copolymers during solution casting is successfully investigated by neutron scattering for the first time. Two copolymers comprising of deuterated polystyrene and poly(n-butyl acrylate) (P(dS-b-nBMA)) of different volume ratios of 50:50 and 35:65 ($P(dS\text{-}b\text{-}nBMA)_{50:50}$, $P(dS\text{-}b\text{-}nBMA)_{35:65}$) are representing lamellar and cylindrical ordering, respectively. The films are cast from the good solvent toluene and the bad solvent dimethylformamide (DMF). Cast from toluene the two polymer solutions exhibit different drying kinetics as observed by in-situ NR. $P(dS\text{-}b\text{-}nBMA)_{50:50}$ shows a solvent loss exhibiting a time dependence of $\propto t$. For $P(dS\text{-}b\text{-}nBMA)_{35:65}$ two regimes are

evident, the first also following $\propto t$, the second $\propto t^{0.25}$. The retarded solvent evaporation in the later stage is due to the evolving structure hindering the diffusion of the solvent to the surface. The structures in both films are maintained from their first appearance on throughout the drying process. However, the spacings of the inner structures decrease with ongoing drying. The dry state is investigated by TOF-GISANS, revealing highly ordered structures. Furthermore, a detailed identification of the observed Bragg peaks and the corresponding spacings is performed. The drying of $P(dS\text{-}b\text{-}nBMA)_{35:65}$ cast from DMF is also followed with in-situ NR, revealing a solvent loss consisting of several regimes, starting with a regime $\propto t^{0.90}$ which stepwise slows down. The reflectivity reveals an inhomogeneous SLD profile within the scattering depth in the beginning. At later times the reflectivity collapses due to a strong roughening of the surface as a consequence of the use of the bad solvent DMF. The drying of $P(dS\text{-}b\text{-}nBMA)_{50:50}$ and $P(dS\text{-}b\text{-}nBMA)_{35:65}$ cast from DMF is monitored with in-situ TOF-GISANS measurements. This is the first successful in-situ TOF-GISANS experiment conducted at a liquid-air interface. The depth resolved analysis allows to reveal depth- and time-resolved structure formation in the drying solution. While the whole drying process is found to take more than two days under the chosen conditions, drastic structural changes occur within less than one day.

Future projects could focus on the details of the different failure mechanisms observed in this work. GISAXS/GISANS measurements carried out during the rupture of the adhesive bond could reveal important details about the kinetics involved in the different failure mechanisms. External parameters which mimic challenging environments for adhesive applications, e.g. high relative humidity at elevated temperatures, should be provided. Furthermore, the characterization of the adhesive performance should be extended to peel-tests, representing a further application-motivated test for adhesives, which is well-suited for studies aiming at adhesive-adherent interfaces. Peel-tests would, for instance, also allow for investigations of the adhesive strength of metal layers grown on PSAs by sputtering.

Appendices

A. Contact angle measurements

In this section the contact angle data along with the corresponding fits are presented for the adherents stainless steel and titania. The data and corresponding fits for aluminum are presented in section 6.1.1.

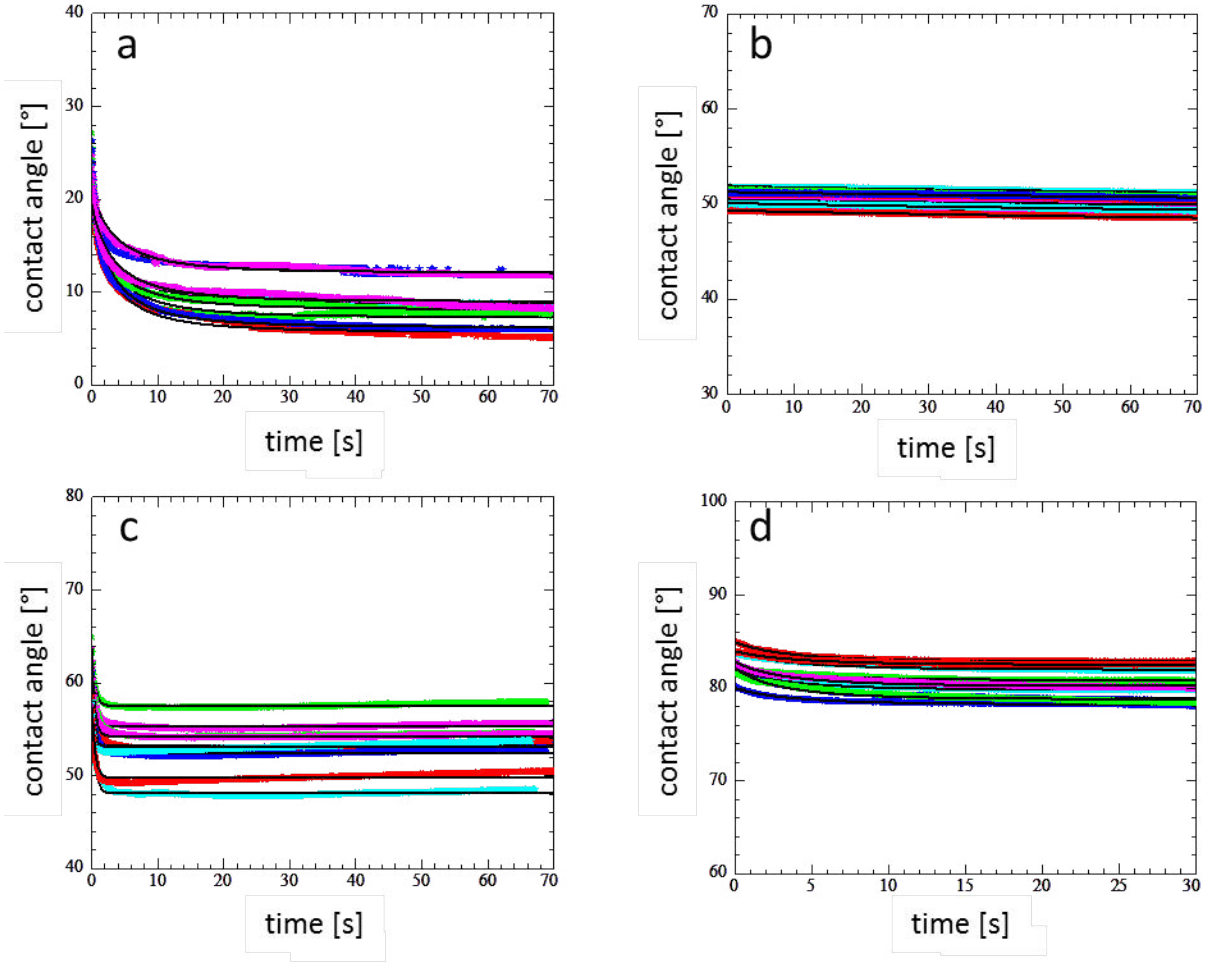

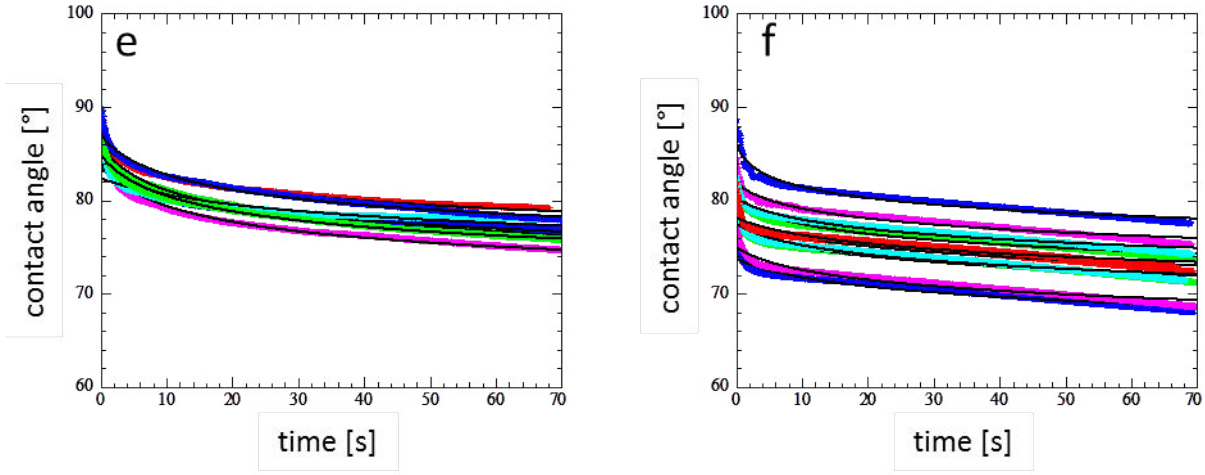

Figure A.1.: Time dependent contact angles of the different test liquids: a) paraffin oil, b) diiodomethane, c) ethylene glycol, d) formamide, e) glycerol and f) water on stainless steel. The colored symbols represent the measured data, the black solid lines the corresponding fits.

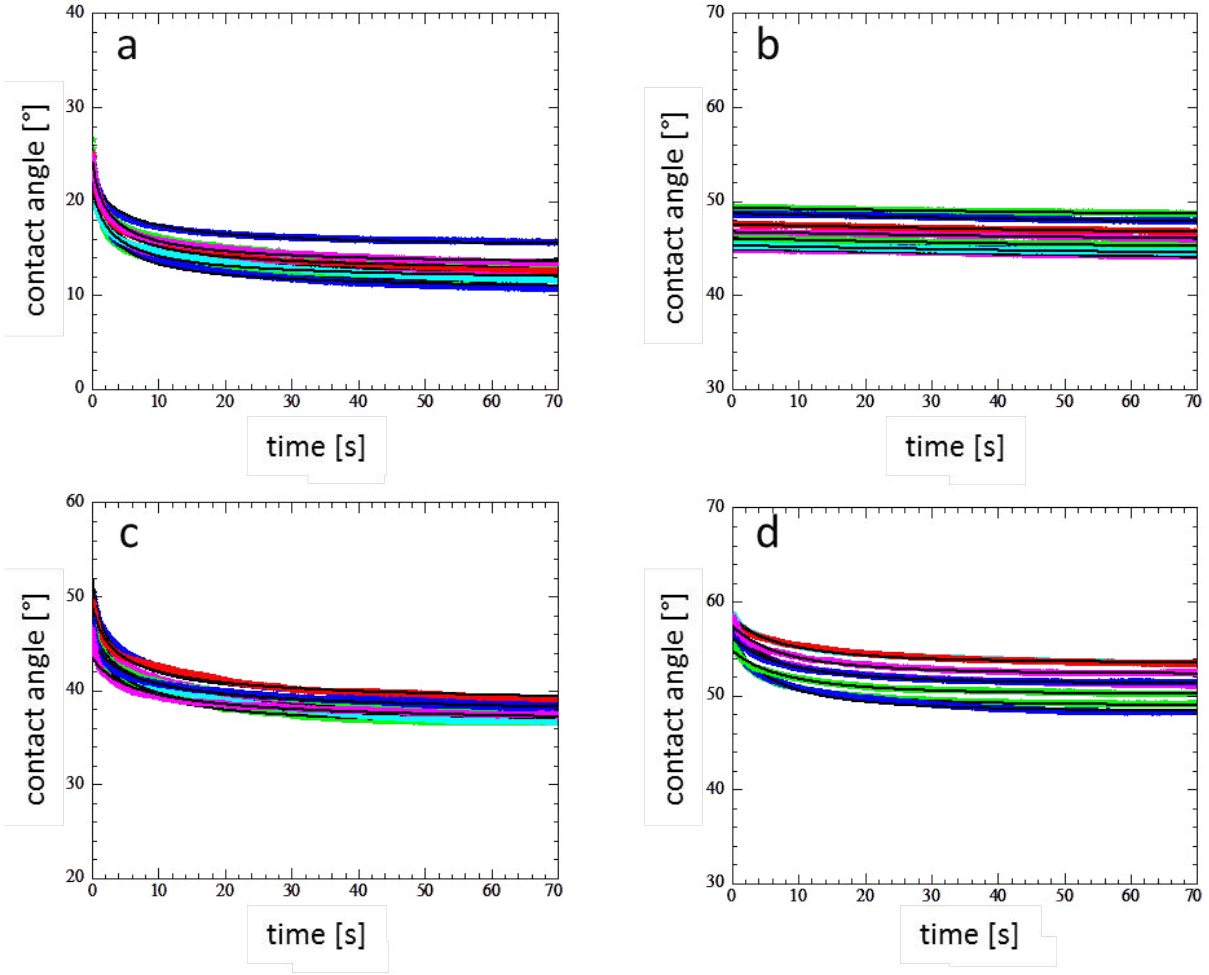

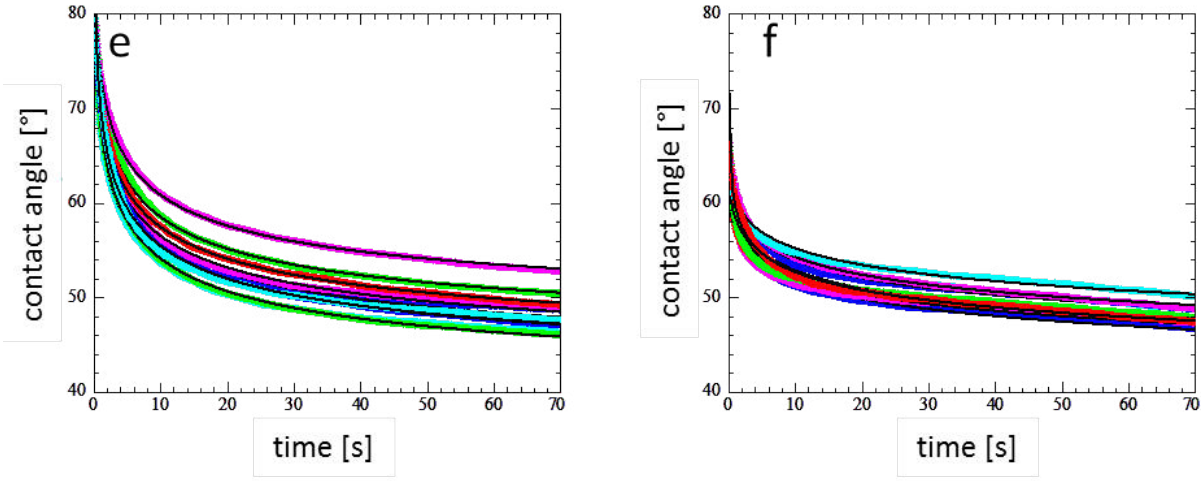

Figure A.2.: Time dependent contact angles of the different test liquids: a) paraffin oil, b) diiodomethane, c) ethylene glycol, d) formamide, e) glycerol and f) water on titania. The colored symbols represent the measured data, the black solid lines the corresponding fits.

Bibliography

[1] J. Comyn, *Adhesion Science, RSC Paperbacks*. The Royal Society of Chemistry, 1997.

[2] P. Spencer, Q. Ye, J. Park, R. Parthasarathy, O. Marangos, A. Misra, B. S. Bohaty, V. Singh, and J. S. Laurence, "Dentin/adhesive interface in teeth," in *Structural Interfaces and Attachments in Biology*, pp. 133–151, Springer, 2013.

[3] P. Müller-Buschbaum, T. Ittner, E. Maurer, V. Körstgens, and W. Petry, "Pressure-sensitive adhesive blend films for low-tack applications," *Macromolecular Materials and Engineering*, vol. 292, no. 7, pp. 825–834, 2007.

[4] C. Creton, "Pressure-sensitive adhesives: An introductory course," *MRS Bulletin*, vol. 28, pp. 434–439, 2003.

[5] R.-z. Chen, R.-m. Cheng, G.-q. Li, Y.-d. Liu, Y.-w. Chen, and X.-c. Xu, "Study on preparation and properties of uv curing polyacrylate pressure-sensitive adhesive," *China Adhesives*, vol. 15, no. 8, p. 28, 2006.

[6] A. B. Foster, P. A. Lovell, and M. A. Rabjohns, "Control of adhesive properties through structured particle design of water-borne pressure-sensitive adhesives," *Polymer*, vol. 50, no. 7, pp. 1654–1670, 2009.

[7] C. W. Hock, "The morphology of pressure-sensitive adhesive films," in *Journal of Polymer Science Part C: Polymer Symposia*, vol. 3, pp. 139–149, Wiley Online Library, 1963.

[8] Z. Czech, A. Kowalczyk, J. Kabatc, and J. Świderska, "Uv-crosslinkable acrylic pressure-sensitive adhesives for industrial application," *Polymer bulletin*, vol. 69, no. 1, pp. 71–80, 2012.

[9] C. C. Anderson, "Adhesives, 1969," *Industrial & Engineering Chemistry*, vol. 61, no. 8, pp. 48–52, 1969.

[10] E. Maurer, S. Loi, D. Wulff, N. Willenbacher, and P. Müller-Buschbaum, "Microscopic structure in pressure sensitive adhesives: an ultrasmall angle x-ray study," *Physica B: Condensed Matter*, vol. 357, no. 1, pp. 144–147, 2005.

[11] A. Lindner, T. Maevis, R. Brummer, B. Lühmann, and C. Creton, "Subcritical failure of soft acrylic adhesives under tensile stress," *Langmuir*, vol. 20, no. 21, pp. 9156–9169, 2004.

[12] Y. Peykova, S. Guriyanova, O. V. Lebedeva, A. Diethert, P. Müller-Buschbaum, and N. Willenbacher, "The effect of surface roughness on adhesive properties of acrylate copolymers," *International Journal of Adhesion and Adhesives*, vol. 30, no. 4, pp. 245–254, 2010.

[13] A. Diethert and P. Müller-Buschbaum, "Probing the near-surface composition profile of pressure sensitive adhesive films with x-ray reflectivity," *The Journal of Adhesion*, vol. 87, no. 12, pp. 1167–1190, 2011.

[14] A. J. Kinloch, *Adhesion and adhesives: science and technology*. Springer, 1987.

[15] H.-J. Butt, K. Graf, and M. Kappl, *Physics and Chemistry of Interfaces*. Wiley-VCH, 2003.

[16] D. Henderson, D.-M. Duh, X. Chu, and D. Wasan, "An expression for the dispersion force between colloidal particles," *Journal of Colloid and Interface Science*, vol. 185, pp. 265–268, 1997.

[17] C. Kittel, *Einführung in die Festkörperphysik*. Oldenbourg Verlag, 2013.

[18] J. N. Israelachvili, *Intermolecular and Surface Forces*. Academic Press, 2011.

[19] H. Y. Erbil, *Surface Chemistry of Solid Liquid Interface*. Blackwell Publishing, 2006.

[20] L. Sharpe and H. Schonhorn, "Contact angle, wettability and adhesion," *ACS Series*, no. 43, p. 189, 1964.

[21] P. de Gennes, "Wetting: Statics and dynamics," *Reviews of Modern Physics*, vol. 57, pp. 827–863, 1985.

[22] M. Geoghegan and G. Krausch, "Wetting at polymer surface and interfaces," *Progress in Polymer Science*, vol. 28, pp. 261–302, 2003.

[23] A. Neumann, D. Renzow, H. Reumuth, and I. E. Richter, "Der einfluss der rauhigkeit auf die benetzung," *Fortschrittsberichte über Kolloide und Polymere*, vol. 55, no. 1, pp. 49–54, 1971.

[24] V. W. Funke, G. Hellwig, and A. Neumann, "Bestimmung der einfriertemperatur von polymeren aus der temperaturabhängigkeit der benetzung," *Die Angewandte Makromolekulare Chemie*, vol. 8, no. 1, pp. 185–193, 1969.

[25] D. K. Owens and R. Wendt, "Estimation of the surface free energy of polymers," *Journal of applied polymer science*, vol. 13, no. 8, pp. 1741–1747, 1969.

[26] F. M. Fowkes, "Attractive forces at interfaces," *Industrial & Engineering Chemistry*, vol. 56, no. 12, pp. 40–52, 1964.

[27] D. A. Dillard, A. V. Pocius, and M. Chaudhury, *Adhesion Science and Engineering: Vol.1 The Mechanics of Adhesion*. Elsevier Science, 2002.

[28] G. Strobl, *The Physics of Polymers*. Springer, 2007.

[29] J. Dealy and D. Plazek, "Time-temperature superposition—a users guide," *Rheol. Bull*, vol. 78, no. 2, pp. 16–31, 2009.

[30] A. J. Crosby, K. R. Shull, H. Lakrout, and C. Creton, "Deformation and failure modes of adhesively bonded elastic layers," *Journal of Applied Physics*, vol. 88, no. 5, pp. 2956–2966, 2000.

[31] A. S. Cantor, "Glass transition temperatures of hydrocarbon blends: Adhesives measured by differential scanning calorimetry and dynamic mechanical analysis," *Journal of applied polymer science*, vol. 77, no. 4, pp. 826–832, 2000.

[32] I. González, J. R. Leiza, and J. Asua, "Exploring the limits of branching and gel content in the emulsion polymerization of n-ba," *Macromolecules*, vol. 39, no. 15, pp. 5015–5020, 2006.

[33] H. Mizumachi, "Theory of tack of pressure sensitive adhesive. i," *Journal of applied polymer science*, vol. 30, no. 6, pp. 2675–2686, 1985.

[34] D. Kaelble, "Theory and analysis of peel adhesion: adhesive thickness effects," *The Journal of Adhesion*, vol. 37, no. 1-3, pp. 205–214, 1992.

[35] N. Amouroux, J. Petit, and L. Léger, "Role of interfacial resistance to shear stress on adhesive peel strength," *Langmuir*, vol. 17, no. 21, pp. 6510–6517, 2001.

[36] A. Falsafi, F. S. Bates, and M. Tirrell, "Role of chain architecture in the adhesion of block copolymers," *Macromolecules*, vol. 34, no. 5, pp. 1323–1327, 2001.

[37] A. Agirre, J. Nase, E. Degrandi, C. Creton, and J. M. Asua, "Improving adhesion of acrylic waterborne psas to low surface energy materials: Introduction of stearyl acrylate," *Journal of Polymer Science Part A: Polymer Chemistry*, vol. 48, no. 22, pp. 5030–5039, 2010.

[38] A. Zosel, "The effect of fibrilation on the tack of pressure sensitive adhesives," *International journal of adhesion and adhesives*, vol. 18, no. 4, pp. 265–271, 1998.

[39] R. H. Plaut, N. L. Williams, and D. A. Dillard, "Elastic analysis of the loop tack test for pressure sensitive adhesives," *The Journal of Adhesion*, vol. 76, no. 1, pp. 37–53, 2001.

[40] K. Kamagata, T. Saito, and M. Toyama, "The methods of measuring tackiness of pressure sensitive adhesive tapes," *Journal of Adhesion*, vol. 2, pp. 279–291, 1970.

[41] Z. Miyagi and K. Yamamoto, "Viscoelastic analysis of shear adhesion test for pressure-sensitive adhesive tape," *The Journal of Adhesion*, vol. 21, no. 3-4, pp. 243–250, 1987.

[42] J. P. Phillips, X. Deng, R. R. Stephen, E. L. Fortenberry, M. L. Todd, D. M. McClusky, S. Stevenson, R. Misra, S. Morgan, and T. E. Long, "Nano-and bulk-tack adhesive properties of stimuli-responsive, fullerene-polymer blends containing polystyrene-block-polybutadiene-block-polystyrene and polystyrene-block-polyisoprene-block-polystyrene rubber-based adhesives," *Polymer*, vol. 48, no. 23, pp. 6773–6781, 2007.

[43] X. Wang, X. Xiao, and O. Tsui, "Surface viscoelasticity studies of ultrathin polymer films using atomic force microscopic adhesion measurements," *Macromolecules*, vol. 34, no. 12, pp. 4180–4185, 2001.

[44] B. N. Balzer, M. Gallei, K. Sondergeld, M. Schindler, P. Müller-Buschbaum, M. Rehahn, and T. Hugel, "Cohesion mechanisms of polystyrene-based thin polymer films," *Macromolecules*, vol. 46, no. 18, pp. 7406–7414, 2013.

[45] C. Creton and H. Lakrout, "Micromechanics of flat-probe adhesion tests of soft viscoelastic polymer films," *Journal of Polymer Science Part B: Polymer Physics*, vol. 38, no. 7, pp. 965–979, 2000.

[46] R. E. Webber, K. R. Shull, A. Roos, and C. Creton, "Effects of geometric confinement on the adhesive debonding of soft elastic solids," *Physical Review E*, vol. 68, no. 2, p. 021805, 2003.

[47] A. Gent, "Compression of rubber blocks," *Rubber chemistry and technology*, vol. 67, no. 3, pp. 549–558, 1994.

[48] H. Lakrout, P. Sergot, and C. Creton, "Direct observation of cavitation and fibrillation in a probe tack experiment on model acrylic pressure-sensitive-adhesives," *The Journal of Adhesion*, vol. 69, no. 3-4, pp. 307–359, 1999.

[49] C. Creton, "Testing soft adhesives with the butt joint geometry," *Proceedings of Swiss Bonding*, 2002.

[50] K. R. Shull and C. Creton, "Deformation behavior of thin, compliant layers under tensile loading conditions," *Journal of Polymer Science Part B: Polymer Physics*, vol. 42, no. 22, pp. 4023–4043, 2004.

[51] I. Chikina and C. Gay, "Cavitation in adhesives," *Physical review letters*, vol. 85, no. 21, p. 4546, 2000.

[52] T. Yamaguchi, H. Morita, and M. Doi, "Modeling on debonding dynamics of pressure-sensitive adhesives," *The European Physical Journal E: Soft Matter and Biological Physics*, vol. 20, no. 1, pp. 7–17, 2006.

[53] C. Creton, J. Hooker, and K. R. Shull, "Bulk and interfacial contributions to the debonding mechanisms of soft adhesives: extension to large strains," *Langmuir*, vol. 17, no. 16, pp. 4948–4954, 2001.

[54] U. Gedde, *Polymer physics*. Springer, 1995.

[55] G. R. Strobl, *The physics of polymers*, vol. 2. Springer, 1997.

[56] A. D. McNaught and A. Wilkinson, *Compendium of chemical terminology*, vol. 1669. Blackwell Science Oxford, 1997.

[57] G. H. Fredrickson and S. T. Milner, "Thermodynamics of random copolymer melts," *Physical review letters*, vol. 67, no. 7, pp. 835–838, 1991.

[58] T. A. Albahri, "Accurate prediction of the solubility parameter of pure compounds from their molecular structures," *Fluid Phase Equilibria*, 2014.

[59] A. F. Barton, *CRC handbook of solubility parameters and other cohesion parameters*. CRC press, 1991.

[60] J. Brandrup, E. H. Immergut, E. A. Grulke, A. Abe, and D. R. Bloch, *Polymer handbook*, vol. 89. Wiley New York, 1999.

[61] J. H. Hildebrand and R. L. Scott, *The solubility of nonelectrolytes*. Reinhold Pub. Corp., 1950.

[62] G. Scatchard, "Equilibria in non-electrolyte solutions in relation to the vapor pressures and densities of the components.," *Chemical Reviews*, vol. 8, no. 2, pp. 321–333, 1931.

[63] M. Tolan, *X-ray scattering from soft-matter thin films*. Springer, 1999.

[64] G. Renaud, R. Lazzari, and F. Leroy, "Probing surface and interface morphology with grazing incidence small angle x-ray scattering," *Surface Science Reports*, vol. 64, no. 8, pp. 255–380, 2009.

[65] F. Abelès, "Les applications des couches minces en polarimétrie," *Le Journal de physique et le radium*, vol. 11, p. 403, 1950.

[66] L. G. Parratt, "Surface studies of solids by total reflection of x-rays," *Physical review*, vol. 95, no. 2, pp. 359–369, 1954.

[67] F. El Feninat, S. Elouatik, T. Ellis, E. Sacher, and I. Stangel, "Quantitative assessment of surface roughness as measured by afm: application to polished human dentin," *Applied surface science*, vol. 183, no. 3, pp. 205–215, 2001.

[68] L. Nevot and P. Croce, "Caractérisation des surfaces par réflexion rasante de rayons x. application à l'étude du polissage de quelques verres silicates," *Revue de Physique appliquée*, vol. 15, no. 3, pp. 761–779, 1980.

[69] A. Nelson, "Co-refinement of multiple-contrast neutron/X-ray reflectivity data using *MOTOFIT*," *Journal of Applied Crystallography*, vol. 39, pp. 273–276, Apr 2006.

[70] C. Braun, "Parratt32, version 1.6," 2002.

[71] J. A. N. B. C. M. P.A. Kienzle, K.V. O'Donovan, "Ncnr reflectometry software," 08 2014.

[72] M. Björck and G. Andersson, "*GenX*: an extensible X-ray reflectivity refinement program utilizing differential evolution," *Journal of Applied Crystallography*, vol. 40, pp. 1174–1178, Dec 2007.

[73] H. Kiessig, "Interferenz von röntgenstrahlen an dünnen schichten," *Annalen der Physik*, vol. 402, no. 7, pp. 769–788, 1931.

[74] J. Lekner, "Reflection theory and the analysis of neutron reflection data," *Physica B: Condensed Matter*, vol. 173, no. 1, pp. 99–111, 1991.

[75] C. Dyer, Z. Jiang, J. Bozell, T. Rials, W. T. Heller, and M. Dadmun, "Effect of chain structure on the miscibility of cellulose acetate blends: a small-angle neutron scattering study," *Soft Matter*, vol. 9, no. 12, pp. 3402–3411, 2013.

[76] T. Russell, "X-ray and neutron reflectivity for the investigation of polymers," *Materials Science Reports*, vol. 5, no. 4, pp. 171–271, 1990.

[77] M. A. Ruderer and P. Müller-Buschbaum, "Morphology of polymer-based bulk heterojunction films for organic photovoltaics," *Soft Matter*, vol. 7, no. 12, pp. 5482–5493, 2011.

[78] G. Kaune, M. Memesa, R. Meier, M. A. Ruderer, A. Diethert, S. V. Roth, M. D'Acunzi, J. S. Gutmann, and P. Müller-Buschbaum, "Hierarchically structured titania films prepared by polymer/colloidal templating," *ACS applied materials & interfaces*, vol. 1, no. 12, pp. 2862–2869, 2009.

[79] K. Sarkar, C. J. Schaffer, D. M. González, A. Naumann, J. Perlich, and P. Müller-Buschbaum, "Tuning the pore size of zno nano-grids via time-dependent solvent annealing," *Journal of Materials Chemistry A*, vol. 2, no. 19, pp. 6945–6951, 2014.

[80] S. Roth, M. Burghammer, C. Riekel, P. Müller-Buschbaum, A. Diethert, P. Panagiotou, and H. Walter, "Self-assembled gradient nanoparticle-polymer multilayers investigated by an advanced characterization method: microbeam grazing incidence x-ray scattering," *Applied physics letters*, vol. 82, no. 12, pp. 1935–1937, 2003.

[81] P. Müller-Buschbaum, S. Roth, M. Burghammer, A. Diethert, P. Panagiotou, and C. Riekel, "Multiple-scaled polymer surfaces investigated with micro-focus grazing-incidence small-angle x-ray scattering," *EPL (Europhysics Letters)*, vol. 61, no. 5, p. 639, 2003.

[82] P. Müller-Buschbaum, "Grazing incidence small-angle x-ray scattering: an advanced scattering technique for the investigation of nanostructured polymer films," *Analytical and bioanalytical chemistry*, vol. 376, no. 1, pp. 3–10, 2003.

[83] P. Müller-Buschbaum, J. Gutmann, and M. Stamm, "Dewetting of confined polymer films: an x-ray and neutron scattering study," *Physical Chemistry Chemical Physics*, vol. 1, no. 17, pp. 3857–3863, 1999.

[84] P. Müller-Buschbaum, *Structure Determination in Thin Film Geometry Using Grazing Incidence Small-Angle Scattering*, ch. Polymer Surfaces and Interfaces: Characterization, Modification and Applications, pp. 17–46. Springer Berlin Heidelberg, 2008.

[85] P. Müller-Buschbaum, *Applications of Synchrotron Light to Scattering and Diffraction in Materials and Life Sciences*, vol. 776, ch. A Basic Introduction to Grazing Incidence Small-Angle X-Ray Scattering, pp. 61–89. Springer Berlin Heidelberg, 2009.

[86] R. Lazzari, "Isgisaxs: a program for grazing-incidence small-angle x-ray scattering analysis of supported islands," *Journal of Applied Crystallography*, vol. 35, no. 4, pp. 406–421, 2002.

[87] G. H. Vineyard, "Grazing-incidence diffraction and the distorted-wave approximation for the study of surfaces," *Physical Review B*, vol. 26, no. 8, pp. 4146–4159, 1982.

[88] V. Holỳ and T. Baumbach, "Nonspecular x-ray reflection from rough multilayers," *Physical Review B*, vol. 49, no. 15, pp. 10668–10676, 1994.

[89] S. Sinha, E. Sirota, S. Garoff, and H. Stanley, "X-ray and neutron scattering from rough surfaces," *Physical Review B*, vol. 38, no. 4, pp. 2297–2311, 1988.

[90] Y. Yoneda, "Anomalous surface reflection of x rays," *Physical review*, vol. 131, no. 5, pp. 2010–2013, 1963.

[91] H. Dosch, B. Batterman, and D. Wack, "Depth-controlled grazing-incidence diffraction of synchrotron x radiation," *Physical review letters*, vol. 56, no. 11, p. 1144, 1986.

[92] M. Bass, E. W. Van Stryland, D. R. Williams, and W. L. Wolfe, *Handbook of optics*, vol. 2. McGraw-Hill, 2001.

[93] P. West, *Introduction to Atomic Force Microscopy: Theory, Practice, Applications*. P. West, 2006.

[94] F. J. Giessibl, "Advances in atomic force microscopy," *Reviews of modern physics*, vol. 75, no. 3, p. 949, 2003.

[95] H. Schonhorn and R. Hansen, "Surface treatment of polymers for adhesive bonding," *Journal of Applied Polymer Science*, vol. 11, no. 8, pp. 1461–1474, 1967.

[96] E. B. Dismukes, "The effect of drop size on the accuracy of surface tension determinations by the sessile drop method.," *The Journal of Physical Chemistry*, vol. 63, no. 2, pp. 312–314, 1959.

[97] T. Menke, Z. Funke, R.-D. Maier, and J. Kressler, "Surface tension measurements on ethene-butene random copolymers and different polypropenes," *Macromolecules*, vol. 33, no. 16, pp. 6120–6125, 2000.

[98] H. Y. Erbil and R. A. Meric, "Evaporation of sessile drops on polymer surfaces: Ellipsoidal cap geometry," *The Journal of Physical Chemistry B*, vol. 101, no. 35, pp. 6867–6873, 1997.

[99] A. Diethert, K. Ecker, Y. Peykova, N. Willenbacher, and P. Müller-Buschbaum, "Tailoring the near-surface composition profiles of pressure-sensitive adhesive films and the resulting mechanical properties," *ACS applied materials & interfaces*, vol. 3, no. 6, pp. 2012–2021, 2011.

[100] A. M. van den Berg, P. J. Smith, J. Perelaer, W. Schrof, S. Koltzenburg, and U. S. Schubert, "Inkjet printing of polyurethane colloidal suspensions," *Soft Matter*, vol. 3, no. 2, pp. 238–243, 2007.

[101] D. Clemens, P. Gross, P. Keller, N. Schlumpf, and M. Könnecke, "Amor–the versatile reflectometer at sinq," *Physica B: Condensed Matter*, vol. 276, pp. 140–141, 2000.

[102] M. Gupta, T. Gutberlet, J. Stahn, P. Keller, and D. Clemens, "Amor—the time-of-flight neutron reflectometer at sinq/psi," *Pramana*, vol. 63, no. 1, pp. 57–63, 2004.

[103] R. Campbell, H. Wacklin, I. Sutton, R. Cubitt, and G. Fragneto, "Figaro: The new horizontal neutron reflectometer at the ill," *The European Physical Journal Plus*, vol. 126, no. 11, pp. 1–22, 2011.

[104] S. Roth, G. Herzog, V. Körstgens, A. Buffet, M. Schwartzkopf, J. Perlich, M. A. Kashem, R. Döhrmann, R. Gehrke, A. Rothkirch, K. Stassig, W. Wurth, G. Benecke, C. Li, P. Fratzl, M. Rawolle, and P. Müller-Buschbaum, "In situ observation of cluster formation during nanoparticle solution casting on a colloidal film," *Journal of Physics: Condensed Matter*, vol. 23, no. 25, p. 254208, 2011.

[105] A. Buffet, A. Rothkirch, R. Dohrmann, V. Körstgens, M. M. Abul Kashem, J. Perlich, G. Herzog, M. Schwartzkopf, R. Gehrke, P. Müller-Buschbaum, and S. V. Roth, "P03, the microfocus and nanofocus x-ray scattering (minaxs) beamline of the petra iii storage ring: the microfocus endstation," *Journal of synchrotron radiation*, vol. 19, no. 4, pp. 647–653, 2012.

[106] G. Benecke, "https://dpdak.desy.de/," 2014.

[107] R. Kampmann, M. Haese-Seiller, V. Kudryashov, V. Deriglazov, M. Tristl, C. Daniel, B. Toperverg, A. Schreyer, and E. Sackmann, "The potential of the horizontal reflectometer refsans/frm-ii for measuring low reflectivity and diffuse surface scattering," *Physica B: Condensed Matter*, vol. 350, no. 1, pp. E763–E766, 2004.

[108] R. Kampmann, M. Haese-Seiller, V. Kudryashov, B. Nickel, C. Daniel, W. Fenzl, A. Schreyer, E. Sackmann, and J. Raedler, "Horizontal tof-neutron reflectometer refsans at frm-ii munich/germany: First tests and status," *Physica B: Condensed Matter*, vol. 385, pp. 1161–1163, 2006.

[109] L. A. Cannon and R. A. Pethrick, "Effect of the glass-transition temperature on film formation in 2-ethylhexyl acrylate/methyl methacrylate emulsion copolymers," *Macromolecules*, vol. 32, pp. 7617–7629, 1999.

[110] A. Aymonier, E. Papon, J.-J. Villenave, P. Tordjeman, R. Pirri, and P. Gérard, "Design of pressure-sensitive adhesives by free-radical emulsion copolymerization of methyl methacrylate and 2-ethylhexyl acrylate. 1. kinetic study and tack properties," *Chemistry of materials*, vol. 13, no. 8, pp. 2562–2566, 2001.

[111] F. Sauzedde and D. Hunkeler, "Determination of the composition of statistical copolymers by liquid chromatography under limiting conditions of adsorption," *International Journal of Polymer Analysis and Characterization*, vol. 6, no. 3-4, pp. 295–314, 2001.

[112] A. Sharma and G. Reiter, "Instability of thin polymer films on coated substrates: rupture, dewetting, and drop formation," *Journal of colloid and interface science*, vol. 178, no. 2, pp. 383–399, 1996.

[113] J. Forrest, K. Dalnoki-Veress, J. Stevens, and J. Dutcher, "Effect of free surfaces on the glass transition temperature of thin polymer films," *Physical review letters*, vol. 77, no. 10, p. 2002, 1996.

[114] D. Delarios and B. Deal, "Effect of silicon surface cleaning procedures on oxidation kinetics and surface chemistry," *Applied Surf*, vol. 30, pp. 17–24, 1987.

[115] M. Weldon, V. Marisco, Y. Chabal, D. Hamann, S. Christman, and E. Chaban, "Infrared spectroscopy as a probe of fundamental processes in microelectronics: silicon wafer cleaning and bonding," *Surface Science*, vol. 368, pp. 163–178, 1996.

[116] W. Kern, "The evolution of silicon wafer cleaning technology," *Journal of the Electrochemical Society*, vol. 137, no. 6, pp. 1887–1892, 1990.

[117] P. Müller-Buschbaum, "Influence of surface cleaning on dewetting of thin polystyrene films," *The European Physical Journal E: Soft Matter and Biological Physics*, vol. 12, no. 3, pp. 443–448, 2003.

[118] W. Kern, ed., *Handbook of Semiconductor Wafer Cleaning Technology*. Noyes Publications, 1993.

[119] H. Walter, C. Harrats, P. Müller-Buschbaum, R. Jérôme, and M. Stamm, "Adsorption of ampholytic diblock copolymers from dilute aqueous solution at the solid/liquid interface," *Langmuir*, vol. 15, no. 4, pp. 1260–1267, 1999.

[120] D. Schubert, "Spin coating as a method for polymer molecular weight determination," *Polymer bulletin*, vol. 38, no. 2, pp. 177–184, 1997.

[121] T. Thurn-Albrecht, J. Schotter, G. Kästle, N. Emley, T. Shibauchi, L. Krusin-Elbaum, K. Guarini, C. Black, M. Tuominen, and T. Russell, "Ultrahigh-density nanowire arrays grown in self-assembled diblock copolymer templates," *Science*, vol. 290, no. 5499, pp. 2126–2129, 2000.

[122] C. Black, C. Murray, R. Sandstrom, and S. Sun, "Spin-dependent tunneling in self-assembled cobalt-nanocrystal superlattices," *Science*, vol. 290, no. 5494, pp. 1131–1134, 2000.

[123] C. Sanchez, B. Julian, P. Belleville, and M. Popall, "Applications of hybrid organic–inorganic nanocomposites," *Journal of Materials Chemistry*, vol. 15, no. 35-36, pp. 3559–3592, 2005.

[124] C. Sanchez and B. Lebeau, "Design and properties of hybrid organic–inorganic nanocomposites for photonics," *Mrs Bulletin*, vol. 26, no. 05, pp. 377–387, 2001.

[125] S. Roth, H. Walter, M. Burghammer, C. Riekel, B. Lengeler, C. Schroer, M. Kuhlmann, T. Walther, A. Sehrbrock, R. Domnick, and P. Müller-Buschbaum, "Combinatorial investigation of the isolated nanoparticle to coalescent layer transition in a gradient sputtered gold nanoparticle layer on top of polystyrene," *Applied physics letters*, vol. 88, no. 2, p. 021910, 2006.

[126] V. Zaporojtchenko, K. Behnke, A. Thran, T. Strunskus, and F. Faupel, "Condensation coefficients and initial stages of growth for noble metals deposited onto chemically different polymer surfaces," *Applied surface science*, vol. 144, pp. 355–359, 1999.

[127] A. Giahi, M. El Alaoui Faris, P. Bassereau, and T. Salditt, "Active membranes studied by x-ray scattering," *The European Physical Journal E: Soft Matter and Biological Physics*, vol. 23, no. 4, pp. 431–437, 2007.

[128] M. J. Leonard and H. H. Strey, "Phase diagrams of stoichiometric polyelectrolyte-surfactant complexes," *Macromolecules*, vol. 36, no. 25, pp. 9549–9558, 2003.

[129] D. R. Lide, *CRC handbook of chemistry and physics*. CRC press, 2004.

[130] A. Wexler and S. Hasegawa, "Relative humidity-temperature relationships of some saturated salt solutions in the temperature range 0 to 50 °c," *Journal of Research of the National Bureau of Standards*, vol. 53, no. 1, pp. 19–26, 1954.

[131] J.-K. Chen, F.-H. Ko, K.-F. Hsieh, C.-T. Chou, and F.-C. Chang, "Effect of fluoroalkyl substituents on the reactions of alkylchlorosilanes with mold surfaces for nanoimprint lithography," *Journal of Vacuum Science & Technology B*, vol. 22, no. 6, pp. 3233–3241, 2004.

[132] M. A. Ruderer, S. Guo, R. Meier, H.-Y. Chiang, V. Körstgens, J. Wiedersich, J. Perlich, S. V. Roth, and P. Müller-Buschbaum, "Solvent-induced morphology in polymer-based systems for organic photovoltaics," *Advanced Functional Materials*, vol. 21, no. 17, pp. 3382–3391, 2011.

[133] F. Teles and L. Fonseca, "Applications of polymers for biomolecule immobilization in electrochemical biosensors," *Materials Science and Engineering: C*, vol. 28, no. 8, pp. 1530–1543, 2008.

[134] E. Kress-Rogers, *Handbook of biosensors and electronic noses: medicine, food, and the environment*. CRC Press, 1996.

[135] S. N. Gorb, M. Sinha, A. Peressadko, K. A. Daltorio, and R. D. Quinn, "Insects did it first: a micropatterned adhesive tape for robotic applications," *Bioinspiration & biomimetics*, vol. 2, no. 4, p. S117, 2007.

[136] A. Diethert, Y. Peykova, N. Willenbacher, and P. Muller-Buschbaum, "Near-surface composition profiles and the adhesive properties of statistical copolymer films being model systems of pressure sensitive adhesive films," *ACS Applied Materials & Interfaces*, vol. 2, no. 7, pp. 2060–2068, 2010.

[137] J. Class and S. Chu, "The viscoelastic properties of rubber–resin blends. i. the effect of resin structure," *Journal of applied polymer science*, vol. 30, no. 2, pp. 805–814, 1985.

[138] C. Galan, C. Sierra, J. Fatou, and J. Delgado, "A hot-melt pressure-sensitive adhesive based on styrene–butadiene–styrene rubber. the effect of adhesive composition on the properties," *Journal of applied polymer science*, vol. 62, no. 8, pp. 1263–1275, 1996.

[139] G. Kraus and T. Hashimoto, "Structural changes in melts of butadiene–styrene and isoprene–styrene block polymer-based pressure-sensitive adhesives," *Journal of Applied Polymer Science*, vol. 27, no. 5, pp. 1745–1757, 1982.

[140] A. Aymonier, E. Papon, G. Castelein, M. Brogly, and P. Tordjeman, "Influence of surface and bulk structures of acrylic psa films onto their tack properties," *Journal of colloid and interface science*, vol. 268, no. 2, pp. 341–347, 2003.

[141] A. Marcais, E. Papon, J.-J. Villenave, P. Tordjeman, R. Pirri, and P. Gerard, "Tack properties of methyl methacrylate and 2-ethylhexyl acrylate emulsion copolymers: influence of the polymerisation process," in *Macromolecular Symposia*, vol. 151, pp. 497–502, Wiley Online Library, 2000.

[142] A. Aymonier, D. Leclercq, P. Tordjeman, E. Papon, and J.-J. Villenave, "Control of structure and tack properties of acrylic pressure-sensitive adhesives designed by a polymerization process," *Journal of applied polymer science*, vol. 89, no. 10, pp. 2749–2756, 2003.

[143] F. González Garcia, B. G. Soares, M. E. Leyva, and A. Z. Simões, "Influence of aliphatic amine epoxy hardener on the adhesive properties of blends of mono-carboxyl-terminated poly (2-ethylhexyl acrylate-co-methyl methacrylate) with epoxy resin," *Journal of applied polymer science*, vol. 117, no. 5, pp. 2762–2770, 2010.

[144] M. Koller, "Controlling adhesion via surface enrichment," 2013.

[145] F. Jarisch, "Controlling adhesion via relative humidity," 2014.

[146] M. Schindler, A. Kriele, and P. Müller-Buschbaum, "Reorganization of the near-surface composition in pressure sensitive adhesive films stored in nitrogen atmosphere," *The Journal of Adhesion*, vol. 88, pp. 684–698, 2012.

[147] M. Schindler, S. Pröller, T. Geue, and P. Müller-Buschbaum, "Near-interface composition in pressure sensitive adhesives at the adhesive–adherent interface," *Macromolecular Reaction Engineering*, vol. 7, no. 10, pp. 549–554, 2013.

[148] S. Rokhlin and D. Marom, "Study of adhesive bonds using low-frequency obliquely incident ultrasonic waves," *The Journal of the Acoustical Society of America*, vol. 80, no. 2, pp. 585–590, 1986.

[149] S. Rokhlin, A. Lavrentyev, and B. Li, "Ultrasonic evaluation of environmental durability of adhesive joints," *Research in Nondestructive Evaluation*, vol. 5, no. 2, pp. 95–109, 1993.

[150] P. Boinard, R. Pethrick, W. Banks, and R. Crane, "Non destructive evaluation of adhesively bonded composite structures using high frequency dielectric spectroscopy," *Journal of materials science*, vol. 35, no. 6, pp. 1331–1337, 2000.

[151] R. Hosemann and S. Bagchi, *Direct analysis of diffraction by matter*. North-Holland Publishing Company Amsterdam, 1962.

[152] J. Brandrup, E. H. Immergut, and E. A. Grulke, *Polymer Handbook*. Wiley-Interscience, 4 ed., 1999.

[153] D. Kwok, A. Leung, C. Lam, A. Li, R. Wu, and A. Neumann, "Low-rate dynamic contact angles on poly (methyl methacrylate) and the determination of solid surface tensions," *Journal of colloid and interface science*, vol. 206, no. 1, pp. 44–51, 1998.

[154] S. R. Da Rocha, K. L. Harrison, and K. P. Johnston, "Effect of surfactants on the interfacial tension and emulsion formation between water and carbon dioxide," *Langmuir*, vol. 15, no. 2, pp. 419–428, 1999.

[155] J. P. Donley and G. H. Fredrickson, "Properties of random multiblock copolymer melts near surfaces," *Macromolecules*, vol. 27, no. 2, pp. 458–467, 1994.

[156] J. M. PigŁowski and M. Bryjak, "Surface studies of poly (methyl methacrylate)/poly (styrene-co-acrylonitrile) blends," *European polymer journal*, vol. 34, no. 11, pp. 1669–1673, 1998.

[157] C. Creton and P. Fabre, "Tack," *Adhesion science and engineering*, vol. 1, pp. 535–576, 2002.

[158] A. J. Nolte, N. D. Treat, R. E. Cohen, and M. F. Rubner, "Effect of relative humidity on the young's modulus of polyelectrolyte multilayer films and related nonionic polymers," *Macromolecules*, vol. 41, no. 15, pp. 5793–5798, 2008.

[159] R. Levicky, T. M. Herne, M. J. Tarlov, and S. K. Satija, "Using self-assembly to control the structure of dna monolayers on gold: a neutron reflectivity study," *Journal of the American Chemical Society*, vol. 120, no. 38, pp. 9787–9792, 1998.

[160] Q. Zhong, E. Metwalli, G. Kaune, M. Rawolle, A. M. Bivigou-Koumba, A. Laschewsky, C. M. Papadakis, R. Cubitt, and P. Müller-Buschbaum, "Switching kinetics of thin thermo-responsive hydrogel films of poly (monomethoxy-diethyleneglycol-acrylate) probed with in situ neutron reflectivity," *Soft Matter*, vol. 8, no. 19, pp. 5241–5249, 2012.

[161] P.-W. Yang, T.-L. Lin, I.-T. Liu, Y. Hu, and M. James, "In situ neutron reflectivity studies of the adsorption of dna by charged diblock copolymer monolayers at the air–water interface," *Soft Matter*, vol. 8, no. 27, pp. 7161–7168, 2012.

[162] A. Diethert, E. Metwalli, R. Meier, Q. Zhong, R. A. Campbell, R. Cubitt, and P. Müller-Buschbaum, "In situ neutron reflectometry study of the near-surface solvent concentration profile during solution casting," *Soft Matter*, vol. 7, no. 14, pp. 6648–6659, 2011.

[163] R. Wool and K. O'connor, "A theory crack healing in polymers," *Journal of Applied Physics*, vol. 52, no. 10, pp. 5953–5963, 1981.

[164] Y. M. Boiko and R. E. Prud'Homme, "Bonding at symmetric polymer/polymer interfaces below the glass transition temperature," *Macromolecules*, vol. 30, no. 12, pp. 3708–3710, 1997.

[165] Y. M. Boiko and R. E. Prud'Homme, "Strength development at the interface of amorphous polymers and their miscible blends, below the glass transition temperature," *Macromolecules*, vol. 31, no. 19, pp. 6620–6626, 1998.

[166] J. Arnold, "The effects of diffusion on environmental stress crack initiation in pmma," *Journal of materials science*, vol. 33, no. 21, pp. 5193–5204, 1998.

[167] Y. M. Boiko, "Autoadhesion of glassy polymers," in *Macromolecular Symposia*, vol. 316, pp. 71–78, Wiley Online Library, 2012.

[168] L. Smith and V. Schmitz, "The effect of water on the glass transition temperature of poly (methyl methacrylate)," *Polymer*, vol. 29, no. 10, pp. 1871–1878, 1988.

[169] D. T. Wu, G. H. Fredrickson, J.-P. Carton, A. Ajdari, and L. Leibler, "Distribution of chain ends at the surface of a polymer melt: compensation effects and surface tension," *Journal of Polymer Science Part B: Polymer Physics*, vol. 33, no. 17, pp. 2373–2389, 1995.

[170] J. Mallegol, O. Dupont, and J. Keddie, "Morphology and elasticity of waterborne acrylic pressure-sensitive adhesives investigated with atomic force microscopy," *Journal of adhesion science and technology*, vol. 17, no. 2, pp. 243–259, 2003.

[171] E. Canetta and A. K. Adya, "Atomic force microscopic investigation of commercial pressure sensitive adhesives for forensic analysis," *Forensic science international*, vol. 210, no. 1, pp. 16–25, 2011.

[172] P. Müller-Buschbaum, L. Schulz, E. Metwalli, J.-F. Moulin, and R. Cubitt, "Lateral structures of buried interfaces in aba-type triblock copolymer films," *Langmuir*, vol. 24, no. 15, pp. 7639–7644, 2008.

[173] J. Venables, "Adhesion and durability of metal-polymer bonds," *Journal of Materials Science*, vol. 19, no. 8, pp. 2431–2453, 1984.

[174] J. H. Rose, J. R. Smith, and J. Ferrante, "Universal features of bonding in metals," *Physical Review B*, vol. 28, no. 4, p. 1835, 1983.

[175] A. Higgins, "Adhesive bonding of aircraft structures," *International Journal of Adhesion and Adhesives*, vol. 20, no. 5, pp. 367–376, 2000.

[176] M. Sikorski, "The adhesion of metals and factors that influence it," *Wear*, vol. 7, no. 2, pp. 144–162, 1964.

[177] H. S. Chung, G. H. Park, T. Kim, H. Ahn, D.-H. Kim, and I. Chung, "Synthesis and properties of thermally stable pressure sensitive adhesives for lcd devices," *Molecular Crystals and Liquid Crystals*, vol. 583, no. 1, pp. 43–51, 2013.

[178] G. Gümüssoy, "Investigation of the metal-polymer interactions and their influence on the performance of pressure sensitive adhesives," Master's thesis, TU München, 2012.

[179] H. Chatham, "Oxygen diffusion barrier properties of transparent oxide coatings on polymeric substrates," *Surface and Coatings Technology*, vol. 78, no. 1, pp. 1–9, 1996.

[180] C. Charton, N. Schiller, M. Fahland, A. Holländer, A. Wedel, and K. Noller, "Development of high barrier films on flexible polymer substrates," *Thin Solid Films*, vol. 502, no. 1, pp. 99–103, 2006.

[181] M. D. Rao, "Recent applications of viscoelastic damping for noise control in automobiles and commercial airplanes," *Journal of Sound and Vibration*, vol. 262, no. 3, pp. 457–474, 2003.

[182] A. Zosel, "Adhesion and tack of polymers: Influence of mechanical properties and surface tensions," *Colloid and Polymer Science*, vol. 263, no. 7, pp. 541–553, 1985.

[183] D. V. Kilpadi and J. E. Lemons, "Surface energy characterization of unalloyed titanium implants," *Journal of biomedical materials research*, vol. 28, no. 12, pp. 1419–1425, 1994.

[184] A. Rudawska and E. Jacniacka, "Analysis for determining surface free energy uncertainty by the owen–wendt method," *International Journal of Adhesion and Adhesives*, vol. 29, no. 4, pp. 451–457, 2009.

[185] A. Carre and J. Schultz, "Polymer-aluminium adhesion. i. the surface energy of aluminium in relation to its surface treatment," *The Journal of Adhesion*, vol. 15, no. 2, pp. 151–161, 1983.

[186] L. Boulange-Petermann, B. Baroux, and M.-N. Bellon-Fontaine, "The influence of metallic surface wettability on bacterial adhesion," *Journal of adhesion science and technology*, vol. 7, no. 3, pp. 221–230, 1993.

[187] M. Mantel and J. Wightman, "Influence of the surface chemistry on the wettability of stainless steel," *Surface and Interface analysis*, vol. 21, no. 9, pp. 595–605, 1994.

[188] M. Toyama, T. Ito, H. Nukatsuka, and M. Ikeda, "Studies on tack of pressure-sensitive adhesive tapes: On the relationship between pressure-sensitive adhesion and surface energy of adherends," *Journal of Applied Polymer Science*, vol. 17, no. 11, pp. 3495–3502, 1973.

[189] C. Solliard and M. Flueli, "Surface stress and size effect on the lattice parameter in small particles of gold and platinum," *Surface Science*, vol. 156, pp. 487–494, 1985.

[190] M. K. Bernett and W. Zisman, "Effect of adsorbed water on the critical surface tension of wetting on metal surfaces," *Journal of Colloid and Interface Science*, vol. 28, no. 2, pp. 243–249, 1968.

[191] P. G. Saffman and G. Taylor, "The penetration of a fluid into a porous medium or hele-shaw cell containing a more viscous liquid," *Proceedings of the Royal Society of London. Series A. Mathematical and Physical Sciences*, vol. 245, no. 1242, pp. 312–329, 1958.

[192] A. Chiche, P. Pareige, and C. Creton, "Role of surface roughness in controlling the adhesion of a soft adhesive on a hard surface," *Comptes Rendus de l'Académie des Sciences-Series IV-Physics*, vol. 1, no. 9, pp. 1197–1204, 2000.

[193] N. Kaiser, "Review of the fundamentals of thin-film growth," *Applied optics*, vol. 41, no. 16, pp. 3053–3060, 2002.

[194] G. H. Gilmer and M. H. Grabow, "Models of thin film growth modes," *Journal of Metals*, vol. 39, no. 6, pp. 19–23, 1987.

[195] M. H. Grabow and G. H. Gilmer, "Thin film growth modes, wetting and cluster nucleation," *Surface science*, vol. 194, no. 3, pp. 333–346, 1988.

[196] J. Venables, G. Spiller, and M. Hanbücken, "Nucleation and growth of thin films," *Reports on Progress in Physics*, vol. 47, no. 4, p. 399, 1984.

[197] T. Strunskus, M. Kiene, R. Willecke, A. Thran, C. Bechtolsheim, and F. Faupel, "Chemistry, diffusion and cluster formation at metal-polymer interfaces," *Materials and Corrosion*, vol. 49, no. 3, pp. 180–188, 1998.

[198] J. Kanzow, P. S. Horn, M. Kirschmann, V. Zaporojtchenko, K. Dolgner, F. Faupel, C. Wehlack, and W. Possart, "Formation of a metal/epoxy resin interface," *Applied surface science*, vol. 239, no. 2, pp. 227–236, 2005.

[199] E. Bauer and J. H. van der Merwe, "Structure and growth of crystalline superlattices: From monolayer to superlattice," *Physical Review B*, vol. 33, no. 6, p. 3657, 1986.

[200] J. H. Van der Merwe, "Misfit dislocation generation in epitaxial layers," *Critical Reviews in Solid State and Material Sciences*, vol. 17, no. 3, pp. 187–209, 1991.

[201] G. Kaune, M. A. Ruderer, E. Metwalli, W. Wang, S. Couet, K. Schlage, R. Röhlsberger, S. V. Roth, and P. Müller-Buschbaum, "In situ gisaxs study of gold film growth on conducting polymer films," *ACS applied materials & interfaces*, vol. 1, no. 2, pp. 353–360, 2008.

[202] E. Metwalli, S. Couet, K. Schlage, R. Röhlsberger, V. Körstgens, M. Ruderer, W. Wang, G. Kaune, S. Roth, and P. Müller-Buschbaum, "In situ gisaxs investigation of gold sputtering onto a polymer template," *Langmuir*, vol. 24, no. 8, pp. 4265–4272, 2008.

[203] X. Yang, A. Alexeev, M. A. Michels, and J. Loos, "Effect of spatial confinement on the morphology evolution of thin poly (p-phenylenevinylene)/methanofullerene composite films," *Macromolecules*, vol. 38, no. 10, pp. 4289–4295, 2005.

[204] P. Dannetun, M. Boman, S. Stafström, W. Salaneck, R. Lazzaroni, C. Fredriksson, J. Brédas, R. Zamboni, and C. Taliani, "The chemical and electronic structure of the interface between aluminum and polythiophene semiconductors," *The Journal of chemical physics*, vol. 99, no. 1, pp. 664–672, 1993.

[205] W. U. Huynh, J. J. Dittmer, and A. P. Alivisatos, "Hybrid nanorod-polymer solar cells," *science*, vol. 295, no. 5564, pp. 2425–2427, 2002.

[206] F. Padinger, R. S. Rittberger, and N. S. Sariciftci, "Effects of postproduction treatment on plastic solar cells," *Advanced Functional Materials*, vol. 13, no. 1, pp. 85–88, 2003.

[207] W. Ma, C. Yang, X. Gong, K. Lee, and A. J. Heeger, "Thermally stable, efficient polymer solar cells with nanoscale control of the interpenetrating network morphology," *Advanced Functional Materials*, vol. 15, no. 10, pp. 1617–1622, 2005.

[208] G. Kaune, E. Metwalli, R. Meier, V. Körstgens, K. Schlage, S. Couet, R. Röhlsberger, S. V. Roth, and P. Müller-Buschbaum, "Growth and morphology of sputtered aluminum thin films on p3ht surfaces," *ACS applied materials & interfaces*, vol. 3, no. 4, pp. 1055–1062, 2011.

[209] F. Huang, M. Kief, G. Mankey, and R. Willis, "Magnetism in the few-monolayers limit: A surface magneto-optic kerr-effect study of the magnetic behavior of ultrathin films of co, ni, and co-ni alloys on cu (100) and cu (111)," *Physical Review B*, vol. 49, no. 6, p. 3962, 1994.

[210] J. L. Viovy, D. Beysens, and C. M. Knobler, "Scaling description for the growth of condensation patterns on surfaces," *Physical Review A*, vol. 37, no. 12, p. 4965, 1988.

[211] M. Schwartzkopf, A. Buffet, V. Körstgens, E. Metwalli, K. Schlage, G. Benecke, J. Perlich, M. Rawolle, A. Rothkirch, B. Heidmann, G. Herzog, P. Müller-Buschbaum, R. Röhlsberger, R. Gehrke, N. Stribeck, and S. V. Roth, "From atoms to layers: in situ gold cluster growth kinetics during sputter deposition," *Nanoscale*, vol. 5, no. 11, pp. 5053–5062, 2013.

[212] Z. Ge and S. Liu, "Functional block copolymer assemblies responsive to tumor and intracellular microenvironments for site-specific drug delivery and enhanced imaging performance," *Chemical Society Reviews*, vol. 42, no. 17, pp. 7289–7325, 2013.

[213] Y. Yang, D. Pan, K. Luo, L. Li, and Z. Gu, "Biodegradable and amphiphilic block copolymer–doxorubicin conjugate as polymeric nanoscale drug delivery vehicle for breast cancer therapy," *Biomaterials*, vol. 34, no. 33, pp. 8430–8443, 2013.

[214] S. Mura, J. Nicolas, and P. Couvreur, "Stimuli-responsive nanocarriers for drug delivery," *Nature materials*, vol. 12, no. 11, pp. 991–1003, 2013.

[215] O. B. Ayyub, J. W. Sekowski, T.-I. Yang, X. Zhang, R. M. Briber, and P. Kofinas, "Color changing block copolymer films for chemical sensing of simple sugars," *Biosensors and Bioelectronics*, vol. 28, no. 1, pp. 349–354, 2011.

[216] O. B. Ayyub, M. B. Ibrahim, R. M. Briber, and P. Kofinas, "Self-assembled block copolymer photonic crystal for selective fructose detection," *Biosensors and Bioelectronics*, vol. 46, pp. 124–129, 2013.

[217] J. Qiao, L. Qi, Y. Shen, L. Zhao, C. Qi, D. Shangguan, L. Mao, and Y. Chen, "Thermal responsive fluorescent block copolymer for intracellular temperature sensing," *Journal of Materials Chemistry*, vol. 22, no. 23, pp. 11543–11549, 2012.

[218] M. P. Stoykovich and P. F. Nealey, "Block copolymers and conventional lithography," *Materials Today*, vol. 9, no. 9, pp. 20–29, 2006.

[219] S. Pujari, M. A. Keaton, P. M. Chaikin, and R. A. Register, "Alignment of perpendicular lamellae in block copolymer thin films by shearing," *Soft Matter*, vol. 8, no. 19, pp. 5358–5363, 2012.

[220] M. C. Orilall and U. Wiesner, "Block copolymer based composition and morphology control in nanostructured hybrid materials for energy conversion and storage: solar cells, batteries, and fuel cells," *Chemical Society Reviews*, vol. 40, no. 2, pp. 520–535, 2011.

[221] M. Rawolle, M. A. Niedermeier, G. Kaune, J. Perlich, P. Lellig, M. Memesa, Y.-J. Cheng, J. S. Gutmann, and P. Müller-Buschbaum, "Fabrication and characterization of nanostructured titania films with integrated function from inorganic–organic hybrid materials," *Chemical Society Reviews*, vol. 41, no. 15, pp. 5131–5142, 2012.

[222] R. Krishnan, M. E. Mackay, P. M. Duxbury, A. Pastor, C. J. Hawker, B. Van Horn, S. Asokan, and M. S. Wong, "Self-assembled multilayers of nanocomponents," *Nano letters*, vol. 7, no. 2, pp. 484–489, 2007.

[223] M. Adachi, A. Okumura, E. Sivaniah, and T. Hashimoto, "Incorporation of metal nanoparticles into a double gyroid network texture," *Macromolecules*, vol. 39, no. 21, pp. 7352–7357, 2006.

[224] P. Busch, M. Rauscher, D.-M. Smilgies, D. Posselt, and C. M. Papadakis, "Grazing-incidence small-angle x-ray scattering from thin polymer films with lamellar structures-the scattering cross section in the distorted-wave born approximation," *Journal of applied crystallography*, vol. 39, no. 3, pp. 433–442, 2006.

[225] P. Busch, M. Rauscher, J.-F. Moulin, and P. Muller-Buschbaum, "Debye-scherrer rings from block copolymer films with powder-like order," *Journal of Applied Crystallography*, vol. 44, no. 2, pp. 370–379, 2011.

[226] R. Weidisch, G. Michler, H. Fischer, M. Arnold, S. Hofmann, and M. Stamm, "Mechanical properties of weakly segregated block copolymers: 1. synergism on tensile properties of poly (styrene-b-n-butylmethacrylate) diblock copolymers," *Polymer*, vol. 40, no. 5, pp. 1191–1199, 1999.

[227] H. Fischer, R. Weidisch, M. Stamm, H. Budde, and S. Höring, "The phase diagram of the system poly (styrene-block-n-butyl methacrylate)," *Colloid and Polymer Science*, vol. 278, no. 11, pp. 1019–1031, 2000.

[228] Z. Di, D. Posselt, D.-M. Smilgies, and C. M. Papadakis, "Structural rearrangements in a lamellar diblock copolymer thin film during treatment with saturated solvent vapor," *Macromolecules*, vol. 43, no. 1, pp. 418–427, 2009.

[229] C. M. Papadakis, Z. Di, D. Posselt, and D.-M. Smilgies, "Structural instabilities in lamellar diblock copolymer thin films during solvent vapor uptake," *Langmuir*, vol. 24, no. 24, pp. 13815–13818, 2008.

[230] A. Böker, A. Knoll, H. Elbs, V. Abetz, A. H. Müller, and G. Krausch, "Large scale domain alignment of a block copolymer from solution using electric fields," *Macromolecules*, vol. 35, no. 4, pp. 1319–1325, 2002.

[231] R. Mieczkowski, "The determination of the solubility parameter components of polystyrene by partial specific volume measurements," *European polymer journal*, vol. 24, no. 12, pp. 1185–1189, 1988.

[232] Z. Ge and C. Xiao, "Compatibility studies with blends based on poly (n-butyl methacrylate) and polyacrylonitrile," *Journal of applied polymer science*, vol. 115, no. 6, pp. 3357–3364, 2010.

List of publications

Publications related to the dissertation

- M. Schindler, A. Kriele and P. Müller-Buschbaum, "Reorganization of the near-surface composition in pressure sensitive adhesive films stored in nitrogen atmosphere", *The Journal of Adhesion*, 2012, 684-698.
- M. Schindler, S. Pröller, T. Geue and P. Müller-Buschbaum, "Near-interface composition in pressure sensitive adhesives at the adhesive-adherent interface", *Macromolecular Reaction Engineering*, 2013, 549-554.
- M. Schindler, M. Koller and P. Müller-Buschbaum, "Pressure sensitive adhesives under the influence of relative humidity: inner structure and failure mechanisms", *ACS Applied Materials & Interfaces, submitted.*
- M. Schindler, J.-F. Moulin and P. Müller-Buschbaum, "Adhesive-adherent interfaces probed with grazing incidence small angle neutron scattering", *Journal of Applied Crystallography, submitted.*

Further publications

- B. N. Balzer, M. Gallei, K. Sondergeld, M. Schindler, P. Müller-Buschbaum, M. Rehahn and T. Hugel, "Cohesion mechanisms of polystyrene-based thin polymer films", *Macromolecules*, 2013, 7406-7414.
- M. Al-Hussein, M. Schindler, M.A. Ruderer, J. Perlich, M. Schwartzkopf, G. Herzog, B. Heidmann, A. Buffet, S.V. Roth and P. Müller-Buschbaum,"In-situ x-ray study of the structural evolution of gold nano-domains by spray deposition on thin conductive P3HT films", *Langmuir*, 2013, 2490-2497.
- M. Rawolle, K. Sarkar, M.A. Niedermeier, M. Schindler, P. Lellig, J.S. Gutmann, J.-F. Moulin, M. Haese-Seiller, A. Wochnik, C. Scheu and P. Müller-Buschbaum, "Infiltration of polymer hole-conductor into mesoporous titania structures for solid-state dye-sensitized solar cells", *ACS Applied Materials & Interfaces*, 2013, 719-729.

- R. Meier, M. Schindler, P. Müller-Buschbaum and B. Watts, "Residual solvent content in conducting polymer blend films mapped with scanning transmission x-ray microscopy", *Physical Review B*, 2011, 174205.

Scientific reports

- M. Schindler, R. Meier, M. A. Ruderer and P. Müller-Buschbaum, "Analysis of solvent residuals in thin films of conducting polymers", *Chair of Functional Materials, Annual Report*, 2009.
- M. Schindler, R. Meier, B. Watts and P. Müller-Buschbaum, "STXM-studies on the solvent content of thin conducting polymer films", *Chair of Functional Materials, Annual Report*, 2010.
- M. Schindler, A. Kriele and P. Müller-Buschbaum, "Reorganization of the near-surface composition in pressure sensitive adhesive films stored in nitrogen atmosphere", *Chair of Functional Materials, Annual Report*, 2011.
- M. Schindler, R. A. Campbell and P. Müller-Buschbaum, "Evolution of the near surface composition of pressure sensitive adhesives", *Chair of Functional Materials, Annual Report*, 2012.
- M. Schindler, S. Pröller, T. Geue and P. Müller-Buschbaum, "Investigation of the near-interface composition in pressure sensitive adhesives at the adhesive-adherent interface", *Chair of Functional Materials, Annual Report*, 2013.
- M. Schindler, M. Philipp, K. Sarkar, D. Magerl, J. Perlich and P. Müller-Buschbaum, "Inner structure of pressure sensitive adhesive films prepared by spray deposition", *Photon Science DESY, Annual Report*, 2011.

Conference talks

- M. Schindler, "Was über Reflektometrie", *Young Neutron Researchers Seminar 2011*, Garching (Germany).
- M. Schindler and P. Müller-Buschbaum, "Influence of interface interactions on the inner structure of pressure sensitive adhesive films", *DPG Frühjahrstagung*, Berlin (Germany), 25.-30.03.2012.
- M. Schindler, "Polymer mechanics", *E13 SummerSchool 2012*, Rudolfshütte (Austria).

Conference poster presentations

- M. Schindler, R. Meier and P. Müller-Buschbaum, "Analysis of solvent residuals in thin films of conducting polymers", *DPG Frühjahrstagung*, Regensburg (Germany), 21.-26.03.2010.
- M. Schindler, R. Meier and P. Müller-Buschbaum, "Solvent content of thin conducting polymer films", *FRM2 Usermeeting 2010*, Garching (Germany).
- M. Schindler, R. Meier, B. Watts and P. Müller-Buschbaum, "Solvent mapping in conducting polymer blend films using scanning transmission x-ray microscopy", *DPG Frühjahrstagung*, Dresden (Germany), 13.-18.03.2011.
- M. Schindler, M. Al Hussein, A. Buffet, S. V. Roth and P. Müller-Buschbaum, "Spray deposition of pressure sensitive adhesives followed in-situ with GISAXS", *GISAXS 2011*, Hamburg (Germany).
- M. Schindler, O. Soltwedel and P. Müller-Buschbaum, "Residual solvent in adhesive polymer films", *FRM2 Usermeeting 2012*, Garching (Germany).
- M. Schindler, E. Metwalli, S.V. Roth and P. Müller-Buschbaum, "Growth kinetics of metal films sputtered on adhesive polymer films followed with in-situ GISAXS", *DPG Frühjahrstagung*, Regensburg (Germany), 10.-15.03.2013.
- M. Schindler, S. Pröller, J.F. Moulin, T. Geue and P. Müller-Buschbaum, "Adhesive-adherent interfaces probed with neutron reflectivity and GISANS", *FRM2 Science Meeting 2013*, Grainau (Germany).
- M. Schindler, S. Pröller, T. Geue and P. Müller-Buschbaum, "Structure of adhesive-adherent interfaces probed by neutron scattering", *DPG Frühjahrstagung*, Berlin (Germany), 30.03.-04.04.2014.

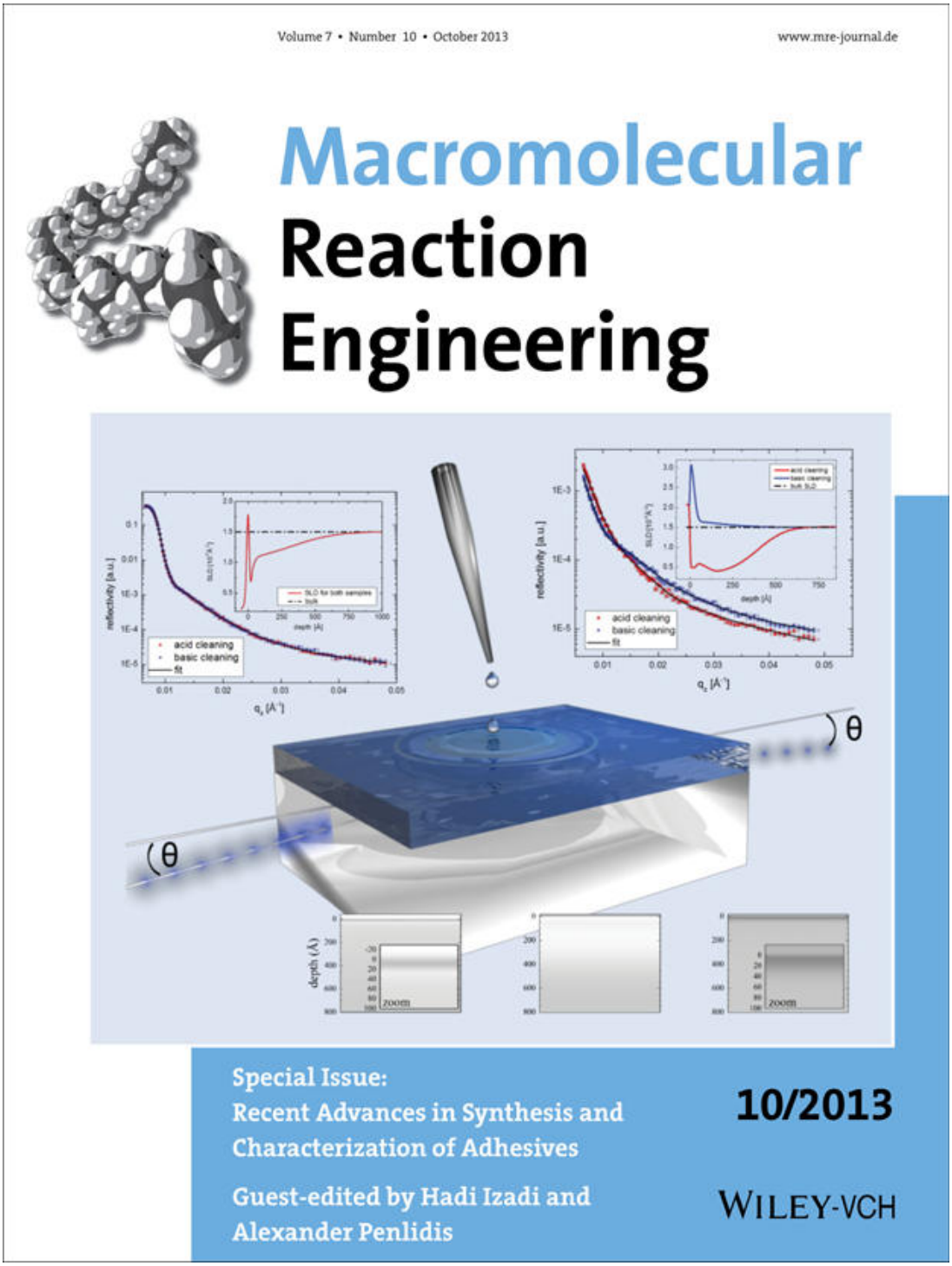

Cover picture featured on *Macromolecular Reaction Engineering Special Issue: Recent Advances in Synthesis and Characterization of Adhesives*, Volume 7, Issue 10, October 2013.

Acknowledgements

First of all, I thank Prof. Dr. Peter Müller-Buschbaum for the opportunity to work in the interesting field of polymer physics and scattering investigations.
I want to thank the secretaries Marion Waltzki and Susanna Fink. Thank you (and David) for all the interesting and funny coffee-breaks!
A lot of colleagues helped during the many beamtimes I took part in in the course of my work. I want to thank all of the people involved in the measurements: Dr. Eva Herzig, Dr. Robert Meier, Claudia Palumbiny, Martine Philipp, Kuhu Sarkar, David Magerl, Dr. Qi Zhong, Dr. Monika Rawolle, Dr. Ezzeldin Metwalli, Daniel Mosegui-Gonzalez and Stephan Pröller.
I am very grateful to all the beamline scientists who helped during the measurements and also afterwards, namely Thomas Geue, Jochen Stahn and Ben Watts from PSI, Jean-Francois Moulin from MLZ, Richard Campbell and Philip Gutfreund from ILL and finally, Matthias Schwartzkopf, Stephan V. Roth and Adeline Buffet from DESY. Moreover, I want to thank the collaborators at the campus in Garching Armin Kriele, Barbara Russ, Bizan N. Balzer and Thorsten Hugel.
Furthermore, I want to thank the students Manuel Koller and Ferdinand Jarisch for their good work and their contributions to the present thesis, as well as for their sense of humor, which made work a lot more enjoyable.
For the proof reading of the present thesis, I am indebted to Stephan Pröller, Claudia Palumbiny, Christoph Schaffer and Daniel Mosegui-Gonzalez. I am very grateful to our technicians for their help, most of all Raffael Jahrstorfer, Reinhold Funer and Lukas Hein. Furthermore, I want to thank the whole team of E13 for the good times I could enjoy in the last years.
The most important people are acknowledged the last. I want to thank my wife Nina, my daughter Leni, my parents, my brother, my grand-parents, and all others who helped me also through tough times and with whom I spent way too less time in the last months. Thank you for your patience, encouragement and support throughout the last years.